

Understanding and Engineering Zinc Oxide Nanolayer Contacts for Silicon-based Tandem Photovoltaics

by

Yan Wang

A thesis presented for the degree of

Doctor of Philosophy

Supervised by Professor R S Bonilla

Wolfson College

University of Oxford

April, 2026

Abstract

Understanding and engineering zinc oxide nanolayer contacts for silicon-based tandem photovoltaics

Yan Wang

Wolfson College, Department of Materials, University of Oxford

Thesis submitted for the Degree of Doctor of Philosophy in Materials

Trinity Term, 2026

Silicon-based tandem photovoltaics require transparent conducting oxide (TCO) contacts that simultaneously deliver optical transparency, electrical conductivity, and silicon surface passivation. Current architectures rely on indium tin oxide, whose scarcity constrains terawatt-scale deployment. Aluminium-doped zinc oxide (AZO) is a compelling earth-abundant alternative, but standard AZO layers do not naturally passivate silicon, and the interface physics governing passivation in these systems has remained poorly understood. This thesis develops the ALD-deposited SiO_X/AZO/AlO_X nanolayer stack as a multifunctional passivating contact and establishes the underlying mechanisms.

Systematic optimisation of the ALD precursor dosing ratio (H_2O:DEZ:TMA = 4:3:2.5), identified from a review of ~ 130 deposition runs, yielded a record-low recombination current density J_0 = 0.87 fA/cm^2 and an implied open-circuit voltage iV_{OC} > 740 mV on n-type silicon without an amorphous silicon interlayer. Direct XPS measurement of the buried Si/AZO interface revealed upward band bending in the silicon, opposite in polarity to the downward bending previously assumed in theoretical studies of AZO-based contacts. A 450 °C air anneal followed by controlled cooling produced effective lifetimes above 1.3 ms at 1×10^{15} cm^{-3} ECD, with the cooling rate emerging as a dominant processing variable and a beneficial kinetic window identified near 300 °C. Neutron reflectometry identified the AlO_X cap as an active hydrogen reservoir from which hydrogen migrates toward the interface during thermal processing, while the bulk AZO hydrogen content is invariant with cooling rate.

Using Kelvin-probe surface photovoltage, synchrotron XPS, transient-SPV, and ToF-SIMS, the field-effect and chemical passivation channels were decoupled for the first time in an AZO-based contact. Hydrogen released from the AlO_X cap accumulates near aluminium-containing sites at the Si/AZO interface and shifts the interfacial chemistry toward Si–H termination, while air-driven oxygen-vacancy annihilation in the AZO modulates the upward band bending at the Si surface. Because the anneal reduces this band bending yet raises the effective lifetime by two orders of magnitude, chemical passivation is identified as the dominant contribution, with the field effect a second-order channel tuned by the cooling protocol. The resulting mechanism model provides a rational basis for the continued development of indium-free passivating contacts and a scalable pathway to sustainable high-efficiency tandem photovoltaics.

Acknowledgements

Looking back, the path makes more sense than it did at the time. I think the version of me who kept asking, from primary school onwards, what any of this was for, would finally be satisfied with the answer. Doing science is hard, and I expect to keep doing it for a long time. But luckily, I was not alone in this fight. This dissertation would not be possible without the help of many important people in my life.

First and foremost, I would like to express my deepest gratitude to my supervisor, Prof. Ruy S. Bonilla. Thank you for your immense trust in me. Whenever I felt lost, your guidance gave me a clear direction to head in. You taught me how to do rigorous science, and how to think independently about which problems are worth doing. I appreciate your patience in mentoring me, giving me the freedom to explore, grow, and thrive. I am also grateful to Pietro P. Altermatt—your commitment to climate-driven research has shaped how I think about the wider purpose of this work. I also gratefully acknowledge financial support from the China Oxford Scholarship Fund (COSF).

I owe a sincere debt to my academic collaborators, whose generosity has shaped this thesis beyond what a single laboratory could achieve. Prof. Lars Bannenberg from TU Delft welcomed me into the world of thin-film reflectometry. Our long, unhurried conversations kept showing me angles on this work I would not have found alone. To Amy Navarathna, Rebekah Fraser, Jack Swallow, Matthew Sharpe, Sarah Fearn, David Grinter, and Thomas Dittrich, I am deeply thankful: each of you offered not only expertise, but also the moments around a spectrometer where a number suddenly meant something. I would also like to acknowledge the Begbroke and DWB cleanrooms, and in particular Radka Chakalova and Paul Pattinson, without whom none of the day-to-day lab work would have happened. I am also grateful to my examiners, Prof. Robert Hoye and Prof. Stuart Boden, for their thoughtful and constructive feedback, which has helped to strengthen and refine this thesis.

To the Bonilla lab, my scientific home for these years—Matt, Theo, John, Shuze, Dong, Soumya, Juan, Isabel, Avery, Erica, Xinya, Yuelin, Boom, Francesc, Paul, Darshit, James, May, Astoria, Zongtao, Mikael, Emma, and Grace—thank you for the discussions, the late evenings, the conference adventures, and the feeling of being in the same trenches as a group. A special word for Matt, John, and Theo: in different ways, each of you has been a mentor to me, sharpening my thinking. To Matt: thank you for being so generous with your time and intellect. Your constant feedback and your willingness to push back on my ideas have made me a better scholar. I will always carry those lessons with me. Shuze, Dong, and Soumya—you are far more than colleagues for me;

you became friends whose sweetness and good humour made the hardest weeks bearable. And Juan, thank you for the everyday help around the lab that so often goes unspoken.

To my friends, both near and far, you have been my constant anchors. Sijin, Jiayi, Mei, Ruixuan, Xiaohang, Maïlys, Yajing, Lechen, Xiao, Tingyu, Weijia, Jianing, Sijing, Catherine, Yuxing, and Shuting—across time zones and across the ordinary distances of life, you have kept me grounded: through late-night calls, shared jokes, and the enduring comfort of our shared past. To my housemates, Matilda and Max, thank you for lightheartedness and ease of the everyday company.

To my partner, Rory Fryer—your love has been the constant strength that powered me through all of this. Thank you for the conversations that re-lit my curiosity when it dimmed, for believing in this work on the days I struggled to, and for the countless ways, seen and unseen, you have made my life deeply beautiful.

Last but not least, I dedicate this work to my beloved parents. Thank you for your unconditional love and support over all my years. You never asked for a return, but you always gave me the confidence and sense of security to pursue my dreams. Whatever I have managed to build here, I have built standing on the ground you held for me. You are my solid rear guard, and this achievement belongs to you as much as it belongs to me.

Finally, I thank myself for my curiosity and resilience. The route to self-realisation is never easy, but I am on my way.

I have always felt like an "old soul" since I was young, finding resonance in ancient wisdom. To summarise this gruelling yet rewarding journey, I quote Mencius: "When heaven is about to confer a great office on any man, it first exercises his mind with suffering, and his sinews and bones with toil. It exposes his body to hunger, and subjects him to extreme poverty. It confounds his undertakings. By all these methods it stimulates his mind, hardens his nature, and supplies his incompetencies."

Preface

This thesis presents the research I conducted as a DPhil student from January 2023 to April 2026. No part of this thesis has been submitted for a degree at Oxford or any other institution. Contributions from other authors are fully acknowledged within the text, with appropriate references provided.

Throughout the course of this work, I have authored or contributed to the following publications:

1. Y. Wang, T. Hobson, J. Swallow, S. McNab, J. O'Sullivan, A. Soeriyadi, X. Niu, R. C. Fraser, A. Dasgupta, S. Maitra, P. P. Altermatt, R. S. Weatherup, M. Wright, R. S. Bonilla, "Impact of precursor dosing on the surface passivation of AZO/AlO_X stacks formed using atomic layer deposition," *Energy Adv.*, vol. 4, pp. 553–564, 2025.

Candidate's contribution: All experimental work and analyses presented were performed by me independently with the exception of (i) laboratory-based X-ray photoelectron spectroscopy (XPS) measurements conducted with the help from T. Hobson and J. Swallow, (ii) ellipsometry measurements conducted with the help from R. C. Fraser, and (iii) surface photovoltage measurements conducted with the help from S. McNab. Aside from these contributions, co-authors provided supervision and manuscript feedback only.

Use in this thesis: Chapter 4.

2. Y. Wang, A. Navarathna, T. D. C. Hobson, M. Wright, A. Morisset, T. Famprikis, J. O'Sullivan, P. P. Altermatt, R. S. Weatherup, L. Bannenberg, R. S. Bonilla, "Understanding the thermal history of nanolayer AZO/Al_2O_3 transparent and conductive passivating contacts for silicon solar cells," *in preparation*.

Candidate's contribution: All experimental work and analyses presented were performed by me independently, with the exception of (i) reflectometry experiments conducted jointly with A. Navarathna and L. Bannenberg at the Reactor Institute Delft, (ii) synchrotron-based XPS at Diamond Light Source (Beamline B07) was performed by me with assistance from Theodore D. C. Hobson. (iii) time-of-flight secondary ion mass spectrometry (ToF-SIMS) experiments conducted jointly with S. Fearn at Imperial College London. Aside from these contributions, co-authors provided supervision and manuscript feedback only.

Use in this thesis: Chapter 5 and Chapter 6.

3. Y. Wang, T. Dittrich, R. S. Bonilla, "Understanding transient surface photovoltage spectroscopy on AZO/Al_2O_3 nanolayers for Si-based solar cell passivation," *in preparation*.

Candidate's contribution: All sample preparations and data interpretations presented were performed by me independently, with the exception of the transient surface photovoltage measurements, data processing, and figure plotting conducted by T. Dittrich at Helmholtz-Zentrum Berlin. Aside from this contribution, co-authors provided supervision and manuscript feedback only.

Use in this thesis: Chapter 6.

4. M. K. Sharpe, M. Wright, C. D. McAleese, Y. Wang, T. D. C. Hobson, X. Niu, A. Morisset, R. S. Bonilla, “Characterisation of solar cell nanolayer interfaces using time-of-flight elastic recoil detection analysis,” *Sol. Energy Mater. Sol. Cells,* vol. 296, 2026.

Candidate’s contribution: Sample preparation and data interpretation for the AZO/AlO_X stack only. Other experimental work and analyses were performed by the co-authors.

Use in this thesis: Appendix E, Figure A 88.

5. T. D. C. Hobson, Y. Wang, M. Wright, S. Maitra, T. Abdul-Fattah, H. Zhong, Y. Xiong, X. Niu, P. Ferrer, D. Grinter, H. J. Snaith, R. S. Bonilla, “The electronic and chemical properties of silicon/zinc-oxide interfaces for multifunctional nanolayer transparent electrodes,” *in preparation*.

Candidate’s contribution: Sample preparation, lifetime characterisation, joint participation in synchrotron beamtime shifts, and partial contribution to data interpretation. Other experimental work and analyses were performed by the co-authors.

Use in this thesis: Appendix B, Figure A 82.

6. M. Wright, S. Maitra, T. D. C. Hobson, Y. Wang, P. Ferrer, D. C. Grinter, R. S. Weatherup, R. S. Bonilla, “Studying UV-induced degradation of aluminium-doped ZnO (AZO)/Al_2O_3 passivation stacks with X-ray absorption spectroscopy,” *under submission*.

Candidate’s contribution: Sample preparation and joint participation in synchrotron beamtime shifts. Other experimental work and analyses were performed by the co-authors.

Use in this thesis: None.

7. X. Niu, J. C. Gutiérrez G., J. O’Sullivan, S. Maitra, Y. Wang, Y. Xiong, J. Winger, T. Abdul-Fattah, P. de Rouffignac, A. A. R. Watt, R. S. Bonilla, “Thermally driven area-selective deposition enabling direct-write thin films,” *under submission*.

Candidate’s contribution: Microscopic and elemental characterisation, interpretation of PtO_x optical properties, and associated manuscript contributions. Other experimental work and analyses were performed by the co-authors.

Use in this thesis: None.

8. D. Trevadia, Y. Wang, X. Niu, T. D. C. Hobson, T. Matsui, M. Muller, R. S. Bonilla, “A simulation roadmap to zinc and titanium oxide passivating contact solar cells,” *in preparation*.

Candidate’s contribution: Provision of AZO/AlO_X optoelectronic and passivation data for simulation fitting, and iterative interpretation of simulation outputs. Other computational work was performed by the co-authors.

Use in this thesis: None.

List of Acronyms

Al-BSF	Aluminium back surface field
ALD	Atomic layer deposition
ARC	Anti-reflection coating
AZO	Aluminium-doped zinc oxide
BM	Burstein–Moss (shift)
BGR	Bandgap renormalisation
CAGR	Compound annual growth rate
CPD	Contact potential difference
CTE	Coefficient of thermal expansion
CVD	Chemical vapour deposition
Cz	Czochralski (silicon)
DEZ	Diethylzinc
DMAI	Dimethylaluminium isopropoxide
ECD	Excess carrier density
EDS	Energy-dispersive spectroscopy
EELS	Electron energy loss spectroscopy
ERDA	Elastic recoil detection analysis
ETL	Electron transport layer
FCA	Free carrier absorption
FGA	Forming gas anneal
FIB	Focused ion beam
FTIR	Fourier-transform infrared spectroscopy
Fz	Float-zone (silicon)
GIXRD	Grazing incidence X-ray diffraction
GZO	Gallium-doped zinc oxide
HAADF	High-angle annular dark field
HAXPES	Hard X-ray photoelectron spectroscopy
HRTEM	High-resolution transmission electron microscopy
HTL	Hole transport layer
ICL	Interconnection layer
IEA	International Energy Agency
IRENA	International Renewable Energy Agency
ITO	Indium tin oxide

IZO	Indium zinc oxide
KP	Kelvin probe
KP-SPV	Kelvin probe surface photovoltage
LCOE	Levelised cost of electricity
NR	Neutron reflectometry
PCE	Power conversion efficiency
PERC	Passivated emitter and rear cell
PL	Photoluminescence
PV	Photovoltaics
QSS-PC	Quasi-steady-state photoconductance
RCA	Radio Corporation of America (clean)
RSF	Relative sensitivity factor
SE	Spectroscopic ellipsometry
SHJ	Silicon heterojunction
SIMS	Secondary ion mass spectrometry
SLD	Scattering length density
SPV	Surface photovoltage
S-Q	Shockley–Queisser (limit)
SRH	Shockley–Read–Hall (recombination)
SRV	Surface recombination velocity
STEM	Scanning transmission electron microscopy
TCE	Transparent conducting electrode
TCO	Transparent conducting oxide
TEM	Transmission electron microscopy
TMA	Trimethylaluminium
ToF-SIMS	Time-of-flight secondary ion mass spectrometry
TOPCon	Tunnel oxide passivated contact
UHV	Ultra-high vacuum
UPS	Ultraviolet photoelectron spectroscopy
UV	Ultraviolet
VASE	Variable angle spectroscopic ellipsometry
VBO	Valence band offset
XPS	X-ray photoelectron spectroscopy
XRD	X-ray diffraction
XRR	X-ray reflectometry
ZOPCon	Zinc oxide passivating contact

List of Symbols

Greek symbols

α	Absorption coefficient (cm^{-1})
χ	Electron affinity (eV)
Δn	Excess carrier density (cm^{-3})
ε	Dielectric constant (permittivity) (F/m)
η	Power conversion efficiency (%)
λ	Wavelength (nm)
μ	Carrier mobility ($cm^2/(V \cdot s)$)
μ_e	Electron mobility ($cm^2/(V \cdot s)$)
μ_h	Hole mobility ($cm^2/(V \cdot s)$)
ρ	Resistivity ($\Omega \cdot cm$)
σ	Capture cross-section (cm^2)
σ_n	Electron capture cross-section (cm^2)
σ_p	Hole capture cross-section (cm^2)
τ_{eff}	Effective minority carrier lifetime (ms or µs)
τ_{bulk}	Bulk carrier lifetime (ms or µs)
φ	Work function (eV)
φ_{sp}	Work function of the electron analyser (eV)
θ_c	Critical angle (reflectometry) (°)

Latin symbols

B	Radiative recombination coefficient (cm^3/s)
C_n	Auger coefficient for electrons (cm^6/s)
C_p	Auger coefficient for holes (cm^6/s)
d	Film thickness (µm or nm)
D_{it}	Interface defect density ($cm^{-2}eV^{-1}$)
E_B	Binding energy (eV)
E_C	Conduction band minimum energy (eV)
E_F	Fermi level energy (eV)
E_{Fn}	Electron quasi-Fermi level (eV)
E_{Fp}	Hole quasi-Fermi level (eV)
E_g	Bandgap energy (eV)
E_V	Valence band maximum energy (eV)

G	Carrier generation rate ($cm^{-3}s^{-1}$)
iV_{OC}	Implied open-circuit voltage (V)
J_0	Recombination current density (fA/cm^2)
J_{SC}	Short-circuit current density (mA/cm^2)
k_B	Boltzmann constant (J/K or eV/K)
n	Electron concentration / refractive index (cm^{-3} / [Dimensionless])
n_i	Intrinsic carrier concentration (cm^{-3})
N_d	Donor doping concentration (cm^{-3})
p	Hole concentration (cm^{-3})
q	Elementary charge (C)
Q_f	Fixed charge density (cm^{-2})
R_{sheet}	Sheet resistance (Ω/sq)
S_{eff}	Effective surface recombination velocity (cm/s)
S_n	Electron surface recombination velocity (cm/s)
S_p	Hole surface recombination velocity (cm/s)
T	Temperature / Transmittance (°C / %)
V_{OC}	Open-circuit voltage (mV or V)
V_{surf}	Surface voltage (V)

Table of Contents

Chapter 1. Introduction 1
1.1 Climate Change 1
1.2 Photovoltaic Energy Generation 2
1.3 Silicon Solar Cells 3
1.3.1 Recombination and Passivation 3
1.3.2 Evolution of Industrial Solar Cell Architectures 4
1.3.3 Fundamentals of Passivating Contacts 5
1.3.4 The Transition to Tandems 6
1.4 Multifunctional Transparent Conducting Oxides (TCOs) for Tandem Solar Cells 6
1.5 Aluminium-doped Zinc Oxide (AZO) as Passivating Contact 9
1.6 Aims and Objectives 11
1.7 Structure of This Thesis 11
Chapter 2. Literature Review 13
2.1 Recombination and Passivation in Silicon Solar Cells 13
2.1.1 Energy Loss Channels and Theoretical Limits 13
2.1.2 Surface Recombination Challenges 16
2.1.3 Passivation Mechanisms 17
2.1.4 Characterisation Metrics 19
2.1.4.1 Surface Recombination Velocity (SRV) 19
2.1.4.2 Effective Carrier Lifetime 19
2.1.4.3 Surface Saturation Current Density 20
2.1.4.4 Implied Open-Circuit Voltage 21
2.2 Evolution of Passivating Contacts and Tandem Architectures 21
2.3 TCO as Interconnection Layer (ICL) in Tandems 22
2.3.1 Concept of Passivating TCOs 22
2.3.2 Criteria for TCOs in Photovoltaic Devices 25
2.3.3 TCOs as Interconnections in Monolithic Tandems 26
2.3.4 Indium Scarcity Bottleneck 28
2.3.5 Indium-Free Alternatives 28
2.4 Atomic Layer Deposition-AZO (ALD-AZO) as a Passivating Contact 29
2.4.1 Material Properties of AZO 29
2.4.2 ALD for AZO Thin Film Synthesis 32
2.4.3 Surface Passivation from AZO/AlO_X Thin Film Stacks 35
2.5 Summary of Scientific Gaps 39
Chapter 3. Materials and Experimental Methods 42
3.1 Sample Preparation 42

3.1.1 Silicon Wafers 42
3.1.2 Surface Cleaning and Oxide Formation 43
3.1.3 ALD 44
3.1.4 Annealing 45
3.1.5 Etching of AlO_X Capping Layer 46
3.2 Passivation Measurement 47
3.2.1 Photoconductance Decay 47
3.2.2 Photoluminescence Imaging 49
3.3 Electrical Properties 49
3.4 Optical Properties 52
3.4.1 Ultraviolet–visible (UV–vis) Spectrophotometry 52
3.4.2 Ellipsometry 53
3.5 Structural and Compositional Characterisations 55
3.5.1 Electron Microscopy 55
3.5.2 X-ray Photoelectron Spectroscopy (XPS) 56
3.5.3 Time-of-Flight Secondary Ion Mass Spectrometry (ToF-SIMS) 59
3.5.4 Reflectometry and Diffraction Techniques 61
3.5.4.1 X-ray Reflectometry (XRR) 61
3.5.4.2 Grazing Incidence X-ray Diffraction (GIXRD) 63
3.5.4.3 Neutron Reflectometry (NR) 64
3.6 Surface Photovoltage (SPV) Spectroscopy 66
3.6.1 Kelvin Probe (KP) 66
3.6.2 SPV 67
3.6.3 Transient-SPV 69
Chapter 4. Precursor Control for Optimised AZO Passivation 72
4.1 Introduction to Precursor Modulation 72
4.2 Optimisation of Passivation via Dosing Control 73
4.2.1 Recipe Design via Partial Pressure Modulation 74
4.2.2 Lifetime Analysis and Passivation Performance 75
4.2.3 Annealing Dynamics and Thermal Stability 76
4.3 Structural and Compositional Analysis 78
4.3.1 Crystallographic Phase and Texture 78
4.3.2 Nanostructural Interface and Elemental Uniformity 79
4.3.3 Chemical Stoichiometry and Dopant Activation 80
4.4 Optoelectronic Performance and Band Alignment 84
4.4.1 Electrical Transport 84
4.4.2 Carrier Mobility and Scattering Mechanisms 86
4.4.3 Optical Transparency and Bandgap Narrowing 92
4.4.4 Band Structure and Interface Alignment 95

4.4.5 Thickness Optimisation 100
4.5 Discussion and Summary 102
4.5.1 Discussion 102
4.5.2 Summary 105
Chapter 5. Post-Deposition Thermal Processing and Cooling Dynamics 107
5.1 Introduction 107
5.2 Establishing a Thermal Processing Protocol 108
5.2.1 Impact of Annealing Ambient 108
5.2.2 Peak Temperature 109
5.2.3 Selection of Dwell Duration 111
5.3 Cooling Rate as a Determinant of Passivation Quality 112
5.3.1 Decoupling Thermal Budget and Cooling Rate 112
5.3.2 Impact of Cooling Dynamics on Passivation 113
5.4 Quantifying the Cooling-Rate Dependence 116
5.4.1 Monotonic Relationship Between Cooling Rate and Passivation 116
5.4.2 Pulse Annealing 118
5.4.3 Ramp Halt Temperature Dependence 120
5.5 Structural Response of the AZO/AlO_X Stack to Thermal Treatment 122
5.5.1 Reference Configurations 122
5.5.2 Peak-Temperature and Cooling-Rate Structural Comparisons 124
5.6 Hydrogen Depth Profiles under Different Thermal Regimes 127
5.6.1 Temperature-Dependent Hydrogen Redistribution 127
5.6.2 Cooling-Rate-Dependent Hydrogen 128
5.7 Optoelectronic Properties Under Optimised Thermal Processing 129
5.7.1 Optical Transparency and Absorption Edge 129
5.7.2 Electrical Transport Properties 133
5.8 Discussion and Summary 135
5.8.1 Interpretation of Principal Findings and Mechanisms 135
5.8.2 Comparisons with Literature 136
5.8.3 Limitations and Uncertainties 137
5.8.4 Practical Implications and Future Directions 138
Chapter 6. Decoupling Field-Effect and Chemical Passivation at the Si/AZO Interface 139
6.1 Introduction 139
6.2 KP-SPV Band Bending 140
6.2.1 As-deposited and Annealed Si/AZO Samples Without AlO_X Deposition 141
6.2.2 As-Deposited Si/AZO Samples With AlO_X Etching 142
6.2.3 Cooling Rate and Capping Layer Effects on Field Effect 144
6.3 Band Alignment Under Different Cooling Rates 146
6.3.1 Band Bending and Valence Band Offset 146

6.3.2 In-situ Evolution of Si 2p Under Vacuum Annealing 148
6.3.3 Bulk AZO Stoichiometry After Annealing 149
6.3.4 Reconciling the Band-Bending Discrepancy Across Geometries 150
6.4 Decoupling of Passivation Mechanisms 152
6.4.1 Sub-Bandgap Response and Relaxation Dynamics 152
6.4.2 Decoupling Field-Effect and Chemical Passivation via Transient Kinetics 154
6.4.3 Reading Field-Effect Strength from SPV_{max} 156
6.5 Chemical Origin of Interface Passivation 158
6.5.1 Hydrogen Migration Towards the Interface 159
6.5.2 Chemical Bonding State of Interfacial Hydrogen 161
6.5.3 Si–H Bond Formation and Interface Defect Passivation 164
6.6 Overall Summary of Physical and Chemical Mechanisms 165
6.6.1 Identification of the Hydrogen Pathway for Chemical Passivation 165
6.6.2 Field-Effect and Chemical Passivation 166
6.6.3 Methodological Limitations 167
6.7 Summary 168
Chapter 7. Summary and Future Work 169
7.1 Context and Objectives 169
7.2 Principal Contributions 169
7.2.1 Record Passivation from Precursor Partial-Pressure Control (Chapter 4) 169
7.2.2 Cooling Rate as A Dominant Processing Variable (Chapter 5) 170
7.2.3 Direct Identification of the Hydrogen Pathway (Chapter 6) 170
7.3 Synthesis of Findings 171
7.4 Future Work 171
7.5 Implications for the Field 172
References 175
Appendix A: iV_{OC} data for all samples per precursor dosing condition in Chapter 4 197
Appendix B: Additional information on lab-and synchrotron-XPS in Chapters 4 and 6 199
Appendix C: Additional information on Ellipsometry data in Chapters 4 202
Appendix D: Additional data for annealing (cooling) study in Chapter 5 204
Appendix E: Additional information on Time-of-Flight Elastic Recoil Detection (ToF-ERD) 206
Appendix F: Additional information on SPV and transient-SPV 208
Appendix G: Additional information on ToF-SIMS 211

List of Figures

Figure 1.1 Schematic depiction of the evolution of high-efficiency silicon solar cell architectures: (a) PERC, (b) SHJ, and (c) TOPCon. Reproduced after ref [23]. 5
Figure 1.2 Sketch of a common perovskite/silicon tandem solar cell. The middle ITO layer that collects charge carriers and connects the top and bottom cells is highlighted and marked (*). Layer thicknesses are not to scale: the silicon bottom cell is a ~130–180 μm wafer, whereas the entire perovskite top cell, including its transport layers, is of the order of 1 μm, with the perovskite absorber itself typically 400–800 nm. Reproduced after ref [39]. 8
Figure 2.1 Schematic diagram of the three recombination mechanisms: radiative (photon emission), Auger, and non-radiative Shockley-Read-Hall (SRH) recombination via a defect state at energy E_T. Electrons are represented by blue circles, and holes by green. 13
Figure 2.2 Schematic illustration of surface passivation strategies on n-type silicon: (a) an unpassivated bare surface with high interface state density; (b) the suppression of these states through chemical passivation; and (c) the effect of both chemical and field-effect passivation. Filled and open circles denote electrons and holes, respectively, while horizontal black lines represent the distribution of surface states within the bandgap. 18
Figure 2.3 Schematic illustration of the dependence of recombination rate on carrier concentration asymmetry for an n-type substrate. 19
Figure 2.4 Schematic diagrams of (a) PERC solar cell (b) TOPCon solar cell (c) SHJ solar cell (d) two-junction two-terminal tandem solar cell with SHJ bottom cell. Reproduced after ref [84]. 22
Figure 2.5 Schematic illustration of the trade-off between electrical conductivity and optical losses in TCOs as a function of N. The increase in absorption with N is approximately linear, but may deviate due to mobility degradation at high doping levels. 25
Figure 2.6 Schematic of the current continuity and recombination layer of a 2T perovskite-silicon tandem solar cell. Reproduced after ref [115]. 27
Figure 2.7 Projected annual PV production capacity (in GW_p, represented by colour scale and contours) plotted against indium consumption per W_p and the percentage of 2019 global indium supply utilised. Reproduced after ref [84]. 28
Figure 2.8 Absorption coefficient at λ = 1100 nm vs. resistivity of TCOs: hydrogen-doped indium oxide (IOH), ITO, AZO and ZnO. Reproduced after ref [97]. 29
Figure 2.9 Crystal structure and simulated X-ray diffraction pattern of ZnO. (a) Atomic arrangement of ZnO in the hexagonal wurtzite structure, showing tetrahedral coordination between Zn and O atoms; (b) Schematic of the wurtzite unit cell with crystallographic directions; Reproduced after ref [130] (c) Simulated X-ray diffraction (XRD) pattern highlighting the characteristic diffraction peaks of wurtzite ZnO, with dominant reflections such as (100), (002), and (101); Reproduced after ref [131]. 32

Figure 2.10 Schematic diagram of the ALD ZnO surface reactions when the average ratio of –OH surface ligands: one DEZ molecule is 1.5. Reproduced after ref [152]. 33
Figure 2.11 Schematic diagram of (a) the dehydroxylation method; (b) the omitting co-reactant dose method. Idealised schematics of the expected distribution of two precursor atoms (green stands for DEZ, and orange for TMA) (c) before and (d) after adopting the omitting co-reactant dose method. For simplicity, a monolayer coverage per cycle was assumed. Reproduced after ref [151]. 35
Figure 2.12 Effective minority carrier lifetime of n-type Si samples passivated by ALD ZnO:B. The samples compare different processing conditions: (1) as-deposited ZnO:B (~75 nm) following RCA clean; (2) same as (1) after 450 °C forming gas anneal (FGA); (3) ZnO:B with an AlO_X cap prior to 450 °C FGA; (4) p-type Si with ZnO:B, AlO_X cap, and 450 °C FGA; and (5) an optimised n-type process including an additional HF dip and FGA up to 475 °C. Stars indicate implied open-circuit voltage (iV_{OC}) under 1-sun illumination. Reproduced after ref [45]. 36
Figure 2.13 (a) iV_{OC} values for SiO_2/AZO/AlO_X stacks by spatial ALD on undiffused FZ and n^+-diffused CZ n-type c-Si wafers with RCA and UV/O_3 SiO_2 layers, respectively. The ZnO and AlO_X films were both 30 nm thick. Consecutive annealing steps were performed for 5 min in FGA. (b) Recombination current density plotted as a function of sheet resistance (Rsheet) for various passivating contact technologies. The red stars represent the performance of the ALD-deposited AZO/AlO_X stack. Reproduced after ref [47]. 37
Figure 2.14 (a) Schematic illustration of the ZOPCon solar cell architecture employing an AZO-based rear passivating contact. (b) Cross-sectional Transmission Electron Microscopy (TEM) image and c) High-Angle Annular Dark-Field Scanning Transmission Electron Microscopy (HAADF STEM) image detailing the interface structure of the rear stack. (d) Light *J–V* curves under standard test conditions with different thicknesses of AZO. Reproduced after ref [50]. 39
Figure 3.1 Schematic diagram of the supercycle method. Reproduced after ref [151]. 44
Figure 3.2 Schematic of the WCT-120 Sinton Lifetime Tester. 47
Figure 3.3 Van der Pauw measurement configuration. Schematic of (a) the sample with four-point contacts A-D on top, and (b) the standard vdP measurement set-up. (c) Contact size correction factor for vdP measurements. l represents the length of the sample, while δ represents the width of the metal contact. Reproduced after ref [186]. 50
Figure 3.4 Schematic diagram of the UV–vis spectrophotometer. Light from deuterium (UV) and tungsten (visible) lamps is monochromated and split into reference and sample beams. The transmitted intensities are detected by photodiodes and processed to obtain the wavelength-dependent absorbance. 53
Figure 3.5 Schematic illustration of the ellipsometry measurement principle. 54
Figure 3.6 Schematic illustration of (a) the XPS photoemission process; (b) energy band alignment at a TCO/Si interface, illustrating the core-level and valence band energy differences used in the Kraut method to determine the VBO. 57
Figure 3.7 Schematic diagram of the ToF-SIMS measurement principle. 60

Figure 3.8 Schematic diagram of (a) X-ray reflection at an interface between vacuum (refractive index n=1) and a material with n < 1, showing the refraction and reflection of the incident beam according to Snell's law; (b) total external reflection for incident angles below the critical angle, including the formation of an evanescent wave at the interface. Reproduced after ref [204]; (c) representative X-ray reflectivity curve highlighting key features such as the critical angle, interference fringes, and the influence of thickness and interfacial roughness. Reproduced after ref [205]. 62
Figure 3.9 (a) Schematic diagram of Bragg diffraction from lattice planes with spacing d. (b) Conventional XRD geometry, where both the incident angle ω and detector angle 2θ are varied. (c) GIXRD configuration with a fixed grazing incidence angle ω. 64
Figure 3.10 Schematic of NR geometry. Reproduced after ref [216]. 65
Figure 3.11 Schematic of the Kelvin Probe setup for an AZO sample. The tip is oscillated close to the sample, generating an AC backing current i_b, nullified by applying a backing voltage V_b.....67
Figure 3.12 (a) Energy level diagram of the metal tip and sample when electrically isolated; (b) Upon electrical connection, charge redistribution occurs until the Fermi levels align, resulting in a CPD; (c) Application of a backing potential V_b compensates the CPD to enable measurement. 67
Figure 3.13 Schematic band diagrams of a semiconductor surface under dark (a), (b) and illuminated (c), (d) conditions. (a) and (c) correspond to one type of interface charge, while (b) and (d) represent the opposite charge condition, leading to different initial band bending directions. Reproduced after ref [223]. 68
Figure 3.14 Schematic of the transient-SPV measurement setup. Reproduced after ref [226]. 69
Figure 4.1 (a) Schematic diagram of the prepared sample for the passivation investigation; (b) TEM image of an AZO/AlO_X stack deposited before thickness optimisation (63 cycles AZO, 180 cycles AlO_X, compared with 105 and 250 cycles for the optimised stack in (a)). A platinum (Pt) layer, deposited during the focused ion beam (FIB) preparation to protect the sample surface, is also visible at the top. 73
Figure 4.2 Pressure ratio profiles of different precursor purges in ALD. Note: The pressure profiles are offset to allow for comparison. 74
Figure 4.3 Effective lifetime as a function of excess carrier density of the champion samples from the four different pressure profiles. Their J_0, iV_{OC}, and lifetime values are listed in Appendix A (Table A 13). The analysis plots for the optimised champion sample are shown in Appendix A (Figure A 79). 76
Figure 4.4 PL image of the champion sample from the optimised recipe. 76
Figure 4.5 iV_{OC} values vs. annealing time for the champion sample undergoing post-deposition annealing at 450 °C. 77
Figure 4.6 GIXRD spectra of as-deposited (black) and annealed (red) standard 16 nm AZO / 26 nm AlO_X samples in the range of 30°- 40°. 79

Figure 4.7 (a) High-resolution high-angle annular dark field (HAADF) TEM image of the crystal structure and defects in AZO. (b) The enlarged image is the obtained EDS micrograph for a local region of interest. (c) The averaged EDS has been plotted for elemental analysis of AZO. 80
Figure 4.8 XPS survey spectra illustrating the effects of surface Ar sputtering at 4 kV for 5 mins, for an annealed Al-rich sample. 81
Figure 4.9 (a) Example of fitting of Zn 3p & Al 2p core level peaks in XPS spectra, for optimised case only; (b) Al 2p/Zn $3p_{3/2}$ ratio across annealed, sputter-cleaned samples with the four different pressure profiles, determined from the integrated intensity of Zn $3p_{3/2}$ and Al 2p core peaks, as measured with XPS. The peak fitting curves for samples from the four different recipes are shown in Appendix B, Figure A 80. 82
Figure 4.10 Resistivity and sheet resistance of samples from the different profiles. 85
Figure 4.11 Mobility and carrier concentration of samples from the four different pressure profiles. The electron mobility is shown on the left axis with pink triangles, and carrier concentration is on the right axis with cyan hexagons. 91
Figure 4.12 Resistivity as a function of annealing time for AZO/AlO_X sample processed under the optimised pressure profile. The AZO films were annealed with an AlO_X capping layer, which was subsequently removed prior to measurement. For consistency, the non-annealed sample (0 min) was also deposited with an AlO_X cap and etched prior to measurement. 92
Figure 4.13 Transmittance curves of single-sided 40-nm-thick AZO samples on fused quartz (Section 3.1.1) from the four different pressure profiles in the wavelength range of (a) 200-1200 nm; (b) 400-600 nm. 93
Figure 4.14 Tauc plots from the optical band diagram of samples from the four different pressure profiles. 95
Figure 4.15 AZO Band diagram deduced from the combination of XPS and UV-vis. The bulk electronic band structure of the AZO films was deduced by combining the valence band maximum (VBM) measured from standard XPS surface scans with the apparent optical gap (E_g) obtained from UV-vis spectroscopy. 97
Figure 4.16 Valence band offset of optimised AZO sample and Si substrate, as determined from XPS measurements via the Anderson method ($\Delta E_{V,AM}$) from bulk valence band positions, and the Kraut method ($\Delta E_{V,KM}$) from valence band positions at the AZO/Si interface. Conduction band positions are inferred from the apparent optical gaps determined by transmission measurements (Section 3.4.1). 100
Figure 5.1 (a) Lifetime curves of AZO samples annealed in air and N_2 at 450 °C. (b) PL image of AZO samples annealed in air (left two pieces) and forming gas (right two pieces) at 450 °C. 109
Figure 5.2 Effective lifetime values measured as a function of annealing duration at 450 °C in air. All samples were followed by a 10-min slow cooling after the annealing dwell. 111
Figure 5.3 Schematic of six temperature profiles representing distinct thermal histories during post-deposition annealing. 113

Figure 5.4 Effective minority carrier lifetime of SiO_2/AZO/AlO_X passivation stacks annealed under varying thermal conditions. The data compares three peak temperature regimes (300 °C, 450 °C, 600 °C) and two cooling dynamics (fast cooling vs. slow cooling). 116
Figure 5.5 (a) Schematic of the temperature profiles for 4 different cooling rates (CR1-CR4) during post-annealing cooling from 450 °C. (b) Effective lifetime curves as a function of excess carrier density for 4 different cooling rates. The curves shown represent the closest-to-mean representative sample for each cooling condition. 117
Figure 5.6 PL images of AZO passivation samples cooled at four different rates. Top-left: CR1 (slowest), bottom-left: CR2, top-right: CR3, bottom-right: CR4 (fastest). The colour scale indicates PL intensity proportional to effective lifetime. The PL images correspond to the representative samples shown in Figure 5.5 (b). 118
Figure 5.7 Schematic illustration of the pulse annealing protocol, here with an example of a 10-minute heating one. Samples underwent repeated cycles of heating (450 °C for 5, 10, or 15 minutes), slow cooling down for 10 minutes, and lifetime measurement. The orange markers indicate measurement points after each cooling step. 118
Figure 5.8 Effective lifetime evolution as a function of accumulated pulse annealing duration at 450 °C. Three pulse intervals are compared: 5 minutes (purple diamonds), 10 minutes (orange triangles), and 15 minutes (green squares). 120
Figure 5.9 Schematic of the temperature profiles for the ramp halt cooling profiles (CP1-CP5). All samples underwent identical annealing at 450 °C for 20 minutes, followed by holding at different intermediate temperatures before slow cooling to ~ 210 °C. 120
Figure 5.10 Effective lifetime as a function of ramp halt temperature. The 300 °C hold yields optimal passivation, which identifies 300 °C as a critical temperature window for interface optimisation during cooling. 122
Figure 5.11 Schematic diagrams of the first batch of XRR sample configurations. Sample 3 depicts the standard AZO/AlO_X sample structure. Samples 1 and 2 have no AZO underlayer, and Sample 4 has no AlO_X cap. All annealed samples (2, 3, 4) were treated at 450 °C for 20 min on a hotplate in air with a 10-min slow cool-down. 123
Figure 5.12 XRR results of the samples shown in Figure 5.11 exhibiting (a) reflectivity curves and (b) the SLD depth profiles fitted based on (a). 123
Figure 5.13 XRR results of samples shown in Table 5.3 exhibiting the fitted SLD depth profiles of three different thermal treatment samples (blue: Sample 3, as-deposited; yellow: Sample 4, 600 °C slow-cooled; green: Sample 1, 500 °C slow-cooled) 126
Figure 5.14 XRR results of samples shown in Table 5.3 exhibiting the fitted SLD depth profiles of two different cooling rate samples (blue: Sample 1, slow cooled; yellow: Sample 2, fast cooled) 126
Figure 5.15 NR results corresponding to Samples 1 (500 °C slow-cooled), 3 (as deposited), and 4 (600 °C slow-cooled) from Table 5.3. 128

Figure 5.16 NR results corresponding to Samples 1 (slow-cooled) and 2 (fast-cooled) from Table 5.3. 129
Figure 5.17 Transmittance spectra of various (a) ZnO and (b) AZO film configurations on glass substrates. For samples without AlO_X, both sides were deposited with 20 nm ZnO/AZO (40 nm in total); For samples with AlO_X, both sides were deposited with 20 nm ZnO/AZO + 20 nm AlO_X (80 nm in total). 130
Figure 5.18 (a) Tauc plots for various AZO and ZnO film configurations. The peak near 3.40 eV in the ZnO traces, and the minimum above it, arise from excitonic absorption at the ZnO band edge; the linear regions used for the extrapolations lie below this structure. (b) Apparent optical gap vs. configuration (ZnO: blue; AZO: pink), grouped by thermal state (as-deposited, annealed) and AlO_X deposition condition (with AlO_X, without AlO_X). Error bars in (b) are ± 0.01 eV on the individual values; a difference between any two points carries ± 0.02 eV. See text for the estimation. Inset: schematic of the bifacial sample structures, with the grey layer representing glass. 133
Figure 5.19 Resistivity of uncapped AZO films as a function of film thickness for as-deposited (black) and annealed (red) conditions. 134
Figure 5.20 Carrier mobility (left, black) and carrier concentration (right, red) of uncapped AZO films of 20 nm and 56 nm thickness in as-deposited and annealed conditions. 135
Figure 6.1 Schematic of the sample configurations and annealing states used throughout this chapter. All samples in Sections 6.2 and 6.3 were fabricated on silicon substrate A (~ 4 Ω·cm n-type CZ c-Si wafers, ~ 135 µm thick, solar-grade, saw-damage etched; ~ 4 × 4 cm in size for samples in Section 6.2, ~ 0.8 × 0.8 cm in size for samples in Section 6.3). All samples in Sections 6.4 and 6.5 were fabricated on silicon substrate B (30–60 Ω·cm n-type CZ c-Si wafers, ~ 675 µm thick, semiconductor-grade, chemo-mechanically polished ultra-flat; ~ 4 × 4 cm in size). All samples were RCA cleaned and had a ~1.2 nm chemically grown SiO_X interlayer (Sections 3.1.1 and 3.1.2). The measured effective lifetime values shown in the figure correspond to samples fabricated on substrate B. The trend of the lifetime value differences among them also applies to samples fabricated on substrate A. 140
Figure 6.2 Box plot of the pristine Si/AZO (AlO_X has never been deposited) CPD values in four different conditions: as-deposited sample measured in dark and under illumination; slow-cooled sample measured in dark and under illumination. The 2D map of these two samples is shown in Appendix F, Figure A 89. 142
Figure 6.3 Box plot of the as-deposited Si/AZO (AlO_X etched before SPV measurements) CPD values in dark and under illumination. The 3D map of this sample is shown in Appendix F, Figure A 90. 143
Figure 6.4 Box plot of the annealed Si/AZO/AlO_X (AlO_X etched after annealing and before SPV measurements) CPD values in four different conditions: fast-cooled sample measured in dark and under illumination; slow-cooled sample measured in dark and under illumination. The 2D map of these two samples is shown in Appendix F, Figure A 91. 145

Figure 6.5 In-situ XPS of (a)-(b) with AlO_X capping layer/standard AZO stacks; (c)-(d) AZO samples without AlO_X capping layer. (a) and (c) show the temperature profiles during in-situ measurements; (b) and (d) show the Si $2p_{3/2}$ binding energy changes in accordance with in-situ annealing and cooling. Samples were in the configuration of Si/2nm AZO/2nm AlO_X, or Si/4nm AZO. 149
Figure 6.6 Contour plots of the transient SPV signal as a function of photon energy (vertical axis) and delay time after the laser pulse (horizontal axis) for the four AZO samples. (a)-(d): Sample 1-4 in Figure 6.1. The colour scale encodes the SPV amplitude in mV on a logarithmic scale, with warm colours (pink-red-yellow) representing the largest positive SPV amplitudes and cool colours (green-blue) representing smaller positive amplitudes. Black pixels correspond to signals at or below the instrument noise floor (|SPV| < ~1 mV). 154
Figure 6.7 Transient SPV line-cuts extracted from Figure 6.6 at five representative photon energies for the four samples. (a)-(d): Sample 1-4 in Figure 6.1. The vertical blue reference line marks the electron diffusion time across the 675 μm silicon substrate (~5 μs). In (d), the pink shaded region (~ 10^{-4} to ~ 2×10^{-3} s) highlights the bulk-limited regime in which Sample 4 sustains a near-constant plateau long after Samples 1–3 have entered their decay; the red arrow marks the decay knee near ~ 10^{-3} s, whose order of magnitude matches the 2 ms bulk lifetime measured independently by QSSPC. 156
Figure 6.8 ToF-SIMS results showing H- intensity between as-deposited (blue) and annealed (orange) standard 16nm AZO/26nm AlO_X samples. The depth axis 0 nm is defined by the Si^- half peak centroid. 160
Figure 6.9 ToF-SIMS results showing (a) as-deposited and (b) annealed H- and SiO- signal amplitude of standard AZO/AlO_X samples. Data were smoothed using a 10-point moving average. 161
Figure 6.10 ToF-SIMS results showing (a) OH^-, (b) $ZnOH^-$, (c) $AlOH^-$, and (d) AlH^- intensities between as-deposited (blue) and annealed (orange) standard AZO/AlO_X samples. 163
Figure 6.11 Depth profile of the $^{29}SiH^-/^{29}SiHO^-$ intensity ratio for the as-deposited (blue) and annealed (orange) standard AZO/AlO_X samples. Dotted lines show the raw ratio computed point-by-point; solid lines are the same data after 10-point moving-average smoothing. The elevated ratio extending to depths > 10 nm is attributed to knock-on redistribution of H into the silicon by the primary ion beam and does not represent a physical hydrogen concentration at that depth (see main text). 165
Figure 6.12 Schematic of the passivation model for the SiO_X/AZO/AlO_X passivating contact. Hydrogen released from the AlO_X cap during the 450 °C anneal migrates toward the Si/SiO_X interface and forms Si–H termination (chemical passivation). Ambient-O_2 in-diffusion annihilates oxygen vacancies in the AZO, modulating the upward band bending already present at the Si surface (field-effect passivation). The net effect of the anneal is to reduce that band bending, as the passivation of acceptor-type interface states removes negative interface charge. 168

Figure A 79 (a) Effective lifetime, (b) J_0 and (c) iV_{OC} analysis plots for the highest τ_{eff} vs. Δn of samples in profile C (Optimised). Analysis is conducted following the algorithm and code reported in github.com/OxfordInterfacesLab/PySintonAnalysis. 198
Figure A 80 XPS spectrum range covering Zn $3p_{1/2}$ & $3p_{3/2}$ and Al 2p core levels for the 4 annealed samples in Chapter 4, with fitted integrated intensity for Zn $3p_{3/2}$ and Al 2p in each case. Fitting was carried out in CasaXPS using Tougaard background and convolved Gaussian/Lorentzian lineshape. 199
Figure A 81 XPS spectra showing Si 2p core levels at the AZO/SiO_X/Si interface under different sputter time. AZO layer is thinned by sputtering with Ar gun (4 keV) such that Si core levels can be detected and the shift in Si 2p and Zn 3p peaks relative to bulk positions allows band-bending to be estimated in Section 4.4.4 200
Figure A 82 The fitted band diagram of Si/AZO interface of (a) as-deposited and (b) annealed Si/2nm AZO/2nm AlO_X samples measured without sputtering via synchrotron-XPS. 200
Figure A 83 The XPS spectrum for the three Si/SiO_X/2nm AZO/2nm AlO_X samples in Table 6.2, with fitted integrated intensity for Zn 3p and Si 2p in each case. 200
Figure A 84 The XPS spectrum for the two Si/SiO_2/annealed AZO samples in Table 6.3, with fitted integrated intensity for (a) and (c) Zn 3p, and (b) and (d) O 1s in each case. 201
Figure A 85 Spectroscopic ellipsometry data for 40-nm-thick AZO films deposited under the four precursor pressure profiles described in Section 4.2.1. Refractive index n as a function of wavelength. 202
Figure A 86 Spectroscopic ellipsometry data for 40-nm-thick AZO films deposited under the four precursor pressure profiles described in Section 4.2.1. Extinction coefficient k as a function of wavelength. 203
Figure A 87 The fitting curves and measured spectroscopic ellipsometric curves of the optimised sample in Chapter 4. 203
Figure A 88 ToF-ERD analysis of the passivation stacks. The ToF-ERD measurements and initial data processing presented here were performed by our collaborator Matthew K. Sharpe at the Surrey Ion Beam Centre, utilising a 16 MeV $^{127}I^{8+}$ ion beam with an incident and exit angle of 69.5°and a scattering angle of 41°. A summary of the relevant data are reproduced here from the raw datasets for comparison. (a) Representative Time-of-Flight versus Energy (ToF-E) 2D coincidence histogram for the AZO/AlO_X sample, illustrating the distinct kinematic separation of recoiled elements (H, C, O, Al, Si, and Zn). (b) Extracted hydrogen (H) concentration (at.%) at specific layer locations within the AZO/AlO_X stack, comparing the as-deposited and annealed conditions. (c, d) Elemental depth profiles obtained via modelling from the experimental data for the AZO/AlO_X samples in the (c) as-deposited and (d) annealed states. At each depth, the total atomic composition is normalised to 100% to clearly delineate the material structure. 207

Figure A 89 2D SPV mapping of Si/AZO (AlO_X has never been deposited). (a) As-deposited sample measured in dark; (b) As-deposited sample measured under illumination; (c) Slow-cooled sample measured in dark; (d) Slow-cooled sample measured under illumination. 209
Figure A 90 3D SPV mapping of as-deposited Si/AZO (AlO_X etched before SPV measurements) (a) in dark, and (b) under illumination. 209
Figure A 91 2D SPV mapping of annealed AZO/AlO_X (AlO_X etched after annealing and before SPV measurements). (a) Fast-cooled sample measured in dark; (b) Fast-cooled sample measured under illumination; (c) Slow-cooled sample measured in dark; (d) Slow-cooled sample measured under illumination. 210
Figure A 92 The SPV signal as a function of photon energy at different time delays for the four samples, revealing details about charge separation via interface states. Shaded regions labelled A (near/sub-bandgap, photon energy $\lesssim$ 1.1 eV), B (above-bandgap early decay, 20 ns–100 µs), and C (late-stage decay, ≥100 µs). 210
Figure A 93 ToF-SIMS results showing (a) Al^- and (b) $^{68}ZnO^-$ intensities between as-deposited (blue) and annealed (orange) standard AZO/AlO_X samples. 211
Figure A 94 ToF-SIMS results showing (a) $Al_2O_3^-$ intensity, (b) $Al_2O_3^-/AlO^-$ intensity ratios, and (c) ZnO_2^-/ZnO^- intensity ratios between as-deposited (blue) and annealed (orange) standard AZO/AlO_X samples. 212
Figure A 95 ToF-SIMS results showing $^{29}SiO^-$ intensity between as-deposited (blue) and annealed (orange) standard AZO/AlO_X samples. 212
Figure A 96 ToF-SIMS results showing (a) $^{29}SiH^-/Si^-$ and (b) $^{29}SiHO^-/Si^-$ intensity ratios between as-deposited (blue) and annealed (orange) standard AZO/AlO_X samples. 212

List of Tables

Table 3.1 Summary of silicon substrates used in this work. 42
Table 3.2 Summary of sample structures used across this thesis. 43
Table 3.3 Wet etching results of AlO_X capping layer using ellipsometry. 47
Table 4.1 The approximate pressure peak for each precursor and their ratios in the four different ALD pressure profiles. 74
Table 4.2 n, k, and thickness of samples from the four different pressure profiles measured from ellipsometry. Data is acquired at 600 nm wavelength. The complete spectroscopic dispersion data, including n(λ) and k(λ) across the full measured wavelength range (210 – 1690 nm) for all four pressure profiles, are provided in Appendix C (Figure A 85 and Figure A 86). The fitting curves and measured curves of the optimised sample are provided in Appendix C, Figure A 87. 102
Table 5.1 Summary of passivation metrics across different annealing temperature regimes. Dwell times were adjusted to ensure fair comparison of activation potential. All samples were followed by a 10-min slow cooling after the annealing dwell. 110
Table 5.2 XRR fitting results of thickness, density, and roughness on different samples and layers. The fitted thicknesses carry an uncertainty of approximately 1%, that is ± 0.2–0.5 nm over the range tabulated. The density and roughness are more strongly correlated with one another and are correspondingly less well determined, and for the bilayer samples the total stack thickness is better constrained than the individual sub-layers. See Section 3.5.4.1 for the basis of these figures. 124
Table 5.3 The second batch of XRR samples: their annealing conditions and effective lifetime values. 125
Table 6.1 Sample preparation conditions and their KP-SPV results (CPD values are in mean ± standard deviation) in Section 6.2.1 - 6.2.3. 143
Table 6.2 XPS results on ΔE_{CL} (Si-TCO) of samples featuring Si/2nm AZO/2nm AlO_X. The fitting curves of the peaks are shown in Appendix B, Figure A 83. 148
Table 6.3 XPS results on Zn $3p_{3/2}$/O 1s Lattice between fast-cooled and slow-cooled samples. Samples were made with the configuration of Si/16nm AZO/26nm AlO_X, annealed, and then etched off the AlO_X capping layer, leaving Si/annealed AZO. The fitting curves of the peaks are shown in Appendix B, Figure A 84. 150
Table A 12 iV_{OC} values for 5 samples per condition in group A, B, C, D with the average and standard deviation values calculated. (A, B, C, D represent Al-rich, Zn-deficient, optimised, and H2O-deficient, respectively) 197
Table A 13 J_0, iV_{OC}, and lifetime (@ 1E15 ECD) values of all the champion samples in group A,B,C,D. (A, B, C, D represent Al-rich, Zn-deficient, optimised, and H2O-deficient, respectively) 197
Table A 14 Effective lifetime (μs @ 1E15 ECD) as a function of both peak temperature and dwell time. All samples were followed by a 10-min slow cooling after the annealing dwell. It shows the shift in passivation dynamics. Lower temperatures require extended thermal budgets to overcome the

activation barrier, whereas a high temperature (600 °C) initiates rapid degradation following a brief activation window. The optimal balance is achieved at 450 °C. 204
Table A 15 Effective lifetime (μs @ 1E15 ECD) as a function of both peak temperature and cooling rates under the thermal profiles in Figure 5.3. Raw data for Figure 5.4. 204
Table A 16 Effective lifetime (μs @ 1E15 ECD) as a function of cooling rates (CR) under the thermal profiles in Figure 5.5 (a). 205
Table A 17 Effective lifetime (μs @ 1E15 ECD) as a function of ramp halt temperature under the thermal profiles in Figure 5.10. 205

Chapter 1. Introduction

1.1 Climate Change

The Earth's climate is changing rapidly. Atmospheric carbon dioxide (CO_2) concentration has risen from ~280 ppm in pre-industrial times to over 425 ppm as of early 2026 [1-3]. This increase is primarily driven by the combustion of fossil fuels for energy generation. The consequences are already visible: in 2024, the global mean temperature was ~1.55 °C above pre-industrial levels [4, 5], and extreme weather events, rising sea levels, and ecosystem disruptions are becoming more frequent and severe.

The energy sector is the largest contributor to global greenhouse gas emissions, accounting for ~75.7% of total emissions [6]. Electricity and heat production alone contribute ~29.7% [6]. Consequently, the decarbonisation of the energy sector has become a priority for climate change mitigation. However, the challenge is substantial: global energy demand continues to grow, particularly in developing economies. Meeting such demand while reducing emissions requires a transformation of the energy system.

To provide a global framework for this transition, international climate policy has established ambitious decarbonisation targets. The Paris Agreement aims to limit global warming to 1.5 °C above pre-industrial levels [7]. Achieving this target requires net-zero carbon emissions by 2050, which implies a massive phase-out of fossil fuels and a rapid scale-up of renewable energy sources. Among these alternatives, solar energy has emerged as a leading candidate due to its rapidly declining costs and deployment potential [8]. The International Energy Agency (IEA) projects that global renewable power capacity will double by 2030, with an increase of approximately 4600 GW over the 2025–2030 period [9]. Solar photovoltaics (PV) are hence expected to account for nearly 80% of this expansion,

making them the principal driver of global renewable growth [9]. The transition to clean energy is not only an environmental necessity, but also a major technological and economic undertaking.

1.2 Photovoltaic Energy Generation

Solar energy devices convert sunlight into electric energy via the photovoltaic (PV) effect. Compared with traditional thermal power generation, PV devices have distinct advantages. They contain no moving parts, release zero emissions during the operation phase, and require very little maintenance. Moreover, solar energy is the most abundant energy resource. The solar flux that reaches the Earth's surface in 1.5 hours is larger than the total global energy consumption in a whole year [10]. These characteristics make PV well-suited for large-scale sustainable electricity generation.

Photovoltaic capacity is quoted throughout in peak watts (W_p), the power delivered under standard test conditions of 1000 W m^{-2} AM1.5G irradiance at 25 °C, rather than in watts of delivered energy. The distinction matters because a photovoltaic installation delivers its rated power only under those reference conditions; annual energy yield depends additionally on local irradiance, temperature and system losses, so that capacity in W_p and generation in W are not interchangeable quantities.

In the past two decades, the PV industry has expanded rapidly. Global installed PV capacity has increased from less than 1 GW_p in 2000 to nearly 2.9 TW_p by the end of 2025 [11]. The Compound Annual Growth Rate (CAGR) of PV installations was about 27% between 2014 and 2024 [12], which was accompanied by a record annual addition in 2025, when 647 GW_p of new solar capacity was installed worldwide [11]. This continued acceleration can be largely attributed to its low cost. By 2024, the global weighted average levelised cost of electricity (LCOE) for utility-scale solar PV stabilised at USD 0.043/kWh, making it 41% cheaper than the least-cost fossil fuel-fired alternative [13]. This confirms solar PV as one of the most cost-competitive sources of new electricity generation globally. Such low cost has been possible thanks to enhanced manufacturing throughput, economies of scale, and advancements in cell architecture and module design, which have steadily improved the power conversion efficiency (PCE).

Despite the recent strides, meeting the scale demand for climate change mitigation requires continued reductions in cost and increases in cell efficiency. For a single junction solar cell, the theoretical maximum efficiency is ~33%, known as the Shockley-Queisser (S-Q) limit [14]. To overcome the single junction limit, one widely adopted strategy is to use multiple junctions in a tandem configuration. Such devices employ two or more solar absorber materials with complementary bandgaps for spectral splitting. This approach allows high-energy photons to be absorbed by a wide-bandgap cell at the top, sun-facing side of the tandem stack, reducing thermalisation losses.

As a result, such architecture harvests the energy of the incident photons more effectively than single-junction devices, offering a potential to exceed the 33% limit [15]. Consequently, developing tandem technology is currently regarded as one of the most promising technical routes for the next generation of the PV industry.

1.3 Silicon Solar Cells

Currently, wafer-based crystalline silicon (c-Si) technology plays a dominant role in the global PV market, accounting for ~98% of total PV production in 2024 [12]. This dominance is attributed to the abundance of silicon (the second most common element in the Earth's crust), its well-understood material properties, and a mature industrial manufacturing chain. The research focus is on mitigating specific loss mechanisms in silicon solar cells to match the commercial performance with the record lab efficiency of 27.9% (LONGi, n-type HTBC, 158.66 cm^2 designated area, certified by ISFH, October 2025) [16]. Record efficiencies quoted throughout this thesis are those current at the time of writing (April 2026), as listed in the Solar Cell Efficiency Tables (Version 67) [17].

1.3.1 Recombination and Passivation

The primary obstacle to reaching higher efficiency targets lies in the loss of photoexcited charge carriers, with recombination of photogenerated electron–hole pairs being the most critical among the addressable loss mechanisms. These losses are strongly influenced by defects, which are predominantly located at silicon surfaces and metal–semiconductor contacts. To suppress the high

density of dangling-bond defects at these interfaces, surface passivation has become a key strategy. This is achieved through two complementary mechanisms: chemical passivation, which saturates bonds via dielectric films, and field-effect passivation, which employs fixed charges to repel minority carriers from the surface [18, 19].

1.3.2 Evolution of Industrial Solar Cell Architectures

The evolution of industrial cell architectures has been driven by improvements in surface passivation. Figure 1.1 shows the evolution of silicon solar cell architectures from PERC to passivated contact technologies. Evolving from the aluminium back surface field (Al-BSF) cell, which first entered commercial production in the 1970s, the PERC (Passivated Emitter and Rear Cell) technology effectively passivated the rear silicon surface and thus led the market until the early 2020s [20, 21]. Despite its advances, PERC remained constrained by the direct metal-silicon contacts required for current extraction, as shown in Figure 1.1 (a). At the contact points, the protective passivation layer must be removed to allow the metal electrodes to touch the silicon. Such direct physical contact creates recombination because the high density of electronic states at the metal-semiconductor interface allows charge carriers to annihilate rapidly, losing their energy as heat. To overcome such efficiency limit, the industry shifted toward passivated contact technologies that decouple the metal from the silicon: Silicon Heterojunction (SHJ), shown in Figure 1.1 (b), which utilises thin amorphous silicon layers for superior interface protection; and TOPCon (Tunnel Oxide Passivated Contact), as shown in Figure 1.1 (c), which employs an ultra-thin tunnel oxide to passivate the entire contact area while still allowing carrier transport via a tunnelling mechanism. In 2024, TOPCon was acknowledged as the next dominant commercial successor after PERC, projected to capture 70% of global module sales due to its excellent balance of efficiency, thermal stability, and manufacturing compatibility with existing lines [22].

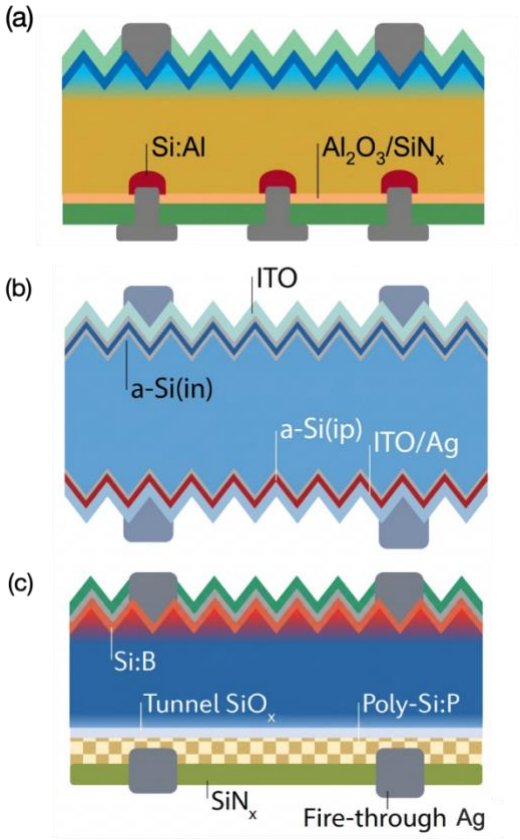


Figure 1.1 Schematic depiction of the evolution of high-efficiency silicon solar cell architectures: (a) PERC, (b) SHJ, and (c) TOPCon. Reproduced after ref [23].

1.3.3 Fundamentals of Passivating Contacts

The success of SHJ and TOPCon has shifted the paradigm from traditional p-n junctions toward the implementation of passivating contacts. A passivating contact is a multilayer architecture that simultaneously achieves two goals: surface passivation and carrier selectivity. For surface passivation, an ultra-thin tunnel oxide or a wide-bandgap semiconductor is deposited between the metal and the silicon. This layer saturates silicon dangling bonds at the silicon surface and provides chemical passivation, reducing the number of defect centres that mediate carrier recombination [24].

Although the metal is separated from the silicon, efficient charge carrier extraction must still be achieved. For carrier selectivity, the contact uses specific band alignment designed to selectively transport one carrier type (e.g. electrons) while blocking the other (holes), ensuring only the majority-carriers reach the metal electrode. By separating the metal from the silicon, these architectures reduce recombination losses at the contact. These passivating contact architectures now define the

performance frontier for single-junction silicon cells and form the foundation for tandem device integration [25].

1.3.4 The Transition to Tandems

In a tandem configuration, high-efficiency architectures such as SHJ and TOPCon serve as ideal bottom cells by leveraging their passivating contacts to provide the high open-circuit voltage (V_{OC}) necessary to maximise the overall efficiency of the multi-junction system. Among various configurations, silicon-perovskite tandems have emerged as one of the most promising candidates [26]. Lead halide perovskite semiconductors offer high single-junction efficiencies, reaching 26.9% on a 1.017 cm^2 cell (certified by NPVM, March 2025) [27]. They also have a tunable bandgap that allows for precise spectral optimisation when paired with silicon. By integrating high-efficiency top cells with passivated silicon bottom cells, monolithic tandem devices have already demonstrated efficiencies exceeding 34%, with a certified record of 35.0% on a 1.0028 cm^2 two-terminal cell (LONGi, certified by ESTI, July 2025) [17, 28], marking a major step beyond the limits of single-junction photovoltaics.

1.4 Multifunctional Transparent Conducting Oxides (TCOs) for Tandem Solar Cells

Transparent conducting oxides (TCOs) are a class of materials with a combination of optical transparency and electrical conductivity that originates from wide bandgaps (typically >3 eV) and degenerate doping [29]. As a result, TCOs are critical components in optoelectronic devices, such as flat-panel displays, touch screens, and solar cells [30].

In high-efficiency photovoltaics, TCOs serve as lateral current collectors, anti-reflection coatings, and protective interlayers [31]. In standard SHJ cells, for instance, indium tin oxide (ITO) is the industry standard for collecting current from the thin-film silicon layers, as previously depicted in Figure 1.1 [32]. Figure 1.2 shows a typical monolithic tandem structure where the perovskite top cell and silicon bottom cell are connected in series. In advanced silicon-perovskite tandems, indium-based TCOs

like ITO or indium zinc oxide (IZO) have become standard materials for the front electrode and a crucial middle layer that connects the top and bottom cells together [26].

Sunlight enters through the top TCO electrode and is absorbed by the perovskite layer. In the perovskite cell, photogenerated electrons move upward to be collected by the top Ag electrode, while holes move downward toward the middle ITO layer. In the silicon cell, photogenerated holes move downward to the back Ag electrode, while electrons move upward toward the middle ITO layer. The middle ITO layer, which is also called an Interconnection Layer (ICL), is crucial for the carrier flow [33]. Holes from the top cell and electrons from the bottom cell meet in the ICL and recombine. This neutralising recombination at the interface allows the electrical current to flow through the entire stack. Beyond facilitating efficient charge transport, the ICL also acts as part of a passivating contact for the silicon surface. For example, when properly integrated on the silicon bottom cell, the ITO-based ICL, together with an underlying passivation layer, can reduce recombination at the interface through a combination of chemical and field-effect passivation. As a result, the interface remains electrically selective while preserving low recombination losses.

However, the heavy reliance on indium, a scarce by-product of zinc mining, has raised concerns over long-term scalability of ITO-based devices and may become a critical supply-chain bottleneck for terawatt-scale deployment [34, 35]. Resource projections indicate that current indium supply levels are incompatible with future global PV expansion unless consumption is significantly reduced [36, 37]. Such scarcity motivates the search for earth-abundant, indium-free alternatives [38].

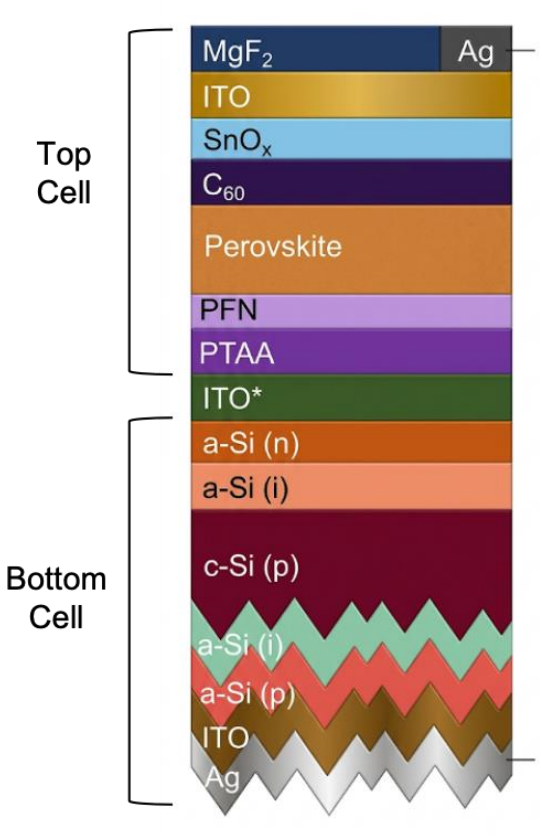


Figure 1.2 Sketch of a common perovskite/silicon tandem solar cell. The middle ITO layer that collects charge carriers and connects the top and bottom cells is highlighted and marked (*). Layer thicknesses are not to scale: the silicon bottom cell is a ~130–180 µm wafer, whereas the entire perovskite top cell, including its transport layers, is of the order of 1 µm, with the perovskite absorber itself typically 400–800 nm. Reproduced after ref [39].

While the state-of-the-art perovskite-silicon tandems employing SHJ bottom cells have already surpassed 34% efficiency [28], the development of cost-effective, indium-free alternatives faces a different reality. Conventional TCOs provide excellent electrical conductivity, but they typically do not offer adequate surface passivation when deposited directly on silicon [40]. As a result, single-junction silicon cells utilising TCO or dopant-free metal-oxide passivating contacts have historically underperformed compared to established passivating contact technologies such as SHJ and TOPCon [24]. This performance gap, caused primarily by the inherent conflict between achieving superior interface passivation and efficient carrier transport, has limited their practical viability for high-efficiency tandem applications. Currently, such conflict remains unresolved because the fundamental interface physics, such as stoichiometric balance and hydrogen redistribution dynamics, are not yet understood. Without a clear physical model, further optimisation is likely to be incremental and empirical rather than systematic. Therefore, if indium-free architectures are to reach the 34%+ benchmark set by their SHJ-based counterparts, a more fundamental understanding of

the underlying interface physics is required [26, 28]. The core challenge I aim to tackle in this work is elucidating the interface physics that enables a TCO electrode to function as a high-quality passivating contact, thus enabling their integration into silicon-based tandem devices.

1.5 Aluminium-doped Zinc Oxide (AZO) as Passivating Contact

Among indium-free candidates, aluminium-doped zinc oxide (AZO) has emerged as a promising alternative because zinc and aluminium are earth-abundant and low-cost [41-43]. However, standard AZO window layers do not naturally passivate the silicon surface [44]. To unlock its potential as a passivating contact, a new synthesis route via Atomic Layer Deposition (ALD) has been recently proposed [45]. The primary advantage of using ALD is its ability to incorporate residual hydrogen from the chemical precursors into the film [46]. During thermal annealing, hydrogen is thought to diffuse to the silicon interface, where it can saturate dangling bonds and improve surface passivation [47]. Additionally, the sequential, self-limiting nature of ALD enables the growth of highly conformal films, which is essential for uniform coverage on the complex textured surfaces of industrial silicon cells [48, 49].

Applying this ALD-based approach to AZO has already led to significant performance gains. In dopant-free metal-oxide contacts, a record PCE of 24.3% (1 cm^2, certified by SIMIT) was recently achieved using an AZO-based stack [50], representing the highest performance for silicon cells where carrier selectivity is driven entirely by metal oxides without using traditional doped silicon layers.

Notably, it is important to distinguish this from other indium-free technologies. Indium-free SHJ solar cells, which retain doped amorphous silicon layers for carrier selectivity while replacing ITO with alternative TCOs such as tantalum-doped tin oxide (TTO), have demonstrated efficiencies exceeding 25% [51]. While these SHJ cells are more efficient, they still suffer from parasitic absorption in their silicon layers. The AZO-based dopant-free architecture aims to avoid this by simplifying the cell structure, but a performance gap remains.

Currently, the record for AZO-based silicon cells remains below the performance required for high-efficiency tandem operation. Experimentally, monolithic perovskite/silicon tandems exceeding 34%

have been achieved predominantly based on high-efficiency SHJ bottom cells, with standalone efficiencies above 26% [28, 52]. Recent modelling indicates that silicon bottom cells can achieve practical efficiencies up to ~28.9% under ideal conditions, while contributing to tandem efficiencies approaching ~37% [53]. Accordingly, bottom-cell efficiencies approaching 28–29% are desirable for sufficient power output under spectrally filtered tandem illumination.

Achieving the >34% efficiency potential of silicon-based tandem cells requires addressing several key scientific questions regarding the AZO/Si interface: First, we need to understand the structural and chemical evolution of the interface during thermal processing. While it is known that ALD precursors and subsequent annealing provide hydrogenation, it remains unclear how the specific hydrogenation dynamics and film stoichiometry evolve under thermal process and how they influence the final structural and chemical states at the interface. Understanding this process is essential for moving from experimental optimisation to a repeatable passivation methodology. Second, it is challenging to decouple the passivation mechanisms for AZO passivating contacts. Determining the relative contributions of chemical passivation (saturating silicon dangling bonds) and field-effect passivation (repelling carriers via electric fields) is critical for enabling rational device optimisation. These mechanisms impose different constraints on interface defect density, carrier concentration, and band alignment. As a result, the distinction could also help to identify the ultimate limits of carrier selectivity and stability achievable with AZO, or other TCO-based contacts. Third, we need to comprehend the physical limitations to charge transport and contact resistance associated with TCO-based passivating contacts. This trade-off remains one of the most challenging topics in the field: improved passivation often comes at a cost of increased contact resistance. Elucidating the interface physics that determines how carriers cross the TCO-silicon barrier is vital for commercial-grade cells. While addressing the contact resistance lies beyond the scope of this thesis, the work presented here aims to address the first two challenges. By investigating the hydrogenation dynamics and electrical properties of the AZO/Si interface, this work provides the scientific basis needed to improve the efficiency of indium-free silicon architectures for tandem integration.

1.6 Aims and Objectives

This thesis aims to develop a mechanistic understanding of ALD-deposited AZO nanolayers as passivating contacts for silicon-based tandem solar cells. In particular, this work seeks to establish the relationships between processing conditions, interface structure, and passivation performance, with emphasis on the role of thermal treatment in determining the final passivating contact properties.

To address this aim, the thesis pursues four main objectives:

(1) To optimise the ALD processing conditions for AZO deposition on n-type silicon and evaluate their influence on surface passivation metrics.

(2) To investigate the role of post-deposition thermal treatment, including annealing and cooling conditions, in determining the final passivation behaviour.

(3) To characterise the structural and chemical properties of the AZO/Si interface and correlate these with the measured passivation performance.

(4) To examine the relative roles of chemical passivation and field-effect passivation in the operation of AZO-based contacts.

More broadly, this work aims to provide a scientific basis for the rational development of indium-free passivating contacts for next-generation silicon-based tandem devices.

1.7 Structure of This Thesis

This thesis is organised into seven chapters. Following this introduction, the structure is as follows:

Chapter 2 reviews the relevant literature on silicon solar cells, surface passivation, TCOs, and the current understanding of oxide-based passivating contacts.

Chapter 3 describes the materials, sample preparation procedures, and experimental methods used throughout this work.

Chapter 4 examines the influence of ALD processing conditions on the passivation properties of AZO nanolayers on silicon.

Chapter 5 investigates the effects of post-deposition thermal treatment on passivation behaviour, with particular attention to the cooling conditions.

Chapter 6 presents the structural, electronic, and chemical characterisation of the AZO/Si interface and relates these observations to the measured passivation response.

Chapter 7 summarises the main findings of the thesis, discusses their implications for indium-free passivating contacts, and outlines directions for future work.

Chapter 2. Literature Review

2.1 Recombination and Passivation in Silicon Solar Cells

2.1.1 Energy Loss Channels and Theoretical Limits

The performance of crystalline silicon solar cells is fundamentally limited by carrier recombination, the process by which photogenerated electron–hole pairs are annihilated before their energy can be extracted. Within the silicon absorber, three recombination mechanisms govern carrier losses: radiative, Auger, and defect assisted recombination, as depicted in Figure 2.1. When considering both intrinsic Auger and Radiative recombination, the practical efficiency limit of crystalline silicon lowers to 29.4% [54, 55], from the 33% S-Q thermodynamic limit for only-radiative recombination, in a single junction [14, 56].

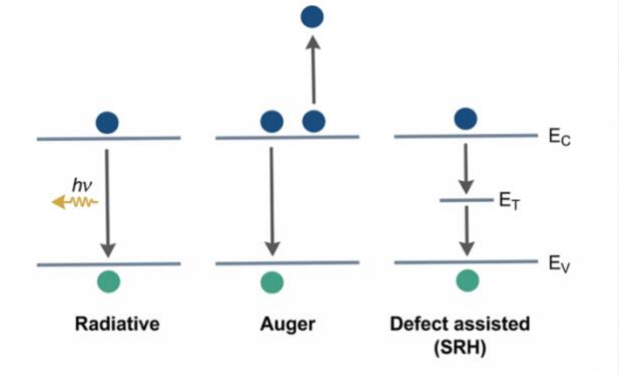


Figure 2.1 Schematic diagram of the three recombination mechanisms: radiative (photon emission), Auger, and non-radiative Shockley-Read-Hall (SRH) recombination via a defect state at energy E_T. Electrons are represented by blue circles, and holes by green.

Radiative recombination (intrinsic) occurs when an electron transitions directly from the conduction band to the valence band. This process emits a photon with energy equal to the bandgap. In indirect semiconductors like silicon, radiative recombination is relatively weak due to the requirement for phonon participation [57]. The net radiative recombination rate is given as [58]:

$$U_{\text{rad}} = B\left(np - n_i^2\right) \tag{2.1}$$

where B is the radiative recombination probability and is specific to the semiconductor, n and p are electron and hole concentrations, respectively, and n_i is the intrinsic carrier concentration. Equation (2.1) is written in the general form, which reduces differently in the two doping regimes. In the moderately doped material used throughout this thesis (n-type, ~4 Ω·cm, N_D ≈ 1.2 × 10^{15} cm^{-3}), the injection levels of interest are comparable to or larger than the doping density, so both n and p vary with illumination, and the rate is superlinear in Δn.

If the silicon is heavily doped, three changes would follow. First, the material would remain in low injection under any practical illumination, so that $n \approx N_D$ and the expression would linearise to $U_{\text{rad}} \approx B \cdot N_D \cdot \Delta n$, giving an injection-independent radiative lifetime $\tau_{\text{rad}} = \frac{1}{BN_D}$. With B = 4.73 × 10^{-15} cm^3 s^{-1} [59], at N_D = 10^{19} cm^{-3}, this is ~21 μs, nearly four orders of magnitude shorter than in the base material. Second, the coefficient B is not itself a constant at high doping: free-carrier screening of the electron–hole Coulomb interaction reduces it [60], and in an optically thick wafer photon recycling lowers the effective value obtained from a lifetime measurement still further, so an accurate treatment requires a doping- and injection-dependent parameterisation [60]. Third, the intrinsic carrier concentration entering the equation must be replaced by an effective value $n_{i,\text{eff}}^2 = n_i^2 \exp\left(\frac{\Delta E_g}{k_B T}\right)$ to account for bandgap narrowing, which becomes significant above ~10^{18} cm^{-3} and enhances all recombination channels [61]. In practice, these effects are subordinate to Auger recombination (Equation (2.2) below), whose rate scales as N_D^2. With C_n = 2.8 × 10^{-31} cm^6 s^{-1}, at 10^{19} cm^{-3} the lifetime is only ~36 ns [62]. This is why the heavily doped regions of a silicon solar cell are intrinsically recombination-limited, and why the passivating-contact architectures discussed in Section 2.2 seek to achieve carrier selectivity through an interfacial layer rather than through heavy doping of the absorber itself.

Auger recombination (intrinsic) involves three particles, which can be either two electrons, one hole (eeh); or two holes, one electron (ehh). When an electron and a hole recombine, the released energy

transfers to a third carrier. This third carrier subsequently loses the energy through thermalisation. The Auger recombination rate can be expressed as [63]:

$$U_{\text{Aug}} = \left(C_n n + C_p p\right)\left(np - n_i^2\right) \tag{2.2}$$

where C_n and C_p are Auger coefficients for electrons and holes, respectively. At room temperature, this mechanism becomes dominant at high carrier concentrations, typically above 10^{17} cm^{-3} [64].

Shockley-Read-Hall (SRH) recombination (extrinsic) is mediated by defect states within the forbidden bandgap. These defect states, arising from impurities, lattice disruptions, or other crystallographic imperfections act as intermediaries that allow photoexcited carriers to recombine more easily. The SRH recombination rate can be expressed as [65, 66]:

$$U_{\text{SRH}} = \frac{np - n_i^2}{\frac{p + p_1}{N_T \sigma_n v_{\text{th}}} + \frac{n + n_1}{N_T \sigma_p v_{\text{th}}}} \tag{2.3}$$

where N_T is the trap density, σ_n and σ_p are the capture cross sections for electrons and holes, respectively, and v_{th} is the thermal velocity. The terms n_1, p_1 represent the electron and hole concentrations when the quasi-Fermi level coincides with the trap energy level E_T, and are given by [67]:

$$\begin{aligned} n_1 &= n_i \exp\left(\frac{E_T - E_i}{kT}\right), \\ p_1 &= n_i \exp\left(\frac{E_i - E_T}{kT}\right) \end{aligned} \tag{2.4}$$

where n_i is the intrinsic carrier concentration, k is the Boltzmann constant, T is the absolute temperature, and E_i is the intrinsic Fermi level. While intrinsic Auger recombination sets the fundamental limit for high-quality wafers, SRH recombination is the dominant loss mechanism in practical devices, particularly at the abruptly terminated crystal lattice occurring at the surfaces [68].

Auger recombination differs from the other two channels in that it cannot be suppressed by improving material quality. It is a three-particle process involving only band states: the energy released when an electron and hole recombine is transferred to a third free carrier rather than to a photon or a defect level. Because it requires no intermediate state in the gap, its rate is fixed by the carrier populations and by the Coulomb interaction between carriers, both of which are intrinsic to the semiconductor. Improving crystal quality removes Shockley–Read–Hall centres and therefore reduces defect-assisted recombination without limit in principle, but it leaves the Auger rate unchanged. In crystalline silicon this constraint is particularly severe because the indirect gap makes radiative recombination weak, so that Auger dominates the intrinsic loss and, together with the residual radiative term, sets the 29.4% single-junction efficiency limit quoted above.

The injection level at which this limit becomes relevant can be estimated directly. One-sun AM1.5G illumination delivers a photon flux above the silicon bandgap of $\varphi \approx 2.7 \times 10^{17}$ cm^{-2} s^{-1}, equivalent to a short-circuit current density of ~43.5 mA cm^{-2}. Distributed uniformly through the 135 µm wafers used in this work, this corresponds to an average generation rate $G = \varphi/W \approx 2.0 \times 10^{19}$ cm^{-3} s^{-1}. Equating this to the Auger rate alone, using an ambipolar Auger coefficient $C_a = 1.66 \times 10^{-30}$ cm^6 s^{-1} [63, 69], gives a steady-state excess carrier density of $\Delta n = (G/C_a)^{1/3} \approx 2.3 \times 10^{16}$ cm^{-3} and a corresponding Auger-limited lifetime of ~1.1 ms. Solving instead self-consistently, with the surface- and bulk-limited lifetime of 3.38 ms measured on the best samples of Chapter 4 included in parallel, gives $\tau_{eff} \approx 1.0$ ms at $\Delta n \approx 2.0 \times 10^{16}$ cm^{-3}, with Auger recombination accounting for approximately 70% of the total recombination rate. The passivation quality achieved in this work is therefore sufficient for the intrinsic Auger channel, rather than the surfaces, to become the dominant loss at one-sun operating injection.

2.1.2 Surface Recombination Challenges

Surface recombination is predominantly defect-assisted and is therefore well described by SRH theory. Accordingly, Equation (2.3) can be reformulated to describe the surface recombination rate:

$$U_S = \frac{n_s p_s - n_i^2}{\frac{p_s + p_1}{N_{st}\sigma_n v_{th}} + \frac{n_s + n_1}{N_{st}\sigma_p v_{th}}} \quad (2.5)$$

where n_s and p_s are the carrier concentrations at the surface, and N_{st} is the density of surface states per unit area (cm^{-2}). The resulting unit of U_S is $cm^{-2}s^{-1}$. At a real surface, there is a continuous distribution of energy states. As a result, the density of interface states, which is often referred to as D_{it}, is a function of energy.

Even small unpassivated regions on a silicon surface can dominate overall device losses [70]. Consequently, suppressing these surface-related losses via advanced passivation is the primary requirement for reaching higher cell efficiency.

2.1.3 Passivation Mechanisms

Modifications to a silicon surface to reduce the recombination rate are globally termed 'surface passivation'. Figure 2.2 illustrates how the surface passivation can be improved. As depicted in Figure 2.2 (a), an unpassivated bare surface exhibits high density of interface states. Two primary methodologies are employed to suppress this.

First, chemical passivation, shown in Figure 2.2 (b), reduces the density of recombination centres by saturating dangling bonds with hydrogen or oxygen atoms. Hydrogen is particularly effective because its small atomic size allows it to penetrate the interface [71]. Such a process is frequently enhanced through thermal annealing, which facilitates hydrogen diffusion toward the silicon-dielectric interface. Chemical passivation reduces interface defect density (D_{it}) from typical values of 10^{13} cm^{-2} eV^{-1} (unpassivated) to the level of 10^{10} cm^{-2} eV^{-1} (well passivated) [72].

The second method, field-effect passivation (Figure 2.2 (c)), manipulates minority carrier concentrations at the surface through fixed charges (Q_f). The effectiveness of the field-effect passivation can be understood from the dependence of the recombination rate on carrier concentrations, which is proportional to the product of electron and hole densities ($R \propto np$), as

illustrated in Figure 2.3 (for n-Si). The recombination rate is maximised when n ≈ p, and is reduced when there is a strong asymmetry between carrier populations.

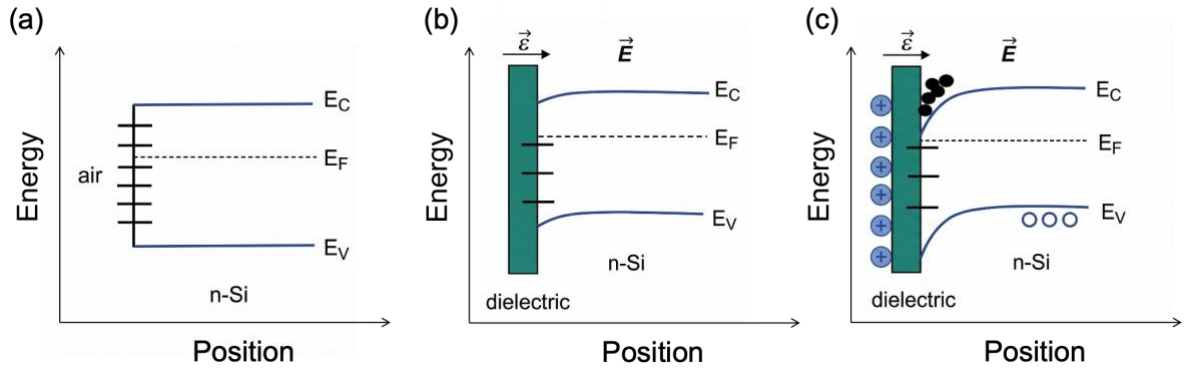


Figure 2.2 Schematic illustration of surface passivation strategies on n-type silicon: (a) an unpassivated bare surface with high interface state density; (b) the suppression of these states through chemical passivation; and (c) the effect of both chemical and field-effect passivation. Filled and open circles denote electrons and holes, respectively, while horizontal black lines represent the distribution of surface states within the bandgap.

To induce carrier asymmetry, one type of charge carrier is accumulated in response to the polarity of a surface electric field, creating a space charge region (SCR). The resulting band bending leads to either an accumulation layer, where the charge consists primarily of majority carriers, or an inversion layer, where enough minority carriers are attracted to the surface to exceed the concentration of bulk majority carriers. Therefore, by inducing either accumulation or inversion, one carrier type is strongly suppressed at the interface, reducing the recombination rate even in the presence of interface defects.

Practical high-efficiency solar cells combine both mechanisms: for example, SHJ cells use intrinsic a-Si:H for chemical passivation and adjacent doped a-Si:H layers for field-effect [73]. TOPCon employs an ultrathin SiO_2 layer for chemical passivation, capped with heavily doped polysilicon for field-effect [74].

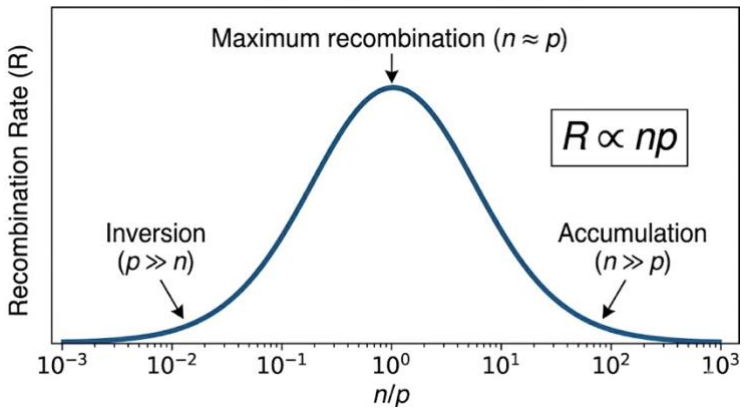


Figure 2.3 Schematic illustration of the dependence of recombination rate on carrier concentration asymmetry for an n-type substrate.

2.1.4 Characterisation Metrics

2.1.4.1 Surface Recombination Velocity (SRV)

In real surfaces, the total recombination can be expressed as an energy-integrated SRH process across the bandgap, often termed effective surface recombination velocity (S_{eff}) [64]. The lower the S_{eff}, the lower the recombination. S_{eff} is defined as:

$$S_{\text{eff}} = \frac{U_s}{\Delta n} \tag{2.6}$$

where U_s is the surface recombination rate and Δn is the excess minority carrier concentration at the surface.

Historically, SRV served as the primary experimental metric for assessing surface quality, as it relates directly to the SRH defect-mediated recombination. Modern characterisation uses contactless photoconductance (PC) decay or transient measurements [75] to extract SRV, because it eliminates the need for physical contacts or specific device structures, allowing for the non-destructive analysis of larger specimen areas.

2.1.4.2 Effective Carrier Lifetime

The central parameter extracted from PC decay measurements is the effective carrier lifetime (τ_{eff}). It represents the average time a photogenerated minority carrier survives before recombining. τ_{eff} integrates bulk (τ_b) and surfaces (τ_s) contributions as:

$$\frac{1}{\tau_{\text{eff}}} = \frac{1}{\tau_b} + \frac{1}{\tau_s} \tag{2.7}$$

The relationship between τ_s and S_{eff} was formalised by Luke and Cheng (Equation (2.8)) [76], and under the condition $S_{\text{eff}} \cdot W/D$ < 0.25 with sufficiently low SRV, it simplifies to Equation (2.9) [77].

$$S_{\text{eff}} = \sqrt{D\left(\frac{1}{\tau_s}\right)} \tan\left(\frac{W}{2}\sqrt{\frac{1}{D}\left(\frac{1}{\tau_s}\right)}\right) \tag{2.8}$$

$$S_{\text{eff}} = \left(\frac{1}{\tau_{\text{eff}}} - \frac{1}{\tau_B}\right)\frac{W}{2} \tag{2.9}$$

where W represents the sample width and D is the carrier diffusion coefficient.

2.1.4.3 Surface Saturation Current Density

Traditionally, the emitter saturation current density (J_{0e}) has been the standard metric to assess the combined recombination originating from surface states in highly doped emitters. For undiffused silicon surfaces where field-effect passivation is significant, the surface saturation current density (J_{0s}) serves as a superior comparative metric [78]. Unlike other metrics, J_{0s} remains largely independent of the surface dopant concentration under practical conditions, offering a purer evaluation of the dielectric film's passivation quality. J_{0s} is typically extracted from contactless PC measurements of τ_{eff}. By isolating the surface lifetime component τ_s, the injection-dependent recombination current parameter $J_0(\Delta n)$ can be determined using the following relation:

$$J_0(\Delta n) = \frac{d}{d(\Delta n)}\left[n_{i,\text{eff}}^2 \sqrt{\frac{D}{\tau_s}} \tan\left(\frac{W}{2}\sqrt{\frac{1}{D\tau_s}}\right)\right] \tag{2.10}$$

where $n_{i,\text{eff}}$ is the effective intrinsic carrier concentration. The final J_{0s} value is typically extracted as a constant by finding the average across the most injection-independent (flattest) region of the $J_0(\Delta n)$ curve [18]. Lower J_{0s} values indicate superior passivation.

2.1.4.4 Implied Open-Circuit Voltage

The implied open-circuit voltage (iV_{oc}) provides a complementary measure of passivation quality. If iV_{OC} is measured at a carrier density equivalent to 1 sun, it is representative of a solar cell under operation. Because the quasi-Fermi level splitting in the semiconductor is dictated by the excess carrier density, iV_{oc} can be calculated directly from the known excess minority carrier concentration Δn obtained during a standard PC τ_{eff} measurement [79]:

$$iV_{oc} = \frac{kT}{q} \ln\left(\frac{\Delta n\left(N_{dop} + \Delta n\right)}{n_{i,\text{eff}}^2}\right) \tag{2.11}$$

where q is the elementary charge, and N_{dop} is the bulk dopant concentration. Higher iV_{oc} values indicate superior passivation.

2.2 Evolution of Passivating Contacts and Tandem Architectures

The evolution of silicon solar cell architectures from Al-BSF through PERC to passivating contact technologies (SHJ and TOPCon) has been driven by the progressive mitigation of recombination at metal–semiconductor interfaces. Figure 2.4 illustrates such a structural evolution in detail. PERC technology, Figure 2.4 (a), reduced rear recombination using dielectric layers but suffered from recombination at direct metal-silicon front contacts, achieving a practical limit at 24.5% by Trina Solar [80].

To overcome this limitation, TOPCon technology (Figure 2.4 (b), employing an ultra-thin tunnel oxide layer capped with doped polysilicon at the rear) and SHJ (Figure 2.4 (c), showing thin intrinsic amorphous silicon (a-Si:H) and TCO layers) have successfully decoupled the highly recombinative metal contacts from the silicon absorber. Consequently, TOPCon and SHJ have achieved certified large-area efficiencies of 26.6% (335.2 cm^2 total area, certified by ISFH, October 2025) and 26.8% (LONGi, 274.4 cm^2 total area, certified by ISFH, October 2022), respectively, while the outright silicon cell record, 27.9% (LONGi, 158.66 cm^2 designated area, certified by ISFH, October 2025), is held by a hybrid back-contact structure combining TOPCon and heterojunction contacts rather than by

either technology alone [81, 82]. Mass-production average efficiencies are 26.6% (JinkoSolar) and 26.8% (LONGi), respectively [81, 83].

To surpass the single-junction limit, the industry is now pursuing monolithic tandem configurations (e.g., perovskite/silicon, as shown in Figure 2.4 (d)), which require the integration of specialised TCO layers. The following sections review the role of TCOs in tandem device architectures and the development of indium-free alternatives.

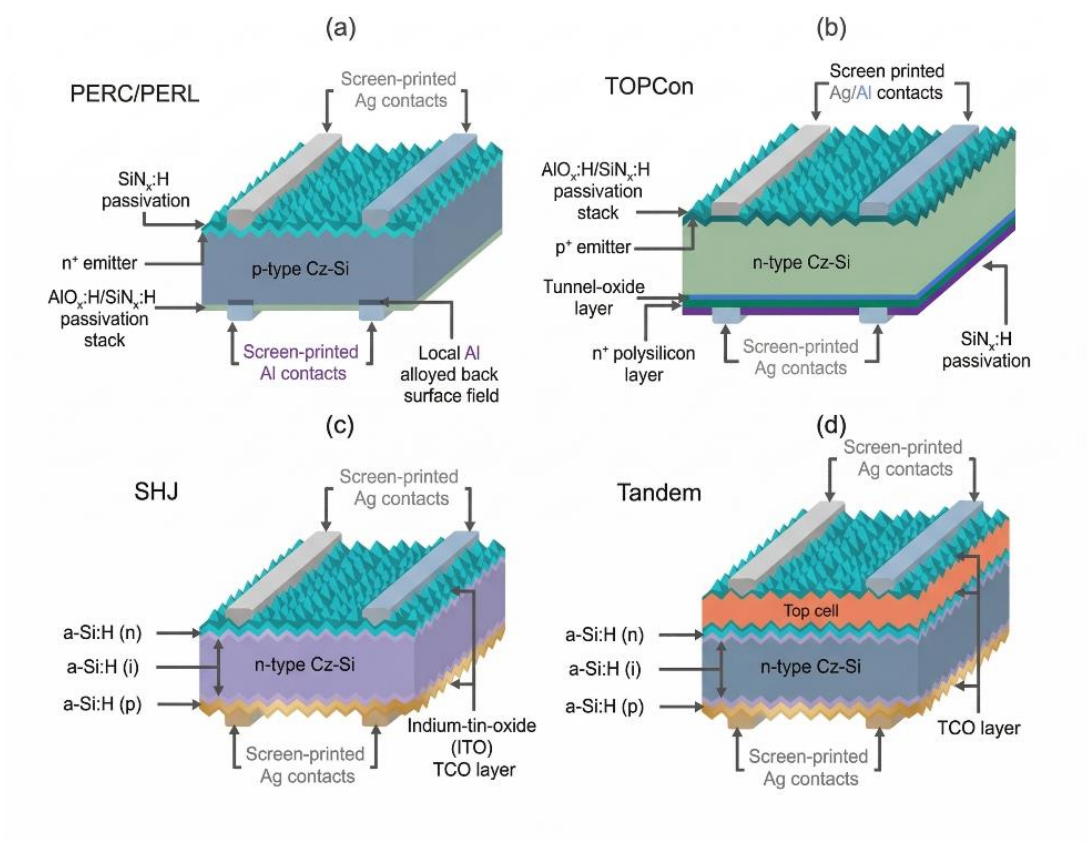


Figure 2.4 Schematic diagrams of (a) PERC solar cell (b) TOPCon solar cell (c) SHJ solar cell (d) two-junction two-terminal tandem solar cell with SHJ bottom cell. Reproduced after ref [84].

2.3 TCO as Interconnection Layer (ICL) in Tandems

2.3.1 Concept of Passivating TCOs

TCOs combine high optical transmittance with high electrical conductivity by using wide-bandgap semiconductors (E_g > 3 eV) which suppresses visible interband transitions and by degenerately doping them to introduce a high concentration of free charge carriers. Therefore, the design of TCOs

is governed by a competition between electrical and optical performance. The resistivity (ρ) of the film is determined by the carrier concentration (N) and mobility (μ), expressed as [85]:

$$\rho = \frac{1}{q \cdot N \cdot \mu} \tag{2.12}$$

where q is the majority-carrier charge. The sheet resistance (R_{sheet}) is expressed as:

$$R_{\text{sheet}} = \frac{\rho}{t} \tag{2.13}$$

where t is thickness. Increasing the doping density (N) effectively reduces the R_{sheet}.

Mobility (μ) in Equation (2.12) can be defined as:

$$\mu = \frac{q\tau}{m^*} \tag{2.14}$$

where τ is the carrier relaxation time, representing the average time between two scattering events, and *m** is the carrier effective mass [86]. Therefore, μ increases when scattering sources are reduced *and m** is minimised [87]. Increasing N can reduce μ via impurity scattering following the Conwell-Weisskopf theory, so careful control is required [88, 89].

Transmittance (T_x) follows the Beer-Lambert law [85, 90]:

$$T_x(\lambda) = \left(1 - R_x(\lambda)\right)^2 \cdot e^{-\alpha(\lambda)\, t} \tag{2.15}$$

where R_x is reflectance, and *α* is the absorption coefficient. According to Equation (2.13) increasing t reduces R_{sheet}, but it also reduces T_x. As a result, t needs to be balanced.

Increasing *N* leads to parasitic optical losses through free carrier absorption (FCA) at longer wavelength, following the Drude model of *α* [88, 90, 91]:

$$\alpha = \frac{\lambda^2 q^3 N}{4\pi^2 \varepsilon_0 c^3 n (m^*)^2 \mu_{\text{opt}}} \tag{2.16}$$

where λ is wavelength, ε_0 is the permittivity of free space, c is the speed of light in vacuum, n is the refractive index, and μ_{opt} is the optical mobility (mobility not inclusive of grain-to-grain scattering).

As *N* increases, *α* rises, particularly at longer λ. Furthermore, a high N shifts the plasma wavelength (λ_p) toward shorter wavelengths. λ_p describes the wavelength at which absorption occurs in a TCO, determined by the natural oscillation frequency of its free electron gas, and is given by [92]:

$$\lambda_p = 2\pi c \sqrt{\frac{m^* \varepsilon_{\text{TCO}}}{N q^2}} \tag{2.17}$$

For incident light $\lambda < \lambda_p$, the real part of the dielectric function is positive, and the TCO behaves as a dielectric, where free electrons cannot respond fast enough to the oscillating electromagnetic field, and light passes through. For $\lambda > \lambda_p$, the real part of the dielectric function is negative, and the TCO becomes reflective or absorptive rather than transparent [91, 92]. For most TCOs, λ_p is in the near-infrared. While visible and ultraviolet light passes through, near-infrared and infrared light is lost [93-95]. As a result, TCOs with high λ_p values are necessary. This is achieved by reducing *N,* and increasing *m**, *μ* and ε_{TCO}.

Standard silicon solar cells rely on wide-bandgap dielectric interlayers (e.g., SiO_2, a-Si, AlO_X, SiN_x) for surface passivation. While effective at suppressing recombination, these insulators inherently block current flow, necessitating complex local patterning (as in PERC) or ultra-thin tunnelling layers (as in TOPCon) for carrier extraction. Unlike standard dielectrics, TCOs are inherently conductive. A passivating TCO that can simultaneously provide surface passivation and efficient carrier transport would unify these dual functions into a single layer, simplifying the device architecture. As a result, developing a single layer that can serve both functions remains a significant research objective [24].

However, achieving simultaneous passivation and optoelectronic performance in TCOs is challenging. To begin with, conventional TCOs do not naturally provide surface passivation when deposited on silicon [45]. Moreover, while TCOs require high carrier concentrations *N* to achieve good electrical conductivity, increasing *N* introduces severe trade-offs. As discussed in relation to Equations (2.14), excessive doping degrades carrier mobility μ via increased ionised impurity

scattering. Furthermore, as defined by Equation (2.16), a high free carrier density increases free carrier absorption FCA, leading to parasitic optical losses at longer wavelengths. Finally, from a passivation perspective, the heavy doping required for high conductivity often introduces structural disorder into the lattice, generating defect states that act as interface recombination centres and degrade chemical passivation [96].

2.3.2 Criteria for TCOs in Photovoltaic Devices

The fundamental optoelectronic behaviour of TCOs highlights the inherent trade-offs between electrical conductivity and optical transparency, which is schematically illustrated in Figure 2.5. These trade-offs directly translate into practical design criteria for photovoltaic applications.

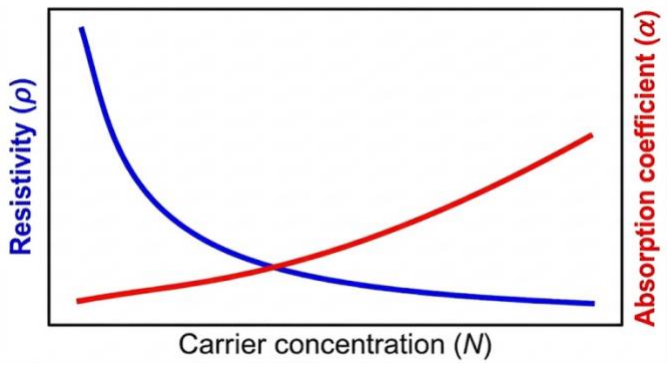


Figure 2.5 Schematic illustration of the trade-off between electrical conductivity and optical losses in TCOs as a function of N. The increase in absorption with N is approximately linear, but may deviate due to mobility degradation at high doping levels.

First, a low optical absorption coefficient is required to minimise parasitic losses. Based on Equation (2.16), free carrier absorption increases with carrier concentration and wavelength, making near-infrared losses particularly significant. In practice, absorption coefficients below ~10^3 cm^{-1} in the visible and near-infrared range are typically targeted [97]. Second, high electrical conductivity is essential for efficient lateral current transport. As described by Equation (2.12), this requires a combination of high carrier concentration and mobility. In practical devices, resistivity values on the order of 10^{-3} Ω·cm are generally required to achieve sufficiently low sheet resistance [86].

In addition to bulk transport and optical properties, the electronic band alignment at the TCO/semiconductor interface is critical. The work function of the TCO must be carefully tuned, for example, through compositional engineering of doped metal oxides [31, 43, 98, 99]. Further practical

requirements include chemical stability during subsequent processing, mechanical adhesion to underlying layers, and thermal stability during device operation [100-102].

2.3.3 TCOs as Interconnections in Monolithic Tandems

Beyond these criteria, TCOs' role as an interconnecting layer (ICL) introduces an additional constraint: managing internal charge recombination without introducing parasitic optical or electrical barriers.

Figure 2.6 illustrates the current flow inside a typical monolithic two-terminal (2T) perovskite-silicon tandem. Maintaining current continuity requires efficient neutralisation of carriers. In Figure 2.6, electrons from the top sub-cell and holes from the rear sub-cell must recombine at the internal interface. However, direct contact between the electron transport layer (ETL) and hole transport layer (HTL) results in work function misalignment. This creates an undesirable p-n junction that imposes a significant energy barrier, impeding electron−hole recombination and reducing the open-circuit voltage [33]. To solve this problem, an effective ICL is incorporated in tandems, as shown in the blue middle layer in Figure 2.6.

An effective ICL must therefore perform a single function: recombine electrons arriving from the top sub-cell with holes arriving from the bottom sub-cell at negligible voltage loss [33, 103, 104]. Two distinct physical mechanisms are used to achieve this [105]. In a tunnel junction (TJ), the adjacent transport layers are degenerately doped (n^+/p^+) so that the depletion region becomes narrow enough (typically < 10 nm) for band-to-band tunnelling; recombination then occurs within the junction itself and no separate conductive layer is required [106]. In a recombination layer (RL), a highly conductive interlayer, most commonly a TCO, but also ultrathin metallic films or conductive polymers, is inserted between the two selective contacts and acts as an electronic sink in which the two carrier populations recombine via metallic or mid-gap states [107]. The two mechanisms are not mutually exclusive: in heavily doped nanocrystalline- or polycrystalline-silicon interconnections, tunnelling and recombination occur within the same region and cannot be separated, and such structures are referred to in the literature as tunnel recombination junctions (TRJs). Figure 2.6 depicts the RL case, which is the case of the AZO layer studied in this thesis.

The choice between a TJ, an RL, or a combined TRJ is determined by the band alignment and the processing constraints of the two sub-cells: TJ-based designs often struggle with the thermal stability and dopant diffusion issues inherent in perovskite processing, whereas RL-based designs require a deposition process that preserves the underlying passivation, while facilitating efficient charge recombination by acting as an electronic sink. Among these conductive interlayers, indium-based TCOs (such as ITO or IZO) are particularly advantageous in current laboratory perovskite-silicon tandem prototypes [108-110]. In such tandem prototypes, indium-based TCOs play critical roles at two locations: (1) as the ICL between the perovskite and silicon sub-cells for current continuity, and (2) as the front transparent contact on the perovskite side for current collection.

Indium-based TCOs are widely adopted in these roles because of their excellent optoelectronic properties. ITO possesses a wide bandgap (3.5–4.3 eV), low resistivity (10^{-4} Ω·cm), and a low absorption coefficient α (typically < 10^4 cm^{-1} in the visible spectrum), making it the current standard for tandem TCO layers [88, 111-114]. However, FCA becomes significant in the near-infrared region, and the reliance on scarce indium presents a critical scalability constraint for terawatt-scale photovoltaic deployment.

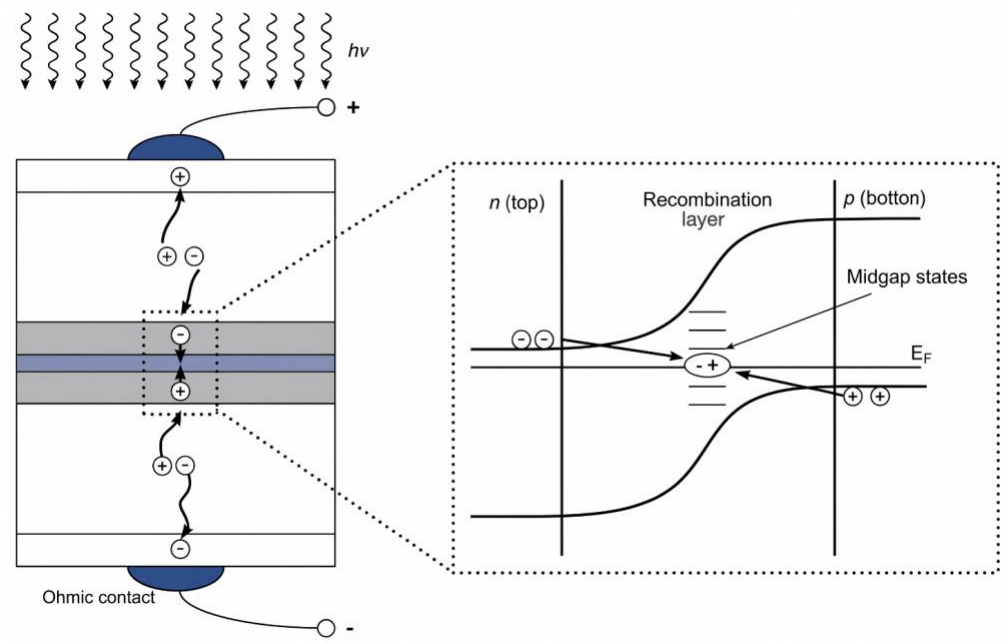


Figure 2.6 Schematic of the current continuity and recombination layer of a 2T perovskite-silicon tandem solar cell. Reproduced after ref [115].

2.3.4 Indium Scarcity Bottleneck

Indium occurs at low concentrations in the Earth's crust (approximately 0.1 ppm comparable to that of silver) and the ongoing growth of the electronics industry continues to escalate the demand for indium in displays, touchscreens, and LEDs [116-118]. The photovoltaic industry now competes with these established applications, which exacerbates supply concerns [84]. Figure 2.7 quantifies the relationship between indium consumption per watt-peak and achievable PV capacity. At ~4.23 mg/W_p and 20% utilisation of the 2019 global indium supply, the achievable capacity is limited to ~100 GW_p. Even when increasing utilisation to 50%, terawatt-scale deployment (~1000 GW_p) is only attainable if indium consumption is reduced to below ~1 mg/W_p. Wang et al. reported that the indium consumption needs to be as low as 0.064 mg/W_p to support 3 TW_p annual production [119]. This limitation therefore motivates the development of indium-free TCOs as alternative materials for scalable tandem photovoltaic technologies.

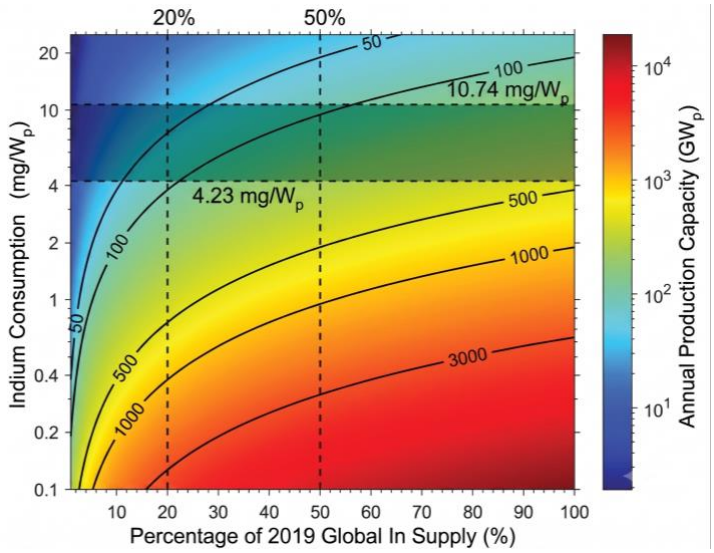


Figure 2.7 Projected annual PV production capacity (in GW_p, represented by colour scale and contours) plotted against indium consumption per W_p and the percentage of 2019 global indium supply utilised. Reproduced after ref [84].

2.3.5 Indium-Free Alternatives

Among alternative TCO materials, undoped tin oxide (SnO_2) has recently attracted significant attention, particularly in SHJ solar cells [120-122]. SnO_2 offers high optical transparency, excellent chemical stability, and favourable band alignment with silicon, making it well-suited for carrier-selective contacts [123]. However, its relatively lower conductivity compared to doped TCOs remains

a challenge for certain applications [124].

Doped zinc oxide (ZnO) films represent another promising class of alternatives [125-127]. Zinc is abundant with a crustal concentration of 70 ppm [128]. Aluminium-doped ZnO (AZO) and gallium-doped ZnO (GZO) can achieve resistivities on the order of 10^{-4}–10^{-3} Ω·cm, approaching those of ITO, while maintaining low optical absorption coefficients typically below 10^4 cm^{-1} in the visible range [126]. Figure 2.8 illustrates the comparison between AZO and ITO on absorption coefficient and resistivity in the near-infrared region. AZO exhibits FCA and conductivity levels comparable to ITO. The best overall combination is achieved by hydrogen-doped indium oxide (IOH), whose high electron mobility allows a given conductivity to be reached at a lower carrier concentration and therefore with less free-carrier absorption. However, IOH is indium-based, and so defines the performance benchmark rather than offering a way around the supply constraint identified in Section 2.3.4. As a result, doped ZnO materials have progressed furthest toward commercial viability, combining earth-abundant composition with competitive optoelectronic performance [129].

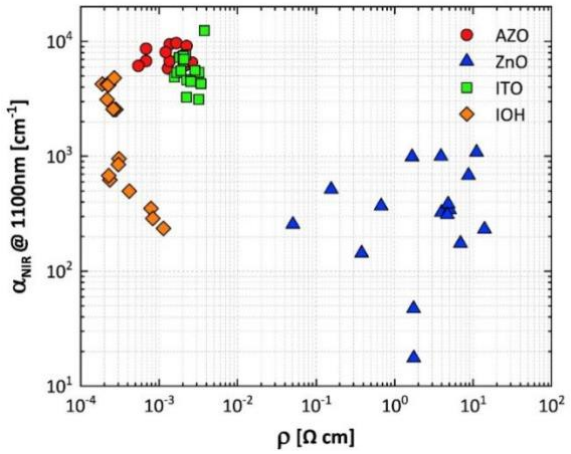


Figure 2.8 Absorption coefficient at λ = 1100 nm vs. resistivity of TCOs: hydrogen-doped indium oxide (IOH), ITO, AZO and ZnO. Reproduced after ref [97].

2.4 Atomic Layer Deposition-AZO (ALD-AZO) as a Passivating Contact

2.4.1 Material Properties of AZO

Understanding the structural and optoelectronic properties of ZnO is essential for engineering AZO's

functional behaviour. Zinc oxide (ZnO) typically crystallises in the hexagonal wurtzite structure. Figure 2.9 (a) and (b) show the atomic arrangement: each Zn(II) is coordinated by four oxygen atoms at the corners of a tetrahedron and each O(−II) by four zinc atoms [130]. The corresponding diffraction pattern, shown in Figure 2.9 (c), exhibits the characteristic reflections of wurtzite ZnO, which are commonly observed in experimental films [131].

The tetrahedra in ZnO are slightly distorted: the c/a ratio is 1.602 against the ideal close-packed value of 1.633, and the resulting asymmetry along [0001] gives the lattice a spontaneous polarisation and polar Zn- and O-terminated basal surfaces. This polarity underlies the strong c-axis texture of the ALD films examined in Section 4.3.1. The tetrahedral coordination does not follow from ionic size. Shannon's radii for four-fold coordinated Zn^{2+} (0.60 Å) and O^{2-} (1.38 Å) give a radius ratio of 0.435 [132], above the 0.414 boundary conventionally taken to separate tetrahedral from octahedral coordination; a purely ionic argument would therefore predict the octahedral rocksalt structure. The tetrahedral geometry arises instead from the covalent part of the Zn–O bond. ZnO has a Phillips ionicity of 0.616, below the critical value of 0.785 separating four- from six-fold coordinated compounds, so sp^3 hybridisation of Zn 4s and 4p with O 2p adds a directional contribution that an ionic model omits [133]. The two arrangements are close in energy: ZnO transforms from wurtzite to rocksalt at about 9 GPa [134].

The ZnO lattice contains various intrinsic defects, such as zinc vacancies (the primary native acceptors), as well as zinc interstitials and oxygen vacancies (the primary native donors) [135-137]. These donor-type defects contribute to the n-type conductivity commonly observed in undoped ZnO.

ZnO has a direct bandgap of approximately 3.37 eV, ensuring high transparency across the visible spectrum, with the absorption edge in the ultraviolet [138]. To enhance conductivity, aluminium (Al) doping is commonly employed. This doping increases the carrier concentration and reduces resistivity, typically to the range of 10^{-4}–10^{-3} Ω·cm, making AZO a viable transparent conducting material [139]. An optimal doping level (typically ~1–2 mol% Al) is required to balance its electrical conductivity and optical transparency [140], a figure returned to in Section 4.4.2. This trade-off is strongly influenced by the deposition method, which determines the resulting microstructure, defect chemistry, and carrier transport properties of AZO films [141].

Aluminium entering this lattice has three destinations with different electrical consequences. Substitution on the tetrahedral cation site, Al_{Zn}, is the intended one and gives a shallow donor a few tens of meV below the conduction band, fully ionised at room temperature [142]; because Al^{3+} (0.39 Å) is smaller than Zn^{2+}, substitution also contracts the lattice. Aluminium can instead occupy an interstitial site, of which the lattice offers an octahedral and a smaller tetrahedral cavity; calculations place cation interstitials on the octahedral site [143]. Interstitial Al is itself a donor; however, it cannot alone explain aluminium that carries no free electron. The third destination is segregation into Al_2O_3-like or $ZnAl_2O_4$-type regions, where Al is electrically inactive. This route is the most relevant to supercycle ALD, in which Al arrives as discrete sub-monolayer pulses rather than atomically dispersed (Section 2.4.2). Section 4.4.2 quantifies which of these destinations dominates in the films of this work.

The native defect population can be characterised by several complementary methods, of which photoluminescence is the most common. The room-temperature spectrum comprises a near-band-edge ultraviolet emission at 3.2–3.3 eV and a broad deep-level emission near 2.4–2.5 eV, whose intensity ratio serves as a measure of crystalline quality [144]. Its chemical specificity is limited, since the green band has been attributed to oxygen vacancies, zinc vacancies, zinc interstitials and residual copper [145].

The excitonic interaction in ZnO is strong. The free-exciton binding energy of about 60 meV is more than twice the thermal energy at room temperature, so excitons are not fully dissociated at 300 K and the absorption edge retains an excitonic contribution [144]. This matters for the optical analysis of Chapter 4 and Chapter 5: the Tauc construction assumes uncorrelated interband transitions, so where excitonic absorption contributes, the extracted value is an apparent optical gap rather than a single-particle bandgap. The contribution is not expected at all doping levels, since free carriers screen the exciton above a Mott density of ~3×10^{18} cm^{-3} [146]. The films of this work carry 1.5–5.1 × 10^{19} cm^{-3} (Section 4.4.2), so excitonic effects should be screened in the doped films but may persist in the undoped ZnO references. Section 5.7.1 returns to this point.

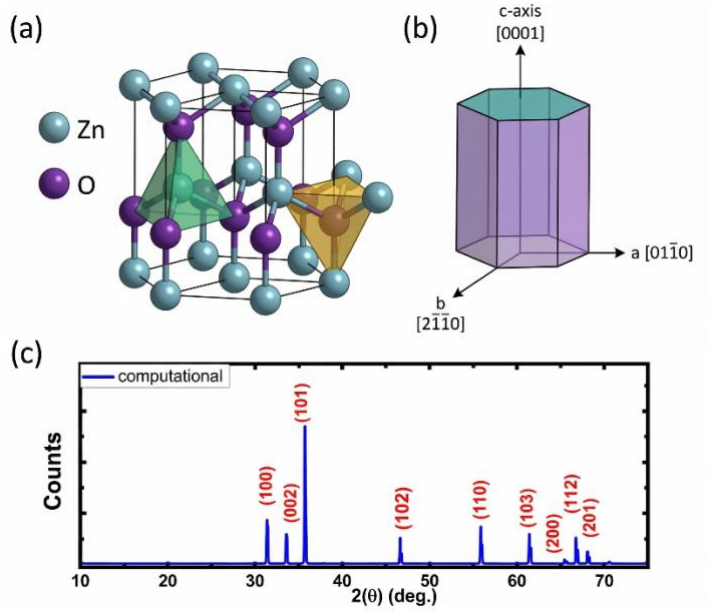


Figure 2.9 Crystal structure and simulated X-ray diffraction pattern of ZnO. (a) Atomic arrangement of ZnO in the hexagonal wurtzite structure, showing tetrahedral coordination between Zn and O atoms; (b) Schematic of the wurtzite unit cell with crystallographic directions; Reproduced after ref [130] (c) Simulated X-ray diffraction (XRD) pattern highlighting the characteristic diffraction peaks of wurtzite ZnO, with dominant reflections such as (100), (002), and (101); Reproduced after ref [131].

2.4.2 ALD for AZO Thin Film Synthesis

Multiple techniques have been demonstrated to deposit AZO thin films. While techniques such as sputtering (RF magnetron) and pulsed laser deposition (PLD) offer reasonable composition control and high crystallinity, they often involve energetic particle bombardment, which can damage the underlying silicon surface and degrade passivation quality [111, 141, 147, 148]. Similarly, chemical vapour deposition (CVD) achieves good coverage but requires complex precursor management [149].

ALD provides strategic advantages for passivating contacts. ALD's self-limiting surface chemistry ensures exceptional conformality and minimal substrate damage, depositing precisely controlled amounts of material (typically sub-monolayer) per cycle [150]. ALD deposition relies on binary reaction sequences. For a typical ZnO deposition, a schematic of the surface reaction is illustrated in Figure 2.10. Common precursors are diethylzinc (DEZ, $Zn(C_2H_5)_2$) and deionised water (H_2O), and the self-terminating half-reactions can be expressed as [151]:

$$\text{Surf-OH} + \text{Zn}(\text{C}_2\text{H}_5)_2 \rightarrow \text{Surf-O-Zn-C}_2\text{H}_5 + \text{C}_2\text{H}_6$$

$$\text{Surf-O-Zn-C}_2\text{H}_5 + \text{H}_2\text{O} \rightarrow \text{Surf-O-Zn-OH} + \text{C}_2\text{H}_6 \quad (2.18)$$

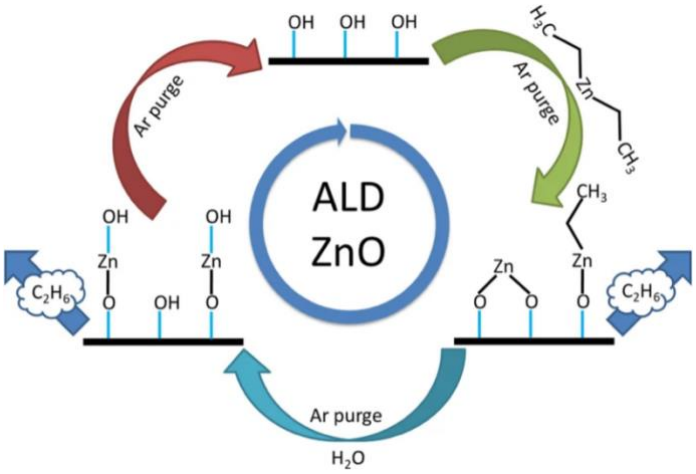


Figure 2.10 Schematic diagram of the ALD ZnO surface reactions when the average ratio of –OH surface ligands: one DEZ molecule is 1.5. Reproduced after ref [152].

To incorporate Al atoms into the ZnO lattice, discrete Al precursor and oxidant pulses are periodically inserted into the host growth sequence. For these AlO_X doping cycles, a widely adopted Al precursor is trimethylaluminium (TMA, $Al(CH_3)_3$). However, in practice, TMA's high reactivity often induces a parasitic transmetalation reaction, which is referred to as etching of ZnO by TMA [153, 154]. TMA can etch the underlying ZnO lattice, forming volatile $Zn(CH_3)_2$ and resulting in severe growth retardation for subsequent ZnO cycles [155, 156]. Furthermore, uncontrolled TMA adsorption leads to the formation of insulating AlO_X clusters that act as carrier scattering centres [157]. To mitigate these effects, advanced dosing strategies are utilised to reduce the availability of reactive surface sites for chemisorption of the dopant precursor. These strategies include the use of inhibitors (e.g., alkyl alcohols (EtOH)) [158], bulkier dopant precursor for steric hindrance (e.g., dimethylaluminium isopropoxide (DMAI, $Al(CH_3)_2\left(O^iPr\right)$)) [159, 160], dehydroxylation [161-163], and omitting the co-reactant dose prior to dosing the dopant precursor [164, 165]. Figure 2.11 (a) depicts the dehydroxylation method. The H_2O pulse is followed by a thermal soak for a prolonged time, which partially dehydroxylates the surface and reduces the density of reactive −OH sites. Figure 2.11 (b) displays the omitting co-reactant dose method, where the dopant precursor is purged right after the

host precursor, and is reactive toward sites that are not covered by the host precursor. This selective adsorption favours the incorporation of Al as substitutional dopants (Al_{Zn}), rather than forming AlO_X clusters. As a result, the free carrier concentration and conductivity of the AZO films are enhanced.

The surface chemistry underlying these strategies is well established. The exchange reaction in which gas-phase TMA converts a surface –ZnOH group into a chemisorbed –Al(OH)(CH_3) species, releasing volatile $Zn(CH_3)_2$, was identified in the original study of ZnO/ Al_2O_3 ALD [154]. Dehydroxylation, in which neighbouring –OH groups condense to a bridging oxygen and water, is a general feature of metal-oxide ALD and the usual explanation for the reduced growth per cycle observed at elevated temperature [151].

Comparison across precursors of different size shows that steric hindrance does control the number of sites available to the dopant precursor. Under otherwise matched conditions, TMA, DMAI and triisopropyl borate deposit approximately 8-10, 4-5 and 3-4 dopant atoms nm^{-2} per dopant cycle, in order of increasing ligand bulk [166]. The doping efficiency rises correspondingly, from ~ 10% for TMA to almost 60% for DMAI [153]. Section 4.4.2 evaluates the corresponding figure for the films of this work. Two chemically unrelated routes to the same end support this reading: pre-dosing an alkyl alcohol inhibitor to occupy –OH sites doubles the carrier density at fixed aluminium content [158], and a 120 s dehydroxylation hold before the TMA dose raises the maximum carrier density from 4×10^{20} to 6×10^{20} cm^{-3} [161]. Three different ways of reducing site availability therefore all raise the doping efficiency, which indicates that site availability, rather than aluminium supply, is the controlling variable.

Two qualifications apply. First, the selectivity is partial rather than absolute: when TMA is dosed directly after DEZ, part of the surface –ZnOH population still undergoes the exchange reaction, so aluminium uptake is reduced but not suppressed [164]. Second, the in-plane distributions sketched in Figure 2.11 (c) and (d) have not been imaged. The arrangement of dopants into planes has been resolved directly by SIMS and by TEM, and these planes are seen to smear out on annealing [164]. However, the lateral arrangement within a plane is inferred from the doping-efficiency measurements above rather than observed. The schematics are presented on that basis.

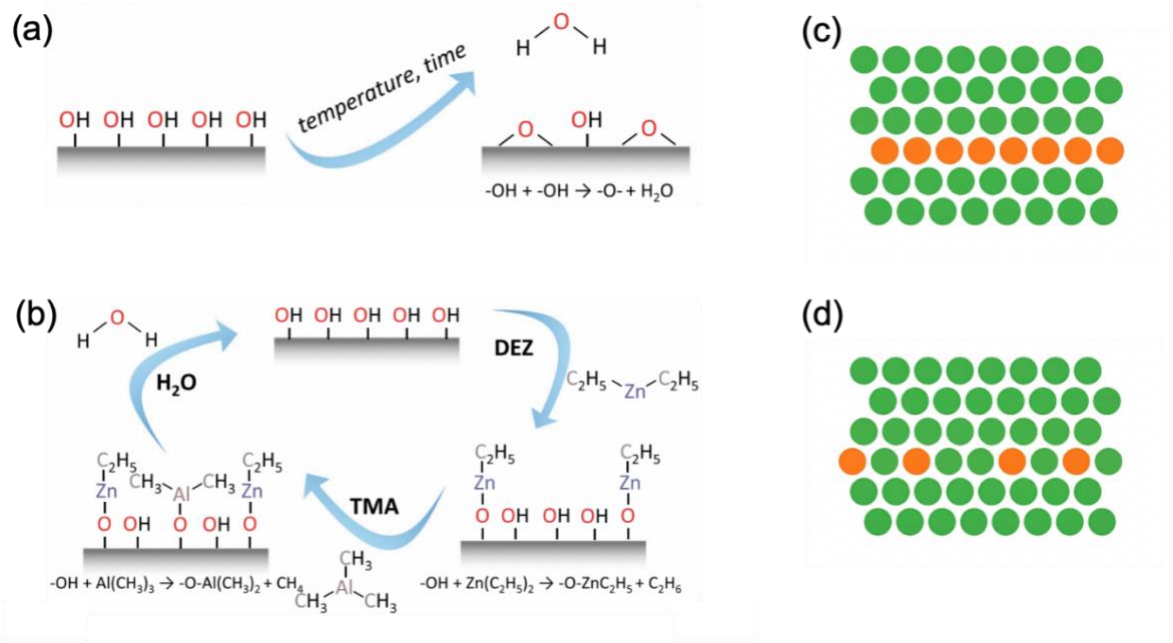


Figure 2.11 Schematic diagram of (a) the dehydroxylation method; (b) the omitting co-reactant dose method. Idealised schematics of the expected distribution of two precursor atoms (green stands for DEZ, and orange for TMA) (c) before and (d) after adopting the omitting co-reactant dose method. For simplicity, a monolayer coverage per cycle was assumed. Reproduced after ref [151].

Critically, ALD AZO films retain hydrogen. H_2O reactant is the primary oxygen precursor in thermal ALD and, given its polar nature and high hydrogen content, is therefore hypothesised to be the dominant source of hydrogen incorporation in the film [167-169]. During subsequent thermal processing, this hydrogen is thought to diffuse through the AZO layer to the silicon interface, where it saturates dangling bonds and provides chemical passivation [170]. This intrinsic passivation capability distinguishes ALD-grown films from sputtered alternatives, which typically lack comparable hydrogen incorporation, and therefore do not provide comparable passivation without an external hydrogen source.

2.4.3 Surface Passivation from AZO/AlO_X Thin Film Stacks

Recent progress has demonstrated that specially engineered AZO-based stacks can provide effective surface passivation on crystalline silicon, despite the inherent difficulty of achieving passivation using conductive oxides [44-47, 50]. The passivation in these stacks is not intrinsic to ZnO itself but arises from a combination of interfacial and chemical effects. The earliest investigation into the viability of doped ZnO as a passivating contact was conducted at TU Eindhoven by van de Loo et al. (2019), where they primarily focused on boron-doped ZnO (ZnO:B) films [45]. They demonstrated that hydrogen retention at the Si/SiO_2 interface is essential for achieving chemical

passivation. In this system, an AlO_X capping layer suppresses hydrogen effusion during annealing, thereby maintaining a high hydrogen concentration at the interface and enabling the passivation of silicon dangling bonds. This performance enhancement is quantitatively demonstrated in Figure 2.12, where the AlO_X-capped ZnO:B stack (sample 3) achieves a peak minority carrier lifetime corresponding to an iV_{OC} of 724 mV, outperforming the uncapped as-deposited (sample 1) and annealed (sample 2) references. Later in 2025, the role of this AlO_X capping layer in preventing hydrogen effusion in the AZO passivation stack was proved by our collaborators at the University of Surrey using time-of-flight elastic recoil detection analysis (ToF-ERDA) to profile hydrogen depth distributions [171].

In addition to chemical passivation, field-effect passivation is also thought to contribute to the overall performance [45]. As discussed in Section 2.4.2, extrinsic doping of ZnO (e.g., via Al incorporation) increases the electron concentration and lowers the work function, resulting in stronger band bending at the silicon interface and lower surface hole concentration in n-type silicon. The relative importance of chemical and field-effect passivation depends on both the doping level and the interface quality, indicating a strong coupling between deposition conditions and passivation behaviour.

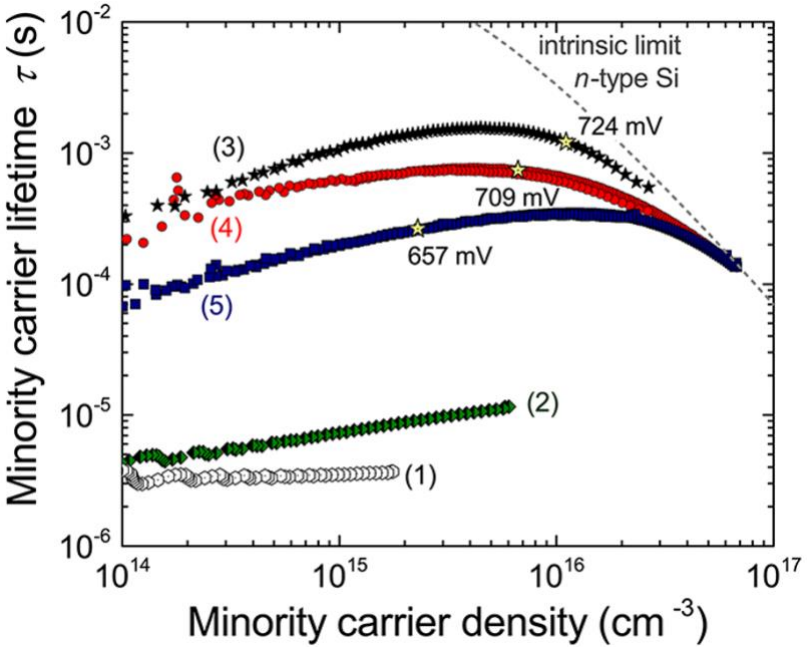


Figure 2.12 Effective minority carrier lifetime of n-type Si samples passivated by ALD ZnO:B. The samples compare different processing conditions: (1) as-deposited ZnO:B (~75 nm) following RCA clean; (2) same as (1) after 450 °C forming gas anneal (FGA); (3) ZnO:B with an AlO_X cap prior to 450 °C FGA; (4) p-type Si with ZnO:B, AlO_X cap, and 450 °C FGA; and (5) an optimised n-type process including an additional HF dip and FGA up to 475 °C. Stars indicate implied open-circuit voltage (iV_{OC}) under 1-sun illumination. Reproduced after ref [45].

After investigating ZnO:B films, in 2021, Macco et al. from TU Eindhoven first demonstrated that high-quality passivation can be achieved by combining ALD-deposited AZO with an AlO_X capping layer and a thin interfacial SiO_2 layer [46]. In this configuration, an iV_{OC} of 730 mV was reported, indicating surface recombination velocities in the range of a few cm/s. In Macco's later work (2022), they used spatial ALD AZO to highlight the industrialisation potential. The activation of this passivation through post-deposition thermal treatment is illustrated in Figure 2.13 (a), which tracks iV_{OC} across a range of cumulative annealing temperatures [47]. While the as-deposited state exhibits poor passivation for all samples, thermal activation leads to a significant performance improvement that peaks at 400–450 °C. In this optimised window, the AZO stack on FZ c-Si wafer outperformed the undoped ZnO references, achieving the highest iV_{OC} values across both substrate types. Notably, annealing beyond 500 °C causes rapid degradation. The same trend was observed in their previous work on temporal ALD AZO contacts, where TEM studies suggested it arises from the roughening and disordering of the interfacial SiO_2 layer.

To benchmark this performance, Figure 2.13 (b) compares J_0 and sheet resistance of the AZO/AlO_X stack against other state-of-the-art passivating contact materials. The AZO-based stack (red stars) achieves J_0 values comparable to established dielectric passivation layers such as a-Si:H and SiN_X, while simultaneously maintaining electrical conductivity. This highlights the unique potential of AZO to combine passivation and carrier transport within a single material system.

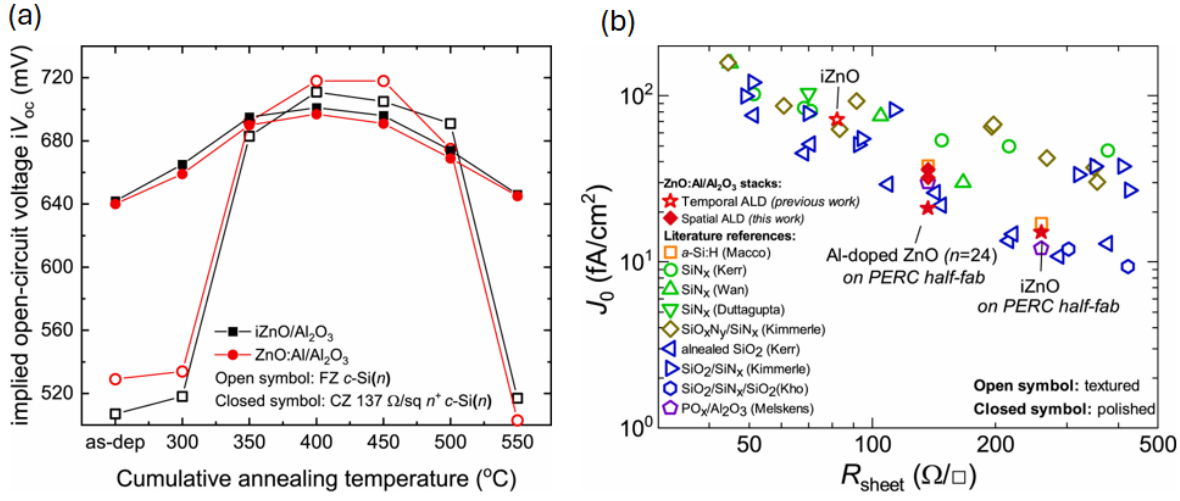


Figure 2.13 (a) iV_{OC} values for SiO_2/AZO/AlO_X stacks by spatial ALD on undiffused FZ and n^+-diffused CZ n-type c-Si wafers with RCA and UV/O_3 SiO_2 layers, respectively. The ZnO and AlO_X films were both 30 nm thick. Consecutive annealing steps were performed for 5 min in FGA. (b) Recombination current density plotted as a function of sheet resistance (Rsheet) for various passivating contact technologies. The red stars represent the performance of the ALD-deposited AZO/AlO_X stack. Reproduced after ref [47].

Building on Macco's approach, Cai et al. (2024) demonstrated a 23.2%-efficient silicon solar cell on a 2.56 cm^2 device area using a SiO_2/AZO/AlO_X stack, confirming the device-level viability of this concept [44]. More recently, Gao et al. (2025) reported ZOPCon (zinc oxide passivating contact) solar cells achieving a champion PCE of 24.3% on a 1 cm^2 cell, certified by the Shanghai Institute of Microsystem and Information Technology (SIMIT), representing the highest efficiency reported to date for metal oxide-based passivating contacts [50]. Notably, the high passivation results presented in this work with the lowest ever reported J_0 value (0.87 fA/cm^2) [172] were submitted prior to these recent publications, demonstrating the potential of this architecture ahead of these recent device reports.

The device architecture from Gao et al. is illustrated schematically in Figure 2.14 (a). It integrates a thin SiO_2 tunnelling layer situated between the n-type silicon base and the AZO film, capped with an ultrathin LiF (1 nm) interlayer beneath the aluminium electrode. Although LiF is a wide-bandgap insulator, at this thickness electrons tunnel through it, while the ionic LiF/Al interface forms a dipole that lowers the effective work function of the aluminium and hence the barrier to electron extraction from the AZO conduction band. The extracted contact resistivity of ~51 mΩ·cm² further demonstrates that such stacks can simultaneously provide good passivation and acceptable carrier transport properties. The cross-sectional transmission electron microscopy (TEM) image in Figure 2.14 (b) and (c) confirms the distinct, uniform multi-layered structure of the rear interface stack. These recent demonstrations of high-efficiency ZOPCon cells indicate that AZO-based passivating contacts are approaching technological relevance. The illuminated current density–voltage (*J*–*V*) curves of n-Si solar cells with ZOPCon under the standard test conditions (1 sun, AM1.5G, 25 °C) is shown in Figure 2.14 (d). After inserting a thin LiF interlayer between the AZO and Al electrodes, the certified PCE was 24.3% (V_{OC} 712 mV, J_{SC} 41.9 mA cm^{-2}, FF 81.4%).

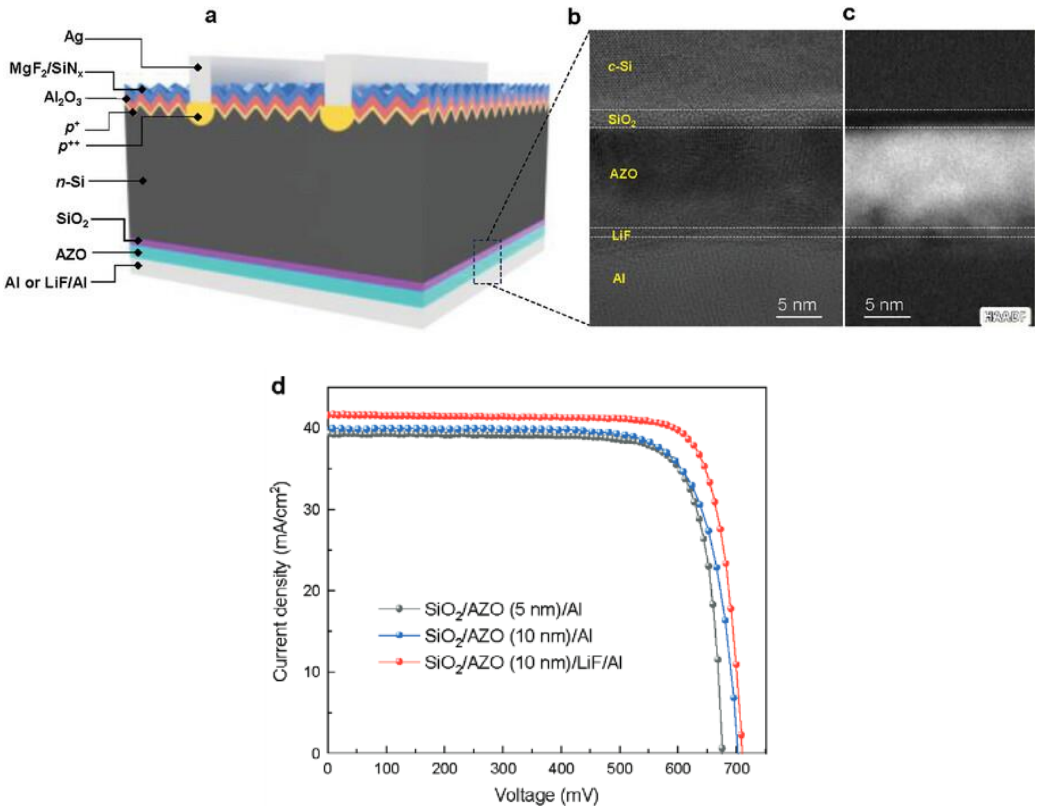


Figure 2.14 (a) Schematic illustration of the ZOPCon solar cell architecture employing an AZO-based rear passivating contact. (b) Cross-sectional Transmission Electron Microscopy (TEM) image and c) High-Angle Annular Dark-Field Scanning Transmission Electron Microscopy (HAADF STEM) image detailing the interface structure of the rear stack. (d) Light *J–V* curves under standard test conditions with different thicknesses of AZO. Reproduced after ref [50].

2.5 Summary of Scientific Gaps

Despite the promising performance demonstrated by SiO_2/AZO/AlO_X passivating contact stacks, the underlying passivation mechanisms remain poorly understood. Current work broadly attributes the passivation to a combination of chemical passivation at the Si/SiO_2 interface via hydrogenation capped by the AlO_X layer, and field-effect passivation arising from work function tuning via doping. Hydrogen-mediated chemical passivation has been experimentally verified in early studies, most notably by van de Loo et al. (2019) using isotope labelling, SIMS, and thermal effusion measurements on boron-doped ZnO. However, the extent to which these findings translate to AZO-based systems remains largely inferred rather than directly established [45].

Subsequent studies, including those by Macco et al. (2021, 2022), have further demonstrated the potential of this approach and provided valuable insights into process-dependent behaviour, such as annealing response, oxide quality, and doping dependence [46, 47]. More recent device-level

demonstrations, including those by Cai et al. (2024) and Gao et al. (2025), have employed advanced characterisation techniques such as ToF-SIMS, TEM, and UPS to probe hydrogen distribution and electronic structure [44, 50]. While these studies collectively support the prevailing model, the detailed passivation mechanisms are not yet established. In particular, the true contributions of chemical and field-effect passivation, as well as their dependence on processing conditions, are still unresolved. This is especially relevant given that this system has received comparatively less investigation than more established technologies such as TOPCon (17 publications vs 1543 publications in 2015-2025, according to Web of Science).

Several critical questions therefore remain open. First, the origin, transport pathways, and bonding configuration of hydrogen within SiO_2/AZO/AlO_X stacks are not yet clearly established, nor is it fully understood how hydrogen is retained during annealing and redistributed across the multilayer structure.

Second, although both chemical passivation and field-effect passivation are known to contribute, their relative roles and temporal evolution during processing have not been systematically decoupled. Existing studies typically probe limited process conditions (e.g., before/after annealing or with/without capping layers), without employing dedicated experimental designs to investigate hydrogen transport dynamics or its interaction with specific interfacial species.

Third, in addition to these mechanistic uncertainties, important aspects of process dynamics remain unexplored. While the role of annealing temperature has been widely studied, the influence of post-annealing cooling dynamics on hydrogen redistribution and defect passivation has received little attention. Additionally, the effect of the annealing atmosphere on hydrogen transport remains unclear, particularly under hydrogen-free conditions.

Fourth, device-level challenges remain. Achieving simultaneously low contact resistivity and excellent passivation is still significant, and current approaches rely on solutions such as ultrathin LiF interlayers that present scalability concerns [173]. In addition, present device architectures are

not yet compatible with industrial requirements such as bifacial operation, high-throughput metallisation, simplified processing workflows, and long-term stability at scale.

This thesis addresses three of these gaps: (1) hydrogen transport mechanisms, (2) decoupling chemical and field-effect passivation, and (3) process dynamics. Chapter 4 examines precursor engineering and establishes optimised deposition parameters. Chapter 5 investigates thermal processing dynamics and their influence on passivation. Chapter 6 employs advanced characterisations to probe structural, electrical, and chemical changes and analyses the passivation mechanisms. Most previous studies on ZnO-based passivating contacts have employed forming gas annealing (FGA), introducing an external hydrogen source during processing. In contrast, this work focuses on annealing in air, where no external hydrogen is supplied and lab conditions can be used, thereby facilitating industrial upscaling. As a result, the observed passivation behaviour is governed primarily by hydrogen originating from the deposited thin films themselves. This distinction enables a more direct investigation of intrinsic hydrogen transport and redistribution within the SiO_2/AZO/AlO_X stack, providing complementary insights into the passivation mechanism.

Chapter 3. Materials and Experimental Methods

3.1 Sample Preparation

3.1.1 Silicon Wafers

Solar-grade phosphorus-doped n-type Cz crystalline silicon (c-Si) wafers (~4 Ω·cm resistivity, 135 μm thickness) and semiconductor-grade, chemo-mechanically polished ultra-flat n-type Cz c-Si wafers (30~60 Ω·cm resistivity, 675 μm thickness) were used as substrates in this project. The wafers were laser-cut into 4 cm × 4 cm samples using a 1064 nm ns infrared laser (Linxuan LX-A1-20W). The choice of moderately doped n-type silicon enables stable surface passivation and minimises bulk recombination effects, allowing the interface properties to be isolated and studied. Table 3.1 summarises the two types of silicon substrates used in this work. Table 3.2 summarises the sample structures used across this thesis.

Table 3.1 Summary of silicon substrates used in this work.

Substrate	Type	Resistivity (Ω·cm)	Thickness (μm)	Grade / Surface	Primary use
A	n-type Cz c-Si	~4	~135	Solar grade, saw-damage etched	Passivation studies (Chapters 4, 5): lifetime, PL; Ellipsometry, XPS, KP-SPV
B	n-type Cz c-Si	30–60	~675 (290 nm thermal SiO_2 on Si)	Semiconductor grade, chemo-mechanically polished (ultra-flat)	Analytical techniques requiring low surface roughness: ToF-SIMS, XRR, GIXRD, NR, Transient-SPV; Electrical measurements (vdP, Hall) requiring isolation from substrate

Table 3.2 Summary of sample structures used across this thesis.

Sample set	Substrate	Stack structure deposited	AZO thickness (nm)	AlO_X cap (nm)	Chapter
Passivation	A	SiO_X/AZO/AlO_X (bifacial)	16	26	4; 5
Electrical	B	AZO on 290 nm SiO_X	40; 20, 28, 56	—	4; 5
UV-vis (Chapter 4)	Fused quartz	AZO single-sided	40	—	4
UV-vis (Chapter 5)	Glass	AZO ± AlO_X (bifacial)	20 per side	(20)	5
XPS	A	AZO ± AlO_X (bifacial)	50 but sputtered to ~1; 2, 4	0; 2, 0	4; 6
XRR / GIXRD / NR	B	SiO_X/AZO/AlO_X (bifacial)	16	26	5
ToF-SIMS	B	SiO_X/AZO/AlO_X (bifacial)	16	26	6
SPV	A	SiO_X/AZO±AlO_X (bifacial)	16	(26)	6
Transient-SPV	B	SiO_X/AZO±AlO_X (bifacial)	16	(26)	6

3.1.2 Surface Cleaning and Oxide Formation

Prior to thin film deposition, the silicon samples underwent a standard surface preparation procedure to remove contamination and control the surface properties. All wet chemistry was carried out in quartz and PTFE beakers, and samples were rinsed in 18.2 MΩ·cm deionised (DI) water between successive steps and dried under a nitrogen stream in the end.

Saw damage was removed using a tetramethylammonium hydroxide (TMAH, $(CH3)_4NOH$) etch (25 wt% TMAH solution at 80 °C for 20 minutes), which removed approximately 10 μm of silicon from each surface; this step was applied to substrate A only, substrate B being supplied chemo-mechanically polished. This was followed by a hydrofluoric acid (HF) dip (5% HF for 60 seconds) to remove the native oxide layer. Subsequently, the samples were cleaned using the standard Radio Corporation of America procedure [174]: RCA1 (NH_4OH (29%):H_2O_2 (30%):H_2O = 1:1:5 by volume, at 75 °C for 10 minutes) to remove organic contamination, followed by RCA2 (HCl (37%):H_2O_2 (30%):H_2O = 1:1:6 by volume, at 75 °C for 10 minutes) to remove metallic contamination. A second HF dip and RCA2 step, under identical conditions to the first, were then applied, resulting in the

formation of an approximately 1.2 nm thick chemically grown SiO_X layer. Samples were transferred to the ALD reactor within 2 hours of the final rinse, to limit regrowth of native oxide. This ultra-thin oxide layer provides surface passivation by forming the primary interface between the silicon substrate and the deposited thin films.

3.1.3 ALD

Aluminium-doped zinc oxide (AZO) and aluminium oxide (AlO_X) nanolayers were grown using a Veeco Savannah thermal ALD system. Diethylzinc (DEZ) and trimethylaluminium (TMA) were used as metal-organic precursors, with H_2O as the oxidant co-reactant. A detailed discussion of the ALD mechanism was provided in Section 2.4.2. The deposition was carried out at 150 °C and a base pressure of 0.2 Torr.

Al doping in ZnO was achieved using a supercycle approach, in which n cycles of ZnO are alternated with m cycles of AlO_X. This sequence is repeated until the desired film thickness is obtained. A schematic illustration of the supercycle approach is shown in Figure 3.1. A and C stand for two different (metal-containing) precursors; B is the co-reactant, and P is the purge step. In the context of this work, A and B correspond to the ZnO sub-cycle DEZ and H_2O pulses, while C and B represent the AlO_X cycle (TMA and H_2O). The purge steps (P) ensure the removal of excess precursors and by-products. The cycle ratio controls the Al incorporation level. However, the periodic insertion of Al-containing cycles may lead to non-uniform dopant distribution [151].

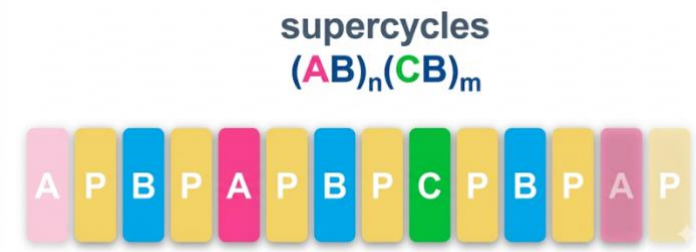


Figure 3.1 Schematic diagram of the supercycle method. Reproduced after ref [151].

When m = 1, the doping level is controlled by the ZnO:AlO_X cycle ratio (n:1). In this work, the ZnO:AlO_X cycle ratio was optimised to 20:1. Notably, the dehydroxylation and omitting co-reactant dose methods discussed in Section 2.4.2 were also implemented, and thus a modified supercycle

sequence was performed. Specifically, for the AlO_X cycle, the standard oxidant exposure (H_2O pulse) following the DEZ pulse was omitted, such that the sequence transitioned directly from the DEZ step to the TMA cycle. In addition, extended purge times were introduced before the AlO_X cycle.

Following AZO deposition (14–40 nm, depending on the intended application), an AlO_X capping layer with thicknesses in the range of 20–30 nm was deposited in the same chamber for different sample sets. Deposition was performed on both sides of the wafer simultaneously. To enable this, samples were suspended on a custom metal frame holder that elevated them above the reactor platen, allowing precursor gases to access both the front and rear surfaces during each ALD half-cycle.

Deposition was carried out with the substrate stage, inner and outer rings, valve manifold and exhaust line all held at 150 °C, within the self-limiting growth window for both the DEZ/H_2O and TMA/H_2O processes. The DEZ, TMA, and H_2O sources were held at room temperature without active heating. For the optimised recipe, the pulse and wait times were 0.014 s / 10 s for DEZ, 0.010 s / 8 s for TMA and 0.017 s / 8 s for H_2O with a freshly charged source; the remaining three recipes were obtained by varying the pulse times to give the peak precursor pressures listed in Table 4.1. Pulse times of this order lie within the saturated regime reported for thermal ALD of ZnO and Al_2O_3 at this temperature [175, 176], so that the growth per cycle is set by the saturation coverage of the chemisorbed precursor rather than by precursor flux or thermal decomposition. The recipe was developed in this work rather than adapted from a published process. Growth per cycle inferred from the film thicknesses in Chapter 4 and Chapter 5 is ~0.15 nm/cycle for the AZO and ~0.10 nm/cycle for the AlO_X, consistent with values reported for these processes [177, 178]. The supercycle is not a linear combination of the two binary processes: the transmetalation reaction described in Section 2.4.2 suppresses ZnO growth for several cycles after each TMA pulse, so the effective growth per cycle is lower than the cycle-ratio-weighted average and the aluminium content is not proportional to the nominal AlO_X cycle fraction.

3.1.4 Annealing

Post-deposition annealing was performed to activate the passivation properties of the films and to study the impact of thermal processes. For samples in Chapter 4, annealing was conducted at

500 °C for 20 minutes in air within a furnace, followed by a controlled cooling process for 10 minutes. A secondary annealing step at 450 °C for 10 minutes on a hotplate was applied prior to passivation measurements. For samples in Sections 5.2–5.4, annealing was performed directly at 450 °C for 20–30 minutes in air on a hotplate, followed by controlled cooling rates to investigate the effect of thermal dynamics on passivation performance.

500 °C was the measured thermocouple temperature, where the set temperature of the furnace was 550 °C. 450 °C was the measured thermocouple temperature value, where the set temperature of the hotplate was also 450 °C. For Sections 5.5-5.6, 600 °C was the measured thermocouple temperature, where the set temperature of the furnace was 670 °C.

3.1.5 Etching of AlO_X Capping Layer

While the AlO_X capping layer is essential for the hydrogenation of the interface during the thermal activation step, it acts as an electrical insulator that would impede carrier transport in the completed device. Therefore, to enable the integration of the AZO passivating contact into the tandem solar cell stack, the AlO_X capping layer needs to be selectively removed post-annealing.

The wet etching process was performed using a solution of 0.1 M sodium carbonate (Na_2CO_3), heated to and maintained at 60 °C. The pH of the solution was adjusted to 11.8 by adding potassium hydroxide (KOH) flakes to ensure high etch selectivity between the cap and the underlying zinc oxide, following the work of Sun et al. [179]. For instance, the samples with ~21 nm AlO_X layers were immersed in the etchant for 2 minutes, a duration optimised to ensure the complete removal of ~21 nm thick AlO_X layer while preserving the underlying AZO film. Immediately after etching, the reaction was quenched by dipping the samples in deionised (DI) water for 5 seconds, then drying with a nitrogen gas stream. The final film thickness was measured using ellipsometry to ensure the AlO_X was removed (<0.3 nm).

Table 3.3 shows an example of such etching results from three different AZO/AlO_X samples.

Table 3.3 Wet etching results of AlO_X capping layer using ellipsometry.

Thickness (nm)	Before Etching				After Etching			
	AlO_X	AZO	SiO_2	(fit)	AlO_X	AZO	SiO_2	(fit)
Sample 1	21.02	23.87	1.20	0.04	0.02	21.91	1.20	0.02
Sample 2	21.98	21.85	300.35	0.04	0.11	22.51	300.00	0.02
Sample 3	21.18	27.18	300.51	0.03	0.28	28.00	300.52	0.02

3.2 Passivation Measurement

3.2.1 Photoconductance Decay

Effective lifetime τ_{eff} was measured from photoconductance decay using a WCT-120 Sinton Lifetime Tester at room temperature in ambient air. Figure 3.2 depicts the schematic set-up of the Sinton tester. Excess carriers are generated by shining light onto the samples, and their decay is monitored by the changes in the conductivity using an induction coil. τ_{eff} can be calculated from:

$$\tau_{\text{eff}} = \frac{\Delta n(t)}{G(t) - \frac{d\Delta n(t)}{dt}} \tag{3.1}$$

where G is the generation rate, and Δn is the excess carrier density extracted from the conductivity measurements.

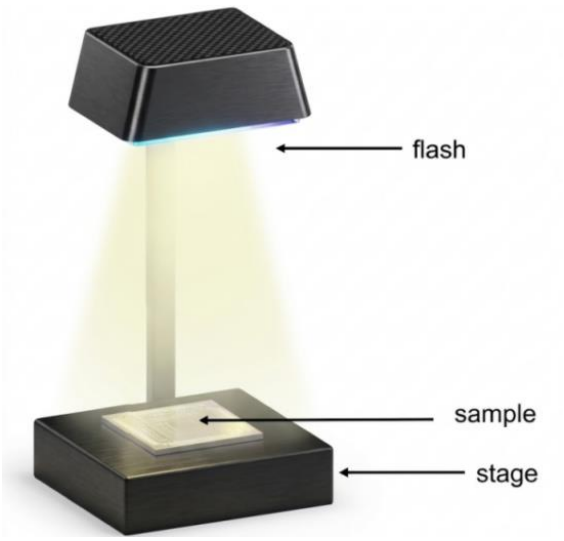


Figure 3.2 Schematic of the WCT-120 Sinton Lifetime Tester.

Depending on the length of the flash, τ_{eff} can be measured in transient mode or Quasi Steady State (QSS) mode. For the transient mode, a short light pulse of 100-200 µs is shone upon the sample to generate excess carriers. The changes in the excess carrier density are monitored after the light is turned off. The simplified Equation (3.1) by assigning $G(t)$=0 can be expressed as:

$$\tau_{eff} = \frac{-\Delta n(t)}{\frac{d\Delta n(t)}{dt}} \tag{3.2}$$

Transient mode does not require a simultaneous measurement of G and is independent of the light optics. τ_{eff} can be deduced from the changes in Δn over time. However, only samples with τ_{eff} longer than the light turn-off time 100 µs are suitable for this mode. QSS mode is then used for samples with shorter τ_{eff}. The sample is illuminated for approximately 10 times longer than its lifetime so that quasi steady state conditions are created, where the generation and recombination are assumed to be in equilibrium at each moment in time. Since carriers are continually generated at a constant rate, the term $\frac{d\Delta n(t)}{dt}$ = 0. The lifetime under QSS conditions is simplified to:

$$\tau_{eff} = \frac{\Delta n(t)}{G(t)} \tag{3.3}$$

$G(t)$ is calculated via a separate measurement of the flash intensity using a light sensor. To convert the flash intensity to $G(t)$, the optical constants of the samples are required. The QSS mode provides a cleaner signal than the transient mode and more accurately reflects real-world solar cell performance under constant light [180].

A 1/64 s light pulse was used to measure all transient-mode samples. The obtained Δn -dependent τ_{eff} can be fitted to analyse the different contributions of bulk and surface. The MATLAB app in [181] was used for analysis, which uses the Kimmerle and Mackel models for extracting J_0 [78, 182].

Because the photoconductance transient yields τ_{eff} as a continuous function of the excess carrier density, the injection level rather than the flash fluence is the physically meaningful parameter, and all effective lifetimes in this thesis are therefore quoted at $\Delta n = 10^{15}$ cm^{-3} unless otherwise stated.

For context, one-sun AM1.5G illumination generates carriers at an average rate of ~ 2.0×10^{19} cm^{-3} s^{-1} in the 135 µm wafers used here, so that the best samples of Chapters 4 and 5 (τ_{eff} ≈ 1.3–3.3 ms) would sit at Δn ≈ 3–7×10^{16} cm^{-3} under open-circuit one-sun conditions; 1×10^{15} cm^{-3} is the conventional benchmark for silicon lifetime samples, while iV_{OC} and J_0 are extracted at one-sun-equivalent generation.

3.2.2 Photoluminescence Imaging

Photoluminescence (PL) imaging was utilised to evaluate the surface passivation uniformity of the AZO/AlO_X stacks. It was carried out on an in-house CellSpot-ELPL tool system from BrightSpot Automation.

PL Imaging provides a spatial map of passivation effectiveness by detecting photons emitted during radiative recombination following a light flash. The PL signal intensity (I_{PL}) is proportional to the local excess carrier concentration: high-intensity regions indicate effective passivation, while low-intensity regions correspond to high Shockley–Read–Hall (SRH) recombination from surface defects or bulk contamination [183]. I_{PL} is given by:

$$A_i \cdot I_{PL} = B(N_D + \Delta n)\Delta n \tag{3.4}$$

Where A_i is the calibration factor, and B is the radiative recombination coefficient.

All passivation studies used samples fabricated on Si substrate A in Table 3.1.

3.3 Electrical Properties

The electrical resistivity of AZO was measured using the van der Pauw (vdP) method [184, 185]. Figure 3.3 (a) depicts a sample with point contacts for the measurement. Its R_{sheet} can be approximated by:

$$e^{-\frac{\pi R_{AB,CD}}{R_{\text{sheet}}}} + e^{-\frac{\pi R_{BC,DA}}{R_{\text{sheet}}}} = 1 \tag{3.5}$$

where $R_{AB,CD}$ and $R_{BC,DA}$ are the horizontal and vertical resistances, $\frac{V_{DC}}{I_{AB}}$ and $\frac{V_{AD}}{I_{BC}}$, measured at 90° with respect to each other. Equation (3.5) applies directly only when $R_{AB,CD} = R_{BC,DA}$, which can be simplified to $R_{\text{sheet}} = \frac{\pi R}{\ln(2)}$. In general cases, where $R_{AB,CD} \neq R_{BC,DA}$, a correction factor f is adopted. R_{sheet} is then expressed as:

$$R_{\text{sheet}} = \frac{\pi}{\ln(2)} \cdot \left(\frac{R_{AB,CD} + R_{BC,DA}}{2}\right) \cdot f \tag{3.6}$$

Equation (3.6) is only valid when the values of $R_{AB,CD}$ and $R_{BC,DA}$ are similar. To ensure this, a symmetrical sample structure is required [185]. Figure 3.3 (b) depicts a typical square AZO measurement configuration with symmetrical gold metal probes in direct contact with the AZO surface.

The Van der Pauw method assumes infinitesimally small contacts to minimise errors from non-uniform current flow. In practice, finite-sized contacts were used, and a geometrical correction factor was applied based on the ratio of contact width (δ) to sample width (l). Figure 3.3 (c) depicts such a correction factor. For the AZO samples, contact dimensions were controlled at the edges such that δ/l remained small (0.05-0.125), resulting in a correction factor of 1.01-1.001. This factor was applied to Equation (3.6) to obtain a corrected R_{sheet}.

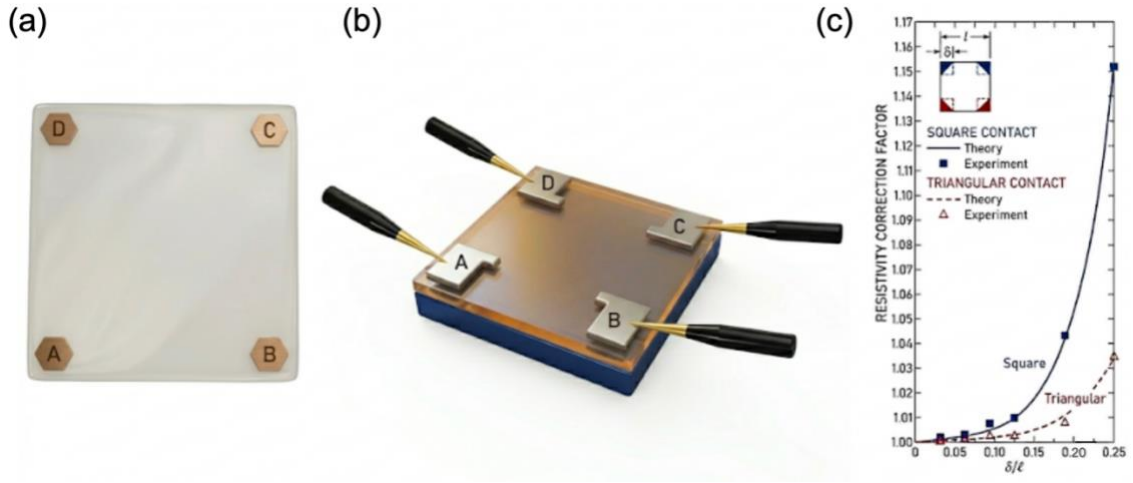


Figure 3.3 Van der Pauw measurement configuration. Schematic of (a) the sample with four-point contacts A-D on top, and (b) the standard vdP measurement set-up. (c) Contact size correction factor for vdP measurements. l represents the length of the sample, while δ represents the width of the metal contact. Reproduced after ref [186].

The vdP method was extended to evaluate mobility via Hall measurements [185]. By applying a uniform magnetic field perpendicular to the sample, a Hall voltage (V_H) is generated due to the Lorentz force acting on charge carriers. The polarity of V_H indicates the conduction type, while its magnitude is used to determine the sheet carrier concentration (N), following:

$$N = \frac{IB}{q|V_H|} \tag{3.7}$$

where I is the current passing through the material. Hall measurements were performed using the vdP configuration (same as Figure 3.3 (b)) by sourcing current between diagonally opposite contacts and measuring the transverse voltage across the remaining contacts (e.g., applying I_{BD} and measuring V_{AC}). To minimise errors arising from contact misalignment and thermoelectric effects, measurements were conducted under both positive and negative magnetic fields, with reversed current and contact configurations (e.g., applying I_{AC} and measuring V_{BD}). The V_H was obtained by averaging the mean of these measurements and is used to calculate N. As $\rho = \frac{1}{q \cdot N \cdot \mu}$ from Equation (2.12), Hall mobility can be derived from Equation (3.7) and expressed as:

$$\mu = \frac{|V_H|}{I \cdot B \cdot R_{\text{sheet}}} \tag{3.8}$$

A magnetic field of B=0.165 T was applied, calibrated using a reference silicon sample with known carrier concentration and mobility. N and μ were then extracted from the measured V_H and R_{sheet}.

For both vdP and Hall effect measurements, signal generation and data acquisition were conducted using a high-impedance Keysight B2901A source measuring unit, controlled virtually in a LabVIEW program. To ensure the reliability of these surface measurements, AZO films were deposited onto Si substrate B in Table 3.1. All vdP and Hall values reported in this thesis are the mean over the four contact permutations described above, taken at both magnetic field polarities, which removes the offset contributions from contact misalignment and thermoelectric voltages. The geometrical contribution from finite contact size is bounded by the correction factor of 1.01–1.001 quoted above, that is, below 1%. Sheet resistance and sheet carrier density are measured directly and are independent of film thickness, and the Hall mobility, which follows from these two quantities alone, is likewise thickness independent. The resistivity and the volume carrier concentration are obtained

by multiplying and dividing by the film thickness, respectively, and therefore carry the ellipsometric thickness uncertainty of ± 0.5 nm on the AZO layers, corresponding to 3% or less across the 16–56 nm range measured here.

3.4 Optical Properties

3.4.1 Ultraviolet–visible (UV–vis) Spectrophotometry

A Varian Cary 5000 UV-Visible-NIR Spectrometer (175 – 3300 nm range, spectral bandwidth to 0.01 nm) was utilised to investigate the optical properties of the AZO. Figure 3.4 depicts a schematic of the measurement setup where light is monochromated and split into reference and sample beams to account for source fluctuations and improve measurement accuracy. UV–vis spectroscopy probes the interaction between incident light and the material by measuring the transmitted or absorbed intensity as a function of wavelength [187]. The absorption coefficient α is derived from the measured transmittance and is used to determine the optical absorption edge [188]. The relationship between α and the measured transmittance T can be expressed as:

$$\alpha = -\frac{1}{d}\ln(T) \tag{3.9}$$

where d is the film thickness. The optical gap was estimated using a Tauc plot [189], following:

$$(\alpha h\nu)^n = A\left(h\nu - E_g\right) \tag{3.10}$$

where $h\nu$ is the photon energy, $\mathrm{E_g}$ is the optical gap, A is a constant, and n depends on the nature of the electronic transition. For direct allowed transitions, $n = 1/2$, which is commonly assumed for AZO [190, 191].

The Tauc construction assumes that absorption near the edge arises from uncorrelated interband transitions. This assumption is only approximate for ZnO at room temperature, since the large exciton binding energy leaves an excitonic contribution at the absorption edge (Section 2.4.1). Values obtained by this method are therefore reported throughout as apparent optical gaps, and are used to compare samples analysed identically rather than as absolute single-particle bandgaps.

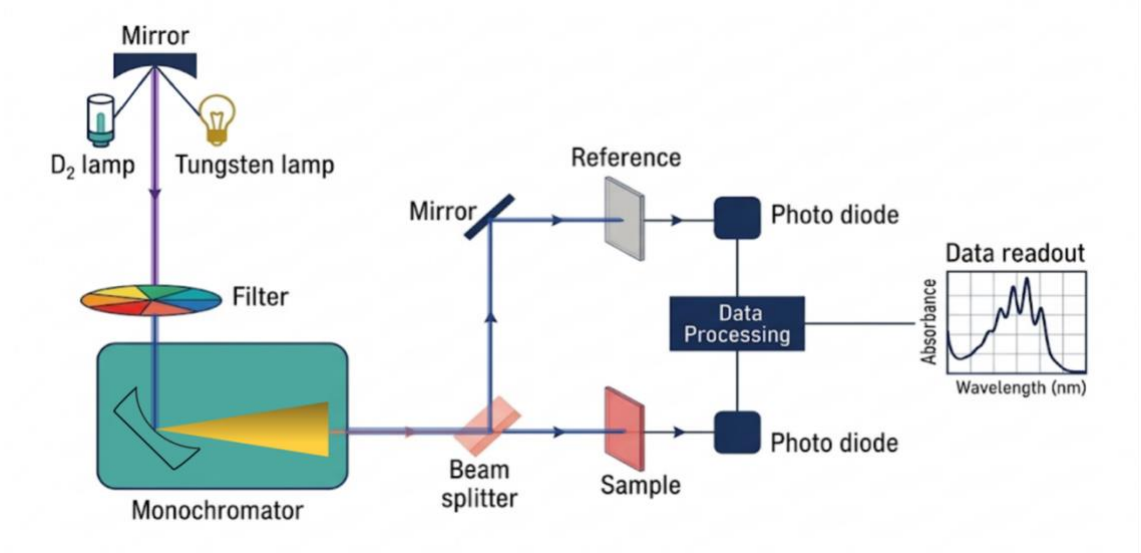


Figure 3.4 Schematic diagram of the UV–vis spectrophotometer. Light from deuterium (UV) and tungsten (visible) lamps is monochromated and split into reference and sample beams. The transmitted intensities are detected by photodiodes and processed to obtain the wavelength-dependent absorbance.

In Chapter 4, transmission measurements were carried out on single-sided 40-nm-thick AZO samples deposited on fused quartz substrates (to enable measurements at UV wavelengths) over a wavelength range of 200 to 1200 nm (to capture the relevant spectral features). In Chapter 5, transmission measurements were carried out on samples deposited on glass substrates with films on both front and back sides, each side having a thickness of 20 nm ZnO or AZO (with and without an extra 20 nm AlO_X) over a wavelength range of 200 to 1200 nm.

3.4.2 Ellipsometry

Ellipsometry is an optical technique widely used to measure the thickness and optical properties of thin films. An FS-1 Film Sense ellipsometer and a J.A. Woollam ellipsometer were used. FS-1 Film Sense ellipsometer measurements were conducted and analysed by me. J.A. Woollam ellipsometer measurements were conducted by Rebekah C. Fraser, Matthew Wright, and me. I performed all data analysis, modelling, and interpretation. Samples measured were fabricated on Si substrate A in Table 3.1.

The modelling parameters used for AZO were refractive index (n) ranging from 1.6 to 2.1, and extinction coefficient (k) ranging from 0 to 0.4 from 210 to 1690 nm wavelength [88].

In Ellipsometry, linearly polarised light is incident on the sample surface at an oblique angle, and the change in polarisation upon reflection is analysed [192, 193]. Figure 3.5 depicts a schematic of the measurement principle. The incident electric field can be decomposed into two orthogonal components: p-polarised light (parallel to the plane of incidence) and s-polarised light (perpendicular to the plane of incidence). Upon reflection from the sample surface, both the amplitude and phase of these components are modified depending on the optical properties and structure of the material. As a result, the reflected light becomes elliptically polarised.

Rather than measuring film properties directly, ellipsometry determines the parameters Ψ and Δ, which describe the amplitude ratio and the phase difference between the p- and s-polarised components of the reflected light. Ψ and Δ are related to the complex reflection coefficients r_p and r_s of the p- and s-polarised light, and are used to extract film thickness and optical constants through model-based fitting, following:

$$\frac{r_p}{r_s} = \tan(\Psi)\ e^{i\Delta} \tag{3.11}$$

Thicknesses quoted in this thesis are the mean of five points measured across each 4 × 4 cm sample. The point-to-point spread is below 0.5 nm for the AZO layers and below 2 nm for the AlO_X caps, and exceeds the fit uncertainty returned by the model at a single point, so this spread is taken as the thickness uncertainty throughout (Section 4.2).

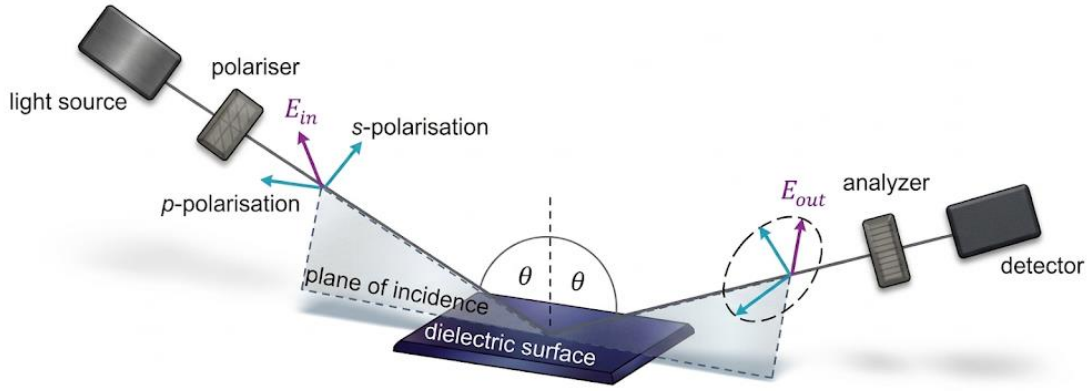


Figure 3.5 Schematic illustration of the ellipsometry measurement principle.

3.5 Structural and Compositional Characterisations

3.5.1 Electron Microscopy

In Chapter 4, the microstructural characterisation of the samples was conducted using two transmission electron microscope (TEM) systems. First, bright-field imaging was conducted on a JEOL JEM-2100 microscope operating at an accelerating voltage of 200 kV, with the column held at its specified operating vacuum of approximately 1×10^{-5} Pa**.** To protect the sample surface from ion beam damage during the lift-out process, a protective Platinum (Pt) strap was deposited prior to milling. The electron-transparent cross-sectional lamellae were prepared using a Focused Ion Beam (FIB) system (Zeiss Crossbeam 540, Carl Zeiss AG), with the specimen chamber under high vacuum at $\leq 1 \times 10^{-5}$ mbar**.** FIB sample preparation and TEM imaging on the JEOL JEM-2100 were performed by Rajat Nama. I conducted the data analysis and scientific interpretation of the resulting micrograph.

An FEI Talos F200X TEM was also employed. The equipment operated at an accelerating voltage of 200 kV, equipped with a field emission gun (FEG) to provide a high-brightness electron beam. The column was maintained at approximately 1×10^{-5} Pa, with the gun chamber below 10^{-7} Pa as required for stable Schottky field emission. Imaging modes included both TEM and STEM modes. In TEM mode, the microscope's lattice resolution is better than 0.2 nm, allowing high-resolution imaging of the crystal structure and defects in the material. In STEM mode, high-angle annular dark field (HAADF) imaging was performed, enabling Z-contrast imaging based on atomic number, with a resolution of approximately 1 nm. Data acquisition and processing were done using the associated Velox software.

Additionally, energy-dispersive X-ray spectroscopy (EDS) was employed for elemental analysis to investigate the composition and distribution of elements in the samples in Chapter 4. The thin sections of the samples were prepared using FIB technology to ensure the sample thickness met the transmission requirements. These techniques were performed in the Thermo Fisher Scientific Inc. Talos F200X scanning/transmission electron microscope (S/TEM) carried out by Jiangsu Institute of Advanced Semiconductors Ltd. I performed the data analysis, plotting, and scientific interpretation of all acquired spectra and micrographs.

3.5.2 X-ray Photoelectron Spectroscopy (XPS)

XPS is a surface-sensitive analytical technique used to determine the elemental composition, chemical states, and electronic structure of materials. In XPS, a monochromatic X-ray beam irradiates the sample, resulting in the emission of photoelectrons from core electronic levels. The kinetic energy of these emitted electrons is measured, providing information about their binding energy and thus the chemical environment of the atoms [194].

Figure 3.6 (a) shows a schematic of the photoemission process, where incident X-ray photons excite core electrons, leading to their emission from the material surface. For a sample in electrical contact with the spectrometer, so that the Fermi levels of the two are aligned, the binding energy referenced to the Fermi level is given by:

$$E_B = h\nu - E_K - \phi_{\mathrm{sp}} \tag{3.12}$$

where $\mathrm{E_B}$ is the binding energy referenced to the Fermi level, $h\nu$ is the photon energy, $\mathrm{E_k}$ is the kinetic energy measured by the analyser, and ϕ_{sp} is the work function of the concentric hemispherical analyser. The work function of the sample does not appear. The photoelectron is retarded by the contact potential difference between sample and analyser, so the recorded kinetic energy is referenced to the vacuum level of the analyser rather than that of the sample; this is what allows binding energies referenced to the Fermi level to be compared directly between samples of differing work function. The analyser work function is not measured independently, but is absorbed into the offset of the binding-energy scale, which is calibrated as described below. Since each element has characteristic core-level binding energies, XPS enables the identification of elemental composition and chemical bonding states within the near-surface region (typically within 2-5 nm).

In addition to compositional analysis, XPS can be used to determine band alignment at material interfaces. A schematic of the energy level alignment is shown in Figure 3.6 (b). The valence band offset (VBO) between the TCO layer and the Si substrate was determined using the Kraut method [195], which combines core-level and valence band measurements from both reference and interface samples:

$$\Delta E_v = \left(E_{CL}^{TCO} - E_{VBM}^{TCO}\right)_{\text{ref}} - \left(E_{CL}^{Si} - E_{VBM}^{Si}\right)_{\text{ref}} + \left(E_{CL}^{Si} - E_{CL}^{TCO}\right)_{\text{int}} \quad (3.13)$$

where E_{CL} and E_{VBM} are the core-level and valence band maximum energies, respectively. The subscripts “ref” and “int” refer to measurements obtained from bulk reference samples and the interface sample. The first two terms represent the energy differences between core levels and valence band maxima in the individual materials, while the final term corresponds to the core-level difference measured at the interface in the Si/SiO_X/AZO sample.

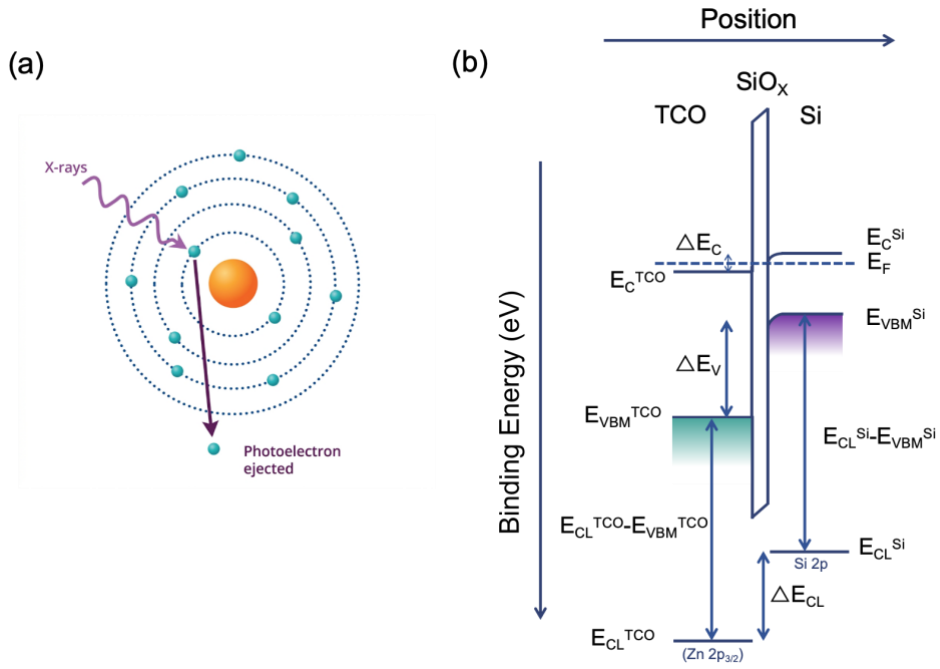


Figure 3.6 Schematic illustration of (a) the XPS photoemission process; (b) energy band alignment at a TCO/Si interface, illustrating the core-level and valence band energy differences used in the Kraut method to determine the VBO.

In Chapter 4, XPS was employed to analyse the elemental ratio of Al and Zn in the films based on the integrated intensity of the Zn 3p and Al 2p core level peaks. Monochromated XPS measurements of the core levels were carried out on a PHI VersaProbe spectrometer in the Department of Materials, University of Oxford, using an Al Kα X-ray source (1486.6 eV) and a hemispherical analyser with the pass energy set to 26 eV. The binding-energy scale was calibrated following ISO 15472 using ion-sputter-cleaned Au, Ag and Cu foils, with the reference values Au $4f_{7/2}$ = 83.96 eV, Ag $3d_{5/2}$ = 368.21 eV and Cu $2p_{3/2}$ = 932.62 eV; the offset of the scale, which contains ϕ_{sp}, was set from the Au $4f_{7/2}$ line and the dispersion from the Cu $2p_{3/2}$ line. Because both the AZO films and the silicon substrates are electrically conductive and were mounted with the top surface in electrical contact with the

sample holder, no charge compensation was applied, and no further charge referencing was necessary. The analysis chamber was held under ultra-high vacuum at a base pressure of ~10^{-9} mbar during measurement. The Al 2p core level was observed to be weak in all samples, consistent with the expected Al concentrations of a few at.%. The Al 2p / Zn $3p_{3/2}$ ratio was estimated from spectra taken after sputter cleaning, by fitting the core level peaks using CasaXPS to extract the integrated intensity [196]. Translating these values to an Al concentration requires knowledge of the RSF, which is specific to the XPS instrument used. Because RSF values were not available for the spectrometer used in Chapter 4's work, the absolute values of concentration could not be known in this case. However, the trends in Al 2p / Zn $3p_{3/2}$ ratios between the samples should nevertheless be representative. Monochromated XPS data acquisition was conducted collaboratively with Jack E. N. Swallow and Theodore D. C. Hobson. Data processing and analysis were performed by Theodore D. C. Hobson and me using CasaXPS software, and I was responsible for the scientific interpretation of all results. Details of the background model and peak constraints are given in Section 4.3.3.

The valence band offsets could be estimated from the Kraut method by directly measuring the band bending at the AZO/Si interface. The interface was characterised by in-situ sputtering through the AZO layer at 4 kV for 15 mins using an Ar+ ion gun, such that a thin (~ 1 nm) layer of AZO remained on the Si surface, thin enough that photoelectrons from the Si 2p core level escape through the AZO layer to be measured. In this interface region, the Si and Zn core levels are expected to shift compared to their bulk values by an energy equal to the shift in Si and AZO valence bands at the interface [195]. Therefore, we measured the position of the Zn 3p and Si 3p core levels at this interface region. The AZO valence band position at the interface was determined from the bulk AZO valence band, shifted by the difference between the bulk and interface Zn 3p core levels. Meanwhile, the Si interface valence band position was determined by adding a fixed value of 98.95 eV to the binding energy of the Si 2p core level, as this is well-defined for Si [197]. The bulk valence band for the Si was then determined from its known doping level using PVLighthouse [198]. The difference between the interface and bulk valence band positions corresponded to the interface band bending, and provided an estimate of the valence band offset between AZO and Si that took account of this

phenomenon. This was only performed for the optimised lifetime sample, due to constraints on equipment access which prevented measurement of all sample types.

In Chapter 6, high-resolution XPS characterisation was conducted at the Versatile Soft X-ray (VERSOX) beamline B07 at Diamond Light Source (Didcot, UK). Unlike the monochromatic Al Kα X-ray source (1486.6 eV) used in Chapter 4, the synchrotron beamline utilises a high-flux, linearly polarised soft X-ray beam with tunable photon energy [199]. The measurements were performed in an ultra-high vacuum (UHV) end station (base pressure < 5×10^{-10} mbar) equipped with a Scienta Omicron hemispherical electron analyser (typically model SES 2002 or similar). To probe the specific chemical environments, spectra were acquired at a photon energy of 1800 eV. The binding-energy scale was referenced to the Au $4f_{7/2}$ line of an evaporated gold film in electrical contact with the sample plate, and the photon energy was calibrated at a photon energy of 1800 eV. Carbon 1s peaks were used as a secondary check on the energy scale to eliminate any possible charging in individual samples. The use of synchrotron radiation provided superior energy resolution compared to laboratory sources. Synchrotron XPS measurements were conducted by me with assistance from Theodore D. C. Hobson. I performed the data processing, analysis, and interpretation using CasaXPS.

Both chapters used samples fabricated on Si substrate A in Table 3.1.

3.5.3 Time-of-Flight Secondary Ion Mass Spectrometry (ToF-SIMS)

Depth profiling analysis was conducted using ToF-SIMS to investigate the elemental composition and interfacial diffusion across the fabricated AZO thin film stacks. The measurements were performed by Sarah Fearn and me, using an IONTOF ToF-SIMS 5 instrument located at the Department of Materials, Imperial College London. I conducted all subsequent data processing, analysis, plotting, and scientific interpretation.

ToF-SIMS is a highly surface-sensitive analytical technique used to identify elemental and molecular species in the near-surface region and to obtain depth-resolved compositional information [200]. Figure 3.7 depicts a schematic representation of the measurement principle. In ToF-SIMS, a pulsed primary ion beam is focused onto the sample surface, where it induces the emission of secondary

ions from the topmost atomic layers. These ions are extracted into a time-of-flight analyser and separated according to their mass-to-charge ratio. Since ions with a lower mass-to-charge ratio travel faster under the same acceleration conditions, they arrive at the detector earlier than heavier ions. By combining pulsed sputtering with sequential analysis, ToF-SIMS can also be used to generate depth profiles of the elemental distribution [201, 202].

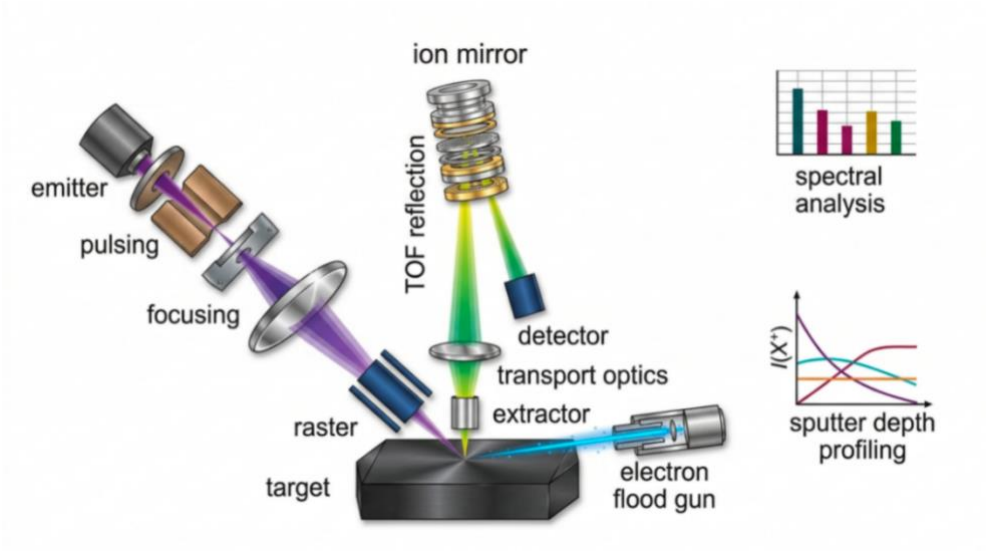


Figure 3.7 Schematic diagram of the ToF-SIMS measurement principle.

The fundamental relationship between the flight time and the mass-to-charge ratio $\frac{m}{z}$ is given by:

$$t = L\sqrt{\frac{m}{2zU}} \tag{3.14}$$

where t is the flight time, L is the flight path length, m is the ion mass, z is the ion charge state, and U is the accelerating voltage. Equivalently, $\frac{m}{z}$ can be expressed as:

$$\frac{m}{z} = \frac{2Ut^2}{L^2} \tag{3.15}$$

ToF-SIMS was used to investigate the near-surface chemical composition and depth-dependent elemental distribution of the sample structures. All measurements were performed under ultra-high vacuum, with the analysis chamber at a base pressure of ~1 × 10^{-9} mbar. The analysis utilised a pulsed primary ion beam of 25 keV Bi^+ beam with a current of ~1 pA. Secondary ions were collected from a centrally gated analytical area of 100 μm^2. To perform depth profiling, material removal was

achieved using a sputtering beam of 500 eV Cs^+ ions, over a larger area of 300 μm^2. The instrument was operated in negative polarity mode, collecting negative secondary ions.

The samples subjected to ToF-SIMS analysis consisted of bifacial structures deposited on Si substrate B from Table 3.1, with an extra 1.2 nm RCA2 chemical-grown SiO_X interface after RCA cleaning. The thin film stacks included AZO (~16 nm) layers, and in specific sample configurations, an additional AlO_X (~26 nm) capping layer. Comparative analyses were performed between as-deposited samples and samples that underwent an annealing process at 450 °C for 20 minutes in an ambient air atmosphere.

3.5.4 Reflectometry and Diffraction Techniques

All the samples characterised by reflectometry and diffraction were fabricated on Si substrate B from Table 3.1, with an extra 1.2 nm RCA2 chemical-grown SiO_X interface after RCA cleaning. They consisted of an AZO layer (~16 nm) capped with an AlO_X layer (~26 nm). To investigate thermal effects, specific samples were subjected to distinct annealing protocols. Details of the annealing protocols will be discussed in Table 5.3, Chapter 5.

3.5.4.1 X-ray Reflectometry (XRR)

Figure 3.8 (a) depicts the schematic of the X-ray reflection principle. In XRR, a collimated X-ray beam is incident on the sample surface at grazing angles, and the reflected intensity is measured as a function of incident angle or momentum transfer [203]. At very small angles, total external reflection occurs below a critical angle α_c, as shown in Figure 3.8 (b), which is determined by the electron density of the material. The reflection and refraction of X-rays at the interface follow Snell's law, which relates the incident and refracted angles through the refractive indices of the two media:

$$n_1 \sin\theta_1 = n_2 \sin\theta_2 \tag{3.16}$$

Above α_c, the reflected intensity decreases and exhibits oscillations (Kiessig fringes) due to interference between X-rays reflected from different interfaces within the layered structure [203]. Figure 3.8 (c) shows a typical X-ray reflectivity curve, illustrating total external reflection, the critical angle, and interference fringes. The periodicity and amplitude of these oscillations contain

information about the film thickness, density, and interfacial roughness. The reflectivity data are commonly analysed as a function of the momentum transfer perpendicular to the surface (q_z), which is defined as:

$$q_z = \frac{4\pi}{\lambda}\sin\theta \tag{3.17}$$

where λ is the X-ray wavelength, and θ is the incident angle. The periodicity of the interference fringes in the reflectivity curve is directly related to the film thickness and can be approximated by:

$$d = \frac{2\pi}{\Delta q_z} \tag{3.18}$$

where d is the film thickness and Δq_z is the spacing between adjacent interference fringes.

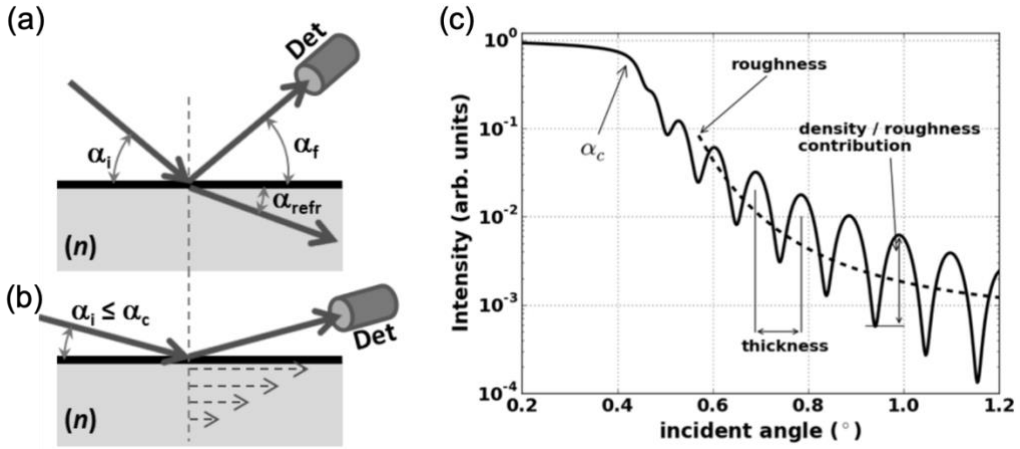


Figure 3.8 Schematic diagram of (a) X-ray reflection at an interface between vacuum (refractive index n=1) and a material with n < 1, showing the refraction and reflection of the incident beam according to Snell's law; (b) total external reflection for incident angles below the critical angle, including the formation of an evanescent wave at the interface. Reproduced after ref [204]; (c) representative X-ray reflectivity curve highlighting key features such as the critical angle, interference fringes, and the influence of thickness and interfacial roughness. Reproduced after ref [205].

XRR measurements were performed using a Bruker D8 Discover diffractometer equipped with a Cu-kα, λ = 0.154 nm) equipped with a LYNXEYE XE detector located at the Reactor Institute Delft (RID), TU Delft, The Netherlands. XRR measurements were performed by Amy Navarathna and me. Data processing and initial fitting were conducted jointly with Lars Bannenberg using GenX software, and I was responsible for the final analysis and integration of these results into the thesis.

The incident beam was parallelised using a Goebel mirror and was collimated using a 0.1 mm slit on the primary side, while the secondary side utilised two 0.1 mm slits to define the detection angle.

To maximise the dynamic range, data acquisition was split into two angular regimes: a low-angle scan ($0 < 2\theta < 2°$) using a 0.1 mm Cu absorber to attenuate the primary beam, and a high-angle scan ($0.6 < 2\theta < 5°$) performed without an absorber. The resulting datasets were stitched using a custom Python script. Structural parameters, including layer thickness, density, and roughness, were extracted by fitting the experimental reflectivity profiles using the GenX software package [206].

Of the parameters returned by the fit, the layer thickness is the most strongly constrained, since it is set by the period of the Kiessig fringes rather than by their amplitude. Inter-laboratory round-robin studies report a reproducibility of 0.04 nm, approximately 0.3%, on the thickness of a well-defined single layer on silicon [207, 208], and a precision of about 1% is routinely achieved on conventional laboratory diffractometers of the type used here [209]. For the 16–56 nm layers measured in this work, 1% corresponds to approximately ± 0.2–0.5 nm. The density and roughness are more strongly correlated with one another and carry larger uncertainty than the thickness, and in the AZO/AlO_X bilayer the two sub-layer thicknesses are themselves correlated, so the total stack thickness is better determined than either layer individually. This should be distinguished from the depth resolution, set by $2\pi/Q_{max}$ with $Q_{max} \approx 3.6$ nm^{-1} and equal to approximately 1.8 nm, which is the smallest structural feature that can be resolved rather than the precision with which a layer thickness is determined. The same parameter correlation affects neutron reflectometry more severely, since its Q-range is narrower and the scattering length density contrast smaller [210], which is taken into account in the XRR and NR comparison of Section 5.6.

3.5.4.2 Grazing Incidence X-ray Diffraction (GIXRD)

GIXRD is a technique used to characterise the crystallographic structure of thin films with enhanced surface sensitivity.

Figure 3.9 depicts the schematics of Bragg diffraction, conventional XRD measurement geometry, and GIXRD configuration. XRD is based on the diffraction of X-rays from periodic atomic planes within a crystalline material [211]. As shown in Figure 3.9 (a), when X-rays are incident on a crystal, constructive interference occurs when the path difference between reflected waves satisfies Bragg's law:

$$n\lambda = 2d \sin\theta \tag{3.19}$$

where λ is the X-ray wavelength, d is the interplanar spacing, θ is the incident angle, and n is the diffraction order.

Figure 3.9 (b) illustrates that in conventional XRD, the incident angle is varied to probe bulk properties. In contrast, as shown in Figure 3.9 (c), GIXRD employs a fixed, small incident angle (typically close to or below the critical angle), which limits the penetration depth of the X-rays and enhances sensitivity to the near-surface region [212]. As a result, GIXRD is particularly suitable for analysing thin films and surface layers while minimising contributions from the substrate.

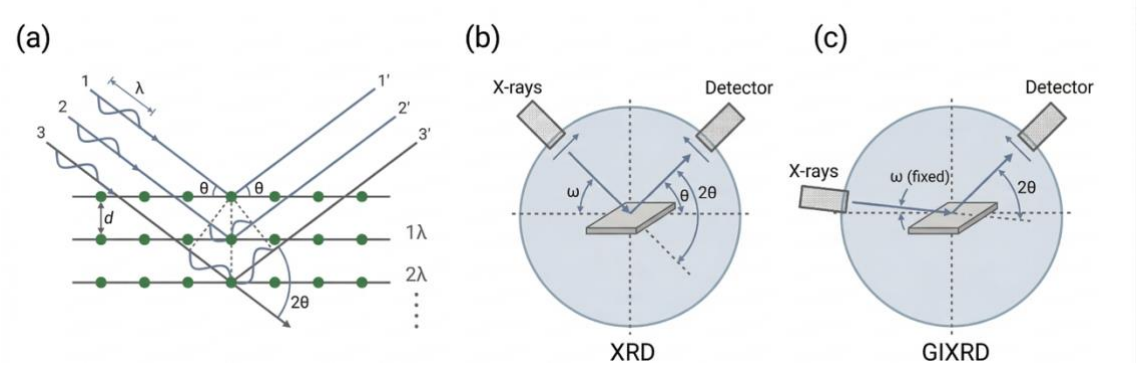


Figure 3.9 (a) Schematic diagram of Bragg diffraction from lattice planes with spacing d. (b) Conventional XRD geometry, where both the incident angle ω and detector angle 2θ are varied. (c) GIXRD configuration with a fixed grazing incidence angle ω.

In Chapter 4, GIXRD measurements were performed on the same Bruker D8 Discover system as XRR. The incident beam angle was fixed at a grazing angle of 0.5° to enhance surface sensitivity and maximise the diffraction volume within the AZO/AlO_X thin film stack. The detector was scanned over a 2θ range of 15° - 60° to record the diffraction pattern.

3.5.4.3 Neutron Reflectometry (NR)

Neutron Reflectometry (NR) is a non-destructive technique used to characterise the depth-dependent structure and composition of thin films and multilayer systems. In NR, a collimated neutron beam is incident on the sample surface at grazing angles, and the reflected intensity is measured as a function of incident angle or momentum transfer [213]. Similar to X-ray reflectometry, total reflection occurs below a critical angle, which is determined by the scattering length density (SLD) contrast between layers [214]. Above this angle, the reflectivity exhibits interference fringes

due to reflections from different interfaces within the sample. Unlike X-rays, which primarily interact with electron density, neutrons interact with atomic nuclei. As a result, NR provides sensitivity to light elements (especially hydrogen) and isotopic contrast that XRR cannot resolve [215]. Figure 3.10 shows a schematic of the neutron reflectometry geometry, illustrating the incident and reflected beams, the definition of reflectivity, and the momentum transfer perpendicular to the surface.

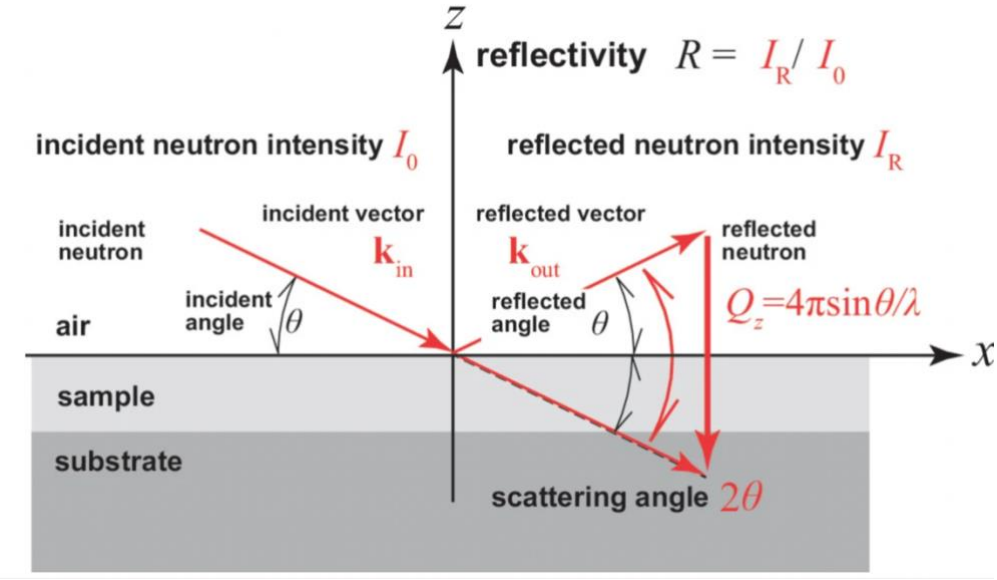


Figure 3.10 Schematic of NR geometry. Reproduced after ref [216].

NR measurement was conducted by Amy Navarathna and me on the time-of-flight ROG neutron reflectometer located at the Reactor Institute Delft (RID), TU Delft, The Netherlands. Data reduction and fitting were performed jointly with Lars Bannenberg, and I conducted the final analysis and interpretation within the context of this thesis.

The instrument operated with a double-disc chopper system (280 mm inter-disc distance) running at 13.2 Hz, providing a neutron wavelength band of $0.3 < \lambda < 1.6$ nm with a wavelength resolution of $\Delta\lambda/\lambda = 0.026$ [217].

Reflectivity profiles were acquired at five incident angles: 8, 16, 24, 48, and 60 mrad. To maintain a consistent illuminated volume, the slit openings were scaled according to the incident angle; at the base angle of 8 mrad, the first and second slits were set to 0.9 mm and 0.3 mm, respectively. This configuration resulted in an angular resolution of $\Delta\theta/\theta = 0.026$ and a total momentum transfer

resolution of ΔQ/Q = 0.036. The beam footprint on the sample surface was calculated to be 32 mm in the umbra and 50 mm in the penumbra.

3.6 Surface Photovoltage (SPV) Spectroscopy

3.6.1 Kelvin Probe (KP)

Kelvin probe (KP) is a non-contact, non-destructive technique used to measure the work function difference between a conducting sample and a reference metal tip. Figure 3.11 depicts a schematic of the KP setup. In practice, a small (~ 0.5×0.5 cm) corner of the AZO sample (~ 4×4 cm) surface was scratched using a diamond pen to expose the underlying silicon. Ag paste was then applied to this region, ensuring no contact with the AZO layer, to provide an electrical connection to the Kelvin probe Al clip and establish the grounding [218, 219]. Figure 3.12 illustrates its working principle, showing (a) the energy alignment before contact, (b) charge redistribution upon contact, and (c) the application of a backing potential to null the induced current. In KP measurements, the work function difference between the sample and the metal tip leads to a contact potential difference (CPD) when the two are electrically connected [220]. Due to this difference, electrons redistribute until the Fermi levels align, resulting in an electrostatic potential between the tip and the sample. The metal tip is mechanically oscillated close to the sample surface, which modulates the capacitance and induces an alternating current. By applying an external backing potential (V_b) that nulls this current, the CPD can be determined.

This compensating potential corresponds to the work function difference between the tip and the sample, and CPD can be expressed as:

$$V_b = -CPD = -\frac{\Phi_m - \Phi_s}{q} \tag{3.20}$$

where, Φ_m and Φ_s are the work functions of the metal tip and sample, respectively, and q is the elementary charge. In the presence of additional charges or band bending effects, the measured potential may include further contributions, and can be expressed as [221]:

$$V_b = -\left(\frac{\Phi_m - \Phi_s}{q} - \frac{Q_{\text{eff}} x_c}{\varepsilon_{\text{TCO}}} - \phi_{scr}\right) \tag{3.21}$$

where Q_{eff} is the effective charge density located at a distance x_c from the interface, ε_{TCO} is the permittivity of the TCO layer, and ϕ_{scr} represents the surface potential associated with the space charge region.

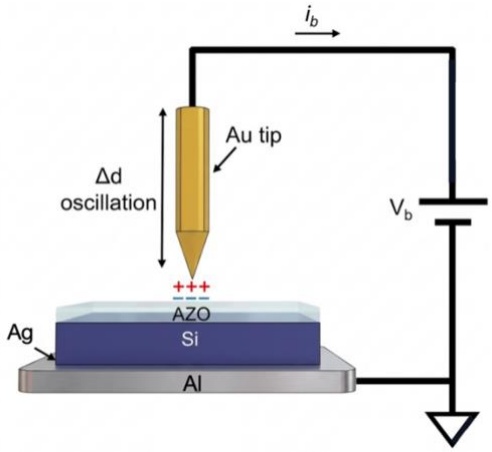


Figure 3.11 Schematic of the Kelvin Probe setup for an AZO sample. The tip is oscillated close to the sample, generating an AC backing current i_b, nullified by applying a backing voltage V_b.

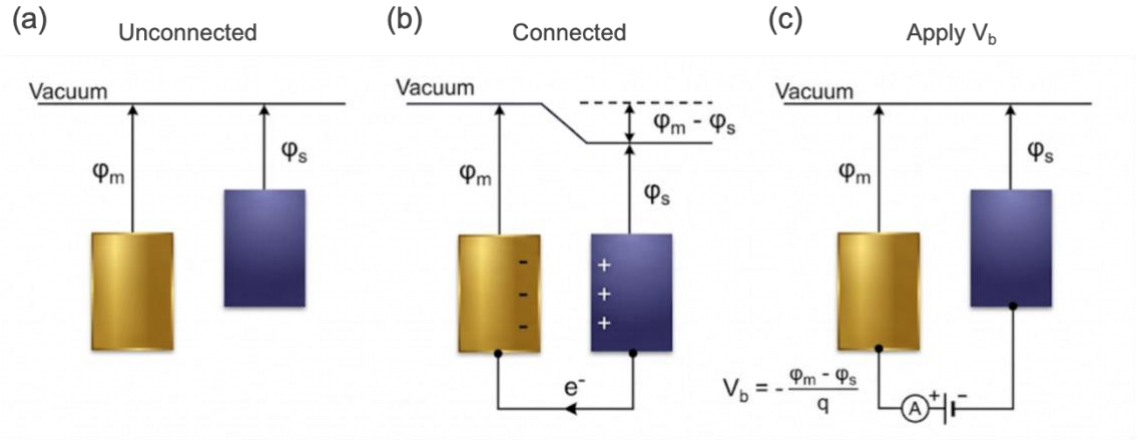


Figure 3.12 (a) Energy level diagram of the metal tip and sample when electrically isolated; (b) Upon electrical connection, charge redistribution occurs until the Fermi levels align, resulting in a CPD; (c) Application of a backing potential V_b compensates the CPD to enable measurement.

3.6.2 SPV

Surface photovoltage (SPV) is a technique used to probe band bending and surface electronic properties by measuring changes in surface potential under illumination [222]. Figure 3.13 shows a schematic of the band structure under dark and illuminated conditions, demonstrating the reduction

of band bending in both cases, regardless of whether the initial band bending is upward or downward [223].

Under illumination, photogenerated electron–hole pairs are generated near the semiconductor surface, leading to an increase in minority carrier concentration. This partially neutralises the space charge region and reduces the band bending at the surface. As a result, the surface potential changes compared to the dark condition. This change in surface potential is detected as the SPV, which can be measured using KP via a variation in CPD, following:

$$\mathrm{SPV} = \mathrm{CPD}_{\mathrm{dark}} - \mathrm{CPD}_{\mathrm{light}} \tag{3.22}$$

where $\mathrm{CPD}_{\mathrm{dark}}$ and $\mathrm{CPD}_{\mathrm{light}}$ are the contact potential differences measured in the dark and under illumination, respectively. The magnitude and sign of the SPV provide information about the direction and extent of band bending, as well as the presence of surface states and fixed charges.

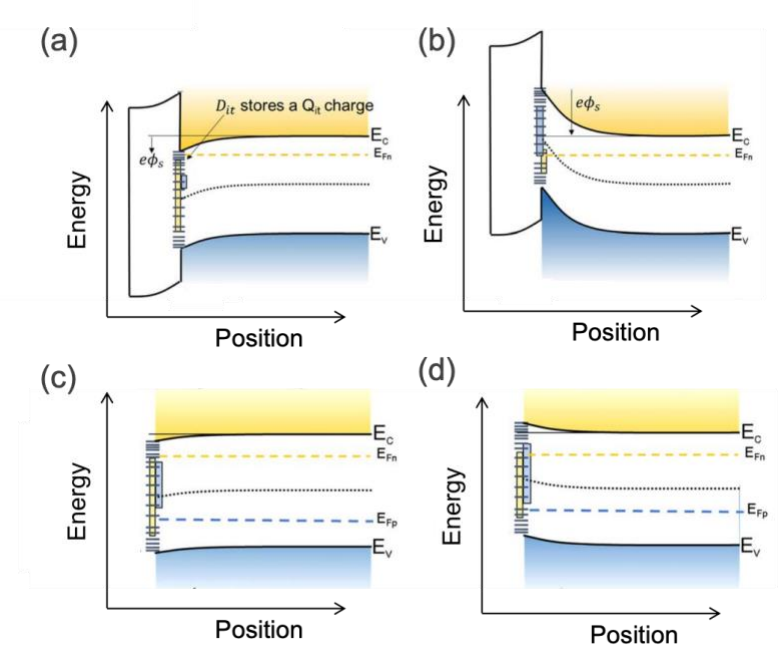


Figure 3.13 Schematic band diagrams of a semiconductor surface under dark (a), (b) and illuminated (c), (d) conditions. (a) and (c) correspond to one type of interface charge, while (b) and (d) represent the opposite charge condition, leading to different initial band bending directions. Reproduced after ref [223].

SPV was measured using a KP Technology Scanning Kelvin Probe (SKP5050) and a 10 mW/cm^2 halogen lamp. A ~1.7×1.7 mm map containing 25 points (step size: ~0.42 mm) was measured using a 2 mm gold probe. Samples were fabricated on Si substrate A from Table 3.1, featuring a 1.2 nm RCA2 chemical-grown SiO_X interface. They consisted of an AZO layer (~16 nm) with and without an

AlO_X capping layer (~26 nm), as deposited and annealed. Some samples were annealed with an AlO_X capping layer, followed by etching of the AlO_X layer for effective contact. Details of the annealing protocols will be discussed in Chapter 6. All CPD values reported in Chapter 6 are arithmetic means of 25 measurements taken at 25 distinct positions across a single sample, and the stated uncertainties are standard deviations.

3.6.3 Transient-SPV

While Kelvin Probe SPV provides steady-state information regarding the band alignment and macroscopic surface potential, transient surface photovoltage (transient-SPV) spectroscopy is employed to investigate the dynamic processes of charge carrier separation and recombination at the Si/AZO/AlO_X interface [224].

Transient-SPV is a time-resolved, constant-photon-flux variant of SPV that probes illumination-induced changes in the surface potential (Equation (3.22)). Figure 3.14 shows the schematic of the transient-SPV measurement setup. The sample is excited by a short laser pulse (e.g., a Nd:YAG laser with a 532 nm wavelength and a nanosecond pulse width) to instantaneously generate excess electron-hole pairs. The transient change in the surface potential is then recorded via capacitive coupling using a transparent conductive electrode (indium tin oxide (ITO) glass) placed above the sample, and the signal is acquired by a high-bandwidth digital oscilloscope [225].

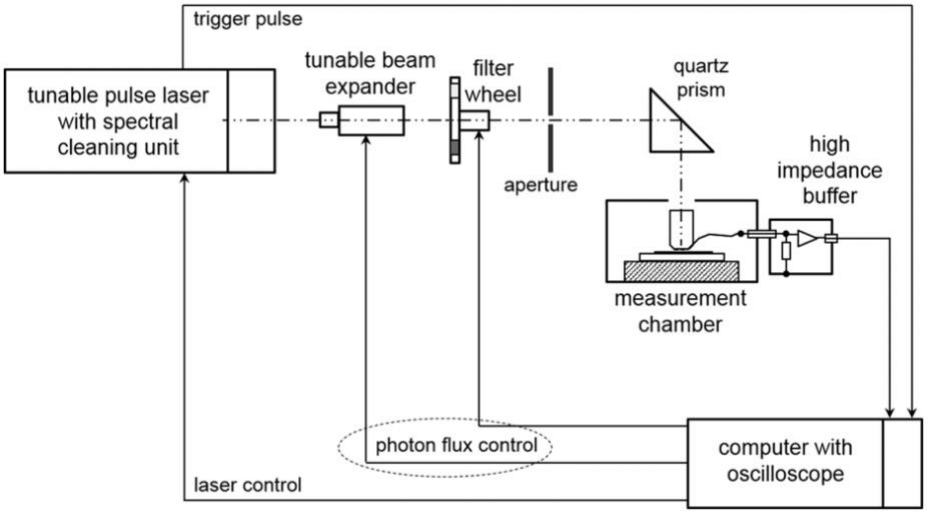


Figure 3.14 Schematic of the transient-SPV measurement setup. Reproduced after ref [226].

Under pulsed illumination, photogenerated excess electron-hole pairs are subsequently separated by the built-in electric field at the Si/AZO interface. The polarity of the SPV signal reveals the direction of charge separation. A positive SPV signal indicates the accumulation of holes at the surface (or interface) and electrons moving toward the bulk, corresponding to the flattening of an upward band bending. Conversely, a negative SPV signal implies electrons drift towards the surface, indicating the flattening of a downward band bending [227, 228].

The maximum amplitude of the transient SPV signal, ΔV_{peak}, reflects the charge extraction capability of the passivating contact. Based on a macroscopic parallel-plate capacitor model, the SPV amplitude (ΔV) is determined by the amount of separated charge and the separation distance, which can be expressed as:

$$\Delta V = \frac{Q \cdot d}{\varepsilon_0 \varepsilon_r} \tag{3.23}$$

Where Q is the amount of photogenerated charge separated, d is the effective charge separation distance (often related to the depletion width), ε_0 is the vacuum permittivity, and ε_r is the relative permittivity of the semiconductor. Therefore, a larger ΔV generally signifies a stronger built-in electric field, which facilitates more efficient initial charge extraction at the interface.

Following the initial charge separation (which corresponds to the peak signal formation via interface states), the SPV signal decays over time as the excess carriers recombine or undergo de-trapping, returning the system to thermal equilibrium. Because the charge carrier dynamics at the Si/AZO interface involve multiple concurrent pathways, the decay transient is rarely a simple single-exponential process. Instead, it can be mathematically conceptualised as a multi-component decay profile [222]:

$$\Delta V(t) = \sum_{i=1}^{n} A_i \exp\left(-\frac{t}{\tau_i}\right) + V_0 \tag{3.24}$$

where A_i represents the weighting amplitude of the i-th decay channel, τ_i is the corresponding characteristic recombination lifetime, and V_0 is the baseline offset. Rather than extracting absolute

carrier lifetimes, this approach enables a temporal separation of distinct relaxation processes in the SPV transients.

The fast decay component is dominated by bulk carrier dynamics, primarily determined by rapid recombination and carrier transport within the semiconductor [229]. In contrast, the slow decay component arises from carrier trapping and de-trapping processes at the Si/AZO interface, which sustain a residual surface potential over longer timescales [230]. The relative contribution of the slow decay therefore serves as an indicator of interface trap density and passivation quality.

The measurements and primary data plotting were performed by Thomas Dittrich at the Helmholtz-Zentrum Berlin, Germany. I conducted the subsequent data analysis, interpretation, and integration of the transient-SPV results into the thesis narrative. Samples were fabricated on Si substrate B from Table 3.1, with an extra 1.2 nm RCA2 chemical-grown SiO_X interface after RCA cleaning. They consisted of an AZO layer (~16 nm) with and without an AlO_X capping layer (~26 nm), as deposited and annealed. Details of the annealing protocols will be discussed in Chapter 6.

Chapter 4. Precursor Control for Optimised AZO Passivation

4.1 Introduction to Precursor Modulation

In atomic layer deposition (ALD), the properties of the resulting thin film are governed not only by the substrate temperature and cycle count but also by the partial pressures of the gaseous precursors delivered during each half-reaction [48]. Precursor modulation refers to the deliberate adjustment of these partial pressures to control the stoichiometry and dopant incorporation within the growing film.

For aluminium-doped zinc oxide (AZO), the relative dosing of diethylzinc (DEZ), trimethylaluminium (TMA), and water (H_2O) determines the Zn:Al:O ratio, which in turn governs the electrical, optical, and passivation properties of the deposited layer.

During the AZO deposition process development, I observed variations in surface passivation quality across sample batches fabricated over a year. These discrepancies persisted despite constant chamber temperature and pulse durations. A closer examination to ~130 different deposition runs during one year revealed that the inconsistencies correlated with the gradual depletion of precursor liquids: as the liquid level fell, the effective partial pressures shifted.

This observation led me to a hypothesis: the precise ratio of precursor partial pressures plays the key role in governing the film surface passivation properties and interface quality. To investigate this effect systematically and to achieve reproducibility, I revised the deposition protocols. The objective of this chapter is therefore to summarise my overall findings of the impact that precursor dosing has on the surface passivation of AZO/AlO_X stacks formed using ALD.

4.2 Optimisation of Passivation via Dosing Control

To validate this hypothesis, my investigation focused on modulating the partial pressures and flow ratios of the three key precursors: water (H_2O), diethylzinc (DEZ), and trimethylaluminium (TMA). This approach used precursor dosing pressure as the primary tuning parameter to control the film stoichiometry.

We conducted experimental validation on symmetrical passivation stacks fabricated on n-type Czochralski (Cz) silicon (Section 3.1.1). Figure 4.1 (a) shows the schematic of the passivation stack, which consisted of a chemically grown interfacial oxide (1.2 nm SiO_2), followed by the functional AZO layer (16 nm ± 0.5 nm), and capped with an aluminium oxide layer (26 nm ± 2 nm).

To confirm the stack configuration, transmission electron microscopy (TEM) was employed. Figure 4.1 (b) presents a cross-sectional TEM micrograph of an AZO/AlO_X stack deposited using the same process. This micrograph was acquired early in the project, before the layer thicknesses were optimised: the sample shown comprises 63 ALD cycles of AZO and 180 cycles of AlO_X, rather than the 105 and 250 cycles used for the optimised stack shown in Figure 4.1 (a), and the layers therefore appear correspondingly thinner (~10 and ~18 nm). The image is therefore used to verify the layer sequence and interface abruptness rather than as a thickness measurement. The image reveals the distinct layer stratification, showing the crystalline silicon substrate, the AZO layer, and the AlO_X capping layer. The interfaces between the Si/AZO and AZO/AlO_X appear sharp and well-defined, indicating minimal interdiffusion during the deposition process.

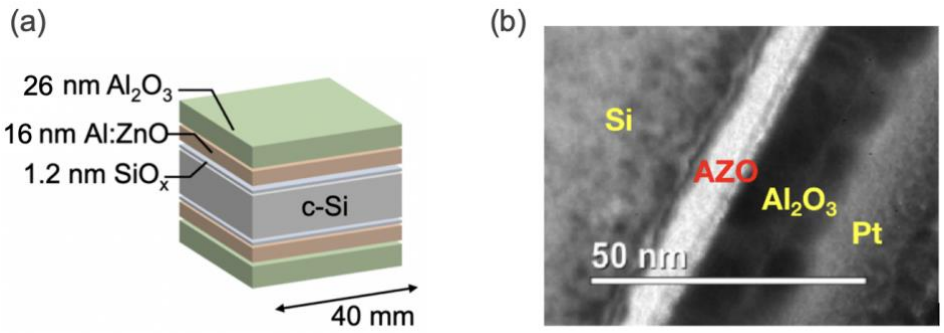


Figure 4.1 (a) Schematic diagram of the prepared sample for the passivation investigation; (b) TEM image of an AZO/AlO_X stack deposited before thickness optimisation (63 cycles AZO, 180 cycles AlO_X, compared with 105 and 250 cycles for the optimised stack in (a)). A platinum (Pt) layer, deposited during the focused ion beam (FIB) preparation to protect the sample surface, is also visible at the top.

4.2.1 Recipe Design via Partial Pressure Modulation

Four distinct dosing protocols were designed to investigate the impact of specific precursor ratios (H_2O:DEZ:TMA) on the passivation properties of AZO, as shown in Figure 4.2. They were established to control the deviations from a balanced stoichiometry in the AZO thin film matrix that was found to provide the best passivation upon reviewing ~ 130 runs over approximately 12 months.

The absolute peak precursor pressures and the H_2O:DEZ:TMA ratios for each recipe are shown in Table 4.1. Each recipe was designed to deviate from the optimised baseline (4:3:2.5) in a single precursor, thereby isolating the effect of excess aluminium, zinc deficiency, or oxidant deficiency on film properties.

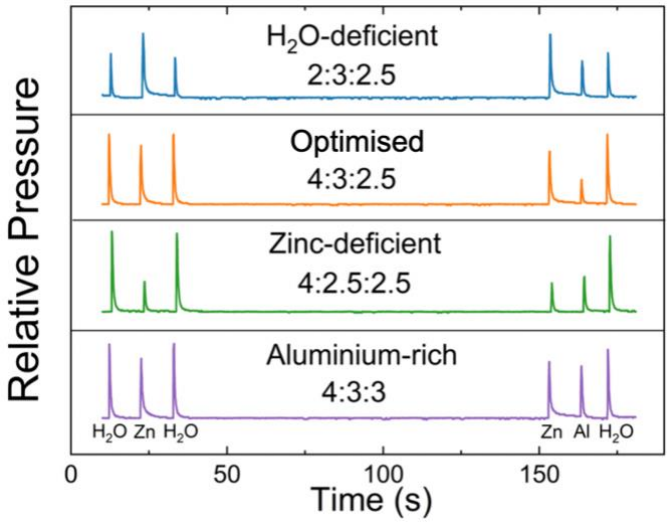


Figure 4.2 Pressure ratio profiles of different precursor purges in ALD. Note: The pressure profiles are offset to allow for comparison.

Table 4.1 The approximate pressure peak for each precursor and their ratios in the four different ALD pressure profiles.

Group	H_2O pressure (mTorr)	DEZ pressure (mTorr)	TMA pressure (mTorr)	Ratio H_2O:DEZ:TMA
Al-rich	0.20	0.15	0.15	4:3:3
Zn-deficient	0.20	0.125	0.125	4:2.5:2.5
Optimised	0.20	0.15	0.125	4:3:2.5
H2O-deficient	0.10	0.15	0.125	2:3:2.5

4.2.2 Lifetime Analysis and Passivation Performance

The passivation quality of the specific dosing protocols was quantified by measuring the effective minority carrier lifetime as a function of excess carrier density (ECD). Figure 4.3 presents the injection-dependent lifetime curves for the champion samples derived from each of the four recipes. Among these, the sample synthesised using the optimised precursor ratio (H_2O:DEZ:TMA = 4:3:2.5) exhibited the lowest recombination losses among the four recipes. At an injection level of 10^{15} cm^{-3}, this sample yields a peak effective lifetime of 3.38 ms.

This lifetime corresponds to an implied open-circuit voltage (iV_{OC}) of approximately 741 mV and a saturation current density (J_0) of 0.87 fA/cm^2. The iV_{OC} is among the highest reported values for AZO-based passivation stacks in the literature, while the J_0 represents the lowest recorded value to date [44, 46, 47, 50]. Appendix A (Table A 12) displays the average and standard deviation of iV_{OC} for 5 samples fabricated and measured per condition.

To verify that these results were not artefacts of localised high-performance regions, photoluminescence (PL) imaging was conducted, as shown in Figure 4.4. The PL intensity map reveals high spatial uniformity, confirming consistent passivation.

The Al-rich recipe yielded results statistically similar to the optimised condition. It achieved an iV_{OC} of 740 mV and a comparable lifetime of 3.25 ms at 1×10^{15} cm^{-3} ECD. This similarity suggests that the passivation mechanism is tolerant to moderate excess aluminium.

However, the passivation quality degrades sharply when the AZO deviates from optimal stoichiometry. The Zn-deficient and H_2O-deficient samples exhibited significantly reduced lifetimes of 1.62 ms and 1.12 ms at 1×10^{15} cm^{-3} ECD, respectively, with corresponding drops in iV_{OC} to 733 mV and 727 mV. The performance drop suggests that passivation quality is sensitive to both zinc deficiency and oxidant deficiency.

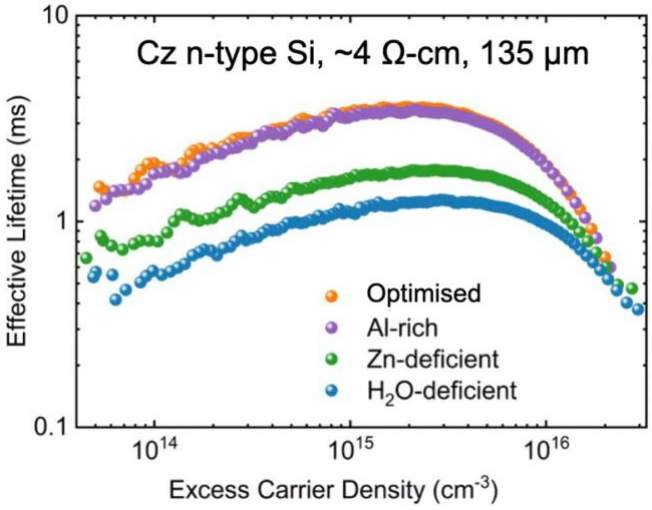


Figure 4.3 Effective lifetime as a function of excess carrier density of the champion samples from the four different pressure profiles. Their J_0, iV_{OC}, and lifetime values are listed in Appendix A (Table A 13). The analysis plots for the optimised champion sample are shown in Appendix A (Figure A 79).

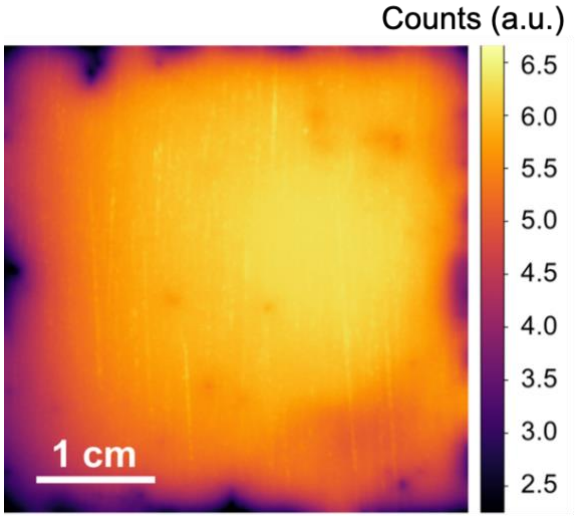


Figure 4.4 PL image of the champion sample from the optimised recipe.

4.2.3 Annealing Dynamics and Thermal Stability

The thermal evolution of the passivation stack was characterised to establish the optimal activation budget. The standard thermal protocol involved a primary furnace anneal at 500 °C for 20 minutes in ambient air, followed by a secondary, cumulative annealing step on a hotplate at 450 °C. The furnace step was utilised to activate hydrogen-mediated passivation across the full stack, while the hotplate step allowed fine-grained control over the thermodynamics in shorter increments. All temperatures reported here refer to the measured thermocouple temperature; the correspondence between set-point and thermocouple-measured values is detailed in Section 3.1.4.

Figure 4.5 illustrates the trajectory of iV_{OC} as a function of the secondary hotplate annealing duration after the initial 20-minute 500 °C anneal in a furnace. The data reveal a clear optimisation window. At 20-minute hotplate annealing (corresponding to 40 minutes total annealing time in Figure 4.5), a maximum iV_{OC} of > 741 mV was observed, while the iV_{OC} achieved at 10-minute hotplate annealing was marginally lower (738 mV). However, this 10-minute step provided the most significant and rapid increase in iV_{OC} compared to the furnace-only value. For practical throughput, a 10-minute hotplate anneal was adopted as the standard baseline for this chapter. It allowed for the rapid synthesis of samples for improved statistics, with iV_{OC} values only marginally lower than the maximum achieved.

The data also indicate that the passivation quality is metastable under prolonged thermal stress. Extending the hotplate annealing duration beyond the 20-minute optimum resulted in a degradation of iV_{OC}. Two mechanisms, both reported in similar metal-oxide systems, may explain this degradation [151, 231, 232]. First, the thermal budget may eventually exceed the activation energy for hydrogen desorption, leading to hydrogen effusion and the reactivation of dangling bonds at the interface [233-235]. Second, the extended dwell time at 450 °C may drive the growth or densification of ZnO crystallites [236]. Such morphological changes can induce stress at the interface or increase the density of grain boundaries, thereby introducing new recombination centres [45, 231, 237]. Thus, precise control of the annealing time is as critical as the deposition stoichiometry in determining the final device performance.

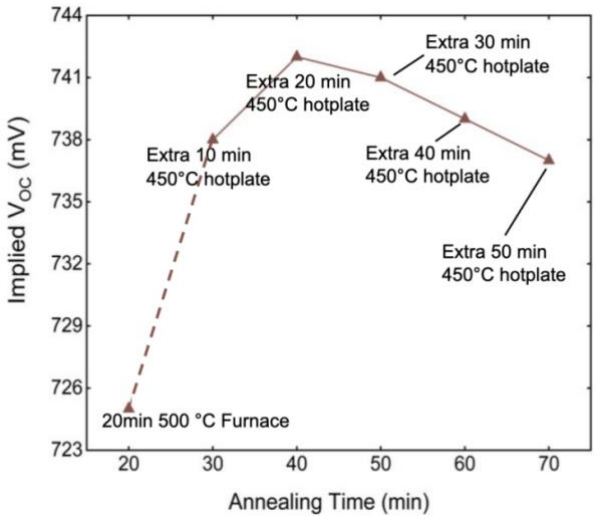


Figure 4.5 iV_{OC} values vs. annealing time for the champion sample undergoing post-deposition annealing at 450 °C.

4.3 Structural and Compositional Analysis

4.3.1 Crystallographic Phase and Texture

The crystallographic phase of the AZO films was determined via grazing incidence X-ray diffraction (GIXRD). Figure 4.6 compares the GIXRD patterns of the as-deposited and annealed standard AZO/AlO_X samples. A dominant peak is centred at approximately 34.6°, corresponding to the (002) plane of the wurtzite ZnO phase. This preferential orientation along the c-axis is characteristic of ALD-grown ZnO films on amorphous substrates [238-240].

The (002) peak position is essentially unchanged after annealing at 450 °C. The Scherrer width corresponding to a ~ 16 nm crystallite size is ~ 1° in 2θ, so a lattice strain of the magnitude anticipated here (a few tenths of a percent) would displace the centroid by only ~0.1°, comparable to the uncertainty with which the centroid of such a broad peak can be located. Figure 4.6 therefore indicates that the films are crystalline as deposited, strongly (002)-textured, and retain this phase and texture through the anneal, without detectable secondary crystalline phases such as $ZnAl_2O_4$ appearing. This sets an upper bound on the amount of Al that can be held in a crystalline secondary phase, and is used in Section 4.4.2 to argue that the electrically inactive Al is likely to reside in amorphous rather than crystalline environments. Direct evidence for densification is instead provided by the X-ray reflectometry results of Section 5.5.2, where the fitted scattering length density of both sub-layers increases upon annealing. This densification is consistent with two concurrent mechanisms. First, thermal energy allows relaxation of intrinsic growth stresses and promotes the incorporation of Al onto substitutional Zn sites (Al_{Zn}) from the non-substitutional environments identified in Section 4.4.2; the smaller ionic radius of Al^{3+} contracts the lattice [241-243]. Second, annealing above 200 °C promotes effusion of residual hydrogen, H_2O, and carbonaceous species trapped during the 150 °C deposition, reducing the free volume within the film [244, 245].

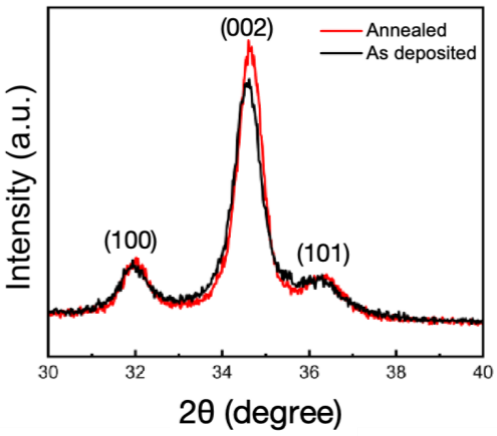


Figure 4.6 GIXRD spectra of as-deposited (black) and annealed (red) standard 16 nm AZO / 26 nm AlO_X samples in the range of 30°- 40°.

4.3.2 Nanostructural Interface and Elemental Uniformity

While XRD provides volume-averaged data, the local nanostructure and interface quality were characterised using High-Resolution Transmission Electron Microscopy (HRTEM). Figure 4.7 (a) presents a cross-sectional micrograph of the optimised sample across the SiO_2/AZO/AlO_X stack. The image reveals a clearly defined stratification of layers with sharp, continuous interfaces, confirming the high conformality characteristic of the ALD process.

The AZO layer itself exhibits as a composite microstructure, where nanocrystallites are embedded within a predominantly amorphous matrix. This amorphous fraction is the plausible host for the segregated Al identified in Section 4.4.2. This semi-crystalline nature suggests the presence of phase boundaries, which act as scattering centres for charge carriers (reducing mobility) or as trap states for recombination [246, 247].

To correlate this microstructure with elemental composition, Energy-Dispersive X-ray Spectroscopy (EDS) mapping was performed (Figure 4.7 (b)). The elemental maps show distinct localisation of oxygen (red), silicon (green), zinc (yellow), and aluminium (blue). There is a consistent distribution of Zn, Al, and O within the AZO matrix, with sharp transitions at the c-Si interface, confirming high film uniformity and successful Al incorporation via ALD.

The dopant distribution is uniform through the bulk of the film, which supports effective field-effect passivation. The atomic fraction profiles derived from the EDS data (Figure 4.7 (c)) illustrate this distribution. The Al concentration fluctuates around an average of ~ 7 at.% within the bulk of the AZO

film. An accumulation of Al is observed near the top surface, while the concentration drops to ~ 0 at.% at the Si/AZO interface. This accumulation is revisited in Section 4.4.2 as evidence of Al segregation. A distribution that is homogeneous through the bulk gives a consistent Fermi level shift across the film interior, which is a prerequisite for the accumulation layer that suppresses minority carrier recombination [170, 246, 248]. The deviation from uniformity at the top surface is taken up in Section 4.4.2.

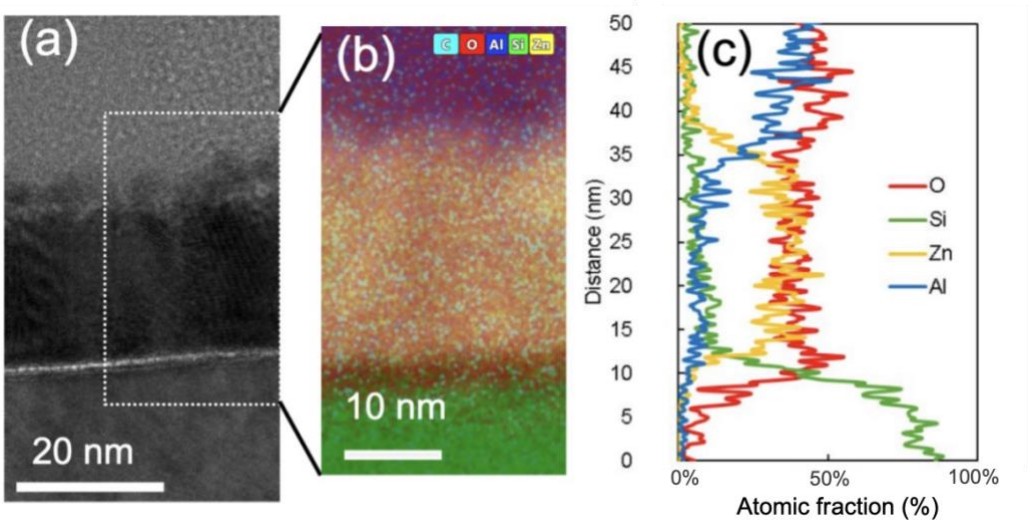


Figure 4.7 (a) High-resolution high-angle annular dark field (HAADF) TEM image of the crystal structure and defects in AZO. (b) The enlarged image is the obtained EDS micrograph for a local region of interest. (c) The averaged EDS has been plotted for elemental analysis of AZO.

4.3.3 Chemical Stoichiometry and Dopant Activation

To investigate how different precursor dosing ratios influence the chemical state and precise stoichiometry of the films, I employed X-ray Photoelectron Spectroscopy (XPS). By comparing the optimised (4:3:2.5) recipe with Al-rich and Zn-deficient variations, XPS complements the bulk-averaged EDS analysis by providing surface-sensitive information on the dopant chemical states. For this analysis, uncapped AZO films (50 nm) were utilised to allow direct access to the AZO surface.

Figure 4.8 shows the initial survey scans, which detected the expected Zn, O, and Al core levels, alongside a carbon signal attributed to atmospheric contamination. Subsequent Ar^+ ion sputtering effectively removed this surface carbon, revealing the bulk composition. The intensity of the core

levels increased post-sputtering, indicating that the bulk film possesses a higher density of metal-oxygen bonds compared to the air-exposed surface.

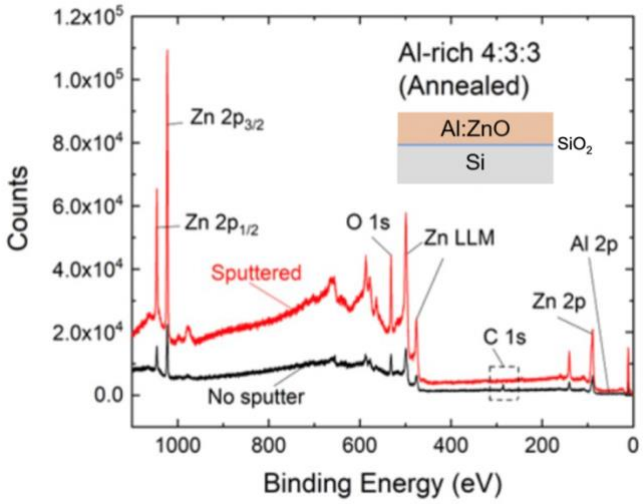


Figure 4.8 XPS survey spectra illustrating the effects of surface Ar sputtering at 4 kV for 5 mins, for an annealed Al-rich sample.

A key metric for the doping efficiency under the impact of varying DEZ and TMA precursor doses is the relative intensity ratio of the aluminium and zinc core levels (Al 2p/Zn $3p_{3/2}$). Figure 4.9 (a) plots an example of the core level peak fitting, and (b) shows such relative intensity ratios. Peaks were fitted in CasaXPS over 65–100 eV, using a Tougaard rather than a Shirley background. The Al 2p signal is weak and lies on the inelastic tail of the much stronger Zn 3p doublet 15 eV above it. Tougaard models that tail from the electron scattering cross-section rather than from the peak area, which is the more reliable approach here. Core levels were fitted with a Gaussian–Lorentzian line shape, representing lifetime and instrumental broadening, respectively. The Zn 3p doublet was constrained to a 2:1 area ratio with a shared width, as its degeneracy requires. Al 2p was fitted as a single component, since its 0.4 eV splitting is below the resolution at 26 eV pass energy. The same background limits, line shape and constraints were used for all four samples. The weak Al 2p signal makes the absolute ratio sensitive to where the background is placed; the comparison between recipes is not. Additionally, because the relative sensitivity factors (RSF) for the specific instrument were unavailable, these ratios serve as a robust comparative index rather than absolute atomic percentages. However, EDS suggests a nominal Al concentration of around 7 at.%. The signal is likewise too weak to resolve the Al 2p chemical state, so substitutional and Al_2O_3-like Al cannot be

separated from these spectra. This EDS value is used to evaluate the doping efficiency in Section 4.4.2.

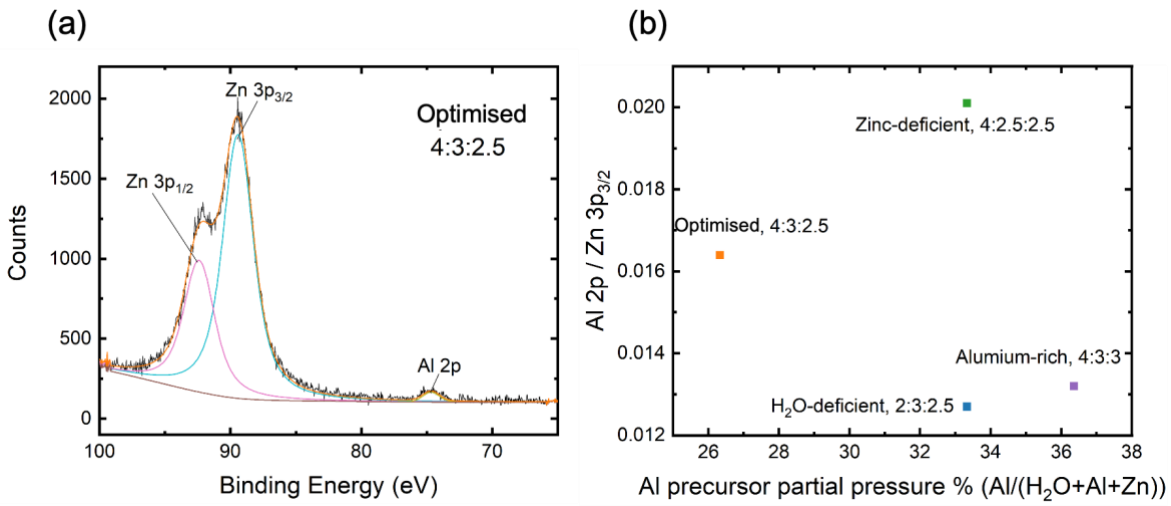


Figure 4.9 (a) Example of fitting of Zn 3p & Al 2p core level peaks in XPS spectra, for optimised case only; (b) Al 2p/Zn $3p_{3/2}$ ratio across annealed, sputter-cleaned samples with the four different pressure profiles, determined from the integrated intensity of Zn $3p_{3/2}$ and Al 2p core peaks, as measured with XPS. The peak fitting curves for samples from the four different recipes are shown in Appendix B, Figure A 80.

The XPS analysis reveals a non-linear relationship between the precursor partial pressures and the incorporated film composition. Specifically, the Al-rich sample, which utilised the highest Al precursor partial pressure of ~ 36.5%, yielded a measured Al 2p/Zn $3p_{3/2}$ ratio of only ~ 0.0135. In contrast, the optimised sample, despite a lower Al partial pressure of ~ 26.5%, achieved a higher actual Al 2p/Zn $3p_{3/2}$ ratio of ~0.0165. A ~ 38% increase in Al partial pressure resulted in a ~ 20% relative decrease in the measured Al/Zn ratio, demonstrating that once the activation pressure for surface reaction is surpassed, further increases in dosing pressure result in diminished incorporation efficiency.

A comparison of samples at the same Al partial pressure (~ 33.5%) reveals a non-linear dependence on the dosing of other precursors. The Zn-deficient sample reached the highest Al 2p/Zn $3p_{3/2}$ ratio of > 0.020, whereas the H_2O-deficient sample at the same coordinate dropped to the lowest observed ratio of ~ 0.0125. These results suggest that the final Al concentration is significantly influenced by competitive adsorption between the DEZ and TMA precursors, as well as the availability of the co-reactant H_2O, rather than the pressure of the Al pulse alone.

The observed non-linear relationship between the precursor partial pressures and Al/Zn ratio is attributed to several concurrent chemical and physical mechanisms. The first mechanism is ligand exchange and chemical etching. The modified ALD supercycle sequence, which transitions directly

from a DEZ pulse to a TMA pulse without an intervening water dose (as described in Section 3.1.3), facilitates direct interaction between TMA and surface-adsorbed Zn-C_2H_5 or Zn-OH groups. As a strong Lewis acid, TMA may participate in exchange reactions that displace surface zinc atoms. This ligand exchange can lead to the formation of volatile Al-Zn organometallic complexes, which may desorb from the surface, effectively removing both the intended Al dopant and the existing Zn matrix.

Second, surface site saturation contributes to the diminished incorporation efficiency at elevated TMA pressures. TMA is the smallest commonly used aluminium ALD precursor, with compact methyl ($–CH_3$) ligands of approximately 2.6 Å [249]. Consequently, TMA molecules themselves impose relatively little steric shielding on adjacent surface sites compared to bulkier precursors such as dimethylaluminium isopropoxide (DMAI) [153, 166]. However, at high partial pressures, the rapid and dense chemisorption of TMA-derived $–Al(CH_3)_2$ species can saturate the available hydroxyl sites within a single half-cycle, effectively blocking additional adsorption not through molecular bulkiness but through surface coverage saturation. This coverage-dependent site blocking reduces the net incorporation efficiency per pulse compared to the optimised case, where moderate TMA pressures allow adsorption across the surface without premature saturation. This mechanism may also explain the peak Al/Zn ratio observed in the Zn-deficient (4:2.5:2.5) sample: the reduced dosage of DEZ freed additional surface hydroxyl groups for TMA adsorption, thereby increasing the fraction of sites available for Al incorporation.

The third mechanism is purging inefficiency and gas-phase loss. At the high concentration levels used for the Al-rich sample (~ 36.5%), the standard purge steps may be insufficient to remove all residual precursors. This can lead to parasitic gas-phase reactions or the formation of TMA dimers and aggregates [250]. These species exhibit lower surface reactivity than monomeric TMA and are more easily removed during the subsequent purge phase, leading to a net loss of active Al precursor.

Figure 4.3 and Figure 4.9 (b) show that the sample with the highest Al ratio (Zn-deficient) did not yield the best passivation performance. This result indicates that passivation performance is not a simple function of Al content, suggesting that beyond a certain threshold, the benefits of increased doping are offset by other physical factors that negatively impact the electronic properties of the thin film and interface. The excessive Al in the Zn-deficient sample likely introduces structural disorder in

the form of segregated Al–O–Al environments, which act as recombination centres [151]; Section 4.4.2 quantifies the fraction of Al involved. In contrast, the optimised sample maintained intermediate values for the final Al/Zn ratio. The superior passivation performance of this sample suggests that its specific chemical composition represents the optimum range for achieving high passivation.

4.4 Optoelectronic Performance and Band Alignment

4.4.1 Electrical Transport

The electrical properties, including resistivity, sheet resistance, carrier mobility, and carrier concentration, were characterised using van der Pauw (vdP) and Hall effect measurements. To facilitate reliable electrical probing, 40-nm-thick AZO films were deposited onto 290-nm SiO_2 on Si wafers. The thick oxide layer provides sufficient electrical isolation to prevent parasitic substrate conduction during van der Pauw and Hall measurements, as verified by the absence of measurable current through control structures without the AZO film.

Figure 4.10 summarises the resistivity (left axis, bars) and sheet resistance (right axis, triangles) across the four different pressure ratio profiles. The optimised recipe yields a resistivity of approximately 5×10^{-3} Ω·cm and sheet resistance of around 1300 Ω/sq. Placing this in the context of Figure 2.8 (Section 2.3.5), the value lies approximately a factor of five above the upper end of the 10^{-4}–10^{-3} Ω·cm range reported for optimised AZO. As discussed below, this offset arises from the extended ambient storage of this particular sample set rather than from an intrinsic limitation of the process: films of the same recipe measured shortly after deposition give ~ 1×10^{-3} Ω·cm (Section 5.7.2), which falls within the AZO range shown in Figure 2.8. Even at this value, the resulting sheet resistance of ~ 1300 Ω/sq remains acceptable for passivating contact interlayers operating with metal finger grids [251-253].

A distinct correlation is observed between the precursor dosing ratios and electrical transport. The H_2O-deficient sample exhibits comparable resistivity (4.8×10^{-3} Ω·cm), indicating that moderate oxidant fluctuations do not significantly impair conductivity when the metal cation ratio is maintained. The Zn-deficient sample displays the highest resistivity (9.8×10^{-3} Ω·cm) and sheet resistance (> 2500

Ω/sq), which aligns with the XPS findings above, confirming that Zn deficiency disrupts the formation of the conductive matrix. This is likely caused by introducing scattering centres or disrupting the lattice continuity required for electron transport. Despite the higher nominal dopant density in the Al-rich sample, the conductivity is lower than that of the optimised sample, likely due to ionised impurity scattering, which will be discussed in detail in the next section.

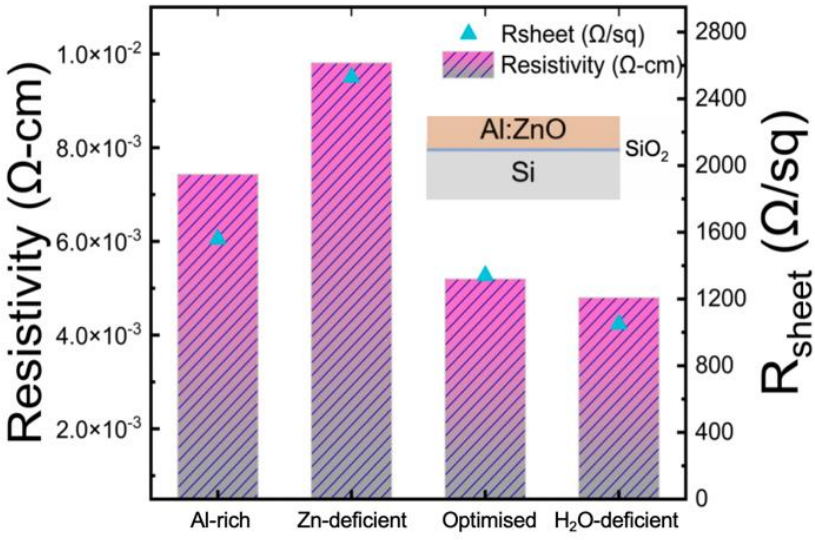


Figure 4.10 Resistivity and sheet resistance of samples from the different profiles.

It is noted that the as-deposited resistivity for the 40-nm-thick sample in this chapter (5×10^{-3} Ω·cm) is approximately five times higher than the value reported for the equivalent sample in Section 5.7.2 (~ 1×10^{-3} Ω·cm). This discrepancy is primarily attributed to differences in ambient exposure history: the samples in this chapter were stored in laboratory air for several months prior to measurement, whereas those in Section 5.7.2 were measured within days of deposition.

The sensitivity of AZO resistivity to ambient aging is well established and arises primarily from the progressive annihilation of oxygen vacancies as atmospheric O_2 and H_2O diffuse into the film [142, 153, 254]. In the 40 nm thickness regime, this bulk degradation is further exacerbated by surface effects. Prolonged atmospheric exposure promotes the formation of a high-resistivity surface depletion layer through the chemisorption of hydroxyl species, which reduces the effective conducting cross-section and enhances surface scattering [197, 255]. A secondary contribution may arise from routine run-to-run variations inherent to vacuum chamber conditioning history, though this effect is marginal compared to ambient aging.

Importantly, the data presented within this chapter are internally self-consistent: all four precursor recipes were deposited and measured within the same experimental session under identical ambient exposure conditions. The relative comparison between recipes, which forms the basis of the conclusions drawn in this chapter, is therefore unaffected by the absolute resistivity offset. The improved measurement protocol adopted in Chapter 5, in which samples were characterised immediately after deposition to minimise ambient-induced aging, provides more representative values of the as-deposited film resistivity.

4.4.2 Carrier Mobility and Scattering Mechanisms

To decouple mobility and scattering effects, I performed Hall effect measurements, with the results illustrated in Figure 4.11. The measured Hall mobility of the optimised sample reached an apparent high value of approximately 80 $cm^2/V{\cdot}s$ at a moderate carrier concentration (1.5×10^{19} cm^{-3}), which sits at the upper bounds reported for ALD-deposited AZO [256].

The integration of Hall effect measurements (Figure 4.11) with XPS compositional analysis (Figure 4.9 (b)) elucidates the role of structural order in determining the electrical properties of the AZO films.

The Zn-deficient sample, despite exhibiting the highest Al incorporation, maintains a relatively low carrier concentration of ~ 2.1×10^{19} cm^{-3}. This indicates a low doping activation efficiency, where excessive Al likely resides in non-substitutional environments (Section 2.4.1), acting as scattering centres that suppress mobility to ~ 30 $cm^2/V{\cdot}s$ [257]. In contrast, the optimised sample achieves a superior electron mobility of ~ 80 $cm^2/V{\cdot}s$, with the lowest carrier concentration. This comparison suggests that the optimised growth condition minimises structural defects and ionised impurity scattering, resulting in a more ordered crystalline lattice. The H_2O-deficient sample exhibits a higher carrier concentration than the optimised sample. In the ALD process, insufficient oxidant exposure pushes the growth into a sub-stoichiometric, Zn-rich regime. This naturally promotes the formation of native point defects, which hinders mobility compared with the optimised sample. These native point defects include oxygen vacancies (V_O^{2+}) and zinc interstitials (Zn_i^{2+}), both of which act as donors that elevate the background electron concentration [258].

The Al-rich sample shows the highest carrier concentration of ~ 5.1 ×10^{19} cm^{-3}, despite its relatively lower Al/Zn ratio compared to Zn-deficient and optimised samples, suggesting that the measured carrier density is not solely governed by Al incorporation. Three factors may contribute. The doping-efficiency calculation later in this section discriminates among them.

First, its doping activation efficiency could be high. In the Al-rich pressure regime, the high TMA flux might facilitate the direct substitution of Al into Zn sites (Al_{Zn}) during the brief window of surface residence, even if much of the Al is subsequently etched away by the mechanisms discussed in Section 4.3.3. This leads to a cleaner substitution where a larger fraction of Al atoms occupy electrically active substitutional sites, rather than electrically inactive environments.

The second factor is a shift in the Zn/O stoichiometry. The intense TMA flux may interfere with the subsequent H_2O pulse's ability to fully oxidise the surface (due to site blocking by bulky methyl ligands). This can result in a film that is Zn-rich, which is possible according to its low Al/Zn ratio. Excess Zn in the form of Zn interstitials (Zn_i) acts as a native donor. Therefore, the high carrier concentration could come from a combination of Al_{Zn} and Zn_i. These two explanations are supported by this sample exhibiting the lowest mobility of the four pressure profiles (~ 16 $cm^2/V{\cdot}s$), likely associated with significant ionised impurity scattering (Al_{Zn}^+ donors) and structural lattice distortion (Zn_i).

The third factor is unintentional hydrogen incorporation due to purge limitations at high pressures. As discussed in Section 4.3.3, at high Al precursor pressures, the purge steps may become less effective at removing reaction by-products (like methane, CH_4) or residual hydroxyl groups (-OH). Hydrogen is a well-documented shallow donor in ZnO, existing as interstitial hydrogen (H_i) or occupying oxygen vacancies (H_O) [142, 254]. Therefore, the high TMA pulse can trap hydrogen at the growth front before the next purge can clear it, leading to a film that is essentially H-doped AZO. This hypothesis can be supported by the second-highest passivation performance of the Al-rich sample among all (Figure 4.3). However, a mechanistic ambiguity remains: it is currently indiscernible whether this good passivation originates primarily from a better field-effect, driven by a strong electrostatic field associated with its high carrier concentration, or from enhanced chemical

passivation, facilitated by unintentional hydrogen incorporation that might lead to reduced interface states upon post-annealing.

Alternative precursors such as DMAI yield doping efficiencies approaching 60%, against ~ 10% for TMA, because steric hindrance limits the surface site density available to the dopant precursor and so prevents cluster formation (Section 2.4.2) [153, 166]. However, the TMA-based process demonstrated here achieves minority carrier lifetimes exceeding 3 ms at 1×10^{15} cm^{-3} ECD and J_0 below 1 fA/cm^2, suggesting that while TMA may be less efficient for maximising conductivity, it offers distinct advantages for interface passivation.

The doping efficiency of these films can be quantified. Following Illiberi et al., it is given by $\xi = \frac{N_e - N_{e0}}{Al\%\left(\frac{\sigma}{2M_{mol}}\right)N_A}$, where N_e is the carrier density of the doped film, N_{e0} that of undoped ZnO, $Al\%$ the cation fraction Al/(Al + Zn) determined by EDS, σ the bulk density of ZnO (5.606 g cm^{-3}), M_{mol} its molar mass (81.4 g mol^{-1}) and N_A the Avogadro constant [259]. The EDS profile of Figure 4.7 (c) covers all detected elements, so I take the cation fraction from the ratio of the Al and Zn plateaux, which give Al ≈ 7 at.% and Zn ≈ 35 at.%. Hence, Al/(Al + Zn) is ~ 17 at.% and Al density is 3.5×10^{21} cm^{-3}. The films of Figure 4.11 had been stored in laboratory air for several months before measurement (Section 4.4.1), so I use instead the Hall data of Section 5.7.2, measured within days of deposition on films of the same recipe. Taking N_{e0} of 7×10^{18} cm^{-3} for undoped ZnO [259], the 20 and 56 nm films, which bracket the 40 nm used here, give ξ of ~ 3% and 12% as deposited, rising to 7% and 22% after annealing. At least three-quarters of the incorporated Al therefore donates no free electron under any condition measured. Taken together, the activation is of order 10%, and this is the figure referred to elsewhere in the thesis.

These values sit where the deposition chemistry predicts. Illiberi et al. associate ξ < 15% with supercycle ALD, in which Al_2O_3 cycles are inserted into the ZnO growth, and reach ~ 70% only by co-dosing the metal precursors so that Al is dispersed atomically rather than delivered in discrete planes [259]. The ~ 10% reported for TMA-based ALD-AZO and the ~ 60% for DMAI (Section 2.4.2) span the same range and reflect the same contrast, and the as-deposited values here bracket the TMA figure.

Two systematic effects act on ξ in opposite directions. The Al content derived from EDS is higher than three independent constraints support. It exceeds what the 20:1 ZnO:AlO_X cycle ratio implies and the 1–2 mol% optimum quoted in Section 2.4.1, and Illiberi et al. report that $Al_XZn_{(1-X)}O$ becomes resistive above Al/(Al + Zn) of ~ 13%, reaching 0.8 Ω·cm, with an insulating $ZnAl_2O_4$ or $(ZnO)_3$ (Al_2O_3) phase forming [259], whereas these films retain the wurtzite structure (Section 4.3.1) and a resistivity of order 10^{-3} Ω·cm (Section 5.7.2). EDS quantification in a film tens of nanometres thick carries a large systematic error, so the true cation fraction is probably lower, and ξ correspondingly higher. Against this, the ξ equation assigns every carrier above N_{e0} to Al, whereas oxygen vacancies (Section 6.2.3), zinc interstitials and interstitial hydrogen (discussed above in this section) all act as donors in these films. As a result, the Al-derived fraction of N_e, and with it the true ξ, is lower than calculated. The figure should therefore be read as an order of magnitude: activation is of order 10%, not of order 100%.

These figures can be turned back on the three factors proposed above for the Al-rich sample. The absolute cation fraction is available only for the optimised recipe, but $\xi \propto N_e/Al\%$ can be compared between recipes using the Al 2p/Zn $3p_{3/2}$ ratios of Figure 4.9 (b), for which the unknown sensitivity factor is common to all four, together with the Hall data of Figure 4.11, acquired on the four films within a single session under matched ambient exposure (Section 4.4.1). On this basis the Al-rich sample shows an apparent activation approximately four times that of the optimised sample. An enhancement of that size would place it well above the ceiling Illiberi et al. associate with supercycle ALD, and that ceiling is set by the discrete, planar delivery of Al rather than by the dosing conditions [259]. Since all four recipes here share the same 20:1 supercycle and the same precursor, the first factor, an unusually high substitutional fraction, is unlikely to be the principal origin of the carrier density of the Al-rich film. The excess is more plausibly carried by the native and hydrogen-related donors of the second and third factors, which these data cannot separate from one another. That assignment is consistent with this sample having the lowest mobility of the four despite the highest carrier density, since V_O^{2+} and Zn_i^{2+} are doubly charged and scatter more strongly per carrier than the singly charged Al_{Zn}^{+}.

Most of the incorporated Al is therefore electrically inactive, and the measurements of this chapter constrain where it sits. Of the three destinations set out in Section 2.4.1, an interstitial site is unlikely to be the principal one. The octahedral interstitial is the site cation interstitials occupy in wurtzite ZnO, but Al^{3+} there is itself a shallow donor. As a result, it would have to be compensated by zinc vacancies, for example, before it removed a carrier. Interstitial Al does not on its own account for Al that donates no electron. Segregation is the remaining route, and GIXRD constrains its form: the films are wurtzite and (002)-textured, with no clear secondary crystalline reflections after annealing (Section 4.3.1), so any $ZnAl_2O_4$ or Al_2O_3 present would have to be X-ray amorphous or too small to diffract coherently. The HRTEM images of Section 4.3.2 show nanocrystallites embedded in a predominantly amorphous matrix, which provides a host for such regions, and the EDS profile of Figure 4.7 (c) shows Al accumulating towards the film surface rather than distributing uniformly. The picture consistent with these observations is Al held in amorphous Al–O–Al environments, that is, the Al_2O_3-like rather than the $ZnAl_2O_4$-type of the two regions described in Section 2.4.1, rather than in a crystalline spinel. The supercycle delivers Al as discrete sub-monolayer AlO_X pulses, so the local concentration within a dopant plane is high enough to favour both clustering and Coulomb repulsion between adjacent charged donors, the two mechanisms Illiberi et al. invoke for the low activation of supercycle films [259].

This assignment is inferred rather than measured directly. Al 2p is separated by less than 1 eV between substitutional and Al_2O_3-like environments, and the Al 2p signal here is too weak to support a two-component fit (Section 4.3.3), so the XPS data of this chapter cannot distinguish them. Resolving the Al chemical state would require hard X-ray photoemission at higher sensitivity, Al K-edge XANES, or local structural probing by EXAFS. The ToF-SIMS $Al_2O_3^-/AlO^-$ ratio of Section 6.5.1 is invariant with annealing within experimental scatter, which indicates that the balance of Al–O environments is not substantially rearranged by the thermal treatment, but the measurement is dominated by the AlO_X cap and does not resolve the AZO layer alone.

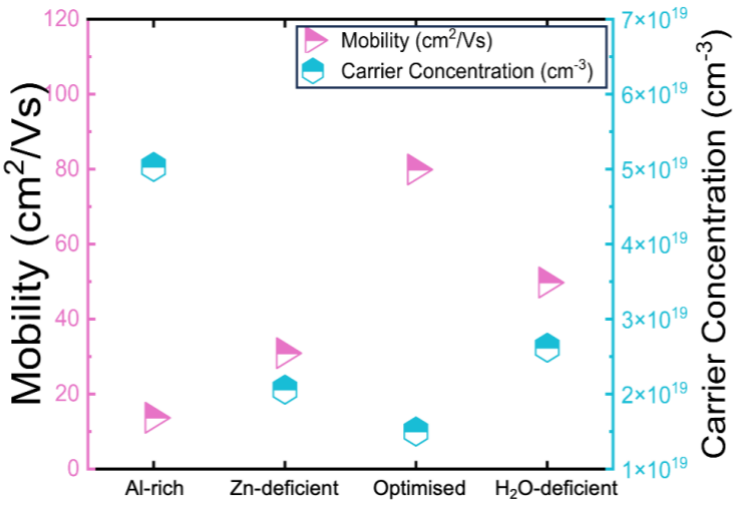


Figure 4.11 Mobility and carrier concentration of samples from the four different pressure profiles. The electron mobility is shown on the left axis with pink triangles, and carrier concentration is on the right axis with cyan hexagons.

The electrical measurements after the post-annealing process were also carried out for pre- vs post-annealing comparisons. Thermal annealing (450 °C, in air) generally leads to an increase in resistivity for bare AZO films due to a reduction in oxygen vacancies from the atmospheric oxygen diffusion, a trend consistent with both literature [260-262] and the findings in Section 5.7.2.

However, from the perspective of industrial device integration, annealing a bare AZO film has limited representative value as the layer will be protected by AlO_X during annealing within the device stack. To better reflect practical conditions, the electrical transport properties were evaluated for samples annealed with an AlO_X capping layer. For resistivity measurements, the capping layer was subsequently removed via chemical etching (Section 3.1.5). As illustrated in Figure 4.12, the capped-and-etched samples maintain a similar level of resistivity of ~ 6×10^{-3} Ω·cm, confirming that the AlO_X layer effectively preserves the conductivity of the underlying AZO, as also observed by Macco et al. [46].

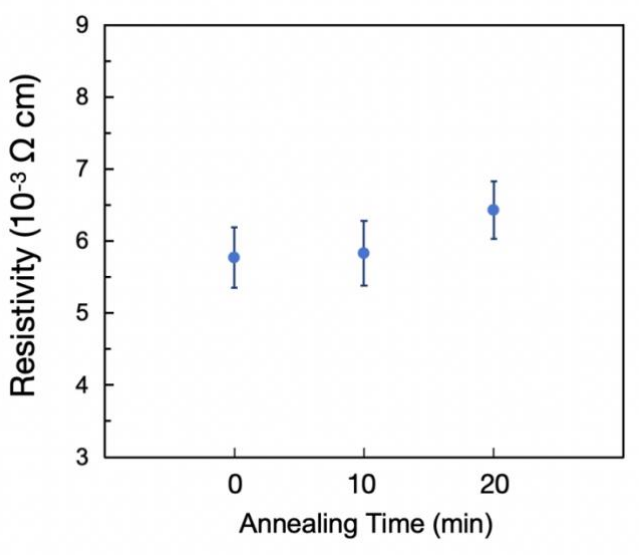


Figure 4.12 Resistivity as a function of annealing time for AZO/AlO_X sample processed under the optimised pressure profile. The AZO films were annealed with an AlO_X capping layer, which was subsequently removed prior to measurement. For consistency, the non-annealed sample (0 min) was also deposited with an AlO_X cap and etched prior to measurement.

4.4.3 Optical Transparency and Bandgap Narrowing

The optical transparency of the TCO is crucial for minimising current losses in solar cells. Figure 4.13 (a) presents the transmission spectra (200–1200 nm) for the AZO nanolayers measured using UV-vis, while Figure 4.13 (b) shows the enlarged spectra ranging from 400-600 nm wavelength.

For wavelengths in the tandem device-relevant range (> 600 nm for interlayers), from Figure 4.13 (a) and (b), all samples exhibit transparency over 98%. Notably, the optimised sample (orange curve) demonstrates the highest transmittance, while the H_2O-deficient sample (blue curve) shows reduced transmittance, particularly in the UV region (< 400 nm). The Al-rich sample exhibits the lowest transmittance across the spectrum. At longer wavelengths, this is consistent with enhanced free carrier absorption (FCA), which scales with carrier concentration [263, 264]. At shorter wavelengths, the reduced transmittance is attributed to a narrowing of the apparent optical gap, as confirmed by the Tauc analysis in Figure 4.14.

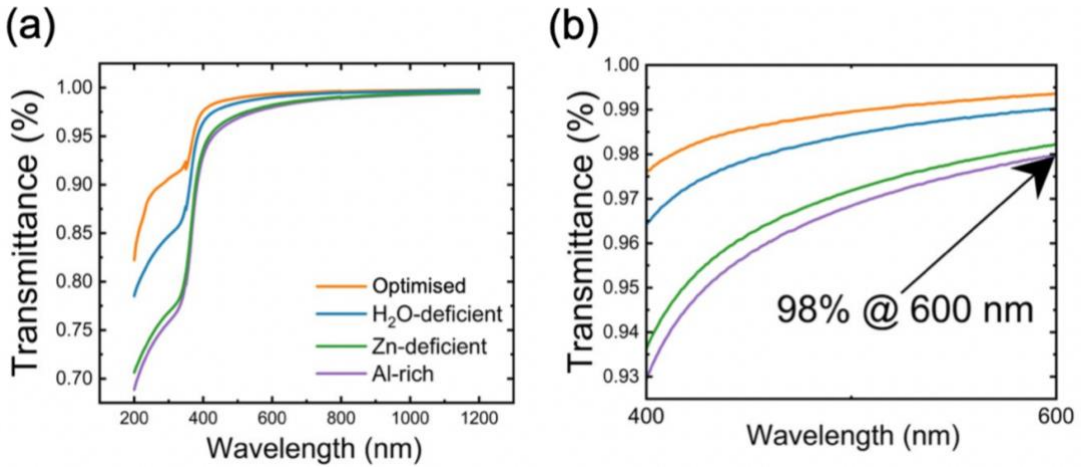


Figure 4.13 Transmittance curves of single-sided 40-nm-thick AZO samples on fused quartz (Section 3.1.1) from the four different pressure profiles in the wavelength range of (a) 200-1200 nm; (b) 400-600 nm.

Furthermore, Figure 4.14 shows the apparent optical gap extracted via Tauc plots. The values are obtained by fitting the linear region of the plot $(\alpha h\nu)^2$ versus photon energy and extrapolating to the intercept at $(\alpha h\nu)^2 = 0$. Most samples cluster around 3.25 eV, with only slight variations. This suggests that while the precursor ratio affects the material properties, the differences among these four samples are small.

Figure 4.14 shows no excitonic feature of the kind identified in the undoped ZnO films of Section 5.7.1. All four films here are degenerately doped, with carrier concentrations of 1.5-5.1 × 10^{19} cm^{-3} (Section 4.4.2), above the Mott density of ~3 × 10^{18} cm^{-3} for ZnO, so the exciton is screened. Its absence on a different substrate and at a different thickness supports the assignment made in Section 5.7.1. The values quoted here are apparent optical gaps in the sense defined in Section 3.4.1.

The optical gap of highly doped semiconductors is governed by two competing effects: the Burstein-Moss (BM) band-filling effect, which increases the apparent bandgap as excess electrons occupy states at the conduction band minimum, and many-body bandgap renormalisation (BGR), which narrows the bandgap through exchange-correlation interactions among free carriers and electron-impurity scattering [263, 264].

In the BM effect, the occupation of conduction band states raises the minimum photon energy required for absorption, producing a blue shift of the absorption edge [265, 266]. Conversely, BGR arises because the dense electron gas lowers the conduction band edge through exchange-

correlation self-energy corrections, while simultaneously screening the nuclear potential experienced by valence electrons, effectively raising the valence band edge [267, 268]. The net optical bandgap can be expressed as [269]:

$$E_{\text{opt}} = E_{g0} + \Delta E_{BM} - \Delta E_{BGR} \tag{4.1}$$

where E_{g0} is the intrinsic bandgap, ΔE_{BM} is the Burstein-Moss widening, and ΔE_{BGR} is the narrowing due to many-body effects. Quantitatively, the BM shift scales as [265]:

$$\Delta E_{BM} = \frac{\hbar^2}{2m_{vc}^*}(3\pi^2 n)^{2/3} \tag{4.2}$$

where $\hbar$ is the reduced Planck constant, n is the carrier concentration, and m_{vc}^* is the reduced effective mass for the optical transition, given by $\frac{1}{m_{vc}^*} = \frac{1}{m_e^*} + \frac{1}{m_h^*}$, where m_e^* and m_h^* are the effective masses of electrons and holes. The BGR contribution scales more weakly with carrier concentration [268]:

$$\Delta E_{BGR} = K \cdot n^{1/3} \tag{4.3}$$

where K stands for a material-specific constant incorporating the dielectric permittivity and exchange-correlation treatment.

The marginal variations in the extracted gap observed in Figure 4.14 suggest that for these AZO samples, the BM widening is largely offset by BGR narrowing. The narrowest optical gap measured for the Al-rich sample (< 3.25 eV) indicates that BGR dominates in this high-doping regime, despite the faster nominal scaling of the BM term ($\Delta E_{BM} \propto n^{2/3}$ vs $\Delta E_{BGR} \propto n^{1/3}$).

The extracted values carry the same uncertainty as those of Section 5.7.1, approximately ± 0.01 eV on an individual gap and ± 0.02 eV on a difference; the spread among the four recipes here is comparable to that figure, so the ordering is indicative rather than resolved. The interpretation below therefore rests on the direction of the trend and on its agreement with the independent Hall data of Figure 4.11, not on the individual values.

This experimental observation is corroborated by the Hall effect data in Figure 4.11. The Al-rich sample, which exhibits the highest carrier concentration (n ≈ 5×10^{19} cm^{-3}), paradoxically displays the

smallest optical gap. Two factors account for the dominance of BGR over BM in this regime. First, the non-parabolicity of the ZnO conduction band causes the effective mass m_{vc}^* to increase at high carrier densities, as electrons occupy states far from the band minimum where the band curvature is reduced [270]. This increasing effective mass diminishes the BM coefficient in Equation (4.2). Second, the Al-rich sample exhibits the lowest mobility (Figure 4.11), indicating substantial structural disorder that produces intense potential fluctuations and band tailing, effectively lowering the measured optical absorption edge below the value expected from the intrinsic bandgap alone. The combined effect of increasing m_{vc}^* and band tailing overcomes the widening provided by carrier filling.

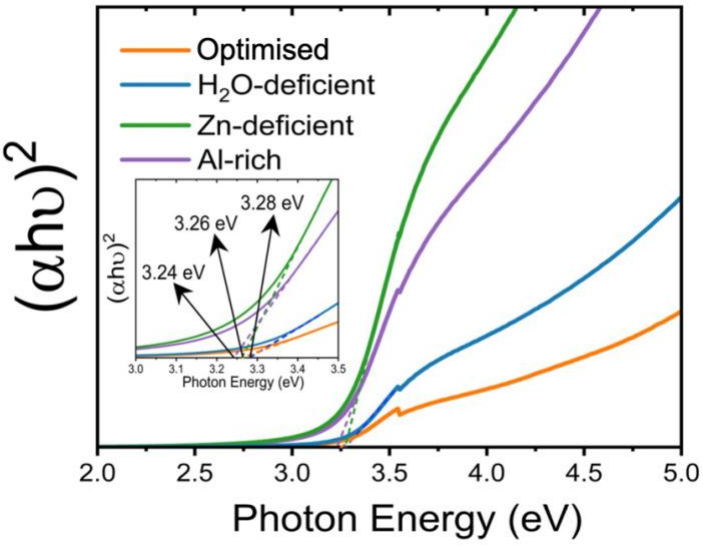


Figure 4.14 Tauc plots from the optical band diagram of samples from the four different pressure profiles.

4.4.4 Band Structure and Interface Alignment

Finally, the electronic band diagrams of AZO samples with various precursor dosing ratio profiles and the Si/AZO interface were constructed to investigate the field-effect passivation.

The band structure relative to the Fermi level is plotted in Figure 4.15.

In degenerately-doped materials, the Fermi level is located within or very close to the conduction band, such that the valence band binding energy satisfies $E_f - E_V \gtrsim E_g$. For all cases but the optimised case, the apparent optical gap and the valence band binding energy measured by XPS are closely aligned ($E_f - E_V \approx E_g$), implying the onset of degenerate doping. For the optimised sample, however, an apparent paradox emerges between its surface and bulk electronic properties. XPS measurements reveal that $E_{g,optical} < E_f - E_V$, positioning the deduced conduction band minimum (E_C)

noticeably below the Fermi level. While this large valence band binding energy would conventionally suggest a heavily degenerate n-type state with the highest doping concentration, this interpretation diverges from the bulk Hall effect measurements (Figure 4.11). The Hall data demonstrate that the optimised sample possesses the lowest carrier density, whereas the Al-rich sample displays the highest.

The discrepancy between the apparent heavy degeneracy derived from surface-sensitive XPS and the low bulk carrier densities obtained from Hall measurements can be attributed to two distinct factors: differences in the thermodynamic annealing state, and Fermi-level shifts caused by sputter damage-induced surface defects. Regarding the annealing state, the Hall measurements were conducted on as-deposited AZO films. At the low ALD thermal budget, most of the incorporated Al remains unactivated in segregated Al–O–Al environments, yielding a low bulk carrier concentration; Section 4.4.2 puts the as-deposited activation between 3% and 12% depending on film thickness, roughly doubling on annealing, which is consistent with the thermally activated state probed here by XPS.

Regarding sputtering, the magnitude of the high degeneracy observed in Figure 4.15 is most likely exaggerated by XPS measurement artefacts. The XPS spectra were acquired after a standard Ar^+ sputter cleaning process to remove carbon; the Si 2p core level measurements as a function of sputter time are plotted in Appendix B, Figure A 81. It is well-documented that ZnO-based materials are vulnerable to the preferential sputtering of oxygen during ion bombardment [271, 272]. This preferential sputtering generates a high density of surface oxygen vacancies, which act as donors and artificially pin the Fermi level deep within the conduction band at the extreme surface [273, 274]. Therefore, the apparent heavy degeneracy observed in the XPS data reflects a combination of the genuine thermal activation of the bulk film and the sputter-induced metallisation of its surface.

Nevertheless, since the operational passivating contacts inherently require thermal annealing to activate passivation, the thermally activated state evaluated by XPS is more representative of the final device physics. Based on these XPS data, we can infer an increased valence band offset at the Si/AZO interface for the optimised ALD recipe; theoretically, such an offset would induce a stronger field-effect, thereby enhancing surface passivation.

In addition, while the Fermi-level shift at the surface includes sputter-induced artefacts, the underlying process of thermal dopant activation is genuine. Therefore, it is reasonable to infer that in the completed devices, the thermal treatment elevates the bulk carrier concentration relative to the as-deposited state (as suggested in Section 5.7.2), thereby contributing a robust field-effect passivation component to the high lifetimes observed. It should also be noted that the optical gap used to position E_C is an apparent value in the sense defined in Section 3.4.1, influenced both by the many-body renormalisation effects discussed in Section 4.4.3 and by the assumptions underlying the Tauc construction. Consequently, the deduced position of E_C relative to E_f carries a systematic uncertainty arising from the use of an apparent rather than a fundamental gap.

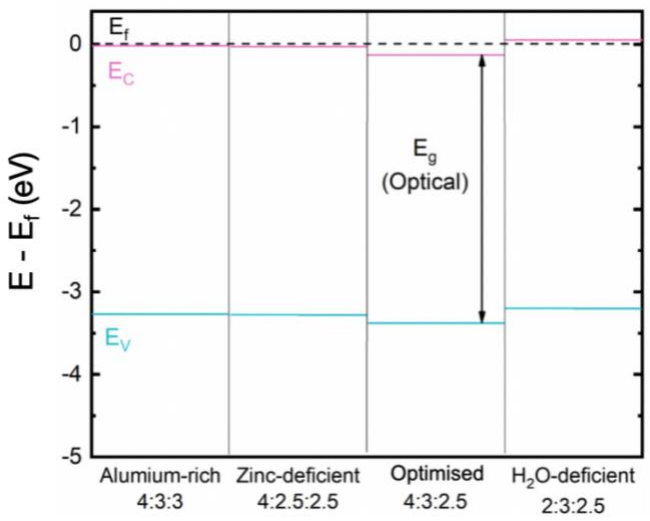


Figure 4.15 AZO Band diagram deduced from the combination of XPS and UV-vis. The bulk electronic band structure of the AZO films was deduced by combining the valence band maximum (VBM) measured from standard XPS surface scans with the apparent optical gap (E_g) obtained from UV-vis spectroscopy.

To further elucidate the mechanisms underlying the superior passivation observed in the optimised sample, a detailed analysis of the Si/AZO interface band alignment was performed. The interface was characterised by in-situ sputtering through the AZO layer at 4 kV for 15 min using an Ar^+ ion gun, such that a thin (~1 nm) layer of AZO remained on the Si surface, thin enough that photoelectrons from the Si 2p core level escape through the AZO layer to be measured.

While the previous sections established comparison across all precursor dosing profiles, this section focuses on the optimised interface to quantify the band bending responsible for the enhanced field-effect passivation. Figure 4.16 shows the valence band offset between the AZO layer and the Si substrate for the optimised sample, calculated by two independent routes. These offsets were

derived by combining the XPS-extracted valence band maximum (VBM) of the AZO with the theoretical VBM of the Si wafer, calculated based on its known resistivity of 4 Ω·cm and n-type doping (the Anderson method) [255]. This calculation places the Si VBM 0.86 eV below the Fermi level. Direct XPS measurement of the Si VBM was considered less reliable because surface defects can shift or pin the Fermi level [197, 275]. Consequently, these results imply a type II (staggered gap) alignment with a valence band offset of 2.52 eV. In contrast, applying the Kraut method (Section 3.5.2, Equation 3.13) [195], which utilises core level shifts at the interface to determine band bending, yielded a significantly larger offset of 3.25 eV, which is equivalent to the optical gap of AZO. This large discrepancy between the Anderson model (2.52 eV) and the Kraut method (3.25 eV) indicates that the Si/AZO interface is not an ideal vacuum-aligned heterojunction, pointing instead to the presence of high-density fixed charges or interfacial dipoles [231]. Crucially, the numerical equivalence (3.25 eV) between the Kraut-derived offset and the AZO optical gap is unlikely to be coincidental; rather, it suggests a thermodynamically driven band-pinning mechanism at the Type II/Type III boundary. If the intrinsic band alignment initially tends toward a true Type III (broken-gap) configuration, where the Si valence band maximum lies above the AZO conduction band minimum, spontaneous interband electron transfer from the Si valence band into the AZO conduction band will occur. This localised charge transfer generates the strong interfacial dipole, which electrostatically shifts the relative band positions until the Si valence band precisely aligns with the AZO conduction band ($E_{V,Si} = E_{C,AZO}$), halting further transfer. As a result, the Kraut-derived offset of 3.25 eV represents an equilibrium state where the valence band offset is constrained by the AZO optical gap.

A transition toward this Type III alignment implies that the Si valence band is positioned near or above the AZO conduction band. Physically, this creates a maximum energy barrier that suppresses minority carrier (hole) transport to the interface more effectively than a standard Type II alignment [276, 277].

Theoretically, contacting n-type AZO with n-type Si should induce downward band bending (accumulation) in the Si to facilitate electron transport. However, the large offset derived from the Kraut method indicates an upward band bending (depletion). Given the excellent surface passivation ($J_0 < 1$ fA/cm^2), which implies a very low density of interface defect states (D_{it}), this upward bending

is unlikely to arise from Fermi level pinning. In addition, the upward band bending is not an artefact from sputter damage in this study, as non-destructive synchrotron XPS measurements on ultra-thin (2–4 nm) AZO layers revealed the same upward bending (see Appendix B, Figure A 82). Surface photovoltage (SPV) characterisations studied in Chapter 6 also confirmed the upward band bending of Si.

Such band bending is more plausibly attributed to an abrupt potential step across the Si/SiO_2/AZO interfaces. This potential step is driven by two interlinked mechanisms. Macroscopically, it reflects the work function equilibration between the n-Si substrate and the highly doped AZO, where electrons transfer from the Si into the AZO to align the Fermi levels, leaving a depletion region in the Si. Microscopically, the upward band bending points to the formation of interfacial dipoles at the ultra-thin SiO_2/AZO interface. The asymmetry in electronegativity among Si, O, Zn, and Al atoms across the chemical bonds creates a localised dipole layer [278]. To account for the observed energy shift, the negative pole of these dipoles must point toward the Si substrate, effectively raising the Si band edges relative to the AZO.

This inherent upward bending creates an electrostatic barrier that repels electrons away from the interface. While such a large offset is theoretically conducive to enhanced field-effect passivation, it may simultaneously pose challenges for contact resistance. As pointed out by Gao et al., the integration of AZO as a carrier-selective contact led to significantly high contact resistivity if the layer thickness or interfacial barriers were not carefully managed [50]. For their SiO_2/AZO/Al configuration, the contact resistivity increased by nearly two orders of magnitude (from ~0.1 to ~10 Ω cm^2) as the AZO thickness scales from 5 nm to 27 nm. Even with the inclusion of a lithium fluoride (LiF) interlayer to lower the work function, the resistive loss remained highly sensitive to the AZO thickness. Contact resistivity measurements for the optimised stack were not performed in this study and remain a key direction for future work.

The combined electrical and optical analyses reveal clear correlations between precursor ratios and functional properties. Notably, the carrier concentrations measured across the four recipes are of the same order of magnitude (~10^{19} cm^{-3}). The principal differentiator is the electron mobility: the optimised sample achieves approximately 80 $cm^2/V{\cdot}s$, substantially higher than the other conditions

(the lowest being < 20 $cm^2/V \cdot s$ from the Al-rich sample). As discussed in Section 2.3.1, increasing mobility with a moderate reduction of carrier concentration is favourable for optical requirements. This elevated mobility is the dominant factor yielding the lowest resistivity and highest transmittance.

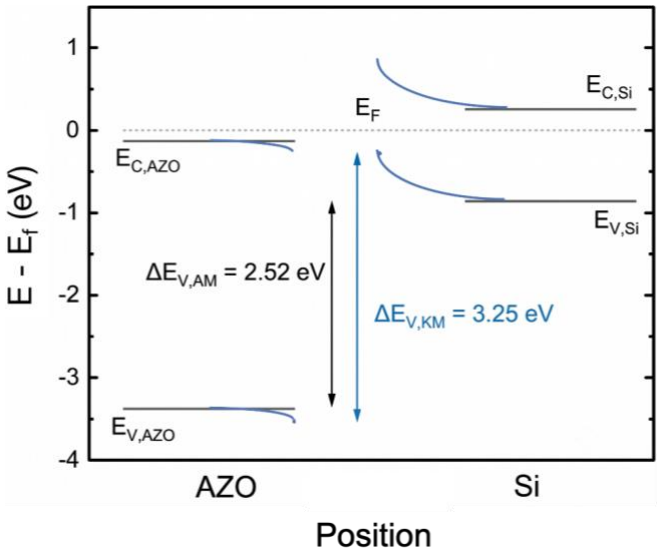


Figure 4.16 Valence band offset of optimised AZO sample and Si substrate, as determined from XPS measurements via the Anderson method ($\Delta E_{V,AM}$) from bulk valence band positions, and the Kraut method ($\Delta E_{V,KM}$) from valence band positions at the AZO/Si interface. Conduction band positions are inferred from the apparent optical gaps determined by transmission measurements (Section 3.4.1).

4.4.5 Thickness Optimisation

While precursor stoichiometry determines the intrinsic material quality (Section 4.2), the device performance is strongly influenced by TCO thickness. Increasing thickness reduces sheet resistance but enhances parasitic absorption, limiting the photon flux reaching the absorber and thus the short-circuit current. Therefore, an optimal thickness needs to be identified. The thickness-dependent resistivity of AZO films, investigated in Chapter 5 (Section 5.7.2), shows that increasing film thickness leads to reduced resistivity.

In the ultra-thin regime (< 20 nm), transport is dominated by surface and grain boundary scattering [256, 279, 280]. As the ALD growth proceeds, the film evolves from a nucleation-dominated morphology to a continuous, columnar grain structure [281, 282]. In thicker films, the grain size typically increases, reducing the density of grain boundaries per unit volume and allowing the bulk mobility properties to dominate [256, 283]. As a result, a minimum thickness threshold is required not only for physical continuity but to escape the high-resistivity regime associated with interface scattering.

To address the optical component of the trade-off, I employed Spectroscopic Ellipsometry (SE) to extract the complex refractive index (n), extinction coefficient (k), and physical thickness of samples deposited under the four distinct pressure profiles. The extracted parameters at a reference wavelength of 600 nm are summarised in Table 4.2.

The ellipsometric modelling reveals significant variations in the optical constants driven by stoichiometry [284, 285]. While Table 4.2 summarises the extracted parameters at a reference wavelength of 600 nm, the full wavelength-dependent n and k spectra are presented in Appendix C for completeness. The k value represents the loss of energy due to absorption, which can be expressed as [286]:

$$k = \frac{\alpha\lambda}{4\pi} \tag{4.4}$$

where α is the absorption coefficient, and λ is the wavelength of light in a vacuum. Here, the k values vary by an order of magnitude. The Zn-deficient sample exhibits the lowest k value (0.003), indicating high transparency. However, as noted in Section 4.4.1, this comes at the expense of very high resistivity, rendering it unsuitable as a TCO. The H_2O-deficient sample displays the highest k value (0.036). This elevated absorption is likely driven by sub-bandgap defect states (oxygen vacancies), confirming the stability vs. conductivity trade-off discussed earlier. The optimised sample presents a balanced profile (0.020) with a thickness of ~ 20 nm, providing a baseline for optical clarity while maintaining the high lifetime discussed in Section 4.2.

These k values correspond to absorption coefficients at 600 nm of 628, 2304, 4189 and 7540 cm^{-1} for the Zn-deficient, Al-rich, optimised and H_2O-deficient films, respectively, all below the 10^4 cm^{-1} criterion in Section 2.3.5 and comparable to the mean visible-range value of ~ 10^4 cm^{-1} reported for AZO of similar structural order [287]. Reported k values for AZO span a wide range, because absorption in the visible is governed primarily by oxygen-vacancy and grain-boundary defect states rather than by Al content [287]; the ordering observed here, in which the H_2O-deficient film is the most absorbing, is consistent with that assignment. The n values measured here (1.74–1.79) lie slightly below the 1.8–2.4 range quoted for ZnO [144] and below the ~1.90 reported for compact AZO [287], consistent with the reduced density of the present films: HRTEM shows nanocrystallites

in a predominantly amorphous matrix (Section 4.3.2) and XRR gives an AZO density of 5.2 g cm^{-3}, ~ 93% of the bulk wurtzite value (Section 5.5.1). A further contribution to the absolute uncertainty in k arises from the ellipsometric fit itself: for films of only ~20 nm, n, k and d are strongly correlated, and the mean squared errors in Table 4.2 (24–55) indicate a correspondingly limited constraint on the absolute value of k. The relative ordering across the four recipes, on which the comparison here rests, is unaffected, since all four films were measured and modelled identically.

Table 4.2 n, k, and thickness of samples from the four different pressure profiles measured from ellipsometry. Data was acquired at 600 nm wavelength. The complete spectroscopic dispersion data, including n(λ) and k(λ) across the full measured wavelength range (210 – 1690 nm) for all four pressure profiles, are provided in Appendix C (Figure A 85 and Figure A 86). The fitting curves and measured curves of the optimised sample are provided in Appendix C, Figure A 87.

Group	n	k	Thickness (nm)	Mean Squared Error (MSE)
Al-rich	1.79	0.011	23.85±0.25	32
Zn-deficient	1.74	0.003	19.38±0.25	24
Optimised	1.76	0.020	19.85±0.27	28
H_2O-deficient	1.77	0.036	22.76±0.58	55

4.5 Discussion and Summary

4.5.1 Discussion

The central finding of this chapter is that precise control of precursor partial pressures during ALD enables AZO-based passivating contacts to achieve surface passivation (iV_{OC} > 740 mV, J_0 = 0.87 fA/cm^2). At the time of publication, this represented the lowest recombination current density reported for any metal-oxide/silicon interface without an intermediate amorphous silicon layer [44-47, 50]. This result demonstrates that earth-abundant, indium-free metal oxides can provide interface quality previously considered exclusive to hydrogenated amorphous silicon interlayers, removing a layer whose parasitic absorption reduces the current available to the silicon sub-cell in a tandem device.

The approach developed in this work, using the H_2O:DEZ:TMA partial pressure ratio as the primary control parameter, departs from the conventional practice of varying cycle count or substrate temperature to tune AZO properties. The identification of an optimised ratio of 4:3:2.5, established by a systematic review of approximately 130 deposition runs, represents an empirical stoichiometric

window within which the competing requirements of passivation, conductivity, and transparency are simultaneously satisfied. The key physical insight is that the optimised condition yields the highest electron mobility (~80 $cm^2/V \cdot s$) among the four recipes, and it is this structural order, manifested as minimal grain boundary scattering and low ionised impurity scattering, that determines the superior passivation, transparency, and conductivity of the optimised films.

The structural and compositional analyses provide mechanistic support for this conclusion. GIXRD shows that the films are crystalline and strongly (002)-textured, with no secondary crystalline phases detected after annealing, while the XRR results of Section 5.5.2 show the densification of the stack. HRTEM reveals a semi-crystalline microstructure with sharp interfaces. The XPS data demonstrate a non-linear relationship between precursor dosing and film composition, which is attributed to competitive adsorption, ligand exchange, and steric effects during the modified ALD supercycle. Importantly, the sample with the highest incorporated Al/Zn ratio (Zn-deficient) did not yield the best passivation, indicating that passivation quality is not a monotonic function of dopant content but instead depends on a balance between substitutional doping, structural order, and defect density. Quantitatively, the doping efficiency of these films is of order 10%, so composition alone is a poor proxy for the active dopant density.

The band alignment analysis revealed a large valence band offset (2.52–3.25 eV) at the Si/AZO interface, with the discrepancy between the Anderson and Kraut methods indicating the presence of interfacial dipoles or fixed charges at the SiO_x/AZO boundary. A notable finding of this work is the observation of upward band bending in the Si substrate, which contrasts with all prior reports on SiO_x/AZO/AlO_x passivating contacts [44-47, 50]. These studies have consistently predicted downward band bending (accumulation) at the c-Si interface; however, this prediction has been derived from theoretical modelling, typically numerical simulations or idealised Fermi-level alignment based on bulk film properties extracted via UPS and UV-vis, rather than from direct measurement of the buried interface. The present work instead probes the Si/AZO interface directly using surface-sensitive XPS through in-situ sputtering, and the results indicate upward band bending (depletion) in the Si substrate. This finding is corroborated by non-destructive synchrotron XPS on ultra-thin (2–4 nm) AZO layers (Appendix B, Figure A 82), which excludes sputter-induced artefacts as the origin,

and by surface photovoltage characterisation (Chapter 6), which confirms the same polarity of band bending under illumination.

An important distinction between the present work and the existing literature is the annealing ambient: all samples in this study (except for one set annealed in forming gas annealing (FGA) as a reference in Section 5.2.1) were annealed in air, whereas previous studies employed FGA. Air annealing could promote the reduction of oxygen vacancies through atmospheric oxygen diffusion, which may strengthen fixed negative charges at the SiO_X/AZO interface or modify the interfacial dipole configuration, both of which could contribute to the observed upward bending. Whether downward bending would be recovered under FGA conditions remains an open question; the direct interfacial characterisation methods developed in this work provide a framework for resolving this question in future studies.

The upward band bending data also highlight an inherent tension between passivation and contact resistance in this architecture. As discussed in Section 4.4.4, the contact resistivity of SiO_2/AZO stacks increases sharply with AZO thickness [50], and the 16–20 nm range employed here for optimal passivation may present a resistive barrier in a completed device. This trade-off between passivation and transport sets a practical constraint on the integration of AZO as an electron-selective contact and motivates the thickness-dependent study in Chapter 5.

The near-cancellation of the Burstein-Moss and bandgap renormalisation effects across all four recipes, yielding optical gaps clustered around 3.25 eV despite varying carrier concentrations, indicates that visible-range transparency is retained even under non-optimised doping conditions, a favourable property for TCO applications in tandem architectures.

Several limitations of the present study should be acknowledged. The doping efficiency of Section 4.4.2 inherits the systematic uncertainty of EDS quantification in a thin film and the assumption that all carriers above the undoped-ZnO level originate from Al; it is therefore an order-of-magnitude estimate rather than a measured quantity. The doping efficiency calculation is restricted to the optimised recipe, since the EDS composition of Figure 4.7 (c) and the fresh Hall data of Section 5.7.2 are both available only for that recipe. The XPS Al 2p/Zn 3p ratios of Section 4.3.3 rank the

four recipes but carry no relative sensitivity factors, so they cannot be converted into absolute cation fractions for the other three, although they support the relative comparison made in Section 4.4.2. The XPS-derived band positions carry systematic uncertainty from Ar^+ sputter damage, which preferentially removes oxygen and artificially shifts the Fermi level into the conduction band; while this artefact was identified and discussed in Section 4.4.4, it prevents quantitative extraction of the true Fermi-level position from the present data. Furthermore, the Hall effect measurements of this chapter were performed on as-deposited films rather than annealed ones, precluding a direct comparison with the thermally activated state probed by XPS. Annealed Hall data for the same recipe are reported in Section 5.7.2 and are used for the doping-efficiency estimate above. The passivation performance itself is characterised on symmetric lifetime structures that do not capture metallisation, contact resistance, or current transport, which are critical for device-level assessment. Finally, the metastable passivation response observed in the annealing study (Section 4.2.3), where iV_{OC} peaks and then degrades under prolonged thermal load, requires further mechanistic investigation and is addressed in Chapter 5.

Despite these limitations, the results establish that a simple TMA-based ALD process using only earth-abundant materials and a chemical SiO_2 interlayer can achieve $J_0 < 1$ fA/cm^2 on n-type silicon. The low deposition temperature (150 °C) and conformal ALD growth are inherently compatible with thermally sensitive perovskite top cells, and the passivation quality achieved here suggests that AZO-based contacts can fulfil the dual role of passivation and lateral transport in tandem architectures, provided thickness-dependent contact resistance is carefully managed.

4.5.2 Summary

This chapter has demonstrated that ALD-grown AZO films with an optimised H_2O:DEZ:TMA partial pressure ratio of 4:3:2.5 achieve record-low recombination losses ($iV_{OC} > 740$ mV, $J_0 = 0.87$ fA/cm^2) for a direct metal-oxide/silicon passivating contact without an amorphous silicon interlayer. The superior passivation is attributed to the high structural order and electron mobility (~ 80 cm^2/V·s) of the optimised film, rather than to maximised dopant incorporation. Consistent with this, the doping efficiency of these films is of order 10%, so most of the incorporated Al is electrically inactive. Direct

interfacial characterisation via XPS reveals upward band bending in the Si substrate and a large valence band offset exceeding 2.5 eV, the first such observation reported for AZO passivating contacts, supporting a field-effect passivation mechanism that diverges from the downward bending assumed in the existing literature. The annealing study reveals a metastable passivation response that motivates the investigation of hydrogen dynamics and structural evolution in Chapter 5.

Chapter 5. Post-Deposition Thermal Processing and Cooling Dynamics

5.1 Introduction

This chapter investigates the post-deposition thermal processing conditions for SiO_2/AZO/AlO_X passivating contacts, with focus on the cooling phase after annealing. Section 5.2 establishes a thermal processing protocol by optimising the annealing ambient, peak temperature, and dwell duration. Sections 5.3 and 5.4 demonstrate that the cooling rate is an independent determinant of passivation quality in the AZO/AlO_X system. Section 5.5 uses X-ray reflectivity (XRR) to probe the structural response of the AZO/AlO_X stack to thermal treatment and to assess whether the cooling-rate contrast can be attributed to differences in layer density, thickness, or roughness. Section 5.6 employs neutron reflectometry (NR) to resolve the depth-dependent hydrogen distribution within the stack and its evolution with annealing temperature and cooling rate. Section 5.7 evaluates the optoelectronic properties under the optimised conditions, and Section 5.8 synthesises the structural and hydrogen data into a mechanistic hypothesis for the observed cooling-rate dependence.

Chapter 4 achieved effective lifetime values above 3 ms at 1×10^{15} cm^{-3} excess carrier density (ECD) using a two-step hybrid anneal (500 °C furnace followed by 450 °C hotplate). This chapter has a different aim: rather than maximising lifetime, I focus on investigating the impacts of thermal dynamics on passivation. I therefore replaced the hybrid process with a single-step hotplate anneal at 450 °C, which gives clean and direct control over the cooling ramp. Sections 5.2.1–5.2.3 establish this baseline process and confirm that it still yields effective lifetime values of > 1 ms at 1×10^{15} cm^{-3} ECD, below the Chapter 4 peak, but sufficient for the mechanistic studies that follow.

5.2 Establishing a Thermal Processing Protocol

Before presenting the ambient, temperature, and dwell-time sweeps, the baseline thermal profile used in Sections 5.2.1–5.2.3 is defined explicitly. I annealed every sample in these three subsections at a set temperature, removed it after a 10-minute (Sections 5.2.2-5.2.3) or 30-minute (Section 5.2.1) natural cool-down from the peak temperature, and then transferred it to lifetime measurement. In ambient air, this 10-minute cool-down corresponds to the cooling rate (CR 2) in Section 5.4 (~ 25 °C/min, averaged from 450 °C to 200 °C). Variations in peak temperature and dwell time were performed while holding this cooling profile constant. The independent effect of cooling rate is isolated in Section 5.4 while keeping other parameters at their values established in Sections 5.2.1–5.2.3.

5.2.1 Impact of Annealing Ambient

The ambient gas during annealing determines the chemical potential of oxygen and hydrogen at the film surface, making it a critical variable for metal oxide passivation stacks. To identify the optimal atmosphere, I annealed identical Si/SiO_2/AZO/AlO_X samples (synthesised using the optimised recipe from Chapter 4) in three distinct environments: ambient air, inert nitrogen (N_2), and forming gas (N_2:H_2, 95:5), all followed by a slow cool-down for 30 minutes before being taken off the hotplate/furnace. While cooling rates vary between the hotplate and furnace, both setups ensure a sufficiently long cooling duration to remain within the slow-cooling criteria defined in Section 5.3.

Figure 5.1 (a) shows that the air-annealed sample achieves higher passivation than the N_2-annealed sample, with peak effective lifetimes of approximately 1 ms at 1×10^{15} cm^{-3} ECD. Figure 5.1 (b) compares the passivation of samples annealed in air and forming gas at 450 °C via photoluminescence (PL) imaging. The four pieces in the PL image originated from the same wafer and were processed under identical deposition conditions. The forming-gas annealed samples exhibit darker areas, indicating inferior passivation. While forming gas is traditionally used to passivate Si/SiO_2 interfaces via hydrogen injection [288-290], two possible pathways explain why annealing in air yields better passivation than in N_2 and forming gas. One explanation is that atmospheric oxygen fills oxygen vacancies (V_O) in the AZO film during annealing, reducing the V_O^{2+}

density and thereby shifting the net fixed charge in the AZO toward more negative values [142, 291]. This shift strengthens the upward band bending at the Si surface and enhances field-effect passivation, an interpretation further developed and tested by KP-SPV in Section 6.2.3. A parallel chemical-passivation contribution from reduced oxygen-vacancy-related defect states density in the AZO/AlO_X network is also plausible but not independently tested here.

Managing hydrogen content is central to silicon solar-cell passivation and long-term stability [292]. For SiN_x:H-based passivation stacks, forming gas annealing (FGA) provides an external hydrogen source that supplements the intrinsic hydrogen reservoir [293]. In the present AZO/AlO_X system, however, the hydrogen supply is expected to originate primarily from ALD precursor residues incorporated within both the AZO film and the AlO_X cap during deposition. The air-annealing result therefore implies that the intrinsic hydrogen content of the as-deposited stack is sufficient for effective passivation, provided that thermal processing facilitates its redistribution to the Si/SiO_x interface. NR measurements test this interpretation in Section 5.6.

Based on these findings, ambient air was selected as the standard atmosphere for all subsequent thermal processing studies.

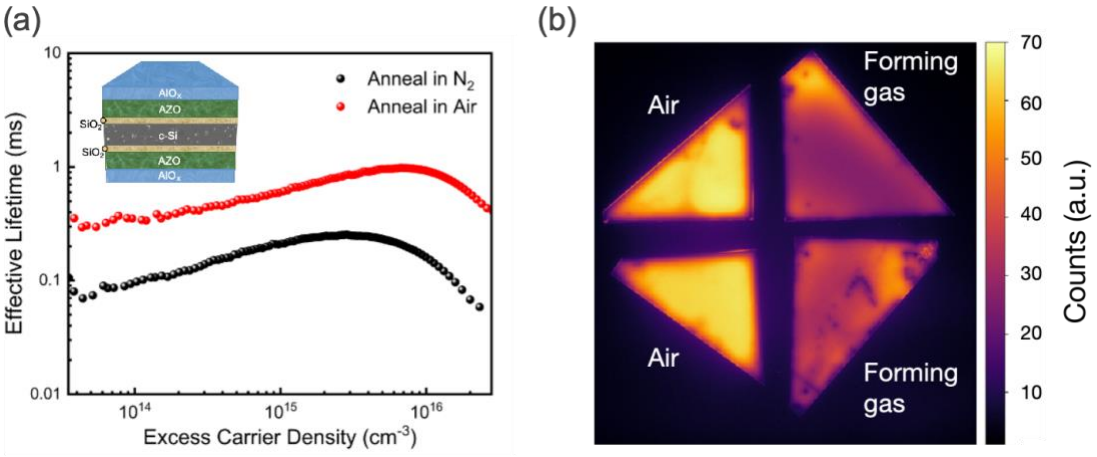


Figure 5.1 (a) Lifetime curves of AZO samples annealed in air and N_2 at 450 °C. (b) PL image of AZO samples annealed in air (left two pieces) and forming gas (right two pieces) at 450 °C.

5.2.2 Peak Temperature

I conducted a thermal sweep from 300 °C to 600 °C on the SiO_2/AZO/AlO_X stack. Table 5.1 shows that the optimum passivation is achieved at 450 °C. The dwell time (defined here as the duration for which the sample is held at the setpoint, measured from the moment the sample reaches the peak

temperature to the moment active cooling begins) is adjusted with peak temperature rather than fixed across the sweep. To account for the strong temperature dependence of activation kinetics, dwell times were individually optimised to capture the maximum passivation potential of each thermal regime. The temporal evolution justifying these selections is provided in Appendix D, Table A 14.

At 300 °C, the effective lifetime remained below 300 µs at 1×10^{15} cm^{-3} ECD even after 30 minutes of annealing. This thermal energy is insufficient to overcome the activation barrier for hydrogen diffusion to the silicon interface, likely from the AlO_X capping layer. Hydrogen diffusion in amorphous oxides is thermally activated, with an onset of appreciable migration in ALD Al_2O_3 around 350–400 °C in the absence of an external hydrogen source [168, 294].

At 600 °C, the effective lifetime dropped below 700 µs at 1×10^{15} cm^{-3} ECD. This degradation is consistent with two established high-temperature loss mechanisms: accelerated hydrogen effusion from the stack, which depletes the hydrogen reservoir before interface passivation is complete; and structural disordering of the interfacial SiO_x layer [46, 47]. The NR data presented in Section 5.6 indicate that 600 °C annealing depletes the AlO_X hydrogen content.

The optimum occurred at 450 °C, which yielded effective lifetimes exceeding 1300 µs at 1×10^{15} cm^{-3} ECD. This temperature likely provides sufficient energy for interfacial defect saturation while remaining below the onset of thermally induced degradation. Accordingly, 450 °C was selected as the fixed peak temperature for all subsequent experiments.

Table 5.1 Summary of passivation metrics across different annealing temperature regimes. Dwell times were adjusted to ensure fair comparison of activation potential. All samples were followed by a 10-min slow cooling after the annealing dwell.

Sample	Temperature (°C)	Dwell Time (min)	Lifetime (µs @ 1×10^{15} cm^{-3} ECD)
Low Temp	300	30	274.1
Mid Temp	350	30	854.6
Optimal	450	20	1311.8
High Temp	600	5	690.8

5.2.3 Selection of Dwell Duration

The annealing dwell time is another control variable. To determine the optimal processing window, I measured the effective lifetime for samples from the same batch annealed for durations ranging from 5 to 40 minutes, all followed by a 10-minute slow cooling. Figure 5.2 shows that the effective lifetime increases monotonically up to 30 minutes before declining.

At 5 minutes, the lifetime is 222 μs at 1×10^{15} cm^{-3} ECD, indicating initial hydrogen activation. With increasing dwell time, the lifetime rises to 941 μs at 15 minutes and 1312 μs at 20 minutes. Beyond 20 minutes, the rate of improvement diminishes: the 25-minute and 30-minute setpoints yield 1389 μs and 1409 μs, respectively. The absolute peak at 30 minutes represents only a ~7% gain over the 20-minute value despite a 50% increase in dwell time. At 35 minutes, the lifetime begins to decline (1321 μs), falling further to 1155 μs at 40 minutes, indicating the onset of degradation.

A 20-minute dwell was selected as the standard protocol. The 30-minute setpoint sits at the boundary of the degradation regime, leaving no safety margin for process fluctuations. In contrast, 20 minutes achieves > 1.3 ms lifetime at 1×10^{15} cm^{-3} ECD and sits within a broad plateau region where the lifetime is insensitive to small variations in dwell time, ensuring process reproducibility. Moreover, this 20-minute baseline supports the cooling-rate investigation in Sections 5.3 and 5.4, where a 20-min anneal with slow cooling is compared against a 30-min anneal with fast cooling, ensuring the fast-cooled sample receives at least as much thermal exposure as the slow-cooled one.

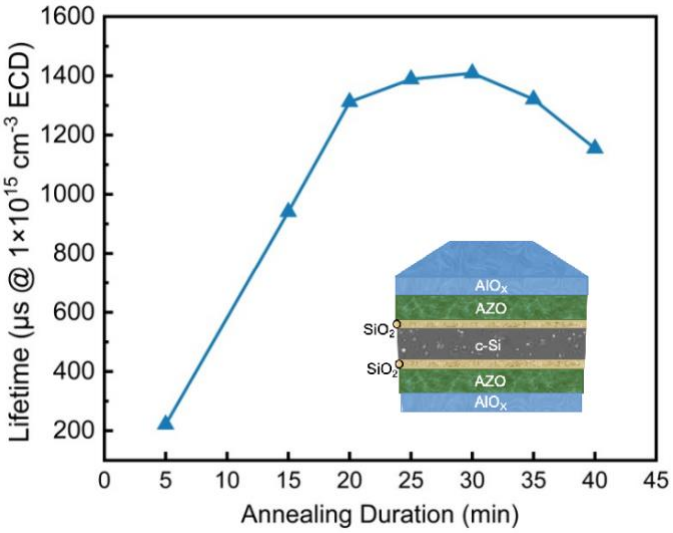


Figure 5.2 Effective lifetime values measured as a function of annealing duration at 450 °C in air. All samples were followed by a 10-min slow cooling after the annealing dwell.

5.3 Cooling Rate as a Determinant of Passivation Quality

Having fixed the thermal parameters for the highest temperature stage (air, 450 °C, 20 min), this section examines the cooling phase, a variable that has been overlooked in thermal processing studies of AZO passivation. I hypothesised that the cooling rate actively determines the final interface state rather than acting as a passive thermal relaxation. To isolate this effect, I designed a thermal matrix that decouples the total thermal budget from the rate of temperature change.

The role of cooling dynamics in determining hydrogen distribution has been established in other silicon photovoltaic systems, although not previously for AZO-based contacts [292, 295, 296]. In the context of light- and elevated-temperature-induced degradation (LeTID) in PERC solar cells, Eberle et al. demonstrated that the cooling ramp after high-temperature firing governs the final hydrogen content in the silicon bulk [297, 298]. Their work showed that slower cooling rates allow neutral hydrogen (H^0) to out-diffuse from the crystalline silicon bulk during the extended cool-down, reducing the total hydrogen concentration and mitigating LeTID. Hammann et al. subsequently confirmed this mechanism through TCAD simulations, demonstrating that hydrogen diffusion during the cooling phase is dominated by fast-diffusing H^0 and that the extent of out-diffusion scales with the residence time at elevated temperatures [292]. The present chapter investigates an analogous but distinct (in mechanism) effect: in the AZO/AlO_X system, the cooling rate is hypothesised to govern not the out-diffusion of hydrogen from the bulk, but the in-diffusion of hydrogen from the AlO_X reservoir towards the Si/SiO_x interface.

5.3.1 Decoupling Thermal Budget and Cooling Rate

During initial process development, I observed a reproducible discrepancy: samples cooled slowly on the hotplate consistently outperformed samples removed immediately after annealing. Control experiments showed that fast-cooled samples underperformed even when held at peak temperature for longer than the slow-cooled samples. This result indicated that the cooling rate itself, rather than the integrated thermal exposure, governs the final passivation quality.

Figure 5.3 shows the six thermal profiles designed to test this hypothesis. A 300 °C anneal serves as a control to confirm the activation barrier observed in Section 5.2.2. The standard slow-cooled profile (450 °C, 20 min) is the baseline from Section 5.2.3, characterised by a 10-minute natural cooling ramp on the hotplate (~ 25 °C/min). The fast-cooled profile (> 100 °C/min) with extended dwell (450 °C, 30 min) is designed so that the fast-cooled sample receives a larger integrated thermal budget than the slow-cooled sample, eliminating insufficient thermal energy as a confounding variable. Fast cooling was achieved by quenching: at the end of the dwell, samples were removed from the hotplate with tweezers and placed directly onto a room-temperature metal plate, which served as a heat sink and cooled the samples below 100 °C within approximately 2 s (> 100 °C/min).

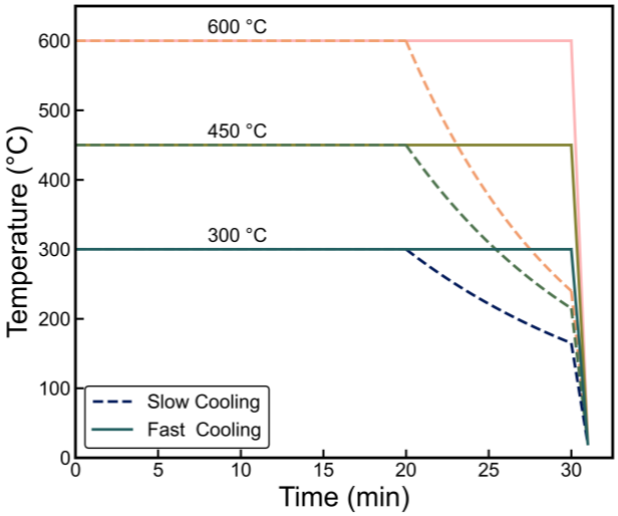


Figure 5.3 Schematic of six temperature profiles representing distinct thermal histories during post-deposition annealing.

5.3.2 Impact of Cooling Dynamics on Passivation

Figure 5.4 presents the effective minority carrier lifetime corresponding to the thermal profiles in Figure 5.3. To ensure statistical robustness, each data point represents the mean and standard deviation of four identically processed samples. The effective lifetime values of all samples are reported in Appendix D, Table A 15. The 450 °C slow-cooled samples exhibit a mean effective lifetime of ~ 1343 µs at 1×10^{15} cm^{-3} ECD, within ~ 2.4% of the ~ 1312 µs at 1×10^{15} cm^{-3} ECD reported in Section 5.2.2. This agreement confirms batch-to-batch reproducibility and sets the experimental uncertainty at ± 7.0% (~ 100 µs at 1×10^{15} cm^{-3} ECD).

At 300 °C, limited passivation activation is observed, with both slow-cooled and fast-cooled samples yielding similar mean lifetimes (~ 204 µs at 1×10^{15} cm^{-3} ECD) and overlapping error bars. This is possibly due to insufficient thermal energy at 300 °C to overcome the activation barrier for appreciable hydrogen migration; the cooling rate exerts negligible influence on passivation. At 600 °C, thermal degradation occurs, and the slow-cooled samples retain a marginally higher lifetime (~ 50 µs vs. ~ 19 µs at 1×10^{15} cm^{-3} ECD), which is of low statistical significance.

At 450 °C, the slow-cooled sample (20-minute dwell) achieves a mean lifetime of ~ 1343 µs at 1×10^{15} cm^{-3} ECD, whereas the fast-cooled sample yields only ~ 938 µs at 1×10^{15} cm^{-3} ECD, despite undergoing an extended 30-minute dwell. From the duration study in Section 5.2.3, a 30-minute dwell with slow cooling was shown to be capable of achieving peak lifetime (~ 1409 µs at 1×10^{15} cm^{-3} ECD). Samples with a larger integrated thermal budget (30 min, fast cool) perform worse than those with a smaller thermal budget (20 min, slow cool) by a margin of ~ 400 µs at 1×10^{15} cm^{-3} ECD. This difference, being roughly four times the batch-to-batch noise floor, indicates that the cooling rate, rather than the total thermal exposure, is the dominant control on the final passivation quality.

This finding draws a direct parallel with the cooling-rate studies on LeTID by Eberle et al. [297, 298], who showed that the cooling ramp of the fast-firing process governs the final hydrogen content and distribution in silicon. Eberle et al. proposed two candidate explanations for the cooling-rate dependence in multicrystalline silicon: internal gettering of metallic impurities during slow cool-down, and enhanced hydrogen out-diffusion [297, 298]. The internal gettering mechanism is not applicable to the present system, as the AZO/AlO_X stacks are deposited on high-purity Cz-Si wafers that are not processed through metal paste firing, and no metallic impurity sources comparable to screen-printed contacts are present [299, 300]. The hydrogen-redistribution mechanism is therefore the relevant point of comparison. In their system, slower cooling allows more time for hydrogen to out-diffuse from the bulk, reducing degradation. As hypothesised in the previous section, the cooling rate acts primarily to drive hydrogen in-diffusion from the cap rather than out-diffusion from the bulk. The analogy with the SiN_X:H/PERC system is phenomenological rather than mechanistic: in both cases, the cooling ramp (rather than the peak thermal budget) determines the final hydrogen distribution. However, the underlying physics differ substantially. In the Hammann model, a temperature-

dependent segregation coefficient governs the switching between hydrogen in-diffusion and out-diffusion across a single SiO_X/Si interface, with the SiN_X acting as a near-infinite source and sink [292]. In the AZO/AlO_X system, hydrogen traverses multiple oxide layers (AlO_X → AZO → SiO_X → Si), each presenting distinct diffusion barriers, and no evidence for a segregation-coefficient reversal exists. The Hammann model therefore cannot be directly transferred to this system. Nevertheless, the shared observation that the cooling phase exerts independent control over passivation quality motivates the hypothesis that a diffusion-limited process during cool-down is the operative mechanism in both systems.

Three mechanisms are considered for the cooling-rate dependence. First, rapid cooling can freeze the hydrogen profile in a non-equilibrium state characteristic of the elevated temperature. Slow cooling, by contrast, provides a temporal window during which hydrogen released from the AlO_X reservoir and the AZO film can migrate under quasi-equilibrium conditions and occupy deep traps at the Si/SiO_X interface. NR measurements test this hypothesis in Section 5.6. Second, slow cooling extends the window during which ambient oxygen can back-fill V_O^{2+}, shifting the net fixed charge in the AZO toward more negative values and strengthening the upward band bending that enhances field-effect passivation. This hypothesis is probed in Chapter 6 through KP-SPV and XPS band-alignment measurements. The third mechanism is thermomechanical stress. The abrupt removal of the sample from the hotplate imposes a sharp thermal gradient across the stack. The mismatch in coefficients of thermal expansion (CTE) between the polycrystalline AZO (~3–6×10^{-6} K^{-1}), amorphous SiO_2 (< 1×10^{-6} K^{-1}), and n-type Cz silicon (~2.6×10^{-6} K^{-1}) generates biaxial tensile stress in the AZO and biaxial compressive stress in the thin interfacial SiO_2 upon cooling, which may damage the Si/SiO_2 transition region [301-304]. Whether this stress is sufficient to introduce recombination centres that offset the benefit of the extended dwell is not tested in this thesis: XRR (Section 5.5) rules out macroscopic density change but does not access atomic-scale interfacial bond reconfiguration. Direct validation would require Raman spectroscopy to quantify the residual biaxial stress in the Si surface layer, or cross-sectional HR-TEM of the Si/SiO_X interface to image any cooling-rate-dependent interfacial damage, which is flagged as follow-up work [305, 306].

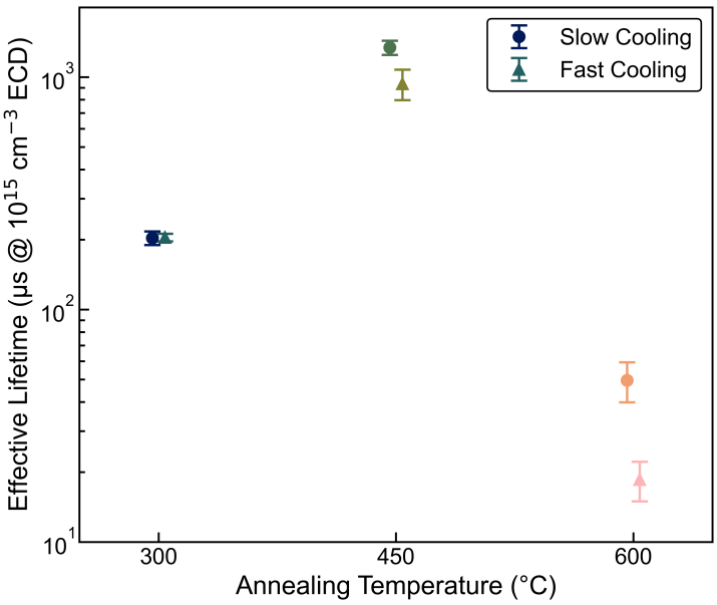


Figure 5.4 Effective minority carrier lifetime of SiO_2/AZO/AlO_X passivation stacks annealed under varying thermal conditions. The data compares three peak temperature regimes (300 °C, 450 °C, 600 °C) and two cooling dynamics (fast cooling vs. slow cooling).

5.4 Quantifying the Cooling-Rate Dependence

For statistical robustness, each thermal condition across the cooling rate (Section 5.4.1) and ramp halt (Section 5.4.3) experiments was replicated on four separately processed samples, with their effective lifetime values presented in Appendix D, Table A 16 and Table A 17. The pulse annealing experiment (Section 5.4.2) was carried out on three representative samples from the same batch to track the high-resolution temporal evolution. Because the ~ 1100 µs difference at 1×10^{15} cm^{-3} ECD between the 5-minute and 15-minute pulse protocols in Section 5.4.2 is more than ten times the intrinsic process variance (± 7%, ~ 100 µs on a 1400 µs signal at 1×10^{15} cm^{-3} ECD), the physical conclusions from these trajectories are robust against run-to-run noise.

5.4.1 Monotonic Relationship Between Cooling Rate and Passivation

To quantify the relationship between cooling rate and passivation quality, I annealed 16 samples at 450 °C and subsequently cooled them at four distinct rates.

Figure 5.5 (a) shows the schematic of the thermal profiles. The cooling rates range from CR1 (controlled ramp-down, slowest) through CR2 (natural convective cooling, the standard baseline) and CR3 (forced-air convective cooling) to CR4 (isothermal quenching, fastest). To keep all samples

at a similar level of thermal exposure, all samples in CR1, CR2, and CR3 underwent identical 20-minute annealing at 450 °C and were subsequently cooled for 10 minutes, while samples in CR4 underwent a 30-minute annealing at 450 °C, and I removed them immediately from the hotplate on a metal piece.

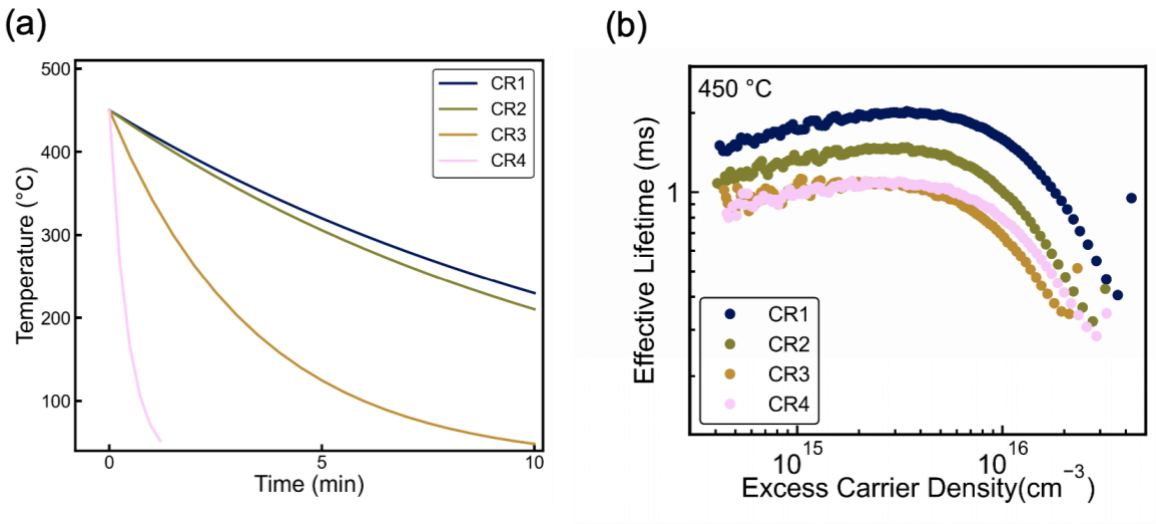


Figure 5.5 (a) Schematic of the temperature profiles for 4 different cooling rates (CR1-CR4) during post-annealing cooling from 450 °C. (b) Effective lifetime curves as a function of excess carrier density for 4 different cooling rates. The curves shown represent the closest-to-mean representative sample for each cooling condition.

Figure 5.5 (b) shows the corresponding effective lifetime measurements. The CR1 condition yields the highest passivation, with a group-mean lifetime of ~ 1683 µs at 1×10^{15} cm^{-3} ECD. Lifetime declines monotonically as the cooling rate increases, with CR4 being the lowest. This trend is consistent with slow cooling extending the residence time at intermediate temperatures, where hydrogen migration remains active. The trend argues against a single discrete thermodynamic event (e.g. a phase transition), which would produce threshold behaviour. Instead, it is consistent with a diffusion-limited process in which the extent of hydrogen redistribution scales continuously with the time available above the diffusion activation temperature, in line with the hydrogen dynamics model of Hammann et al. [292].

Figure 5.6 shows the corresponding photoluminescence (PL) images. The CR1 sample (slowest cooling) exhibits the highest and most uniform emission intensity, confirming consistent passivation across the entire sample surface. The CR4 sample (fastest cooling) shows darker regions and increased spatial non-uniformity, suggesting localised passivation degradation possibly associated with incomplete hydrogen redistribution or thermally induced stress.

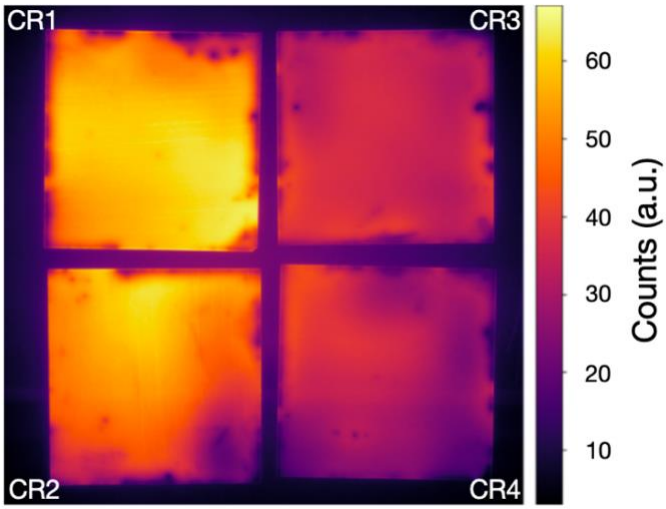


Figure 5.6 PL images of AZO passivation samples cooled at four different rates. Top-left: CR1 (slowest), bottom-left: CR2, top-right: CR3, bottom-right: CR4 (fastest). The colour scale indicates PL intensity proportional to effective lifetime. The PL images correspond to the representative samples shown in Figure 5.5 (b).

5.4.2 Pulse Annealing

To test whether intermittent cooling enhances passivation beyond continuous annealing, I carried out a pulse annealing experiment in which samples received repeated short annealing cycles at 450 °C rather than a single continuous treatment. Figure 5.7 illustrates the pulse annealing protocol. Each sample was annealed at 450 °C for a fixed interval (5, 10, or 15 minutes), slow-cooled for 10 minutes (CR2 in Section 5.4.1), measured, and then returned to the hotplate. This cycle was repeated to accumulate thermal exposure in discrete increments.

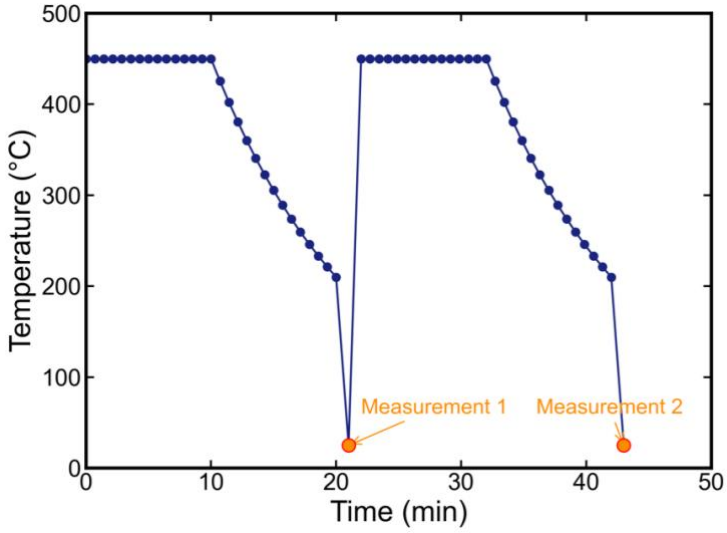


Figure 5.7 Schematic illustration of the pulse annealing protocol, here with an example of a 10-minute heating one. Samples underwent repeated cycles of heating (450 °C for 5, 10, or 15 minutes), slow cooling down for 10 minutes, and lifetime measurement. The orange markers indicate measurement points after each cooling step.

Figure 5.8 presents the lifetime evolution as a function of accumulated annealing time. For all three pulse intervals, the lifetime increases with accumulated thermal exposure, consistent with the progressive hydrogenation of the Si/SiO_2 interface. The 5-minute pulse data show a clear activation curve: lifetime increases from approximately 250 µs at 1×10^{15} cm^{-3} ECD after the first pulse to nearly 2500 µs at 1×10^{15} cm^{-3} ECD after 50 minutes of accumulated time.

The pulse protocol achieves a higher ultimate lifetime (~2500 µs at 1×10^{15} cm^{-3} ECD after 50 min of accumulated 5-min pulses) than continuous annealing (1409 µs at 1×10^{15} cm^{-3} ECD at 30 min, Section 5.2.3). This comparison, however, confounds two effects. Each pulse cycle includes a cool-down ramp through the 300–400 °C window identified in Section 5.4.3 as beneficial for passivation, so the pulse protocol accumulates substantially more residence time within this window than a continuous anneal followed by a single slow cool. The higher ultimate lifetime may therefore reflect accumulated cooling-phase residence rather than an intrinsic advantage of intermittent heating. The 10-min and 15-min pulse protocols plateau at ~1450 µs and ~1300 µs at 1×10^{15} cm^{-3} ECD, respectively, consistent with longer individual pulses approaching or exceeding the optimal continuous dwell and initiating degradation before cooling intervenes.

The superior performance of the 5-minute pulse protocol provides mechanistic insight. Each cooling cycle traverses the intermediate temperature window (around 300-400 °C) where hydrogen mobility remains sufficient for interface migration but Si–H bonds become thermodynamically stable against thermal detrapping [307, 308]. The periodic return to this window enables incremental hydrogen accumulation at the interface without the concurrent degradation (hydrogen effusion, structural disordering) that accompanies extended high-temperature exposure. This interpretation is consistent with the ramp halt results in the following section, which independently identify 300 °C as the critical temperature for passivation optimisation during cooling.

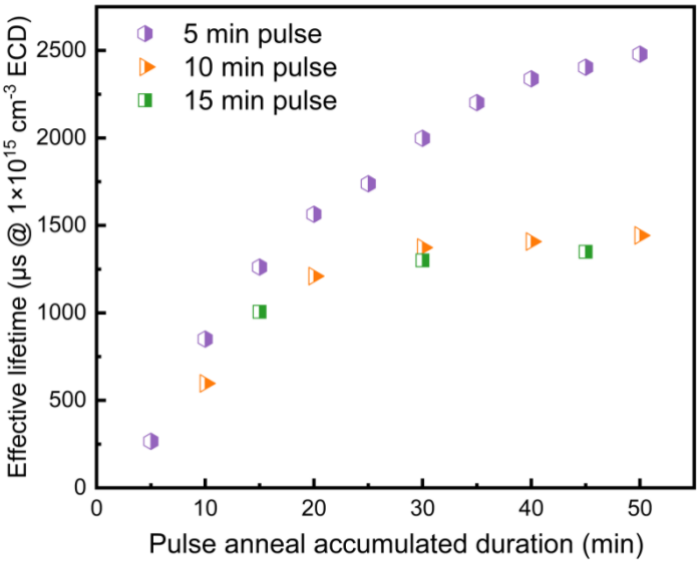


Figure 5.8 Effective lifetime evolution as a function of accumulated pulse annealing duration at 450 °C. Three pulse intervals are compared: 5 minutes (purple diamonds), 10 minutes (orange triangles), and 15 minutes (green squares).

5.4.3 Ramp Halt Temperature Dependence

Having established that slower cooling improves passivation, a natural question arises: at which temperature during the cooling ramp does the extended residence time have the greatest effect? To address this, I designed a ramp halt experiment. I annealed four samples from the same batch at 450 °C for 20 minutes. Each was slowly cooled to a different intermediate temperature (450 °C, 400 °C, 350 °C, 300 °C, or 250 °C), held there for a specified duration, and then cooled slowly to ~ 210 °C. Figure 5.9 shows the cooling profiles (CP1–CP5). Halt durations increase at lower halt temperatures to maintain comparable thermal budgets across the set.

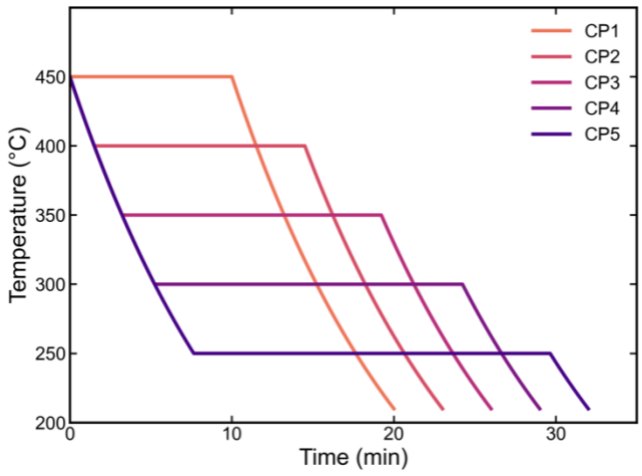


Figure 5.9 Schematic of the temperature profiles for the ramp halt cooling profiles (CP1-CP5). All samples underwent identical annealing at 450 °C for 20 minutes, followed by holding at different intermediate temperatures before slow cooling to ~ 210 °C.

Figure 5.10 presents the effective lifetime as a function of halt temperature. The 300 °C halt (CP4) yields the highest effective lifetime, with a mean value of ~ 1828 µs at 1×10^{15} cm^{-3} ECD. The 450 °C halt is ~ 1409 µs, the 400 °C halt is ~ 1483 µs, and the 350 °C halt is ~ 1716 µs. As the halt temperature is lowered further to 250 °C, the effective lifetime drops to ~1315 µs. This value is statistically indistinguishable from the baseline sample that underwent a 20-minute anneal at 450 °C followed by a standard 10-minute slow cool (~1312 to 1343 µs), potentially signifying a kinetic freezing point: at 250 °C, the thermal energy is insufficient to drive further hydrogen migration, rendering the extended halt time ineffective.

This non-monotonic behaviour identifies 300 °C as a critical temperature window for passivation during cooling. At this temperature, the thermal energy is sufficient to sustain hydrogen mobility and enable continued diffusion to interface states, yet low enough to avoid the degradation mechanisms (hydrogen effusion, structural disordering) that are active at 450 °C.

It is instructive to compare this temperature window with the cooling-rate studies in the SiN_x:H/Si system. Eberle et al. investigated plateau temperatures of 560 °C and 660 °C during the cooling ramp of a fast-firing process with a peak temperature of 800 °C, and found that the 660 °C plateau produced the strongest reduction in bulk hydrogen concentration [297, 298]. Hammann et al. subsequently modelled the out-diffusion as being governed by the integrated residence time above approximately 600 °C [292]. The critical temperature window in the SiN_x:H/Si system (~560–700 °C) is therefore approximately 300 °C higher than the 300 °C window identified here for the AZO/AlO_X stack. This offset likely reflects the lower activation energy for hydrogen migration in amorphous and polycrystalline oxide networks compared to interstitial diffusion in crystalline silicon, or a different rate-limiting step such as hydroxyl dehydration at internal interfaces within the oxide stack rather than bulk interstitial hopping. The two systems therefore share the phenomenology (cooling rate as an independent variable controlling hydrogen redistribution) but operate in distinct thermal regimes governed by different transport physics.

Note that 300 °C is beneficial only during the cooling ramp following high-temperature activation. As shown in Section 5.2.2 and Figure 5.4, a fixed 300 °C anneal does not effectively activate

passivation, confirming that the initial high-temperature step is essential for hydrogen to be released from the AlO_X reservoir, or hydrogen in the AZO film to migrate to the Si/SiO_X interface.

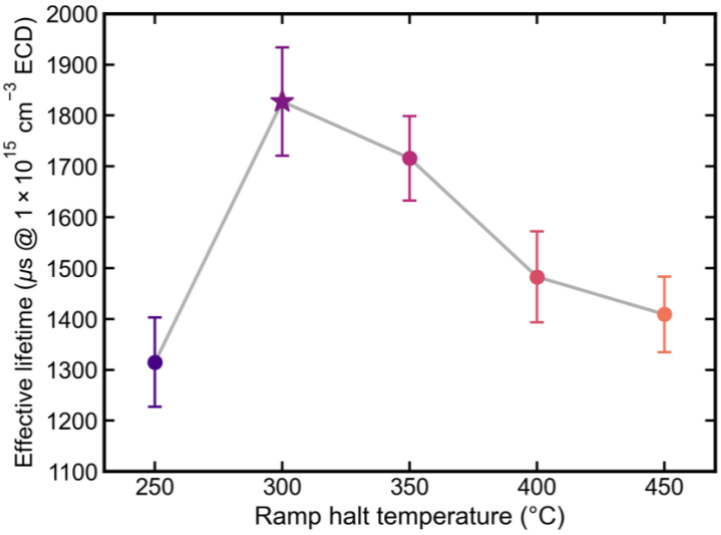


Figure 5.10 Effective lifetime as a function of ramp halt temperature. The 300 °C hold yields optimal passivation, which identifies 300 °C as a critical temperature window for interface optimisation during cooling.

5.5 Structural Response of the AZO/AlO_X Stack to Thermal Treatment

The passivation experiments in Sections 5.2 – 5.4 established that the cooling rate is an independent determinant of interface quality, and proposed two candidate mechanisms: hydrogen redistribution and thermomechanical stress relaxation. This section uses X-ray reflectivity (XRR) to probe the structural response, layer density, thickness, and interface roughness, of the AZO/AlO_X stack as a function of annealing and cooling conditions.

5.5.1 Reference Configurations

I prepared the first batch of XRR samples in four configurations, summarised in Figure 5.11. I annealed Samples 2, 3, and 4 at 450 °C for 20 min on a hotplate in air with a 10-minute naturally slow cool-down (CR2 in Section 5.4.1). This thermal treatment corresponds to the standard slow-cool protocol (CR2) defined in Section 5.4.1. Sample 3 corresponds to the standard AZO/AlO_X stack studied throughout this thesis. Samples 1 and 2 are AlO_X-only references (as-deposited and

annealed), and Sample 4 is an uncapped AZO layer annealed under identical conditions, isolating the effect of the AlO_X cap on the AZO response.

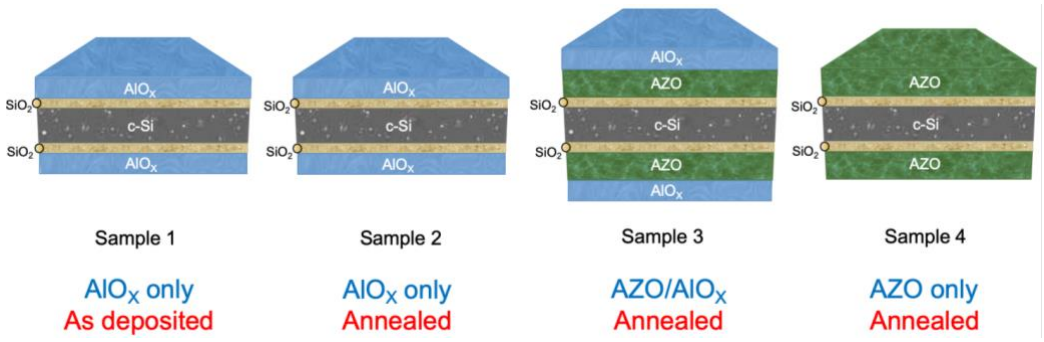


Figure 5.11 Schematic diagrams of the first batch of XRR sample configurations. Sample 3 depicts the standard AZO/AlO_X sample structure. Samples 1 and 2 have no AZO underlayer, and Sample 4 has no AlO_X cap. All annealed samples (2, 3, 4) were treated at 450 °C for 20 min on a hotplate in air with a 10-min slow cool-down.

The reflectivity curves in Figure 5.12 (a) distinguish single- from multi-layer films. Samples 1, 2, and 4, each containing a single film on silicon, display regular Kiessig fringes with a single dominant period [309]. Sample 3 exhibits a beating pattern in which a high-frequency oscillation is superimposed on a low-frequency envelope, as expected from the AZO/AlO_X bilayer.

The scattering length density (SLD) profiles in Figure 5.12 (b) translate these reflectivity data into real-space depth profiles. For Sample 3, the profile begins at the silicon substrate (Distance < 0), shows a dip at Distance ≈ 0 representing SiO_2, followed by a narrow plateau at high SLD (~ 1.4) corresponding to the dense AZO layer, a wider plateau at intermediate SLD (~ 0.9) corresponding to the AlO_X cap, and then a drop to the SLD of air.

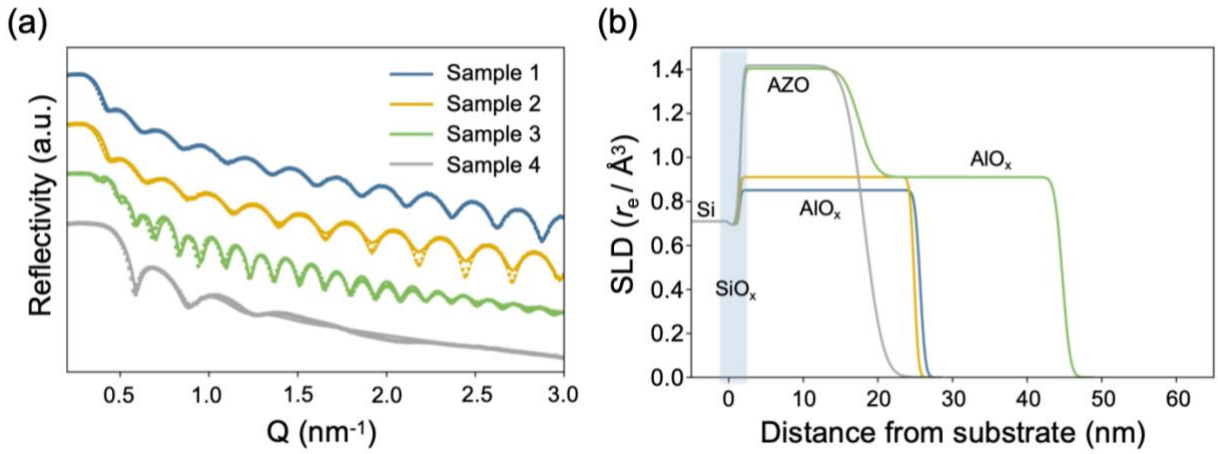


Figure 5.12 XRR results of the samples shown in Figure 5.11 exhibiting (a) reflectivity curves and (b) the SLD depth profiles fitted based on (a).

Table 5.2 reports the fitting results of thickness, density, and roughness on these different samples and layers. Comparing the AlO_X-only samples (Sample 1 vs. Sample 2) isolates the response of the AlO_X layer to annealing. The physical density increases from 2.9 to 3.1 $g \cdot cm^{-3}$, accompanied by a contraction from 24.2 nm to 23.4 nm and a reduction of the surface roughness from 0.6 to 0.5 nm. These changes indicate that annealing allows internal stress relaxation and atomic rearrangement, producing a denser and smoother AlO_X layer.

A comparison of Sample 3 and Sample 4 reveals the role of the AlO_X cap. Both samples reach the same AZO density of 5.2 g/cm^{-3}, showing that the cap does not change AZO density. The AZO upper-surface roughness, however, differs: the uncapped annealed AZO reaches 2.0 nm (Sample 4), whereas the AZO/AlO_X interface in Sample 3 is 1.7 nm. The AlO_X cap therefore acts as a physical barrier, suppressing roughening of the AZO top surface during annealing. The fitted AlO_X thickness in Sample 3 (27.1 nm) is also larger than in the single-layer reference (23.4 nm), which may result from a limited degree of interfacial mixing at the AZO/AlO_X boundary that the XRR fit absorbs into the effective AlO_X thickness [310].

Table 5.2 XRR fitting results of thickness, density, and roughness on different samples and layers. The fitted thicknesses carry an uncertainty of approximately 1%, that is ± 0.2–0.5 nm over the range tabulated. The density and roughness are more strongly correlated with one another and are correspondingly less well determined, and for the bilayer samples the total stack thickness is better constrained than the individual sub-layers. See Section 3.5.4.1 for the basis of these figures.

Sample	Layer	Thickness (nm)	Density (g/cm^3)	Roughness (nm)
Sample 1	AlO_X	24.2	2.9	0.6
Sample 2	AlO_X	23.4	3.1	0.5
Sample 3	AlO_X	27.1	3.1	0.8
Sample 3	AZO	15.9	5.2	1.7
Sample 4	AZO	16.5	5.2	2.0

5.5.2 Peak-Temperature and Cooling-Rate Structural Comparisons

I prepared a second batch of samples in the standard AZO/AlO_X configuration and annealed under different temperatures and cooling regimes, as summarised in Table 5.3. To maximise the

detectability of cooling-induced structural variations via XRR, the 500 °C primary anneal (established in Chapter 4) was employed rather than the 450 °C hotplate baseline. Furthermore, the air-ambient furnace accommodated the 600 °C comparison condition while ensuring uniform atmospheric parameters across all samples. Slow cooling corresponds to a 20 min anneal followed by a 10-minute slow cool-down; fast cooling is achieved by quenching after a 30 min total anneal. The effective lifetimes reported in Table 5.3 are substantially higher than those in Sections 5.2–5.4 (up to 4.69 ms vs. ~1.3–2.0 ms at 1×10^{15} cm^{-3} ECD). This reflects the transition from Substrate A to Substrate B (Section 3.1.1) for the reflectometry batches. Because resolving clean reflectometry data requires semiconductor-grade flatness, substrate B was utilised to ensure accurate measurements and reliable structural fitting. As all samples in this batch share substrate B, the comparative analysis of cooling rates remains valid despite the higher absolute lifetimes.

Table 5.3 The second batch of XRR samples: their annealing conditions and effective lifetime values.

	Sample 1	Sample 2	Sample 3	Sample 4
Condition	500 °C furnace slow cooled	500 °C furnace fast cooled	As deposited	600 °C furnace slow cooled
Effective lifetime (ms at 1×10^{15} cm^{-3} ECD)	4.69	2.17	--	0.93

Figure 5.13 presents the fitted SLD depth profiles of Samples 1, 3, and 4. Compared to the as-deposited state, both the 500 °C and 600 °C annealed samples exhibit a clear upward shift in SLD values across both sub-layers, especially in the AlO_X cap, confirming thermally driven densification of the stack. In addition, the total thickness of the stack reduces significantly after annealing at 600 °C, as evidenced by the inward shift of the film surface.

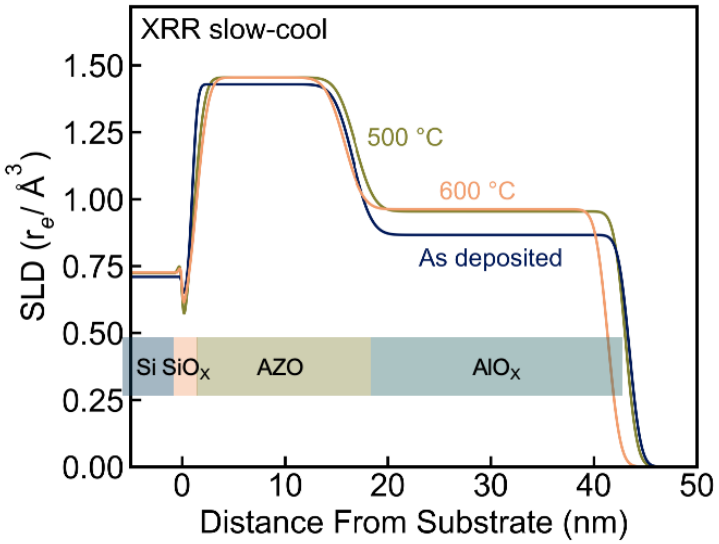


Figure 5.13 XRR results of samples shown in Table 5.3 exhibiting the fitted SLD depth profiles of three different thermal treatment samples (blue: Sample 3, as-deposited; yellow: Sample 4, 600 °C slow-cooled; green: Sample 1, 500 °C slow-cooled).

Figure 5.14 compares the SLD profiles of the slow- and fast-cooled samples annealed at 500 °C. Within the resolution of the fit, the two profiles are indistinguishable: layer thicknesses, densities, and roughnesses are essentially identical. This negative result is informative. At the thickness precision accessible to XRR (± 0.2–0.5 nm, Section 3.5.4.1), the cooling rate does not produce a measurable structural difference in the AZO/AlO$_X$ stack. As a result, the twofold lifetime contrast between these samples (4.69 ms vs. 2.17 ms 1×10^{15} cm^{-3} ECD) cannot be attributed to macroscopic differences in layer density or interface roughness, and is therefore most plausibly attributable to more subtle chemical or hydrogen-related effects. The next section uses NR to test this hypothesis.

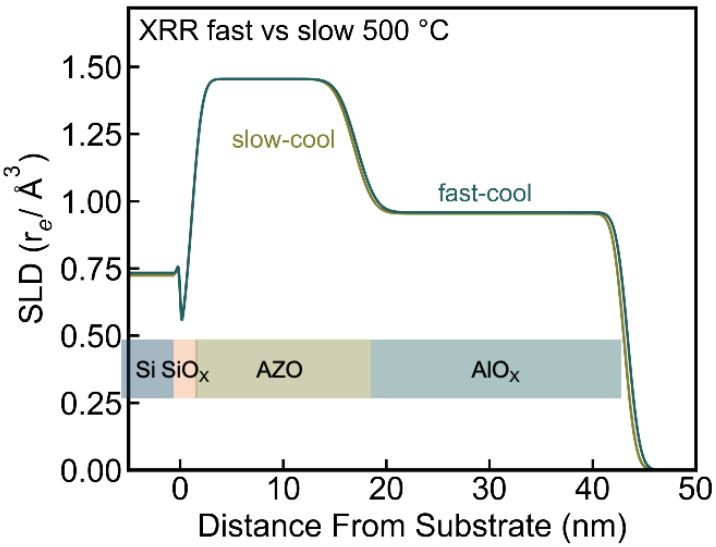


Figure 5.14 XRR results of samples shown in Table 5.3 exhibiting the fitted SLD depth profiles of two different cooling rate samples (blue: Sample 1, slow cooled; yellow: Sample 2, fast cooled).

5.6 Hydrogen Depth Profiles under Different Thermal Regimes

NR is well suited to hydrogen profiling because ^{1}H has a negative coherent scattering length ($b_H \approx -3.74$ fm) [311], meaning that any increase in hydrogen content lowers the effective SLD of a layer; conversely, a higher SLD indicates lower hydrogen content.

5.6.1 Temperature-Dependent Hydrogen Redistribution

Figure 5.15 compares the NR SLD depth profiles of three slow-cooled AZO/AlO_X stacks: as-deposited (Sample 3), 500 °C-annealed (Sample 1), and 600 °C-annealed (Sample 4). The data reveal an opposing evolution of the two layers upon annealing at 500 °C. In the AlO_X region (~18–45 nm from the substrate), the SLD rises, indicating hydrogen loss from the cap. In the AZO region (~2–18 nm), the SLD slightly decreases, indicating a small amount of hydrogen gain. This opposing evolution identifies the AlO_X cap as an active hydrogen reservoir: upon annealing, a fraction of the hydrogen released from the cap migrates downward into the AZO network rather than escaping to the vacuum.

At 600 °C, the AZO SLD is essentially unchanged relative to 500 °C, indicating that the AZO hydrogen content has equilibrated by 500 °C and does not increase further with temperature. The AlO_X SLD, however, rises and approaches that of the AZO, indicating that the residual hydrogen content in the cap has been depleted by outgassing. This depletion provides a direct explanation for the passivation degradation observed at 600 °C (Section 5.2.2 and Table 5.1): once the AlO_X can no longer supply hydrogen during the final stages of the thermal cycle, the interface is left without a source to maintain its passivating Si–H bonds.

This NR evidence is qualitatively corroborated by the elemental depth profiles obtained via ToF-ERD (Appendix E, Figure A 88(a)-(d)). The ERD analysis confirms that the as-deposited AlO_X cap (especially at the topmost surface, Appendix E, Figure A 88(c)) has a substantial initial hydrogen concentration. Furthermore, comparing the ERD profiles before and after annealing (Appendix E, Figure A 88(b)-(d)) reveals that the most significant reduction of hydrogen concentration occurs at the AlO_X topmost surface from 12.23 at.% to 9.81 at.% [171]. This direct compositional observation aligns with the hydrogen loss inferred from the NR SLD increase.

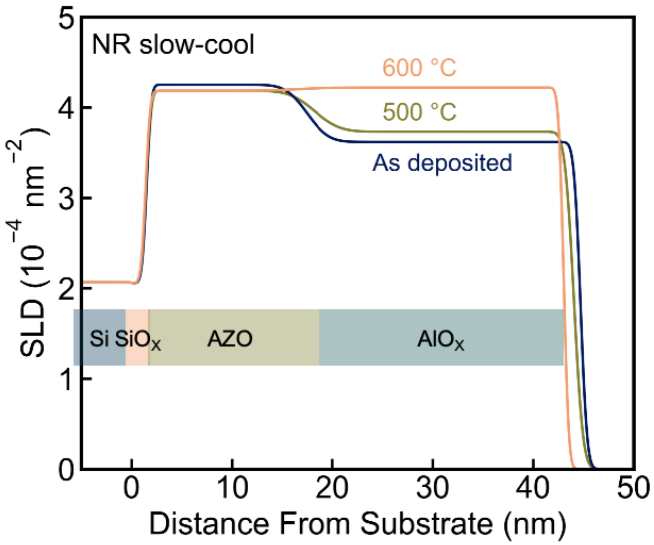


Figure 5.15 NR results corresponding to Samples 1 (500 °C slow-cooled), 3 (as deposited), and 4 (600 °C slow-cooled) from Table 5.3.

5.6.2 Cooling-Rate-Dependent Hydrogen

Figure 5.16 isolates the effect of the cooling rate under a fixed 500 °C thermal budget by comparing the neutron scattering length density (SLD) profiles of the slow-cooled (Sample 1) and fast-cooled (Sample 2) samples from Table 5.3. Although the total physical thickness derived from XRR remains consistent between the two samples, the NR profile of the slow-cooled sample exhibits an apparent thickness contraction at the topmost surface compared to the fast-cooled one.

The discrepancy between XRR and NR thicknesses for the slow-cooled sample is consistent with hydrogen enrichment at the top surface. XRR probes electron density and records the full physical extent of the film, including any surface hydroxylation. NR is strongly sensitive to hydrogen, which has a negative nuclear scattering length, so a hydrogen-rich layer at the top of the film lowers the local SLD toward that of air and is fitted as though the film were thinner. Two concurrent mechanisms plausibly produce this surface enrichment during slow cooling: outward segregation of hydrogen from the AlO_X bulk over the sustained thermal window, and enhanced surface hydroxylation or hydration during extended residence at intermediate temperatures. Fast cooling quenches the oxide network before a comparable fraction of hydrogen can mobilise, locking it inside the bulk cap (as reflected in the slightly lower bulk SLD of the fast-cooled sample) and suppressing surface accumulation.

Within the underlying AZO layer, the SLD profiles of the slow- and fast-cooled samples are indistinguishable: the total AZO hydrogen content is invariant with cooling rate. Because slow cooling drives hydrogen mobility and outward segregation without building a bulk excess in the AZO, the passivation improvement cannot be explained by a simple volumetric hydrogen increase. The most plausible remaining explanation is a change in the chemical bonding environment of hydrogen at or near the Si/SiO_X interface, a hypothesis tested by ToF-SIMS in Chapter 6.

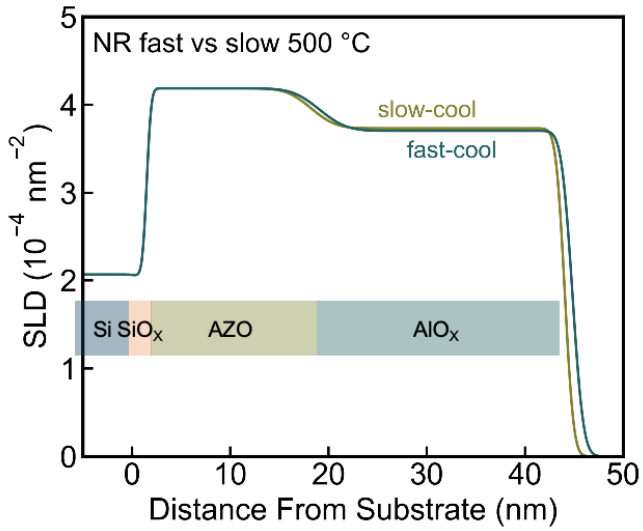


Figure 5.16 NR results corresponding to Samples 1 (slow-cooled) and 2 (fast-cooled) from Table 5.3.

5.7 Optoelectronic Properties Under Optimised Thermal Processing

The previous sections focused on passivation quality. For application as an interconnection layer (ICL) in tandem solar cells, the AZO layer must also achieve adequate optoelectronic properties. This section examines how the optimised thermal processing conditions affect these properties.

5.7.1 Optical Transparency and Absorption Edge

The optical transmittance of AZO and ZnO films was characterised using UV-Vis spectrophotometry. Samples were deposited on glass substrates with films on both front and back sides, each side having a thickness of 20 nm ZnO or AZO (with an additional 20 nm AlO_X where applicable). The annealing conditions are consistent with the standard protocol: 450 °C on a hotplate in air for 20 minutes, followed by a 10-minute slow cool down.

Figure 5.17 presents the transmittance spectra of these samples. All configurations exhibit transmittance exceeding 94% in the 600-1000 nm wavelength range, which is critical for bottom-cell absorption in tandem devices [312-314]. The ZnO films (Figure 5.17 (a)) exhibit spectral variation, indicating that their absorption edge and sub-bandgap absorption are sensitive to the AlO_X capping layer and thermal history. In contrast, the AZO spectra (Figure 5.17 (b)) remain relatively tightly overlapped across all processing conditions, indicating that the optical properties of the Al-doped films are more robust against thermal processing and variations in the AlO_X capping configuration. Furthermore, the AZO films display a slightly higher absolute transmittance (95.2% vs. 94.3% at 600 nm) compared to the ZnO films. Both the optical robustness and high transmittance of AZO align with the requirements for an ICL in tandems, where minimising parasitic absorption during thermal processing is crucial [315].

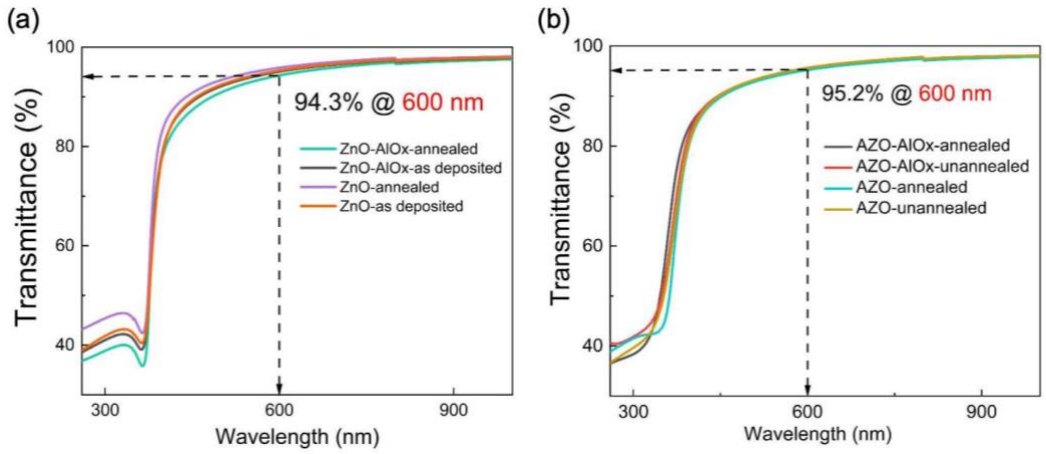


Figure 5.17 Transmittance spectra of various (a) ZnO and (b) AZO film configurations on glass substrates. For samples without AlO_X, both sides were deposited with 20 nm ZnO/AZO (40 nm in total); For samples with AlO_X, both sides were deposited with 20 nm ZnO/AZO + 20 nm AlO_X (80 nm in total).

To quantify the absorption edge underlying the observed optical stability, Figure 5.18 shows the apparent optical gaps of the films extracted using Tauc plot analysis. The extracted values fall within 3.21–3.30 eV for all configurations, consistent with literature reports for ALD-deposited ZnO-based films [284, 285].

An uncertainty is assigned to these values before the differences in Figure 5.18 are interpreted. The dominant contribution is not the noise on the spectrum but the choice of the photon-energy window over which the linear region is fitted [316-318]. With a 1 nm wavelength step, the spacing between data points near the absorption edge is approximately 0.009 eV, an order of magnitude smaller. All

configurations here are analysed by the same procedure, so this contribution is largely common to them and cancels in the comparison between configurations. What remains can be estimated from the data themselves. The four independently prepared ZnO/AZO pairs give gap differences of 0.04, 0.02, 0.04 and 0.06 eV, a standard deviation of 0.016 eV about a mean of 0.040 eV. Since this scatter also includes genuine variation in carrier density among the four AZO films, it is an upper bound. The scatter quoted is that of a difference between two independently extracted values. For two independent quantities with equal uncertainty σ, their difference has uncertainty $\sqrt{2}\sigma$, so a scatter of 0.016 eV corresponds to σ = 0.011 eV for a single extracted gap. An uncertainty of ± 0.01 eV is therefore assigned to the individual values in Figure 5.18 (b), and ± 0.02 eV to a difference between any two of them. This is consistent with the accuracy of better than 0.05 eV reported for Tauc analysis of well-defined absorption edges [319].

The structure near 3.40 eV in Figure 5.18 (a) arises from excitonic absorption at the ZnO band edge. The peak, and the minimum above it, appear in the undoped ZnO films but not in the AZO films. This contrast holds at both film thicknesses studied here, and the same feature is absent from the four AZO films of Chapter 4, which I measured on fused quartz at a different thickness (Figure 4.14). Neither the substrate nor the sample geometry can therefore account for it. Spectroscopic determinations of the ZnO dielectric function resolve an excitonic feature between 3.30 and 3.50 eV, above which the imaginary part of the dielectric function falls until higher interband transitions contribute from about 3.6 eV [320, 321]. The free-exciton binding energy of ZnO is approximately 60 meV (Section 2.4.1), more than twice the thermal energy at room temperature, so this contribution survives at 300 K. Free carriers screen the exciton above the Mott density, which for ZnO lies near 3×10^{18} cm^{-3}; the AZO films carry 1.3-2.5 × 10^{20} cm^{-3} for the 20 nm thickness used here (Section 5.7.2), while the undoped films lie below the threshold. The feature therefore tracks the carrier density measured independently by the Hall effect.

The values extracted by the Tauc construction are for this reason reported as apparent optical gaps rather than single-particle bandgaps. The construction assumes that absorption near the edge arises from uncorrelated interband transitions, an assumption the excitonic contribution violates. The extracted values lie 0.1–0.15 eV below the feature at 3.40 eV, and band tailing in these

nanocrystalline films contributes to the same offset. The linear regions used for the extrapolation lie below the feature, and all configurations are analysed by the same procedure, so the comparison between them is unaffected.

The AZO films give a wider apparent gap than the ZnO films under every condition. The direction of this difference is that expected from the Burstein–Moss effect, in which electrons donated by substitutional Al fill the lowest conduction band states and raise the minimum photon energy for absorption [265, 267, 269]. Its magnitude, however, is comparable to the exciton binding energy, and the excitonic contribution present in the ZnO films but not in the AZO films displaces the ZnO extrapolation in the same direction. The two contributions cannot be separated from these data, and the difference is therefore not interpreted quantitatively. Comparisons within a single material, for which the excitonic contribution is common to both members of the pair, are unaffected.

Beyond the difference between materials, Figure 5.18 (b) shows smaller variations linked to thermal history and capping configuration. Thermal annealing shifts the extracted gap upwards in all four pairs, by 0.01–0.04 eV. Each individual shift is comparable to the ± 0.02 eV uncertainty, but the sign is the same in every pair, which indicates a real trend rather than scatter; it is attributed to thermal relaxation of the film network and improved local structural ordering [322-324]. The effect of the AlO_X cap is smaller, between 0.00 and 0.04 eV, and is not resolved at this uncertainty. The highest single value, 3.30 eV for the annealed AZO/AlO_X stack, would be consistent with additional activation of Al at the AZO/AlO_X interface during the thermal cycle, but this is not established by the present data.

Because all extracted values exceed 3.2 eV, and the absorption edge itself lies at or above 3.4 eV, intrinsic optical absorption is confined to the ultraviolet region. This means that the layers minimise parasitic absorption and maximise photon transmission to the silicon bottom cell.

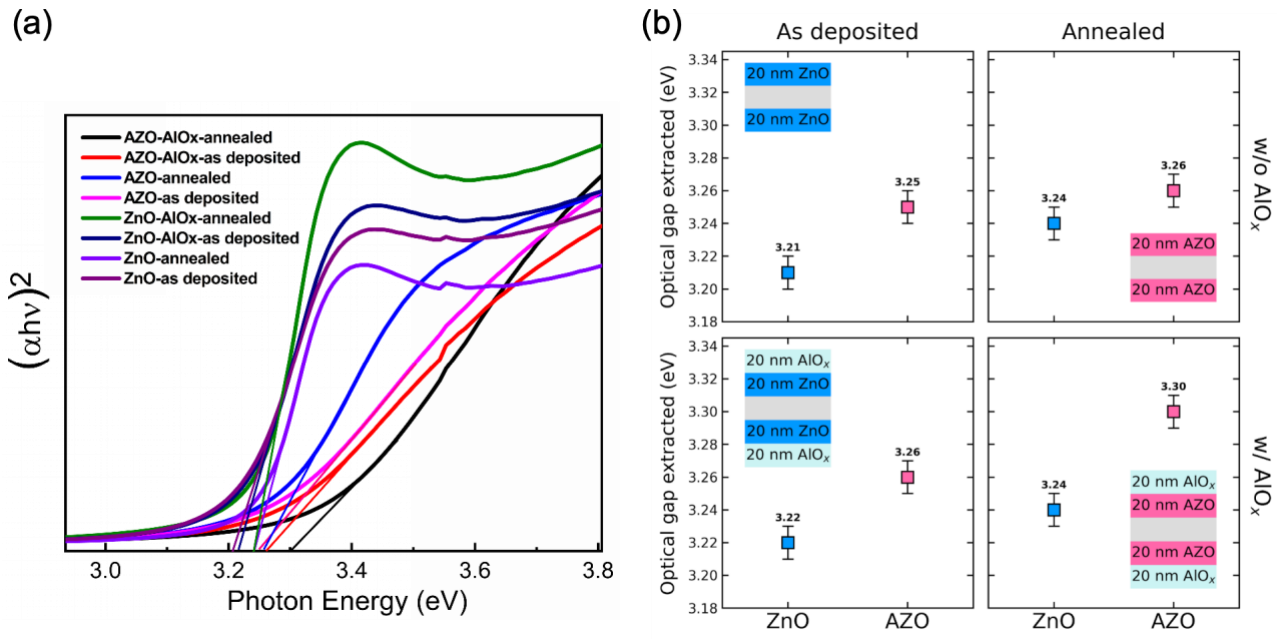


Figure 5.18 (a) Tauc plots for various AZO and ZnO film configurations. The peak near 3.40 eV in the ZnO traces, and the minimum above it, arise from excitonic absorption at the ZnO band edge; the linear regions used for the extrapolations lie below this structure. (b) Apparent optical gap vs. configuration (ZnO: blue; AZO: pink), grouped by thermal state (as-deposited, annealed) and AlO_X deposition condition (with AlO_X, without AlO_X). Error bars in (b) are ± 0.01 eV on the individual values; a difference between any two points carries ± 0.02 eV. See text for the estimation. Inset: schematic of the bifacial sample structures, with the grey layer representing glass.

5.7.2 Electrical Transport Properties

The electrical transport properties of uncapped AZO films on silicon substrate B (290 nm thermal SiO_2 on Si, detailed in Section 3.1.1) were characterised using van der Pauw and Hall effect measurements. Figure 5.19 presents the resistivity of AZO films as a function of film thickness for as-deposited and annealed (450 °C on a hotplate in air for 20 minutes, followed by a 10-minute slow cool down) samples. Resistivity decreases with increasing film thickness for both conditions, consistent with reduced grain boundary scattering and improved crystallinity in thicker films [234, 325, 326]. For 20 nm films, the as-deposited resistivity is 1.42×10^{-3} Ω·cm, decreasing to 0.70×10^{-3} Ω·cm for 56 nm films.

Annealing increases the resistivity in a thickness-dependent manner. For thinner films (20 and 28 nm), the increase is significant, from approximately 1.09×10^{-3} to 3.7×10^{-3} Ω·cm for the 28 nm case. This is likely caused by the diffusion of atmospheric oxygen into the thin film during air annealing, which fills oxygen vacancies (a source of free carriers) and increases depletion regions at grain

boundaries. For thicker films (40 and 56 nm), the annealing-induced increase is smaller, consistent with the bulk of the film acting as a diffusion barrier against atmospheric oxidation.

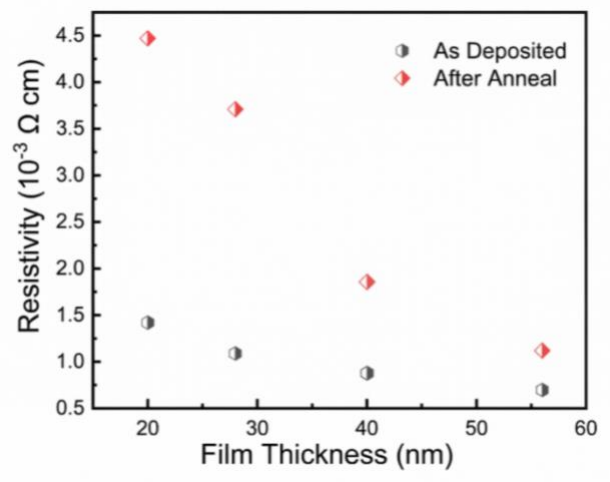


Figure 5.19 Resistivity of uncapped AZO films as a function of film thickness for as-deposited (black) and annealed (red) conditions.

Figure 5.20 elucidates the origins of these resistivity changes via Hall effect measurements. For the 20 nm as-deposited film, the carrier mobility is 34.7 $cm^2/V{\cdot}s$ with a carrier concentration of 1.27×10^{20} cm^{-3}. After annealing, the mobility drops to 5.7 $cm^2/V{\cdot}s$. This decline indicates the dominance of grain boundary scattering, likely induced by the diffusion of atmospheric oxygen, which increases depletion regions at the crystallite interfaces. The carrier concentration increases to 2.46×10^{20} cm^{-3}, possibly due to thermal activation of aluminium dopants. The net effect is the observed increase in resistivity, as the mobility loss outweighs the doping gain.

For the 56 nm films, similar trends are observed but with less pronounced changes. The as-deposited film shows mobility of 21.3 $cm^2/V{\cdot}s$ and carrier concentration of 4.21×10^{20} cm^{-3}. After annealing, mobility decreases to 7.2 $cm^2/V{\cdot}s$, while carrier concentration increases to 7.76×10^{20} cm^{-3}.

These results indicate a trade-off between passivation optimisation and electrical conductivity. The annealing conditions required for optimal passivation degrade TCO conductivity, particularly for thinner films. However, the resistivity values obtained (on the order of 10^{-3} Ω·cm) remain within the acceptable range for transparent conductor applications in solar cells [256, 327, 328]. The rise in carrier density on annealing corresponds to an increase in doping efficiency from approximately 3% to 7% at 20 nm and from 12% to 22% at 56 nm (Section 4.4.2), so the anneal activates Al as well as degrading mobility.

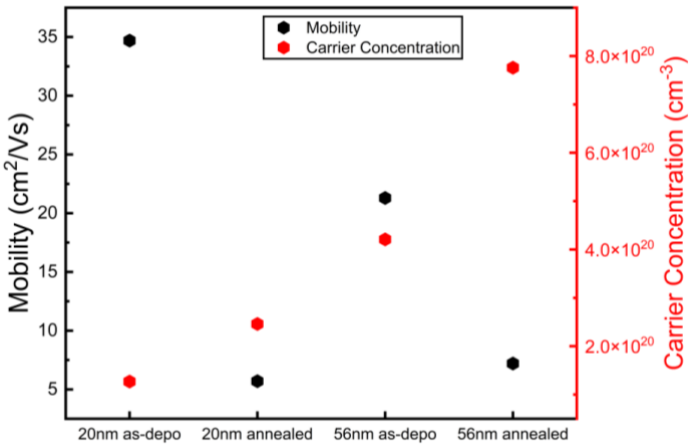


Figure 5.20 Carrier mobility (left, black) and carrier concentration (right, red) of uncapped AZO films of 20 nm and 56 nm thickness in as-deposited and annealed conditions.

5.8 Discussion and Summary

5.8.1 Interpretation of Principal Findings and Mechanisms

This chapter investigated the post-deposition thermal processing of ALD-deposited SiO_X/AZO/AlO_X passivating contacts, from the steady-state annealing stage to the role of the cooling phase. The principal finding is that the cooling rate is an independent determinant of passivation quality, supported by four complementary experimental designs: direct fast-versus-slow contrast (Section 5.3), a continuous cooling-rate sweep (Section 5.4.1), pulse annealing (Section 5.4.2), and ramp-halt temperature profiling (Section 5.4.3).

XRR and NR together narrowed the candidate mechanism from a structural to a chemical hypothesis. XRR showed no measurable differences in density, thickness, or interface roughness between slow- and fast-cooled samples, suggesting macroscopic densification and bulk stress relaxation are not the origin of the passivation contrast. NR, together with ToF-ERD, identified the AlO_X cap as an active hydrogen reservoir: upon annealing, a fraction of the hydrogen released from the cap migrates into the AZO network rather than escaping to the vacuum. The cooling-rate ramp-halt experiments located a critical kinetic window near 300 °C, at which extended residence optimises passivation; a further drop to 250 °C produces no further benefit, consistent with a kinetic freezing point below which hydrogen mobility is insufficient. NR also shows that the bulk AZO hydrogen content is invariant with the cooling rate, so the enhanced passivation is not explained by

a volumetric hydrogen excess in the AZO. The remaining plausible mechanism is a change in the local chemical bonding environment of hydrogen at or near the Si/SiO_X interface.

UV-Vis and Tauc-plot analyses confirmed that the extended thermal processing does not compromise the optoelectronic properties of the stack: the apparent optical gap of the AZO films remains above 3.2 eV across all conditions, and the absorption edge lies at or above 3.4 eV, keeping parasitic absorption confined to the ultraviolet. Electrical transport measurements reveal a thickness-dependent reduction in carrier mobility upon annealing, attributable to atmospheric oxygen incorporation at grain boundaries, but the resulting resistivity (~ 10^{-3} Ω·cm) remains within the acceptable range for transparent-conductor applications. The optimised thermal protocol therefore balances interfacial passivation with viable transparent-conductor performance.

5.8.2 Comparisons with Literature

The phenomenology of cooling-rate-dependent passivation is well established in the SiN_X:H/PERC system and has been extensively modelled by Hammann et al. [292] and Eberle et al. [297, 298]. However, the mechanism in the AZO/AlO_X system differs substantially. In SiN_X firing, the critical kinetic window lies around 560–700 °C, and the operative mechanism is hydrogen out-diffusion from the silicon bulk, driven by a temperature-dependent segregation coefficient at the SiO_X/Si interface with SiN_X acting as an effectively infinite source and sink [292]. In the AZO/AlO_X system, the critical window lies near 300 °C, and the transport pathway is inward diffusion from the top dielectric toward the Si/SiO_X interface, traversing multiple oxide layers with distinct diffusion barriers. The ~ 300 °C offset is consistent with the lower activation energy for hydrogen migration in amorphous and polycrystalline oxide networks relative to interstitial diffusion in crystalline silicon.

The assignment of AlO_X as the active hydrogen reservoir is consistent with two independent lines of evidence from the ALD literature. Guerra-Nuñez et al. demonstrated that ALD-Al_2O_3 growth systematically incorporates hydrogen from the H_2O co-reactant into the bulk network as residual Al–OH groups, so thermal ALD AlO_X is intrinsically hydrogen-rich as deposited [169]. Kinnunen et al. [329] subsequently tracked H/D exchange in these films using rare-isotope precursors and showed that hydrogen in ALD AlO_X is mobile enough to undergo inter-layer exchange even at modest

temperatures, provided the hydrogen concentration is sufficiently high [330]. Combined with the depth-resolved NR evidence in Section 5.6, these reports support the picture of the AlO_X cap as a hydrogen source that supplies the Si/SiO_X interface during the annealing and cool-down through the 300 °C window.

In classical microelectronics and silicon photovoltaics, passivating interfacial dangling bonds conventionally relies on external hydrogen supplied via FGA. Here, cooling-rate engineering of the stack uses the intrinsic hydrogen content of the AZO/AlO_X network, avoiding FGA. This is an advantage for tandem fabrication, where flammable-gas processing introduces integration complexity and safety constraints.

5.8.3 Limitations and Uncertainties

This study is subject to several methodological limitations and uncertainties. First, the structural and compositional metrology has finite sensitivity. XRR resolves layer density to approximately 2–5% [207, 331, 332], so sub-nanometre reconstructions at the Si/SiO_X interface are below the detection limit. NR provides a strong contrast for hydrogen, but the quantitative analysis of absolute hydrogen content was not reported. For the mechanistic arguments developed here, only relative NR SLD differences between samples are used, which are robust against the absolute calibration uncertainty.

Second, the conclusion that the passivation contrast arises from an interfacial chemical bonding change is inferred from the absence of density/thickness changes and the presence of AlO_X-sourced hydrogen migration; direct evidence of the relevant Si–H bonds at the Si/SiO_X interface is beyond the reach of XRR and NR and is addressed in Chapter 6.

Third, the mechanism, thermomechanical stress at the Si/SiO_X interface arising from the CTE mismatch across the stack, was proposed in Section 5.3.2 but is not tested by the metrology reported here. Si-side residual stress measurement by Raman spectroscopy or cross-sectional HR-TEM of the Si/SiO_X interface is identified as the follow-up work.

Fourth, the vertical charge-transport behaviour of the stack was not investigated. Given the upward band bending in silicon identified in Chapter 4, an electrostatic barrier to electron transport is

expected; translating the high minority-carrier lifetimes reported here into an operational device without incurring prohibitive contact resistivity remains a separate integration challenge.

Fifth, the interfacial hydrogen configuration obtained through the 300 °C kinetic window is a metastable state. In tandem architectures, the silicon bottom cell must survive subsequent top-cell processing at 100–150 °C [333, 334]; whether the cooling-optimised Si–H bonds remain stable under this additional thermal load, or whether further out-diffusion occurs, is an open question that requires device-level validation.

5.8.4 Practical Implications and Future Directions

Practically, this chapter suggests that the cooling phase for AZO/AlO_X stacks should be treated as a controlled process parameter rather than a passive ambient cool-down. The identification of a 300 °C kinetic window motivates a two-step thermal profile, high-temperature activation followed by an extended plateau near 300 °C, that decouples defect activation from hydrogen redistribution and may maximise passivation within a restricted total thermal budget.

Scientifically, the conclusion that the passivation enhancement originates from interfacial chemical bonding rather than from bulk compositional changes defines a testable hypothesis. Because spatially averaged techniques (XRR, NR) cannot resolve local chemical speciation, the next step requires probes that are sensitive to electronic structure and local bonding environment. Chapter 6 therefore employs surface photovoltage (SPV), X-ray photoelectron spectroscopy (XPS), and time-of-flight secondary-ion mass spectrometry (ToF-SIMS) to verify the interfacial chemical transformation and band-bending dynamics predicted by the mechanistic model developed here.

Chapter 6. Decoupling Field-Effect and Chemical Passivation at the Si/AZO Interface

6.1 Introduction

Chapter 5 established that the cooling rate following annealing is an independent determinant of passivation quality in the SiO_X/AZO/AlO_X system, and showed through XRR and NR that the passivation contrast between slow- and fast-cooled samples does not originate from structural differences but from the redistribution of hydrogen within the stack. This chapter identifies the electronic and chemical mechanisms responsible, with the specific aim of distinguishing and characterising the respective contributions of field-effect passivation and chemical passivation.

The investigation proceeds through four complementary characterisation stages. Section 6.2 uses Kelvin probe surface photovoltage (KP-SPV) to quantify the interface band bending and built-in electric field under different processing conditions. Section 6.3 employs X-ray photoelectron spectroscopy (XPS) to probe the local band alignment at the buried Si/ AZO interface, and examines an important discrepancy between KP-SPV and XPS measurements. Section 6.4 uses transient surface photovoltage (transient-SPV) spectroscopy, a technique in which time-resolved photovoltage responses to pulsed monochromatic excitation are recorded, to identify chemical passivation through charge trapping and relaxation dynamics. Section 6.5 applies ToF-SIMS to track the spatial redistribution of hydrogen-related secondary ion fragments at the interface, providing indirect evidence for the chemical environment in which hydrogen resides. Section 6.6 draws together the evidence from all four techniques to propose a mechanistic framework for the cooling-rate-dependent passivation enhancement. Together, these findings provide the physical basis for optimising the annealing protocol for the SiO_X/AZO/AlO_X passivation stacks.

Figure 6.1 shows the schematic diagrams of all the sample configurations used in this chapter.

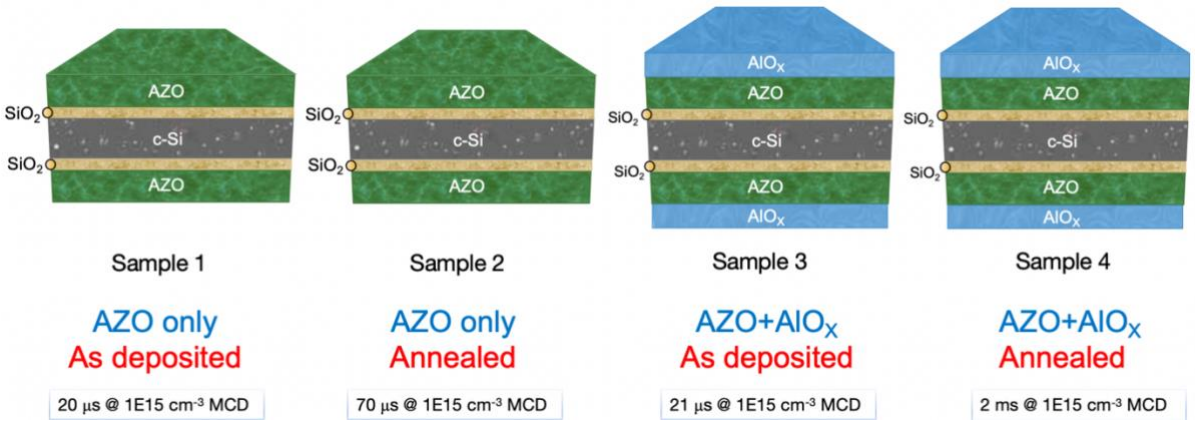


Figure 6.1 Schematic of the sample configurations and annealing states used throughout this chapter. All samples in Sections 6.2 and 6.3 were fabricated on silicon substrate A (~ 4 Ω·cm n-type CZ c-Si wafers, ~ 135 µm thick, solar-grade, saw-damage etched; ~ 4 × 4 cm in size for samples in Section 6.2, ~ 0.8 × 0.8 cm in size for samples in Section 6.3). All samples in Sections 6.4 and 6.5 were fabricated on silicon substrate B (30–60 Ω·cm n-type CZ c-Si wafers, ~ 675 µm thick, semiconductor-grade, chemo-mechanically polished ultra-flat; ~ 4 × 4 cm in size). All samples were RCA cleaned and had a ~1.2 nm chemically grown SiO_X interlayer (Sections 3.1.1 and 3.1.2). The measured effective lifetime values shown in the figure correspond to samples fabricated on substrate B. The trend of the lifetime value differences among them also applies to samples fabricated on substrate A.

6.2 KP-SPV Band Bending

SiO_X is too thin to be resolved as a distinct film, yet it hosts interface states and fixed charges that govern the band bending. For brevity, this interface is referred to as the Si/AZO interface throughout, with the understanding that the SiO_X interlayer is always present.

The investigation compares two sample batches. For the first batch, I deposited the AlO_X cap (26 nm) immediately after AZO deposition (16 nm); annealed (when applied) the sample with the AlO_X cap in place, and then removed the AlO_X layer by wet etching (Section 3.1.5) prior to SPV measurement, leaving only the Si/AZO structure. The as-deposited samples from the same batch underwent AlO_X deposition and etching without any intermediate thermal treatment. The second batch consists of Si/AZO (16 nm) samples that were never coated with AlO_X. Within each batch, the annealed samples were characterised either fast cooling (450 °C → <100 °C in <1 min by removal onto a room-temperature metal plate, Section 5.4.1 CR4) or slow cooling (450 °C → ~ 200 °C over 10 min, natural convective cooling, Section 5.4.1 CR2).

At the time of measurement, all samples retained only the Si/AZO structure, as shown in Figure 6.1 (a) or (b); the AlO_X cap, where applicable, had been removed. The etching protocol (Section 3.1.5)

was calibrated on reference samples using ellipsometry to confirm selective removal of the AlO_X layer.

6.2.1 As-deposited and Annealed Si/AZO Samples Without AlO_X Deposition

To establish a baseline free from any artefacts introduced by AlO_X deposition and etching, SPV measurements were performed on Si/AZO samples that were never coated with AlO_X. Two conditions were examined: as-deposited (no thermal treatment) and annealed (450 °C, 20 minutes in air, followed by 10 minutes slow cooling, as defined above). Figure 6.2 presents box-plot distributions of the CPD values measured in dark and under illumination across the scanned area for both conditions; the SPV for each condition is obtained from the difference between the dark and illuminated means.

The as-deposited sample exhibits a dark CPD of 81.5 mV and an illuminated CPD of −450.4 mV, yielding SPV = 531.9 mV. The annealed sample shows a dark CPD of 197.7 mV and an illuminated CPD of −196.3 mV, yielding SPV = 394.0 mV. The surface photovoltage is defined throughout Section 6.2 as SPV = $CPD_{dark} - CPD_{light}$ (Section 3.6.2, Equation 3.22), such that a positive SPV is consistent with upward band bending at the silicon surface in the dark state.

SPV provides a lower bound on the true dark-state band bending, because its magnitude is reduced by any surface recombination that occurs before full photo-flattening is achieved [223]. As a result, SPV magnitudes measured on samples with very different effective lifetimes cannot be directly compared for band-bending. At low effective lifetimes of 20 and 70 µs at 1×10^{15} cm^{-3} ECD (Figure 6.1, Samples 1 and 2), SPV magnitudes underestimate the true dark-state band bending in both cases. The 3.5 × difference in lifetime between the two samples further biases any direct comparison. Comparing band-bending strength from the SPV magnitudes for these two samples is therefore not justified.

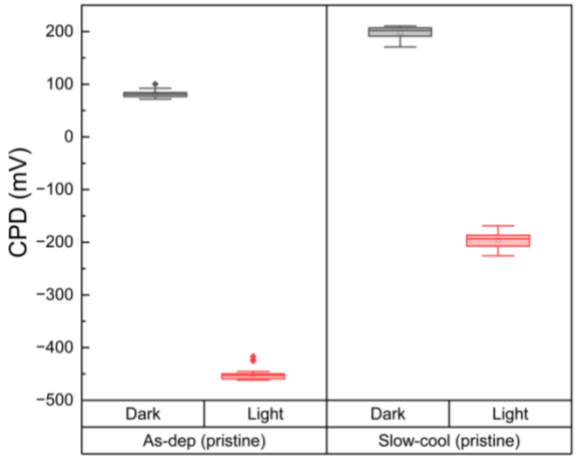


Figure 6.2 Box plot of the pristine Si/AZO (AlO_X has never been deposited) CPD values in four different conditions: as-deposited sample measured in dark and under illumination; slow-cooled sample measured in dark and under illumination. The 2D map of these two samples is shown in Appendix F, Figure A 89.

6.2.2 As-Deposited Si/AZO Samples With AlO_X Etching

To assess whether the AlO_X deposition and etching process itself modifies the SPV baseline, the same measurements were performed on samples that had undergone AlO_X capping and removal.

Figure 6.3 presents box-plot distributions of the dark and illuminated CPD values for the as-deposited Si/AZO sample (AlO_X etched before measurement). The dark-state CPD is −96.1 mV, and under illumination the CPD shifts to −300.1 mV. For this sample, the SPV is 204.0 mV.

The dark CPD value reflects the convolution of the Si and AZO work functions with surface dipoles, adsorbates, and contamination, and is not by itself a reliable probe of the band-bending direction [221]. The sign reversal of the dark CPD between the pristine Si/AZO sample of Section 6.2.1 (+81.5 mV) and the etched sample here (−96.1 mV) is therefore a consequence of the surface-dipole modification introduced by the alkaline etch.

A comparison with the as-deposited sample that underwent AlO_X deposition and etching (Section 6.2.1) reveals a baseline shift. The as-deposited Si/AZO sample shows a positive dark CPD (+81.5 mV) and a large SPV (531.9 mV), whereas the equivalent sample with AlO_X history shows a negative dark CPD (−96.1 mV) and a smaller SPV (204 mV). The ~ 180 mV shift in dark CPD between the two as-deposited configurations is attributed to surface dipole modifications introduced by the alkaline etch process, such as residual hydroxyl groups, etch residues, or restructured oxygen vacancy concentrations at the AZO surface [219, 335]. The Kelvin probe CPD is known to be

sensitive to ambient humidity and surface adsorbates, and since the KP measurements are performed ex situ in air after chemical etching, such surface modifications can introduce uncontrolled dipole layers that shift the vacuum level [336]. Absolute CPD values across samples with different surface-preparation histories therefore cannot be compared without a matched vacuum-level reference. The SPV itself is independent of the absolute vacuum-level calibration and therefore remains the robust cross-sample comparator of band-bending strength.

Table 6.1 summarises the KP-SPV results from Section 6.2.1-6.2.3 for cross-reference. Across all measured conditions, samples with an AlO_X deposition/etch history exhibit smaller SPV magnitudes (204–334 mV) than their pristine Si/AZO counterparts (394–532 mV), confirming the baseline shift imposed by the alkaline etch step.

Table 6.1 Sample preparation conditions and their KP-SPV results (CPD values are in mean ± standard deviation) in Section 6.2.1 - 6.2.3.

Section	Sample & AlO_X history	Anneal	CPD_{dark} (mV)	CPD_{light} (mV)	SPV (mV)
6.2.1	Si/AZO (pristine)	As-deposited	81.5 ± 6.5	−450.4 ± 12.0	531.9 ± 13.7
6.2.1	Si/AZO (pristine)	Slow-cooled	197.7 ± 11.6	−196.3 ± 15.1	394.0 ± 19.0
6.2.2	Si/AZO (etched)	As-deposited	−96.1 ± 5.1	−300.1 ± 10.3	204.0 ± 11.5
6.2.3	Si/AZO (etched)	Fast-cooled	−27.9 ± 7.3	−260.2 ± 17.8	232.3 ± 19.2
6.2.3	Si/AZO (etched)	Slow-cooled	−51.5 ± 16.0	−385.0 ± 14.5	333.5 ± 21.6

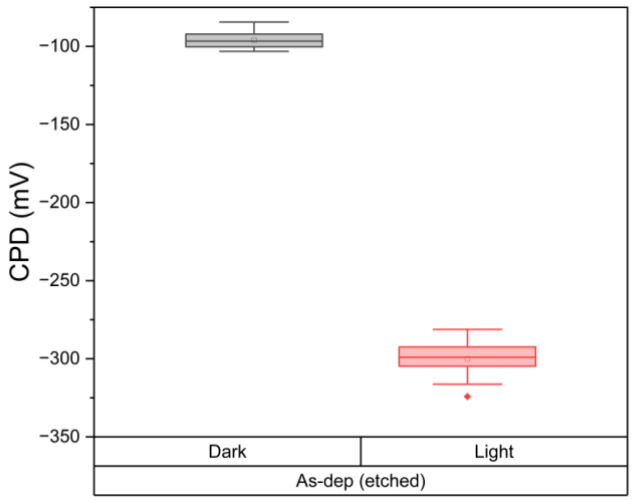


Figure 6.3 Box plot of the as-deposited Si/AZO (AlO_X etched before SPV measurements) CPD values in dark and under illumination. The 3D map of this sample is shown in Appendix F, Figure A 90.

6.2.3 Cooling Rate and Capping Layer Effects on Field Effect

SPV measurements were performed on Si/AZO/AlO_X samples that were annealed at 450 °C in air and subsequently cooled under either fast-cooling or slow-cooling protocols (AlO_X etched after annealing and before KP measurement). Figure 6.4 presents the corresponding box plot for the fast- and slow-cooled samples. The fast-cooled sample exhibits an SPV of 232.3 mV; the slow-cooled sample shows 333.5 mV.

In AZO, n-type conductivity arises primarily from two sources: substitutional Al^{3+} donors on Zn^{2+} sites, which provide one free electron per substitution, and ionised oxygen vacancies (V_o). The presence of these additional donors means that the doping efficiency calculated in Section 4.4.2, which attributes all carriers above the undoped-ZnO level to Al, is an upper estimate. In the ionised state, each V_o^{2+} releases up to two electrons into the conduction band while remaining as a doubly positive fixed charge in the lattice [142, 291]. Annealing AZO films at 400–500 °C in an oxidising atmosphere can fill oxygen vacancies by incorporating ambient oxygen, thereby reducing the number of ionised donors and the associated positive fixed charge [325].

The higher SPV value in the slow-cooled sample indicates that slow cooling increases the net *density* of the negative fixed charges at the interface. This likely reflects the dynamic evolution of point defects during the cooling process: slow cooling allows for more complete oxygen vacancy annihilation and the rearrangement of Al-related sites [261].

Oxygen diffusion in polycrystalline ZnO and AZO is dominated by grain-boundary transport, which is three to four orders of magnitude faster than bulk diffusion and allows exchange with ambient O_2 on the timescale of minutes at 450 °C [261, 337-339]. Over the 20-minute dwell at 450 °C the V_O population approaches its equilibrium concentration for that temperature in both the fast- and slow-cooled samples [340]. The V_O-filling differential between the two cooling protocols is therefore not set by time at 450 °C, where equilibrium is reached in both cases, but by the cooling trajectory itself. The equilibrium V_O concentration is a decreasing function of temperature: as the film cools in air, successive quasi-equilibrium V_O concentrations become progressively lower, and ambient O_2 can incorporate into the film to follow them provided the grain-boundary diffusion remains kinetically

active. Slow cooling keeps the film within the 300–450 °C window longer than fast cooling, allowing the V_O concentration to partially track its falling equilibrium value before kinetic freeze-out. Fast cooling instead quenches the 450 °C V_O concentration into the room-temperature film. This quench-versus-equilibration framing is the standard treatment of point-defect populations under variable cooling rate [341].

The resulting cooling-rate-dependent difference in V_O density is sub-monolayer in magnitude, consistent with the absence of a detectable shift in bulk Zn/O stoichiometry (Section 6.3.3) but sufficient to modulate the areal density of ionised donors near the Si/SiO_X interface probed by KP-SPV.

Since oxygen vacancies act as donors (contributing positive charge), their annihilation increases the net negative charge density. Within the framework of the Kronik–Shapira model [221], and given that both samples here share comparable effective lifetimes so that surface-recombination screening artefacts largely cancel, the larger SPV in the slow-cooled case is most simply interpreted as evidence of stronger upward band bending at the interface. This is in turn consistent with enhanced passivation under slow cooling, although the absolute magnitude of the band-bending difference cannot be quantified from SPV alone [342].

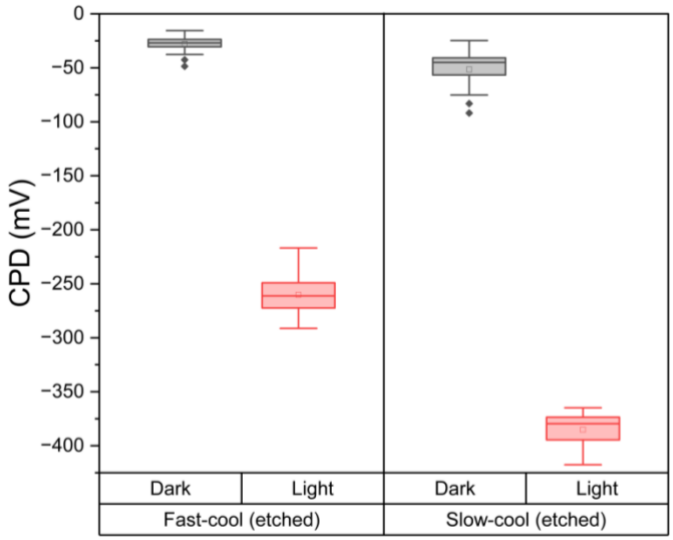


Figure 6.4 Box plot of the annealed Si/AZO/AlO_X (AlO_X etched after annealing and before SPV measurements) CPD values in four different conditions: fast-cooled sample measured in dark and under illumination; slow-cooled sample measured in dark and under illumination. The 2D map of these two samples is shown in Appendix F, Figure A 91.

6.3 Band Alignment Under Different Cooling Rates

While KP-SPV probes the surface potential, which reflects the cumulative electrostatic potential drop across the ~ 16 nm thick AZO film and into the silicon space-charge region, XPS provides access to the local electronic structure at the buried interface within its ~2–5 nm probing depth [343]. The XPS measurements in this section were acquired at the Versatile Soft X-ray (VERSOX) beamline B07 at Diamond Light Source (see Section 3.5.2). A synchrotron source was chosen over a laboratory Al Kα XPS instrument for superior energy resolution, tunable photon energy, and minimising radiation damage.

6.3.1 Band Bending and Valence Band Offset

I measured three representative samples with the model geometry Si/2 nm AZO/2 nm AlO_X (as-deposited, fast-cooled, slow-cooled). This thin stack (2 nm AZO / 2 nm AlO_X) geometry was selected to enable non-destructive probing of the Si/AZO interface.

Table 6.2 summarises their Zn $3p_{3/2}$ and Si $2p_{3/2}$ binding energies, together with the core-level energy difference ΔE_{CL} (Si – TCO) [344]. Within the Kraut framework, the 0.10 eV larger ΔE_{CL} of the slow-cooled sample (9.86 eV vs. 9.76 eV) translates to an approximately 0.10 eV reduction in the valence band offset at the Si/AZO interface, provided that the bulk Si 2p–valence band maximum (VBM) and Zn 3p–VBM core-level-to-valence-band separations are unchanged by the cooling regime. This assumption is supported by experimentally-demonstrated invariance of the Zn 3d/3p–VBM separation in ZnO and AZO under comparable post-deposition treatments [274, 345-347].

The absolute Si $2p_{3/2}$ binding energy provides a measure of the band bending at the silicon surface [335]. From the parameters established in Chapter 4, the valence band maximum of the 4 Ω·cm n-type silicon used here sits 0.86 eV below the Fermi level. Combined with the intrinsic Si $2p_{3/2}$-to-valence-band-maximum separation of 98.74 ± 0.05 eV [197, 348], the flat-band bulk reference binding energy is 99.60 eV.

For the 4 Ω·cm n-type silicon used here (N_D ~ 1.4 x 10^{15} cm^{-3}), the Si-side depletion width for a built-in potential of 0.4-0.5 eV is 500-700 nm, more than two orders of magnitude larger than the Si 2p

inelastic mean free path (~ 2-3 nm at ~ 1.4 keV). The measured Si 2p3/2 binding energy is therefore interpreted as a local probe of the band bending at the Si surface of the 2 nm model stack, rather than as a depth-weighted average within the Si space-charge region [347, 349, 350].

The 2 nm AZO overlayer, being both thin and degenerately doped, is not expected to sustain an appreciable space-charge region of its own; the band-bending magnitude extracted here is therefore specific to the 2 nm overlayer geometry and is used to rank the cooling-rate contrast within that geometry only [351].

The fast-cooled sample exhibits a Si $2p_{3/2}$ binding energy of 99.17 eV, which is ~ 0.49 eV lower than the flat-band value. This shift of the Si 2p core level to lower binding energy is consistent with upward band bending at the silicon surface [349]. The slow-cooled sample shows a binding energy of 99.61 eV, only ~ 0.05 eV below the flat-band reference, indicating that the silicon bands within the XPS probing volume approach flat-band conditions. The fast-cooled sample therefore preserves stronger upward band bending at the Si surface than the slow-cooled sample, as probed directly at the interface. This observation sits in apparent tension with the KP-SPV result in Section 6.2.3, which showed that the slow-cooled sample exhibits a larger SPV. This ultrathin geometry was used at the cost of an expected poorer effective lifetime than that of the device-relevant 16 nm stack. As a result, the absolute SPV-equivalent band bending extracted here should not be directly compared across geometries. The implications of this length-scale and lifetime asymmetry are discussed in Section 6.3.4.

In the AZO overlayer, the Zn $3p_{3/2}$ binding energy shifts from 89.40 eV (fast-cooled) to 89.75 eV (slow-cooled), a 0.35 eV increase. Within the Kraut framework, this shift reflects a combination of the common-mode band-alignment change evidenced by the Si 2p core level (0.44 eV) and a chemical shift associated with local V_O or Al-site rearrangement at the 2 nm interface (0.1 eV) [274, 352]. The latter originates from the TMA-doped sub-layer, where the Zn coordination environment is modified by V_O filling during slow cooling. Dynamic differential charging was excluded by the stability of sequential scans [353, 354]; a steady-state charging contribution cannot be completely excluded and is noted as a methodological limitation in Section 6.6 [355].

Table 6.2 XPS results on ΔE_{CL} (Si-TCO) of samples featuring Si/2nm AZO/2nm AlO_X. The fitting curves of the peaks are shown in Appendix B, Figure A 83.

Binding Energy (eV)	Zn $3p_{3/2}$	Si $2p_{3/2}$	ΔE_{CL} (Si-TCO)
As Deposited	89.40	99.10	9.70
Fast Cool	89.41	99.17	9.76
Slow Cool	89.75	99.61	9.86

6.3.2 In-situ Evolution of Si 2p Under Vacuum Annealing

The in-situ vacuum experiments presented here serve to test whether the thermal cycle alone, in the absence of atmospheric oxygen, is sufficient to modify the Si/AZO band bending. A negative result would support the interpretation (Section 6.2.3) that atmospheric oxygen is required for the cooling-rate-dependent V_O annihilation proposed as the field-effect mechanism.

To follow the band evolution during the thermal cycle, in-situ XPS was conducted, and the Si $2p_{3/2}$ binding energy was tracked during heating and cooling under vacuum. The measurements were conducted at the B07 beamline using hv ≈ 1.8 keV, with the sample mounted on the in-situ heating stage under vacuum. As shown in Figure 6.5, both the AlO_X-capped stack and the uncapped AZO reference exhibit a pronounced drop in Si $2p_{3/2}$ binding energy upon heating to 500 °C, from ~ 99.6 eV at room temperature to ~ 99.22 eV for the capped stack and ~99.10 eV for the uncapped AZO reference. This drop to lower binding energies indicates an increase in the upward band bending at the Si surface. The combination of high temperature and an oxygen-free vacuum environment drives thermal reduction and oxygen desorption within the 2 nm ultrathin AZO film [261], disrupting the stable interfacial bonding configuration established during deposition, and thereby altering the magnitude of the interfacial dipole [219]. Consequently, the local electrostatic potential shifts, pushing the Si energy bands further upward relative to the Fermi level [142].

The difference in the high-temperature Si $2p_{3/2}$ minimum between the capped and uncapped samples (99.22 eV vs. 99.10 eV) indicates that the AlO_X cap partially limits the extent of thermal reduction experienced by the underlying AZO under vacuum, acting as a diffusion barrier that mitigates oxygen out-gassing from the AZO surface.

During the subsequent vacuum cool-down to ~ 100 °C, the Si $2p_{3/2}$ binding energy of both samples only partially recovers to < 99.40 eV, remaining below the ex-situ air-annealed slow-cooled value of ~99.61 eV (Table 6.2), which was cooled down to ~ 200 °C and taken off the hotplate to measure. This observation is consistent with the mechanism proposed in Section 6.2.3: the field-effect enhancement observed under air annealing requires ambient oxygen in-diffusion to drive V_O annihilation.

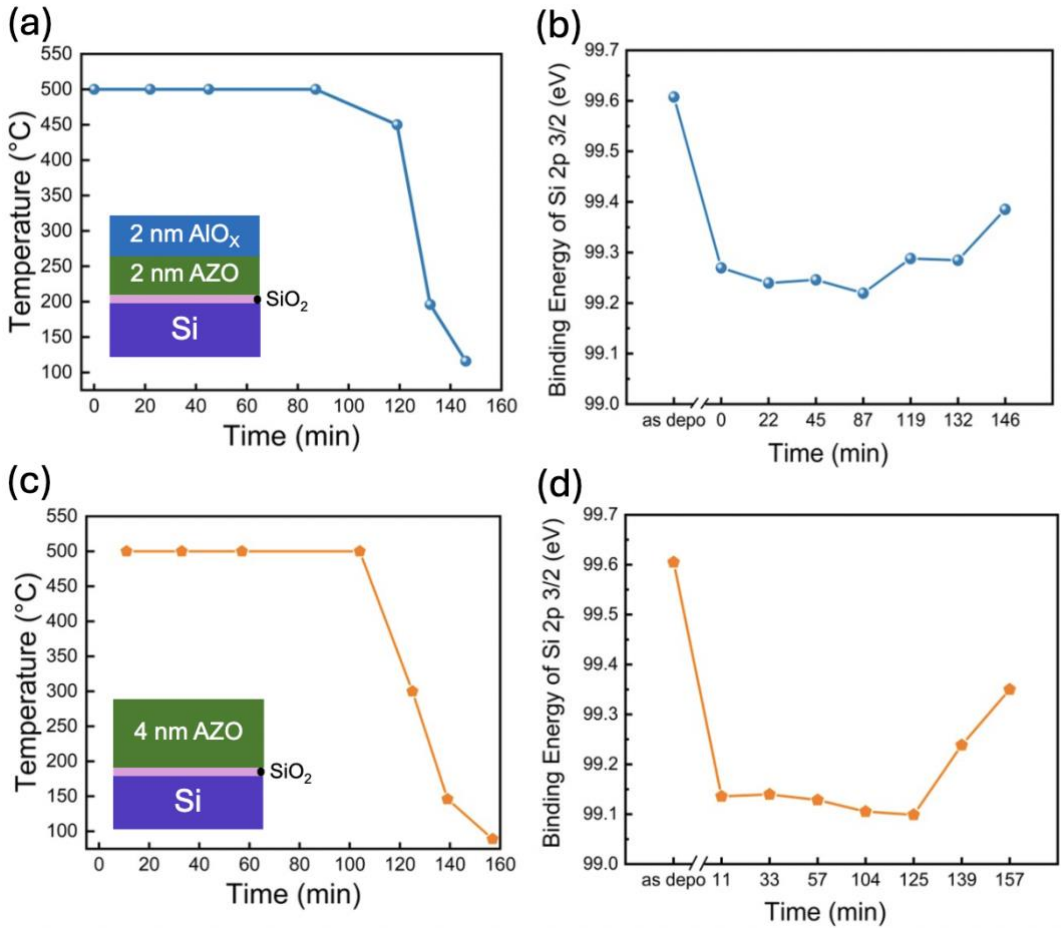


Figure 6.5 In-situ XPS of (a)-(b) with AlO_X capping layer/standard AZO stacks; (c)-(d) AZO samples without AlO_X capping layer. (a) and (c) show the temperature profiles during in-situ measurements; (b) and (d) show the Si $2p_{3/2}$ binding energy changes in accordance with in-situ annealing and cooling. Samples were in the configuration of Si/2nm AZO/2nm AlO_X, or Si/4nm AZO.

6.3.3 Bulk AZO Stoichiometry After Annealing

To verify whether the cooling rate alters the bulk chemical composition of the AZO layer, thicker samples (Si/16 nm AZO/26 nm AlO_X) were annealed ex situ in air under slow- and fast-cooling conditions. The AlO_X capping layer was then chemically removed to expose the AZO surface, and the samples were transferred to the XPS system for analysis. The extracted Zn $3p_{3/2}$ and O 1s (lattice) peak areas are summarised in Table 6.3.

The Zn $3p_{3/2}$ /O 1s (lattice) ratios are 2.48 for the fast-cooled sample and 2.46 for the slow-cooled sample. Monte-Carlo propagation of the peak-fitting procedure yields an uncertainty of approximately 0.02 on these ratios [356]; the lattice stoichiometry of the 16 nm AZO within the top few nm is therefore indistinguishable between the two cooling regimes within the XPS peak-fitting uncertainty.

In the 2 nm film, the bulk-to-interface ratio of AZO is significantly lower than that of the 16 nm film. For the XPS measurements in Section 6.3.1 (Table 6.2), the core level signal contribution originates primarily from Zn atoms near the interface [219, 357]. Under slow cooling, the chemical environment of these atoms is altered due to interfacial reactions with SiO_X (such as the formation of Zn–O–Si bonds) [274]. However, the XPS measurements on a 16 nm AZO film (which probe the top surface after the AlO_X layer is etched) do not capture this interfacial chemistry, which is likely why the Zn 3p/O 1s ratio remains unchanged.

Table 6.3 XPS results on Zn $3p_{3/2}$/O 1s Lattice between fast-cooled and slow-cooled samples. Samples were made with the configuration of Si/16nm AZO/26nm AlO_X, annealed, and then etched off the AlO_X capping layer, leaving Si/annealed AZO. The fitting curves of the peaks are shown in Appendix B, Figure A 84.

Peak Area	Zn $3p_{3/2}$	O 1s Lattice	Zn $3p_{3/2}$/O 1s Lattice
Fast Cool	4264	1719	2.48
Slow Cool	4284	1743	2.46

6.3.4 Reconciling the Band-Bending Discrepancy Across Geometries

KP-SPV and XPS give opposite cooling-rate contrasts: slow cooling produces the larger SPV in the 16 nm stack (333.5 vs. 232.3 mV), but the slow-cooled 2 nm stack approaches flat-band (Si $2p_{3/2}$ shift ≈ 0.05 eV) while the fast-cooled 2 nm stack retains a 0.49 eV upward shift. Resolving this apparent contradiction requires separating two issues: the absolute magnitude difference between the two geometries and the sign reversal of the cooling-rate contrast.

The magnitude difference is reconciled first. Band bending in the silicon is governed by the effective areal charge density (Q_{eff}) delivered to the Si/SiO_X interface. For AZO with carrier concentration in the 10^{19}–10^{20} cm^{-3} range, the Thomas–Fermi screening length is λ_{TF} ≈ 0.5–2 nm [85, 351, 358], so the 2 nm AZO film couples only a fraction of its volumetric charge to Si, whereas the 16 nm film

delivers its full integrated charge density. For identical interfacial dipoles and identical interface state densities, the 2 nm stack therefore produces weaker Si-side bending than the 16 nm stack.

The sign reversal cannot be explained by a single charge population scaling with AZO thickness. It instead reflects the competition between two cooling-rate-dependent processes that act in opposite directions on Q_{eff}, whose relative weights depend on the sample geometry. The first is V_O annihilation in the AZO bulk by ambient O2, which removes positive fixed charge and enhances upward bending (Section 6.2.3). The second is hydrogen-mediated passivation of acceptor-type interface states at Si/SiO_X, including P_b-family dangling bonds and related acceptor-like defects [308, 359]. In n-type silicon, these states sit in the upper half of the bandgap and are filled with electrons, so their passivation removes negative charge and relaxes the bands toward flat-band [360, 361]. Their identification is discussed further in Section 6.4.

A key asymmetry between the two measurement geometries is that the 2 nm XPS samples retain the AlO_X cap, whereas the 16 nm KP-SPV samples have the cap etched after annealing. In the 16 nm AZO stack, the bulk V_O annihilation term dominates under slow cooling, and the net effect is enhanced upward bending, consistent with the observed SPV increase. In the 2 nm stack, the retained AlO_X cap would, in isolation, further enhance bending via its own V_O annihilation, but the total 4 nm AlO_X+AZO volume is too thin for this positive-charge removal to offset the efficient P_b passivation at the Si/SiO_X interface. The P_b term therefore dominates under slow cooling, pulling the 2 nm stack toward flat-band and inverting the observed contrast.

One caveat must be acknowledged alongside this mechanistic picture. In the 2 nm geometry, a steady-state photoemission-induced charging offset of order 0.1–0.5 eV on the AlO_X cap cannot be fully excluded. V_O annihilation during slow cooling closes defect-mediated conduction paths through the AlO_X and reduces its leakage conductance [362], thereby elevating the steady-state surface potential under the X-ray beam and uniformly shifting all overlayer photoemission peaks toward higher binding energy [363]. This artefact quantitatively mimics a real cooling-rate-dependent Si 2p shift, which can be disambiguated by Auger-parameter referencing [354]. A direct resolution would be Hard X-ray Photoelectron Spectroscopy (HAXPES, Ga Kα, hν ≈ 9.25 keV; IMFP ~ 10–15 nm for

Si 2p), which would test whether the Si 2p cooling-rate contrast truly inverts sign between 2 nm and 16 nm AZO [364-366].

6.4 Decoupling of Passivation Mechanisms

The key diagnostic capability of transient-SPV (detailed in Section 3.6.3) lies in its ability to distinguish between field-effect and chemical passivation through four independent signatures: (i) the sub-bandgap photon response, which reveals the energy distribution of interface defect states; (ii) de-trapping features in the decay curves, which probe shallow trap states near the band edges; (iii) the ultimate decay timescale, which reveals whether the lifetime is limited by interface or by bulk recombination; and (iv) the peak amplitude SPV_{max} captured at the nanosecond-scale rise, which measures the dark-state band bending. A transition from interface-limited to bulk-limited dynamics, accompanied by the loss of the sub-bandgap response and of the de-trapping features described below, constitutes strong combined evidence that the density of recombination-active interface defects has been substantially reduced, i.e. that chemical passivation has been achieved [222].

6.4.1 Sub-Bandgap Response and Relaxation Dynamics

Figure 6.6 presents the contour plots of the transient-SPV signal as functions of photon energy and time for the four samples.

All four samples exhibit measurable positive SPV responses at photon energies below the 1.1 eV silicon bandgap [222]. Since sub-bandgap photons cannot excite band-to-band transitions, this response provides direct evidence of charge excitation from localised defect states within the bandgap [221, 222]. In the as-deposited AZO/AlO_X sample (Sample 3), a narrow defect response band is centred near ~0.98 eV. After annealing (Sample 4), this deep-defect response is largely removed and replaced by a continuous distribution closer to the 1.1 eV band edge, indicating passivation (or substantial suppression) of the most recombination-active deep-level defects [367].

Three classes of defect species are accessible to sub-bandgap SPV in Si/ZnO systems at this photon energy. Oxygen vacancies (V_O) in ZnO/AZO have reported deep-donor transition levels 0.9-1.3 eV below the ZnO conduction-band minimum [142, 368]. Zn interstitials and Zn anti-sites act as

shallow-to-mid-gap donors at ~ 0.05-0.5 eV below the ZnO conduction band [369]. P_b-type silicon dangling bonds (•Si≡Si_3) at the Si/SiO_X interface, in the Poindexter-Lenahan notation, have an acceptor-like (0/-) transition level at E_C - 0.25 to E_C - 0.30 eV and a donor-like (+/0) level near E_V + 0.3 eV on n-type Si/SiO_X [308, 359, 360].

The observed ~ 0.98 eV response lies ~ 0.14 eV below the Si band edge at 300 K. This energy does not uniquely identify a single species: it is compatible with excitation from shallow donor-like interfacial states into the Si conduction band, from the Si valence band into acceptor-like P_{b0} (0/−) states (~ 0.82–0.87 eV, slightly lower than observed 0.98 eV), or from sub-bandgap states of ZnO origin near the AZO band edge. The ~ 0.1 eV offset lies within the intrinsic distribution width reported for P_b centres and within the spectrometer resolution (~50 meV) [234, 370], so a unique species assignment from photon energy alone is not possible.

However, the response of the sub-bandgap signal to the AlO_X-mediated anneal is itself chemically selective. Of the three candidate populations, only Si-side P_b dangling bonds react stoichiometrically with atomic hydrogen via the $P_b + H^0 \rightarrow P_bH$ reaction and are effectively suppressed at 450 °C [308, 371, 372]; ZnO-side V_O and Zn-interstitial donors are compensated rather than passivated by hydrogen and show only weak annealing sensitivity in this temperature range [142, 292, 369]. The near-complete disappearance of the sub-bandgap response upon annealing with the AlO_X cap therefore selectively fingerprints the H-passivatable subset of the candidate defect population, and is most consistent with hydrogen-mediated passivation of interfacial dangling bonds. This channel operates in parallel with the V_O-related mechanisms of Sections 6.2.3: the two pathways affect different defect populations and are not mutually exclusive.

Hydrogen is identified as the most plausible agent for three independent reasons: (i) the AlO_X cap is an established interstitial hydrogen reservoir with well-calibrated release kinetics [45, 168, 234]; (ii) the NR data of Section 5.6 directly show reduced hydrogen content in the AlO_X reservoir upon annealing, consistent with H release into the stack; and (iii) the ToF-SIMS data in Section 6.5 independently detect an annealing-induced shift of the interfacial $^{29}SiH^-/^{29}SiHO^-$ ratio towards Si–H termination, which is the diagnostic chemical signature of the $P_b + H^0 \rightarrow P_bH$ reaction [371, 372]. V_O

annihilation in the AZO during oxidative annealing and densification of the SiO_X interlayer may also contribute and are not mutually exclusive with the hydrogen mechanism.

The $P_b + H^0 \rightarrow P_bH$ reaction assumes neutral atomic hydrogen at the Si dangling bond. In the surrounding oxides, however, hydrogen is predicted to be predominantly ionised: in polycrystalline ZnO and AZO, interstitial H acts as a shallow donor (H^+) [135, 142, 254]. The conversion from ionised to neutral H at the Si/SiO_X interface requires electron transfer enabled by the proximity of the Si valence band, and the neutral-H fraction is known to rise sharply with temperature at this interface [18, 373-376]. A full quantitative treatment of the H-charge-state balance across the $AlO_X/AZO/SiO_X/Si$ stack is beyond the scope of this chapter.

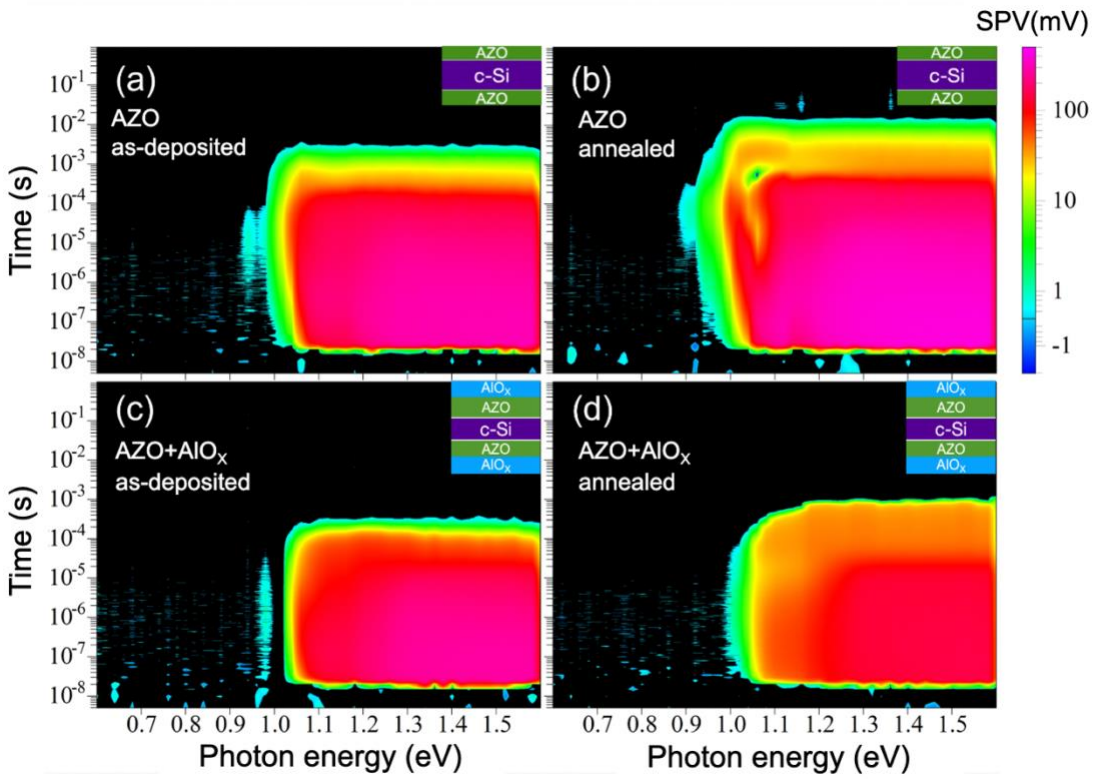


Figure 6.6 Contour plots of the transient SPV signal as a function of photon energy (vertical axis) and delay time after the laser pulse (horizontal axis) for the four AZO samples. (a)-(d): Sample 1-4 in Figure 6.1. The colour scale encodes the SPV amplitude in mV on a logarithmic scale, with warm colours (pink-red-yellow) representing the largest positive SPV amplitudes and cool colours (green-blue) representing smaller positive amplitudes. Black pixels correspond to signals at or below the instrument noise floor (|SPV| < ~1 mV).

6.4.2 Decoupling Field-Effect and Chemical Passivation via Transient Kinetics

Figure 6.7 shows transient-SPV line-cuts extracted from Figure 6.6 at five representative photon energies for the four samples: 0.98 eV and 1.02 eV (sub-bandgap, probing deep defect states), 1.10 eV (near the Si band edge), and 1.28 eV and 1.50 eV (above-bandgap, probing the field-effect

response). The vertical reference line marks the ~ 5 μs electron diffusion time across the 675 μm silicon substrate.

Four comparative observations drive the mechanistic interpretation.

First, panels (a) and (b) (AZO-only, as-deposited and slow-cooled) at 1.02 eV and 1.10 eV show distinct local minima and maxima in the decay slopes, which are the spectral-temporal fingerprints of de-trapping from at least two populations of deep defect states; these features persist across both AZO-only samples regardless of thermal history [222].

Second, the 1.02 eV sub-bandgap response appears prominently only in panel (b): it is marginal in (a) and essentially absent in both AlO_X-capped samples (c) and (d). The AlO_X cap therefore acts not by removing a pre-existing deep-defect response, but by preventing its thermal activation: in the absence of AlO_X, annealing at 450 °C creates or reveals a deep-level state that the AlO_X-capped samples never develop. In parallel, the de-trapping inflections of shallow band-edge trap states are also attenuated in (c, d) relative to (a, b). This is most visible in the 1.10 eV trace (green), which exhibits a shoulder near ~10^{-5} s and a secondary plateau near ~ 2×10^{-4} s in (a) and (b) but decays essentially monotonically in (c).

Third, comparing (c) and (d) (as-deposited vs. annealed AZO/AlO_X) at 1.28 eV and 1.50 eV shows that only the annealed stack sustains a plateau beyond the ~5 μs diffusion timescale. The diagnostic here is the shape of the decay, not the absolute amplitude: Samples 1–3 all retain non-zero SPV at 10^{-4} s, but they are in the downward-sloping middle of their decay, while Sample 4 is still on a near-constant plateau that extends out to ~ 5×10^{-4} s before dropping through a distinct knee near 10^{-3} s. The order of magnitude of this knee matches the 2 ms bulk lifetime measured independently by QSSPC (Figure 6.1). The coexistence of the plateau and the bulk-timescale knee is the diagnostic fingerprint of a transition from surface-recombination-limited to bulk-lifetime-limited relaxation [221, 222].

Fourth, the comparison of (a) and (c) isolates the effect of the AlO_X deposition without thermal activation: the kinetics at 1.28 eV and 1.50 eV and the de-trapping inflections at 1.10 eV are closely similar between Sample 1 and Sample 3, despite the presence of the ~26 nm AlO_X cap in Sample 3.

The AlO_X layer therefore does not deliver appreciable hydrogen to the Si/SiO_X interface in the absence of the thermal cycle, consistent with the Dingemans–Kessels framework in which H release from AlO_X is thermally activated above ~350 °C [234, 307].

Collectively, the a → b → c → d progression maps onto a sequence of physical states: deep-trap-dominated recombination (a, b), deep-trap suppression without bulk-limited kinetics (c), and fully chemically-passivated bulk-limited relaxation (d) [222].

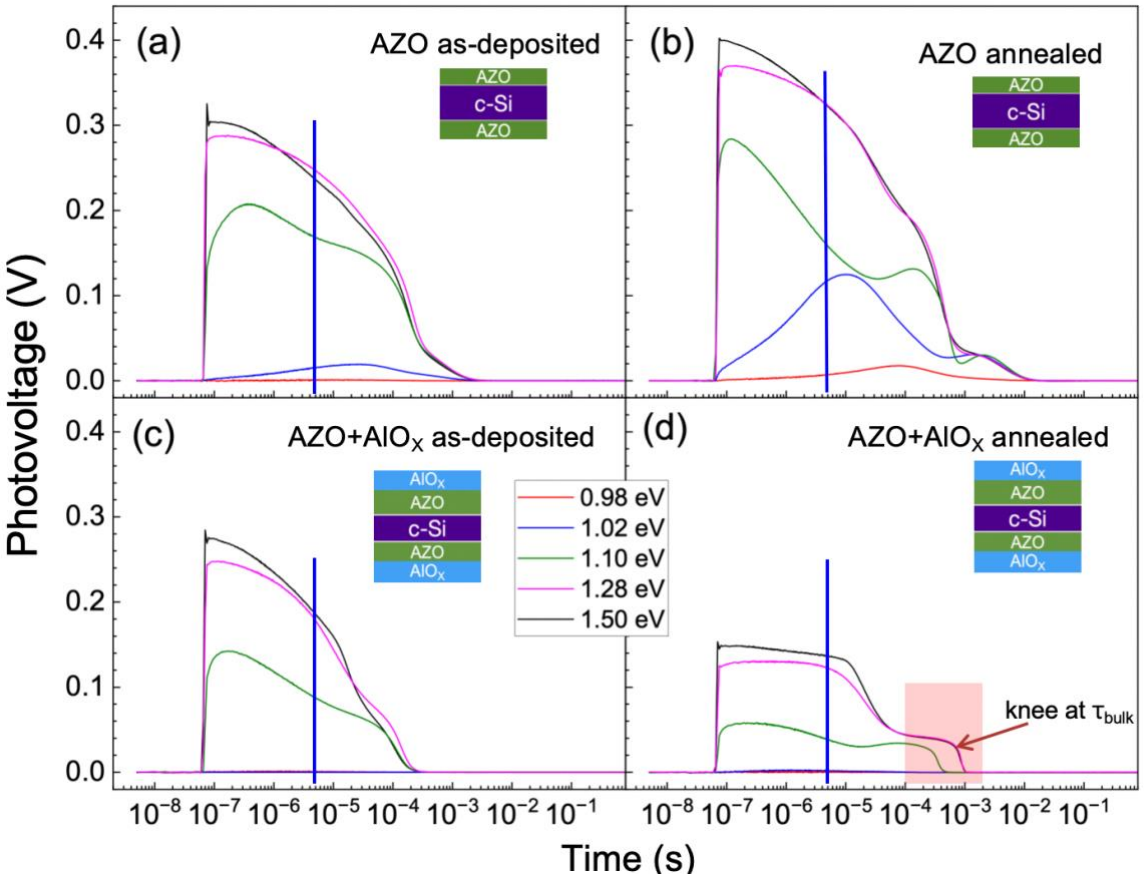


Figure 6.7 Transient SPV line-cuts extracted from Figure 6.6 at five representative photon energies for the four samples. (a)-(d): Sample 1-4 in Figure 6.1. The vertical blue reference line marks the electron diffusion time across the 675 µm silicon substrate (~5 µs). In (d), the pink shaded region (~ 10^{-4} to ~ 2×10^{-3} s) highlights the bulk-limited regime in which Sample 4 sustains a near-constant plateau long after Samples 1–3 have entered their decay; the red arrow marks the decay knee near ~ 10^{-3} s, whose order of magnitude matches the 2 ms bulk lifetime measured independently by QSSPC.

6.4.3 Reading Field-Effect Strength from SPV_{max}

Unlike the quasi-steady-state KP-SPV of Section 6.2, in which the surface potential is sampled after photogeneration and recombination have reached dynamic balance, SPV_{max} in Figure 6.7 is captured at the nanosecond-scale peak of the transient response. Because the observed rise time (~ 100 ns) is more than two orders of magnitude shorter than the surface-recombination time even in the

shortest-lifetime sample (~ 20 µs at 1×10^{15} cm^{-3} ECD in Sample 1), carrier losses during the build-up are negligible, and SPV_{max} provides a close approximation to the dark-state band bending $|\emptyset_{s,dark}|$ across all four samples. The field-effect strength can therefore be read directly from the figure.

Samples 1–3 all reach comparable SPV_{max} of ~ 0.28–0.40 V, indicating a similar dark-state band bending despite their spread in effective lifetimes. The fact that samples with very different recombination rates converge on similar SPV_{max} confirms that the rise-time-limited amplitude is decoupled from the decay dynamics. Sample 4, by contrast, drops to ~ 0.15 V. Because SPV_{max} is set at the rise rather than at the decay, this ~ 50% reduction is a genuine decrease in $|\emptyset_{s,dark}|$ rather than a lifetime artefact, and is attributed to chemical passivation itself. In n-type silicon, acceptor-type Si/SiO_X interface states sit in the upper half of the bandgap and are filled with electrons, contributing a pinning-like negative sheet charge to the interfacial electrostatics. H release from the AlO_X cap passivates these states, removing the associated negative charge and allowing the bands to relax partially toward flat-band. The fall in SPV_{max} from Sample 3 to Sample 4 is therefore a fourth independent signature of chemical passivation, complementing the loss of the 0.98 eV response, the elimination of de-trapping, and the emergence of the bulk-limited plateau-and-knee shape.

The apparent tension with Section 6.2.3 (slow-cooled > fast-cooled > as-deposited in KP-SPV values) does not imply a contradiction, because the two datasets probe different comparison pairs. The KP-SPV is confined to the slow- vs. fast-cooled pair. The as-deposited sample is excluded there because its short effective lifetime suppresses the steady-state SPV below $|\emptyset_{s,dark}|$, whereas Figure 6.7 contrasts as-deposited with slow-cooled using the nanosecond rise amplitude, which is not subject to this lifetime bias. The absolute SPV magnitudes of the slow-cooled sample remain on the same order of magnitude across the two techniques (~333 mV vs. ~150 mV), with the residual difference attributable to the etched vs. retained AlO_X geometry, which alters the surface chemistry and Kelvin-probe coupling but does not itself create additional band bending.

Physically, the V_O-annihilation mechanism in Section 6.2.3 (slow cooling → loss of positive fixed charge in the AZO → enhanced upward bending) and the H-mediated P_b-passivation mechanism identified here (annealing → H reaches the Si/SiO_X interface → acceptor-type states are emptied → partial relaxation toward flat-band) operate simultaneously in every annealed sample; what differs

between comparison pairs is which mechanism dominates. In the slow- vs. fast-cooled pair, the P_b-passivation contribution is similar (both reach 450 °C with the same cap) and the V_O difference dominates. In the as-deposited vs. slow-cooled pair of Figure 6.7, the P_b contribution differs strongly and dominates the net SPV_{max} trend. The two datasets therefore probe complementary faces of the same combined mechanism, consistent with the Si–O–H → Si–H rebalancing, sub-bandgap response disappearance, and loss of de-trapping features reported elsewhere in this chapter.

A complementary view, SPV as a function of photon energy at fixed time delays from 20 ns to 2 ms, is provided in Appendix F (Figure A 92) and confirms the same three features: a persistent sub-bandgap tail in the AZO-only samples that is strongly suppressed in Sample 4, early-decay behaviour dominated by carrier diffusion from a well-passivated surface, and a clean return to baseline at 2 ms in Sample 4 diagnostic of blocked de-trapping channels.

6.5 Chemical Origin of Interface Passivation

The transient-SPV data established that chemical passivation, the elimination of deep interface defect states, is a necessary component of the passivation mechanism. This component is activated only by annealing the AZO stack in the presence of the AlO_X cap. This section uses ToF-SIMS to identify the hydrogen-related chemical processes responsible. All the samples measured in ToF-SIMS follow the sample configuration of Sample 3 or 4 (Si/AZO/AlO_X) in Figure 6.1.

In ToF-SIMS depth profiling, the primary-beam-induced knock-on effect redistributes light atoms such as hydrogen into the underlying substrate, producing an artificial tail in the deeper silicon region and limiting the absolute spatial accuracy of the H^- profile to ~1–2 nm [377, 378]. The absolute width and centroid position of the H^- distribution should therefore not be over-interpreted as a direct measurement of hydrogen distribution on the sub-nanometre scale.

Before presenting the hydrogen data, three features of the ToF-SIMS protocol used here support the conclusions drawn in the following sections. First, all profiles were acquired in dual-beam mode using Cs^+ sputtering and Bi^+ analysis at a chamber pressure below 2×10^{-9} mbar, in line with the recommendations of Zhu et al. [378] for minimising the ambient H^- background. Second, all sample

pairs (as-deposited versus annealed) were profiled under identical primary-beam conditions within the same session, so that any residual knock-on broadening or instrumental drift affects both profiles equivalently and cancels in the relative comparison. Third, wherever a quantitative conclusion is drawn, we rely on the ratio of two same-matrix fragments (e.g., $^{29}SiH^-/^{29}SiHO^-$, Section 6.5.3) rather than on absolute intensities, which largely suppresses the well-known matrix effect in ToF-SIMS [379, 380]. These measures ensure that the trends reported below, spatial redistribution of H^-, emergence of an interfacial AlH^- signal, and the shift of the $^{29}SiH^-/^{29}SiHO^-$ ratio, reflect chemical changes at the Si/AZO interface rather than measurement artefacts [381].

Bulk AZO and AlO_X matrix ion yields (Al^-, $^{68}ZnO^-$) and their oxide fragment ratios ($Al_2O_3^-$, $Al_2O_3^-/AlO^-$, ZnO_2^-/ZnO^-) remain unchanged upon annealing within experimental scatter (Appendix G, Figure A 93 and Figure A 94), indicating that thermal interdiffusion or phase degradation at the scale resolvable by ToF-SIMS does not play a dominant role in the passivation changes reported here [382]. Sub-monolayer interfacial modifications below the XPS/ToF-SIMS detection limit cannot be excluded and are addressed by the hydrogen-specific fragments below.

For hydrogen-related secondary ions, due to the inherent mass interference between $^{28}SiH^-$ and the $^{29}Si^-$ isotope at nominal m/z = 29, the $^{29}SiH^-$ signal was monitored instead. Correspondingly, $^{29}SiHO^-$ was also tracked for consistency. These species serve as interference-free proxies for investigating Si–H bond formation at the interface [383].

6.5.1 Hydrogen Migration Towards the Interface

Figure 6.8 presents the full-stack depth profile of the H^- secondary ion intensity. Comparing the as-deposited (blue) and annealed (orange) profiles, the AlO_X capping layer region (−25 nm to approximately −16 nm) shows a decrease in H^- intensity after annealing, consistent with the hydrogen loss identified by NR. Within the AZO, the two profiles cross at approximately −8 nm: the annealed profile lies below the as-deposited one in the upper half of the layer and above it in the lower half, nearer the silicon. The depletion above the crossover and the enrichment below it are comparable in magnitude, so the hydrogen integrated over the AZO is approximately unchanged, indicating that the anneal redistributes hydrogen within the layer rather than adding to it. The NR

data of Section 5.6 were acquired on samples annealed at 500 °C and show a small hydrogen gain in the AZO under that condition; at the 450 °C used here, the integrated AZO signal is unchanged, and both datasets agree that the AZO does not act as the final destination of the hydrogen released from the cap. It is also consistent with the $ZnOH^-$ profile of Section 6.5.2, and it implies the direction of transport: hydrogen in AZO migrates from the top towards the Si/AZO interface. At the interface itself (near 0 nm) the as-deposited and annealed peaks are the same within the noise, so this displacement is not resolved as a gain in the interfacial H^- signal; the chemical form of the hydrogen there is examined below [288].

Post-anneal densification of the stack acts on the depth calibration in the same direction, but the two profiles are aligned on the Si^- half-peak centroid, so this contribution is smallest in the region near the interface where the enrichment is observed.

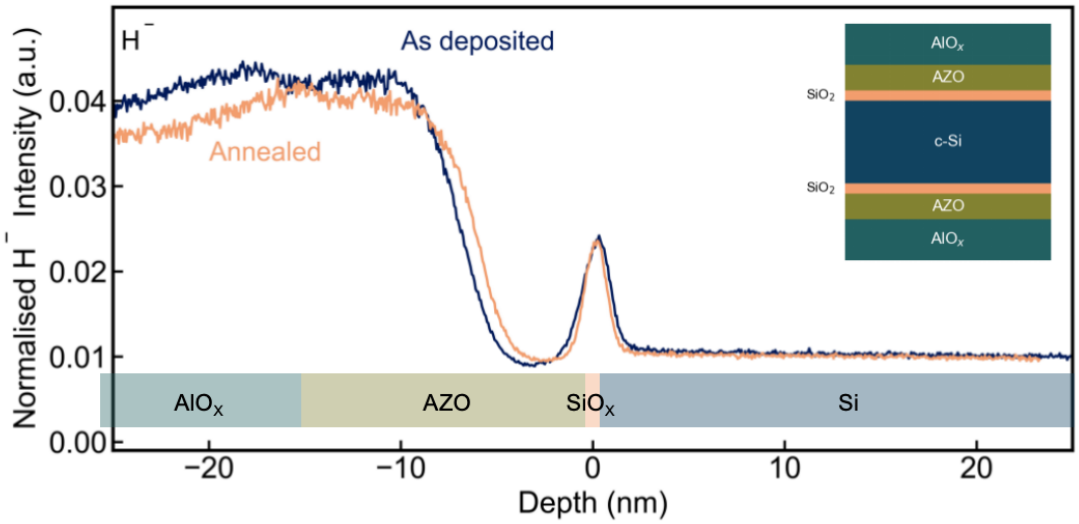


Figure 6.8 ToF-SIMS results showing H- intensity between as-deposited (blue) and annealed (orange) standard 16nm AZO/26nm AlO_X samples. The depth axis 0 nm is defined by the Si^- half peak centroid.

To evaluate the spatial distribution of hydrogen at the interface more precisely, Figure 6.9 aligns the H^- profile with the SiO^- fragment, which represents the interfacial oxide framework. In the as-deposited state (Figure 6.9 (a)), the H^- distribution is broad and its leading edge is spatially offset from the SiO^- peak. After annealing (Figure 6.9 (b)), the H^- profile closely follows the SiO^- signal.

The sputtering yield may also differ between thermally treated samples. Interface densification changes the local atomic density, which alters the sputtering rate and shifts the apparent depth scale [384, 385]. Rigorous depth-scale comparison between samples with different interfacial densities

requires calibration of the sputter rate for each sample. However, the XRR data in Section 5.5.1 show that, relative to the as-deposited states, the densities of AlO_X after annealing increase by 6.9%. While this density change suggests that any resultant depth-scale shift remains within the experimental uncertainty of the profilometry calibration (~ 5-10%), it should be noted that this represents a first-order approximation [201, 381]. For a more rigorous quantitative comparison, sample-specific calibration of the sputtering rate would be required to fully account for these interfacial density variations.

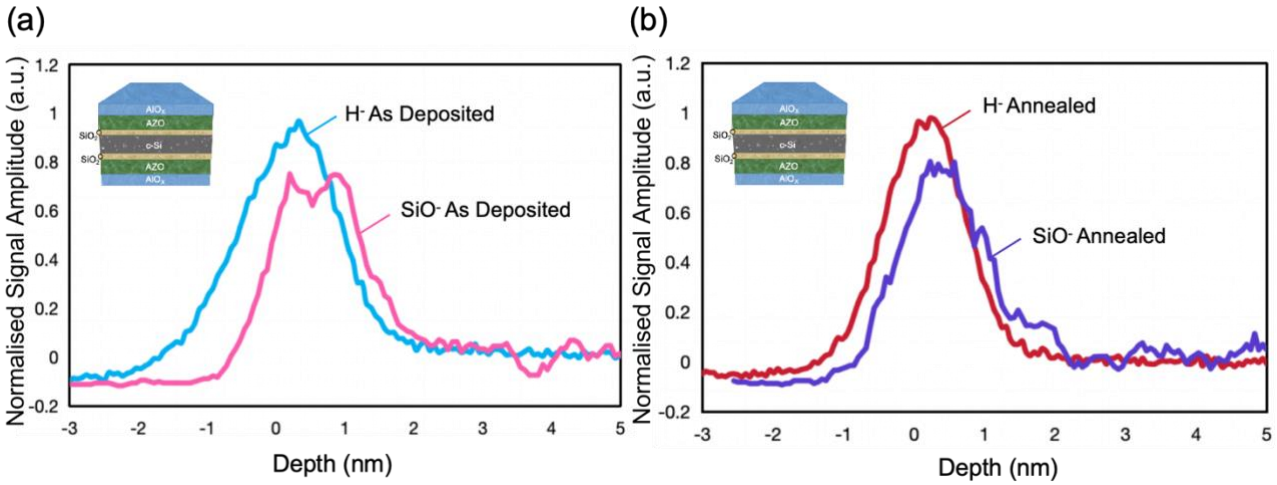


Figure 6.9 ToF-SIMS results showing (a) as-deposited and (b) annealed H- and SiO- signal amplitude of standard AZO/AlO_X samples. Data were smoothed using a 10-point moving average.

6.5.2 Chemical Bonding State of Interfacial Hydrogen

The analysis in Section 6.5.1 established that hydrogen redistributes spatially towards the Si/AZO interface upon annealing, but the chemical form in which it resides there, for example, as an Si–H bond, as part of a hydroxyl group, or associated with Al or Zn cations, cannot be determined from the H^- signal alone. To investigate this chemical form, Figure 6.10 tracks the depth distributions of several hydrogen-related cluster ion fragments. The OH^- fragment (Figure 6.10 (a)), which represents the overall degree of hydration and hydroxylation, shows a clear decrease in signal intensity across both the AlO_X capping layer and the AZO layer after annealing. This indicates that the thermal process removed loosely bound water and weakly associated hydroxyl groups [261].

Within the AZO layer, Figure 6.10 (b) shows the $ZnOH^-$ cluster distribution. This signal also decreases after annealing, indicating that the spatial proximity and chemical association between Zn

and hydrogen- or oxygen-containing groups within the AZO bulk have been weakened. Polyatomic clusters detected by ToF-SIMS may originate either from the direct fragmentation of pre-existing chemical bonds or from the recombination of sputtered atoms within the plasma plume above the surface [381, 382]. While a definitive assignment to lattice Zn–O–H bond breaking is not possible, the relative reduction in $ZnOH^-$ signal indicates that hydrogen migrating from the capping layer does not build up as a bulk reservoir within the AZO, consistent with the H^- profile of Section 6.5.1.

The $AlOH^-$ fragment (Figure 6.10 (c)) exhibits the expected signal decrease in the AlO_X cap region after annealing. However, in the AZO region, the annealed profile shows a broadening and overall increase. Since AZO contains aluminium dopants, this enrichment may indicate that hydrogen diffusing through the AZO lattice interacts with Al sites, or alternatively that pre-existing Al-OH species are redistributed during annealing [234]. At the Si/AZO interface itself (~0 nm), however, the $AlOH^-$ peak remains unchanged, implying that although Al dopants may facilitate hydrogen transport through the AZO layer, the interface does not favour hydrogen storage in hydroxylated (–OH) form.

Figure 6.10 (d) reveals the alternative chemical state. The AlH^- signal at the Si/AZO interface (0 nm) shows a pronounced spike in the annealed sample, approximately double the as-deposited intensity. The AlH^- signal in ToF-SIMS can arise from two distinct origins: (i) pre-existing Al–H bonds in the sample that are sputtered intact or as AlH cluster ions, and (ii) gas-phase recombination of independently sputtered Al and H atoms within the ion plume above the surface. An increase in local H concentration at the interface upon annealing would increase the probability of (ii) even if no new Al–H bonds have formed in the solid. Distinguishing between these two origins is not possible from ToF-SIMS alone and would require complementary vibrational spectroscopy such as FTIR detection of Al–H stretching modes (~1700–1900 cm^{-1}) [386-388], which was not performed in this work. I therefore interpret the AlH^- enhancement as evidence that hydrogen has accumulated in the immediate vicinity of aluminium at the interface, without committing to a specific bonding configuration.

Two features of this AlH^- signal merit discussion. First, the depth profile exhibits an abrupt cutoff at 0 nm, with no signal extending into the silicon substrate. In standard ToF-SIMS depth profiling, light

elements such as hydrogen are susceptible to knock-on broadening. The absence of such broadening indicates that this association is confined to the oxide side of the interface, which is consistent with hydrogen being localised near aluminium on the oxide side of the interface [377]. The absence of knock-on broadening of the AlH^- cluster could equally reflect the larger cluster mass and lower primary-beam energy transfer efficiency compared with atomic H^-, rather than a physically confined reservoir [378]. Second, the absolute signal intensity of AlH^- (~0.0016) is far lower than that of OH^- (~0.1). This difference should not be interpreted as indicating a negligible quantity. In ToF-SIMS, the ionisation probability of a given species depends on the local chemical environment (the matrix effect). Oxygen-rich fragments inherently exhibit high negative-ion yields, whereas the ionisation probability of AlH^- may be orders of magnitude lower. Cross-species comparison of absolute intensities is therefore not meaningful; the physically relevant quantity is the relative change in AlH^- intensity within the same matrix upon annealing.

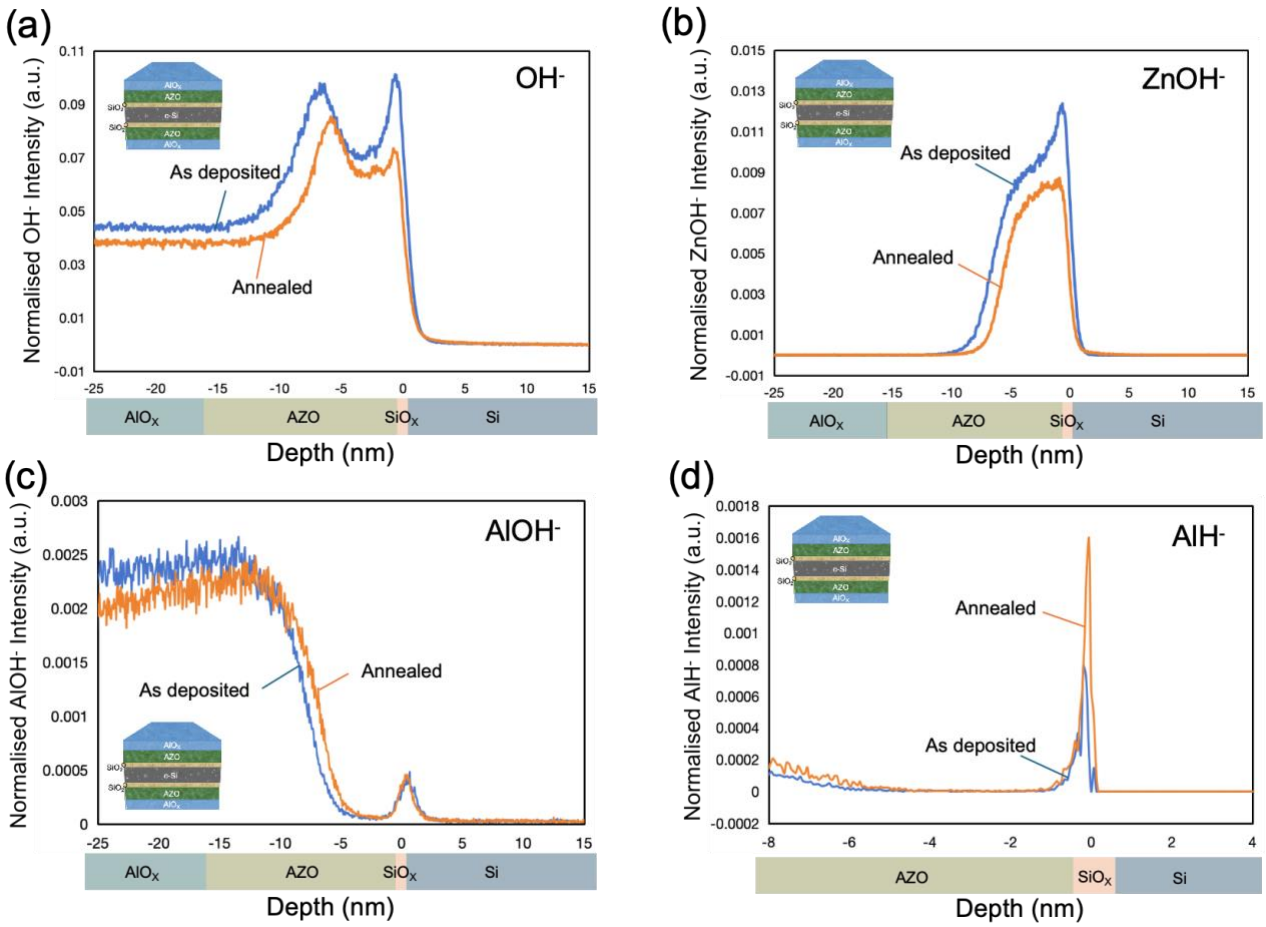


Figure 6.10 ToF-SIMS results showing (a) OH^-, (b) $ZnOH^-$, (c) $AlOH^-$, and (d) AlH^- intensities between as-deposited (blue) and annealed (orange) standard AZO/AlO_X samples.

6.5.3 Si–H Bond Formation and Interface Defect Passivation

Having investigated the interfacial AlH^- signals change, the remaining question is whether this accumulated hydrogen passivates silicon surface dangling bonds. The interfacial $^{29}SiO^-$ peak fragments, the $^{29}SiH^-$ (representing hydrogenated passivation states), and the $^{29}SiHO^-$ (representing hydroxylated or defect states) were tracked. The independent behaviour of each fragment is shown in Appendix G (Figure A 95 and Figure A 96).

Annealing reduces the $^{29}SiHO^-/Si^-$ ratio, whereas the $^{29}SiH^-/Si^-$ ratio remains relatively constant. This contradiction reflects the ToF-SIMS matrix effect: densification alters local atomic packing, causing systematic shifts in ionisation yield [382]. Comparing absolute intensities or single-species ratios across samples with different matrix compositions can yield misleading conclusions [389].

To mitigate the influence of matrix effects, the ratio $^{29}SiH^-/^{29}SiHO^-$ was extracted (Figure 6.11). Because both fragments originate from Si and are generated under identical primary-beam and matrix conditions, their ratio is less susceptible to matrix effects than either single-species intensity [386], although the ratio is not fully matrix-independent because the local chemical environments of Si–H and Si–O–H species differ [78, 390].

As shown in Figure 6.11, compared to the as-deposited sample (blue), the annealed sample (orange) exhibits a pronounced increase in the $^{29}SiH^-/^{29}SiHO^-$ ratio across the entire interface and near-surface region. This shift indicates that annealing removes hydroxylated defect-associated species at the interface, shifting the chemical balance towards Si–H-terminated states [371]. The elevated ratio extends beyond the physical interface into the silicon substrate (>10 nm depth); at 450 °C, bulk diffusion of hydrogen into single-crystal silicon over such distances is thermodynamically improbable, and this deep signal is attributed to knock-on artefacts from the primary ion beam [391-394]. The region of chemical-state transformation is therefore conservatively confined to the physical interface.

The data in Figure 6.11 therefore indicate that the passivation improvement is not simply proportional to the total hydrogen concentration delivered to the interface, but is instead correlated with a selective chemical-state transformation: the shift in balance between hydroxylated Si–O–H-like and hydrogenated Si–H-like interfacial species [308]. This chemical rebalancing most likely

causes the reduction in interface recombination and the corresponding increase in the effective minority carrier lifetime, although a direct causal link between $^{29}SiH^{-}/^{29}SiHO^{-}$ ratio and the Shockley–Read–Hall recombination rate cannot be established from ToF-SIMS alone [65, 395].

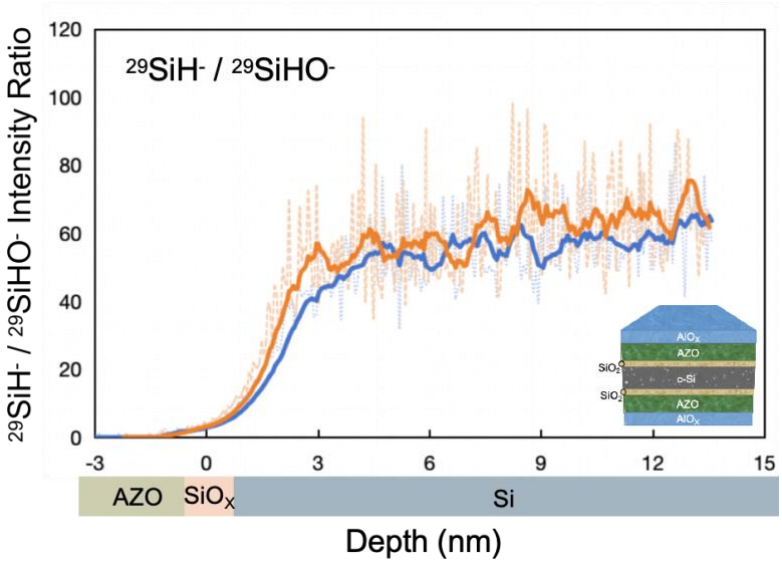


Figure 6.11 Depth profile of the $^{29}SiH^{-}/^{29}SiHO^{-}$ intensity ratio for the as-deposited (blue) and annealed (orange) standard AZO/AlO_X samples. Dotted lines show the raw ratio computed point-by-point; solid lines are the same data after 10-point moving-average smoothing. The elevated ratio extending to depths > 10 nm is attributed to knock-on redistribution of H into the silicon by the primary ion beam and does not represent a physical hydrogen concentration at that depth (see main text).

6.6 Overall Summary of Physical and Chemical Mechanisms

6.6.1 Identification of the Hydrogen Pathway for Chemical Passivation

The principal finding of this chapter is that hydrogen released from the AlO_X cap during the 450 °C anneal migrates toward the Si/SiO_X interface, accumulates near aluminium-containing sites, and shifts the interfacial chemistry toward Si–H termination. Four mutually consistent observations establish this source–transport–endpoint pathway. NR shows hydrogen depletion from the AlO_X cap, with the AZO content invariant with cooling rate (Section 5.6). ToF-SIMS tracks H^{-} redistribution toward the Si/AZO interface and the appearance of an AlH^{-} feature at 0 nm (Sections 6.5). The $^{29}SiH^{-}/^{29}SiHO^{-}$ ratio increases across the interface, identifying the Si–H endpoint (Section 6.5). Transient-SPV confirms the electronic response: suppression of the ~ 0.98 eV sub-bandgap feature, loss of de-trapping, a transition to bulk-lifetime-limited decay, and an SPV_{max} drop from ~ 0.28–0.40 V to ~ 0.15 V, consistent with H-passivation of acceptor-type P_b-like interfacial states [308, 372].

Prior work on AZO-based passivating contacts has reported device-level passivation quality but has not resolved this hydrogen pathway. Gao et al. achieved the current benchmark (24.3% PCE on a SiO_2/AZO/Al_2O_3 stack) with a ToF-SIMS hydrogen profile, but did not probe the interfacial chemical state [50]. Cai et al. and Macco et al. attributed passivation in their AZO contacts to combined hydrogen and field-effect contributions without decoupling the two channels [44, 46, 47]. In each case, the hydrogen source, migration direction, and chemical endpoint at the Si surface have been postulated or observed in aggregate, but not simultaneously established. The synthesis presented here provides the first direct mechanistic resolution of chemical passivation in an AZO-based passivating contact.

6.6.2 Field-Effect and Chemical Passivation

Chemical passivation is the dominant contribution to the passivation of the annealed stack, and the field effect modulates it rather than producing it. Two observations establish this ranking. The pristine Si/AZO samples of Section 6.2.1 exhibit an SPV of 394 mV, exceeding the 333 mV of the full Si/AZO/AlO_X slow-cooled stack, yet reach only ~ 70 µs effective lifetime against > 1 ms at 1×10^{15} cm^{-3} ECD for the capped stack, so stronger band bending does not by itself give better passivation. More directly, the anneal that raises the lifetime by two orders of magnitude reduces the dark-state band bending rather than increasing it, with SPV_{max} falling from ~ 0.28–0.40 V to ~ 0.15 V (Section 6.4.3), since hydrogen passivation of acceptor-type interface states removes the negative charge responsible for part of that bending. The field effect is therefore not the origin of the millisecond lifetimes. Conversely, the as-deposited AZO/AlO_X stack retains deep-trap-dominated relaxation despite carrying the cap (Section 6.4.1), indicating that AlO_X does not release hydrogen without thermal activation. Upward bending nevertheless persists in every state measured, and is modulated by the cooling protocol: slow cooling raises the SPV from 232 to 334 mV between samples of comparable lifetime (Section 6.2.3).

The two mechanisms are separable by their ambient requirements and spatial scales. The in-situ vacuum XPS experiment (Section 6.3.2) produces incomplete Si $2p_{3/2}$ recovery upon cooling, confirming that ambient O_2 drives the V_O annihilation in the AZO that underlies the field-effect

component. The 16 nm AZO bulk stoichiometry is unchanged between cooling protocols (Zn 3p/O 1s ratio, Section 6.3.3), indicating that this modulation is sub-monolayer and that chemical passivation acts at interface termination rather than bulk composition. The two channels are therefore distinct: a bulk-electrostatic response driven by AZO oxygen-vacancy chemistry and ambient-O_2 exchange, and an atomic-scale Si–H reaction fuelled by the AlO_X hydrogen reservoir.

The cooling protocol of Chapter 5 is the analytical lever rather than the primary finding. Slow cooling keeps the film within the 300–450 °C window long enough for the AZO V_O population to approach its low-temperature equilibrium through ambient-O_2 in-diffusion and for AlO_X-released hydrogen to reach the Si/SiO_X interface and enter the $P_b + H^0 \rightarrow P_bH$ reaction (E_a ~ 1.5 eV [361]); fast cooling quenches both [368]. The ~ 40% lifetime contrast is therefore a second-order optimisation superposed on the two-orders-of-magnitude improvement from the anneal itself, and it is this contrast that enables each mechanism to be identified through its independent electronic and chemical signatures.

6.6.3 Methodological Limitations

The most consequential limitation is the geometric asymmetry between the 2 nm XPS model stack and the 16 nm device-relevant geometry used for KP-SPV and ToF-SIMS. The AZO Thomas–Fermi screening length is comparable to 2 nm, so absolute XPS band-bending magnitudes do not transfer quantitatively, and the sign reversal of the cooling-rate contrast (Section 6.3.4) reflects this asymmetry rather than a physical inversion. ToF-SIMS data matched between fast- and slow-cooled samples were not acquired, so the claim that slow cooling drives a more complete $P_b + H^0 \rightarrow P_bH$ conversion is a kinetic inference.

Two further ToF-SIMS constraints are acknowledged here. Sample-specific calibration of the sputter rate across samples of different interfacial density was not performed, and a cross-sample comparison of sputter yields under separately-calibrated conditions was not attempted. The post-anneal density increase of ~ 6.9% in the AlO_X cap (Section 5.5.1) was assumed to remain within the ~ 5-10% profilometry uncertainty (Section 6.5.1), and this first-order approximation is not further tested in this thesis. Further constraints include the inability to disambiguate the interfacial AlH^-

signal from sputter-plume recombination without FTIR, the ~ 50 meV transient-SPV resolution that does not uniquely assign the 0.98 eV response, and the unresolved hydrogen charge state along the AlO_X → AZO → SiO_X → Si pathway [366, 396].

6.7 Summary

This chapter used KP-SPV, XPS, transient-SPV, and ToF-SIMS to resolve the microscopic origin of passivation in the SiO_X/AZO/AlO_X stack. Figure 6.12 illustrates the proposed passivation mechanism. Hydrogen released from the AlO_X cap during the anneal migrates to the Si/SiO_X interface, accumulates near Al-containing sites, and shifts the interfacial chemistry toward Si–H termination, the first such mechanistic resolution in an AZO-based passivating contact. This chemical passivation is the dominant contribution, and operates in parallel with air-driven V_O annihilation in the AZO, which modulates the band bending. The anneal reduces the upward band bending while raising the lifetime by two orders of magnitude, so the field effect is a second-order channel that the cooling protocol tunes rather than the origin of the passivation. Cooling rate served as the analytical lever that modulates the two mechanisms through distinct physics (V_O–O_2 equilibration versus hydrogen transport kinetics), enabling their separate identification within a single sample architecture. The protocol is transferable to other metal-oxide passivating contacts.

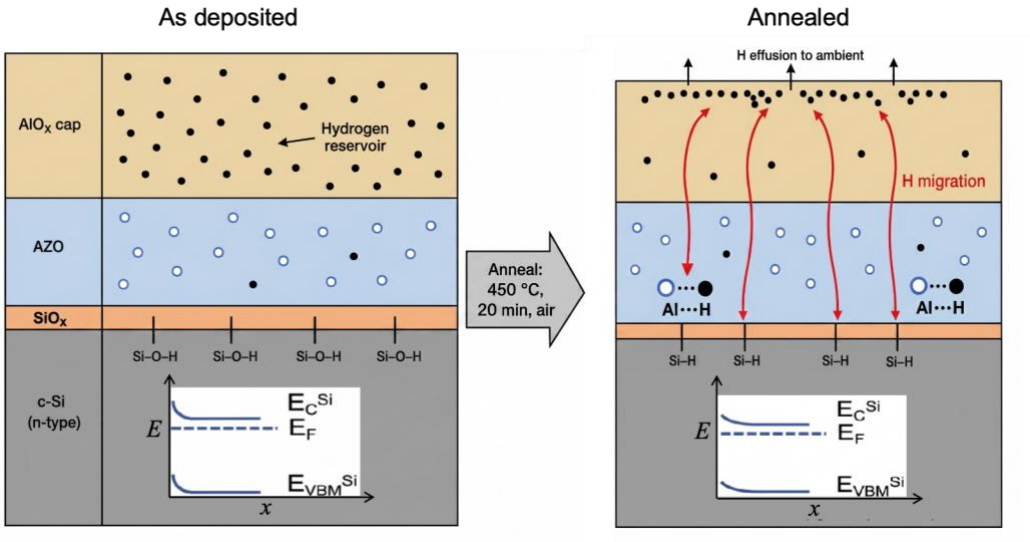


Figure 6.12 Schematic of the passivation model for the SiO_X/AZO/AlO_X passivating contact. Hydrogen released from the AlO_X cap during the 450 °C anneal migrates toward the Si/SiO_X interface and forms Si–H termination (chemical passivation). Ambient-O_2 in-diffusion annihilates oxygen vacancies in the AZO, modulating the upward band bending already present at the Si surface (field-effect passivation). The net effect of the anneal is to reduce that band bending, as the passivation of acceptor-type interface states removes negative interface charge.

Chapter 7. Summary and Future Work

7.1 Context and Objectives

Perovskite/silicon tandem photovoltaics require an interconnection layer that simultaneously transmits near-infrared light, conducts laterally at low sheet resistance, and passivates the underlying silicon surface, ideally without a hydrogenated amorphous silicon (a-Si:H) interlayer. The high sub-bandgap absorption coefficient of a-Si:H introduces parasitic absorption in the near-infrared, which directly reduces the current available to the silicon bottom cell in a monolithic tandem. Indium scarcity further motivates the replacement of indium tin oxide (ITO) by earth-abundant alternatives. Aluminium-doped zinc oxide (AZO) is a leading candidate as an indium-free TCO, however, prior reports have not demonstrated high-quality silicon passivation by AZO without an a-Si:H interlayer. This thesis examines whether an atomic-layer-deposited (ALD) SiO_X/AZO/AlO_X stack can meet the three requirements simultaneously using only earth-abundant materials, through four objectives: optimising the ALD conditions on n-type Si; determining how post-deposition thermal processing governs passivation; characterising the buried Si/AZO interface; and decoupling the chemical and field-effect passivation contributions at this interface.

7.2 Principal Contributions

7.2.1 Record Passivation from Precursor Partial-Pressure Control (Chapter 4)

Adopting the partial-pressure ratio H_2O:DEZ:TMA as the primary control parameter, rather than cycle count or substrate temperature, a review of approximately 130 depositions identified an optimal ratio of 4:3:2.5 that yields J_0 = 0.87 fA/cm^2 and iV_{OC} > 740 mV on planar n-type silicon without an a-Si:H interlayer, among the lowest J_0 reported for any metal-oxide/Si passivating contact without a-Si:H. Superior passivation correlates with the highest Hall electron mobility rather than with maximum Al incorporation, identifying structural order rather than dopant density as the dominant determinant under these conditions. In-situ-sputtered XPS on the buried Si/SiO_X/AZO interface reveals upward

band bending in the silicon, a polarity opposite to the downward bending predicted in prior AZO studies that relied on bulk-film modelling rather than direct interfacial probing. The discrepancy between the Anderson-method (2.52 eV) and Kraut-method (3.25 eV) valence band offsets points to an interfacial-dipole-mediated band-pinning configuration at the Type II/Type III boundary, although alternative fixed-charge scenarios cannot be uniquely excluded by the present data.

7.2.2 Cooling Rate as A Dominant Processing Variable (Chapter 5)

This thesis is the first to document, for an AZO-based passivating contact, a cooling-rate dependence that is independent of the peak annealing temperature or dwell duration. Four controlled cooling profiles at matched thermal budgets produce a monotonic lifetime decline with increasing cooling rate; fast-cooled samples under-perform slow-cooled samples even when the former receive a larger integrated thermal budget. Ramp-halt experiments localise a beneficial window near 300 °C, and pulse annealing, in which repeated short 450 °C dwells are interrupted by cooling, out-performs continuous annealing, consistent with a diffusion-limited rather than a single-event mechanism. XRR rules out macroscopic structural differences between slow- and fast-cooled samples, and NR identifies the AlO_X cap as an active hydrogen reservoir: slow cooling depletes the AlO_X hydrogen content while leaving the AZO bulk hydrogen invariant, pointing to a chemical-state transformation at or near the Si/SiO_X interface rather than a volumetric compositional change.

7.2.3 Direct Identification of the Hydrogen Pathway (Chapter 6)

KP-SPV, synchrotron XPS, transient-SPV, and ToF-SIMS together decouple the field-effect and chemical passivation contributions, the first integrated application of these four techniques to an AZO-based contact. Hydrogen released from the AlO_X cap during annealing migrates toward the Si/SiO_X interface, accumulates near aluminium-containing sites, and shifts the interfacial chemistry toward Si–H termination; to my knowledge this is the first AZO-based passivating contact in which the hydrogen source, migration direction, and chemical endpoint have been jointly resolved. Pristine Si/AZO samples display upward band bending exceeding that of the full stack but reach only ~ 70 µs lifetime at 1×10^{15} cm^{-3} ECD, whereas the full slow-cooled AZO/AlO_X stack reaches millisecond lifetimes. Transient-SPV provides four independent signatures of chemical passivation, suppression

of the ~ 0.98 eV sub-bandgap defect response, loss of de-trapping features, a transition to bulk-lifetime-limited decay, and a drop in SPV_{max}. The anneal reduces the dark-state band bending while raising the lifetime by two orders of magnitude, identifying chemical passivation as the dominant contribution; the field effect persists in every state measured and is tuned at the margin by the cooling protocol.

7.3 Synthesis of Findings

Taken together, the three chapters identify the cooling rate as a single processing parameter that modulates both passivation mechanisms: it sets the extent of oxygen-vacancy annihilation in the AZO (strengthening the field effect) and the time during which hydrogen released from the AlO_X cap remains mobile and able to shift the interfacial termination from Si–O–H-like towards Si–H-like. The 300 °C beneficial window in this system differs from the 560–700 °C window reported for SiN_X:H/PERC fast-firing, consistent with lower activation energies for hydrogen migration in amorphous oxide networks compared with interstitial hopping in crystalline silicon. The cooling-rate concept may therefore offer a design principle transferable to other hydrogen-mediated oxide passivating contacts.

7.4 Future Work

The findings establish a foundation for several natural extensions, each addressing aspects the current work identified but did not fully explore.

I. Device-level integration. Evaluate the optimised stack as the rear contact of a single-junction n-type cell and as the interconnection layer of a monolithic perovskite/silicon tandem. Contact resistivity should be characterised explicitly and, where the upward band bending creates a transport barrier, tuned by work-function-modifying interlayers such as LiF [49].
II. Cooling protocol for industrial throughput. Translate the 300 °C ramp-halt observation into a two-step thermal profile with a targeted plateau duration under representative heating ramps, compatible with in-line photovoltaic processing.

III. Isotopic tracing of the hydrogen pathway. Substitute D_2O in the AlO_X half-cycles only and combine NR with matched ToF-SIMS to test the $AlO_X \rightarrow Si/SiO_X$ migration pathway directly.

IV. Vibrational confirmation by FTIR. Attenuated-total-reflection FTIR probes Al–H stretches at 1700–1900 cm^{-1} and buried Si–H/Si–OH modes, providing independent vibrational confirmation of the AlH^- and $^{29}SiH^-/^{29}SiHO^-$ assignments that ToF-SIMS alone cannot uniquely establish.

V. Matched-cooling ToF-SIMS. Acquire matched depth profiles on fast- and slow-cooled samples to test whether slow cooling drives a more complete Si–OH → Si–H conversion than fast cooling, the one direct observation the present data do not provide.

VI. Non-destructive buried-interface probing. The cooling-rate XPS comparison was performed on a 2 nm model stack; HAXPES through the 16 nm device-relevant AZO would test whether the sign reversal observed between the two geometries is a genuine length-scale effect or an artefact of the thinner stack.

VII. Capped C–V analysis. A capped C–V measurement, as applied to very thin dielectrics in prior work in the Bonilla lab, would independently extract the fixed-charge density Q_f and interface-state density D_{it}, providing the quantitative partition of field-effect and chemical contributions that the present measurements cannot resolve.

VIII. Extension to p-type silicon and alternative ambients. A matched comparison of p-type substrates and of air- versus forming-gas-annealed samples, within the framework of Chapters 5 and 6, would test whether the upward band bending reported here is intrinsic to the Si/AZO junction or specific to the oxidising ambient used in this thesis, with direct consequences for the passivation–contact-resistance trade-off.

7.5 Implications for the Field

The findings reported in this thesis are not limited to the $SiO_X/AZO/AlO_X$ system. They concern how the interface is characterised, how the anneal is specified, how the capping layer can be used, and what now limits the contact.

The results of Chapter 4 have three consequences for how AZO-based passivating contacts are developed. First, the cycle ratio is not a sufficient process specification: all four recipes used the

same ZnO:AlO_X cycle ratio and differed only in precursor partial pressure, yet the resulting J_0 varied by a factor of three, so the dosing conditions need to be reported alongside it. Second, composition is not a sufficient screening metric either. The film with the highest Al/Zn ratio gave neither the best passivation nor the lowest resistivity, and the doping efficiency of these films is of order 10% (Section 4.4.2), so a measure of Al content needs to be accompanied by a measure of activation such as the Hall carrier density. Third, structural order is a target that does not require trade-offs: the recipe with the highest electron mobility gave the best passivation and the lowest resistivity without loss of visible transparency, since the Burstein–Moss shift and bandgap renormalisation offset one another across the range studied (Section 4.4.3).

The band bending measured at the Si/SiO_X/AZO interface changes how contact oxides should be assessed. Studies of AZO-based contacts have predicted downward bending and electron accumulation in the silicon, inferring the interface condition from the bulk work function of the degenerately doped oxide; the direct measurements of Chapter 4 and Chapter 6 give the opposite sign, in both annealed and as-deposited films. Bulk work function describes a free surface, whereas band bending depends on the interfacial dipole, the fixed charge, and the chemistry of the intervening ultrathin oxide. Work-function matching is therefore a starting point rather than a criterion, and a buried-interface measurement, such as buried-interface XPS, HAXPES, or surface photovoltage, is therefore needed alongside it when a new contact oxide is analysed.

The cooling-rate dependence established in Chapter 5 has four consequences for the development of hydrogen-mediated oxide contacts. First, the cooling profile needs to be specified alongside peak temperature and dwell time, since the same nominal recipe run on tools with different cooling characteristics need not give the same passivation. Second, forming-gas annealing may not be required. Air annealing outperformed both nitrogen and forming gas, which opens a possibility where a flammable-gas step could be removed from the process line. Third, once the high-temperature activation step has been carried out, passivation improves further with time spent near 300 °C rather than with a higher peak temperature or a longer dwell, so a two-step profile may deliver a given passivation level at a lower integrated thermal load. Fourth, the beneficial window cannot be transferred from the silicon firing literature: it lies near 300 °C here, against 560–700 °C for SiN_X:H-

fired cells, because hydrogen moves inward from the cap towards the interface rather than outward from the silicon bulk. It therefore has to be located experimentally for each new stack.

Chapter 6 changes what can be asked of an AZO-based contact more than what is known about it. Passivation in these stacks has previously been attributed to chemical and field-effect contributions acting together, without separating them, so optimisation has proceeded empirically: a change of recipe alters the lifetime, but not which mechanism responded. The combination of Kelvin-probe and transient surface photovoltage, synchrotron photoemission, neutron reflectometry and ToF-SIMS used here was assembled to address that gap, and has not to my knowledge been applied together to an AZO-based contact. It supports a mechanism model in which hydrogen released from the AlO_X cap terminates interfacial defects while ambient oxygen annihilates vacancies in the AZO, the former dominant and the latter modulating, each channel carrying its own experimental signature and responding to a different part of the thermal profile. The model rests on converging but indirect evidence, and several of its steps remain untested. Its value is that it is specific enough to be tested: it indicates which measurement should respond to which processing change, so that optimisation can be directed at a mechanism rather than at a lifetime.

Taken together, the findings reported in this thesis move the outstanding question for this contact from passivation to carrier transport. A recombination current density of 0.87 fA/cm^2 on planar n-type silicon, achieved without an amorphous silicon interlayer, is comparable to that of established dielectric schemes. Passivation is therefore no longer what limits the stack; transport is. The contact resistivity of the etched AZO surface was not measured here, and the upward band bending implies an extraction barrier of unknown magnitude. The two are coupled, because the band bending that strengthens the field effect also raises that barrier. An indium-free interconnection built on this stack will therefore have to optimise passivation and transport together rather than in sequence.

References

[1] Met Office, "Atmospheric carbon dioxide rise to remain too fast to track global climate targets in 2026," ed: Met Office, 2026.

[2] NOAA Global Monitoring Laboratory. "Trends in Atmospheric Carbon Dioxide." https://gml.noaa.gov/ccgg/trends/gl_trend.html (accessed 25 March 2026.

[3] Earth.org. "A Graphical History of Atmospheric CO2 Levels Over Time." https://earth.org/data_visualization/a-brief-history-of-co2/ (accessed 25 March 2026.

[4] NOAA Climate.gov. "Climate change: global temperature." https://shorturl.at/veotK (accessed 25 March 2026.

[5] World Meteorological Organization, "WMO confirms 2024 as warmest year on record at about 1.55°C above pre-industrial level," ed: WMO, 2025.

[6] World Resources Institute. "Where Do Emissions Come From? 4 Charts Explain Greenhouse Gas Emissions by Sector." WRI. https://shorturl.at/FY4QN (accessed 25 March 2026.

[7] "Paris Agreement to the United Nations Framework Convention on Climate Change," ed. United Nations,, 2015.

[8] International Energy Agency (IEA), "Solar PV: Tracking Clean Energy Progress," 2025. [Online]. Available: https://www.iea.org/energy-system/renewables/solar-pv

[9] International Energy Agency (IEA), "Renewables 2025 Analysis and forecasts to 2030," ed: IEA, 2025.

[10] U.S. Department of Energy. "How Does Solar Work?" Office of Energy Efficiency & Renewable Energy. https://www.energy.gov/eere/solar/how-does-solar-work (accessed 25 March 2026.

[11] Ember, "World adds a record-breaking 814 GW of solar and wind in 2025," 2026. [Online]. Available: https://ember-energy.org/latest-updates/world-adds-a-record-breaking-814-gw-of-solar-and-wind-in-2025/

[12] Fraunhofer Institute for Solar Energy Systems ISE, "Photovoltaics Report," 2025.

[13] International Renewable Energy Agency (IRENA), "Renewable power generation costs in 2024," 2025.

[14] W. Shockley and H. J. Queisser, "Detailed Balance Limit of Efficiency of p-n Junction Solar Cells," *Journal of Applied Physics,* vol. 32, no. 3, pp. 510–519, 1961, doi: 10.1063/1.1736034.

[15] G. Yang *et al.*, "Towards efficient, scalable and stable perovskite/silicon tandem solar cells," *Nature Photonics,* vol. 19, no. 9, pp. 913–924, 2025/09/01 2025, doi: 10.1038/s41566-025-01732-y.

[16] G. Wang *et al.*, "Silicon solar cells with hybrid back contacts," *Nature,* vol. 647, no. 8089, pp. 369–374, 2025/11/01 2025, doi: 10.1038/s41586-025-09681-w.

[17] Martin A. Green *et al.*, "Solar Cell Efficiency Tables (Version 67)," *Progress in Photovoltaics: Research and Applications,* vol. 34, no. 4, pp. 482–496, 2026, doi: https://doi.org/10.1002/pip.70068.

[18] R. S. Bonilla, B. Hoex, P. Hamer, and P. R. Wilshaw, "Dielectric surface passivation for silicon solar cells: A review," *physica status solidi (a),* vol. 214, no. 7, p. 1700293, 2017, doi: https://doi.org/10.1002/pssa.201700293.

[19] J. Schmidt, R. Peibst, and R. Brendel, "Surface passivation of crystalline silicon solar cells: Present and future," *Solar Energy Materials and Solar Cells,* vol. 187, pp. 39–54, 2018/12/01/ 2018, doi: https://doi.org/10.1016/j.solmat.2018.06.047.

[20] N. C. Mandal *et al.*, "Evolution of PERC from Al-BSF: optimization based on root cause analysis," *Applied Physics A,* vol. 126, 2020.

[21] B. Vicari Stefani *et al.*, "Historical market projections and the future of silicon solar cells," *Joule,* vol. 7, no. 12, pp. 2684–2699, 2023/12/20/ 2023, doi: https://doi.org/10.1016/j.joule.2023.11.006.

[22] JinkoSolar, "TOPCon projected to represent 70% of global sales," in *PVTECH*, ed, 2024.

[23] C. Ballif, F.-J. Haug, M. Boccard, P. J. Verlinden, and G. Hahn, "Status and perspectives of crystalline silicon photovoltaics in research and industry," *Nature Reviews Materials,* vol. 7, no. 8, pp. 597–616, 2022/08/01 2022, doi: 10.1038/s41578-022-00423-2.
[24] T. G. Allen, J. Bullock, X. Yang, A. Javey, and S. De Wolf, "Passivating contacts for crystalline silicon solar cells," *Nature Energy,* vol. 4, no. 11, pp. 914–928, 2019/11/01 2019, doi: 10.1038/s41560-019-0463-6.
[25] D. Yan *et al.*, "Silicon solar cells with passivating contacts: Classification and performance," *Progress in Photovoltaics: Research and Applications,* vol. 31, no. 4, pp. 310–326, 2023, doi: https://doi.org/10.1002/pip.3574.
[26] E. Aydin *et al.*, "Pathways toward commercial perovskite/silicon tandem photovoltaics," *Science,* vol. 383, no. 6679, p. eadh3849, 2024, doi: doi:10.1126/science.adh3849.
[27] N.-G. Park, H. J. Snaith, and T. Miyasaka, "Key advances in perovskite solar cells in 2025," *Nature Reviews Clean Technology,* vol. 2, no. 1, pp. 6–7, 2026/01/01 2026, doi: 10.1038/s44359-025-00128-z.
[28] L. Jia *et al.*, "Efficient perovskite/silicon tandem with asymmetric self-assembly molecule," (in eng), *Nature,* vol. 644, no. 8078, pp. 912–919, Aug 2025, doi: 10.1038/s41586-025-09333-z.
[29] J. Zhang *et al.*, "Deep UV transparent conductive oxide thin films realized through degenerately doped wide-bandgap gallium oxide," *Cell Reports Physical Science,* vol. 3, no. 3, 2022, doi: 10.1016/j.xcrp.2022.100801.
[30] L. Hu, R. H. Wei, X. W. Tang, W. J. Lu, X. B. Zhu, and Y. P. Sun, "Design strategy for p-type transparent conducting oxides," *Journal of Applied Physics,* vol. 128, no. 14, 2020, doi: 10.1063/5.0023656.
[31] A. Klein *et al.*, "Transparent Conducting Oxides for Photovoltaics: Manipulation of Fermi Level, Work Function and Energy Band Alignment," *Materials,* vol. 3, no. 11, pp. 4892–4914, 2010. [Online]. Available: https://www.mdpi.com/1996-1944/3/11/4892.
[32] W. Cui, F. Chen, Y. Li, X. Su, and B. Sun, "Status and perspectives of transparent conductive oxide films for silicon heterojunction solar cells," *Materials Today Nano,* vol. 22, p. 100329, 2023/06/01/ 2023, doi: https://doi.org/10.1016/j.mtnano.2023.100329.
[33] Y. Shao *et al.*, "Innovations in Interconnecting Layers for Perovskite-Based Tandem Solar Cells," *ACS Energy Letters,* vol. 9, no. 10, pp. 4892–4921, 2024/10/11 2024, doi: 10.1021/acsenergylett.4c01703.
[34] H. Sai, T. Koida, and T. Matsui, "Improved electrical contact properties in Indium-free silicon heterojunction solar cells with amorphous SnO2 TCO layers," *Solar Energy Materials and Solar Cells,* vol. 278, p. 113191, 2024/12/01/ 2024, doi: https://doi.org/10.1016/j.solmat.2024.113191.
[35] H. Song, C. Wang, K. Sun, H. Geng, and L. Zuo, "Material efficiency strategies across the industrial chain to secure indium availability for global carbon neutrality," *Resources Policy,* vol. 85, p. 103895, 2023/08/01/ 2023, doi: https://doi.org/10.1016/j.resourpol.2023.103895.
[36] L. Wang *et al.*, "Sustainability evaluations on material consumption for terawatt-scale manufacturing of silicon-based tandem solar cells," *Progress in Photovoltaics: Research and Applications,* vol. 31, pp. 1442 – 1454, 2023.
[37] L. Wagner *et al.*, "Actions for sustainably scalable multi-terawatt photovoltaics," *Nature Reviews Clean Technology,* vol. 2, no. 2, pp. 107–122, 2026/02/01 2026, doi: 10.1038/s44359-025-00129-y.
[38] M. Hanser *et al.*, "Indium-Free Recombination Junctions on Tunnel Oxide Passivating Contacts for Fully Textured Perovskite/Silicon Tandem Solar Cells," *Solar RRL,* vol. 10, no. 5, p. e202500942, 2026, doi: https://doi.org/10.1002/solr.202500942.
[39] Ö. Ş. Kabaklı *et al.*, "Thickness Optimization of Front and Recombination ITO in Monolithic Perovskite/Silicon Tandem Solar Cells," *Solar RRL,* vol. 8, no. 20, p. 2400454, 2024, doi: https://doi.org/10.1002/solr.202400454.
[40] H. Liu, Y. Zhu, W. Xiong, Y. Yang, S. Li, and S. Bai, "Transparent Conductive Oxide Films and Their Applications in Silicon Heterojunction and Perovskite/Silicon Tandem Photovoltaics," *ACS Applied Energy Materials,* vol. 8, no. 7, pp. 4032–4047, 2025/04/14 2025, doi: 10.1021/acsaem.4c03332.

[41] B. Sarma, D. Barman, and B. Sarma, "AZO (Al:ZnO) thin films with high figure of merit as stable indium free transparent conducting oxide," *Applied Surface Science,* vol. 479, pp. 786–795, 02/16 2019, doi: 10.1016/j.apsusc.2019.02.146.
[42] F. Mollica, M. Jubault, F. Donsanti, M. Bouttemy, A. Etcheberry, and N. Naghavi, "Assessment of Indium-Free Transparent Conductive Oxide Back Contacts for High-Efficiency Ultra-Thin Cu (In,Ga)Se2 Solar Cells Down to 250 nm," *Progress in Photovoltaics: Research and Applications,* vol. 33, no. 10, pp. 1109–1123, 2025, doi: https://doi.org/10.1002/pip.70013.
[43] G. T. Chavan *et al.*, "A Brief Review of Transparent Conducting Oxides (TCO): The Influence of Different Deposition Techniques on the Efficiency of Solar Cells," *Nanomaterials,* vol. 13, no. 7, p. 1226, 2023. [Online]. Available: https://www.mdpi.com/2079-4991/13/7/1226.
[44] H. Cai, Z. Zhong, Q. Nong, P. Gao, and J. He, "Design and Optimization of SiOx/AZO Transparent Passivating Contacts for High-Efficiency Crystalline Silicon Solar Cells," *Advanced Functional Materials,* vol. 34, no. 52, p. 2411207, 2024, doi: https://doi.org/10.1002/adfm.202411207.
[45] B. W. H. van de Loo, B. Macco, J. Melskens, W. Beyer, and W. M. M. Kessels, "Silicon surface passivation by transparent conductive zinc oxide," *Journal of Applied Physics,* vol. 125, no. 10, 2019, doi: 10.1063/1.5054166.
[46] B. Macco *et al.*, "Atomic-layer-deposited Al-doped zinc oxide as a passivating conductive contacting layer for n+-doped surfaces in silicon solar cells," *Solar Energy Materials and Solar Cells,* vol. 233, p. 111386, 2021/12/01/ 2021, doi: https://doi.org/10.1016/j.solmat.2021.111386.
[47] B. Macco *et al.*, "Temporal and spatial atomic layer deposition of Al-doped zinc oxide as a passivating conductive contact for silicon solar cells," *Solar Energy Materials and Solar Cells,* vol. 245, p. 111869, 2022/09/15/ 2022, doi: https://doi.org/10.1016/j.solmat.2022.111869.
[48] S. M. George, "Atomic Layer Deposition: An Overview," *Chemical Reviews,* vol. 110, no. 1, pp. 111–131, 2010/01/13 2010, doi: 10.1021/cr900056b.
[49] C.-H. Chen, G. S. R. Mullapudi, K. O. Davis, and P. Banerjee, "Atomic layer deposition (ALD) of passivating, carrier-selective oxides for silicon photovoltaics," *Applied Physics Reviews,* vol. 12, no. 4, 2025, doi: 10.1063/5.0275420.
[50] K. Gao *et al.*, "Efficient Silicon Solar Cells with Aluminum-Doped Zinc Oxide-Based Passivating Contact," *Advanced Functional Materials,* vol. 35, no. 4, p. 2415039, 2025, doi: https://doi.org/10.1002/adfm.202415039.
[51] Q. Zou *et al.*, "Tantalum doped tin oxide enabled indium-free silicon heterojunction solar cells with efficiency over 25 %," *Nano Energy,* vol. 131, p. 110206, 2024/12/01/ 2024, doi: https://doi.org/10.1016/j.nanoen.2024.110206.
[52] J. Huang and L. Mao, "A Review on Perovskite/Silicon Tandem Solar Cells: Current Status and Future Challenges," *Energies,* vol. 18, no. 16, p. 4327, 2025. [Online]. Available: https://www.mdpi.com/1996-1073/18/16/4327.
[53] R. S. Bonilla, "The impact of transparent conducting electrodes on tandem solar cell efficiency," *Joule,* vol. 9, no. 12, p. 102211, 2025/12/17/ 2025, doi: https://doi.org/10.1016/j.joule.2025.102211.
[54] A. Richter, M. Hermle, and S. W. Glunz, "Reassessment of the Limiting Efficiency for Crystalline Silicon Solar Cells," *IEEE Journal of Photovoltaics,* vol. 3, no. 4, pp. 1184–1191, 2013, doi: 10.1109/JPHOTOV.2013.2270351.
[55] T. Niewelt *et al.*, "Reassessment of the intrinsic bulk recombination in crystalline silicon," *Solar Energy Materials and Solar Cells,* vol. 235, p. 111467, 2022/01/01/ 2022, doi: https://doi.org/10.1016/j.solmat.2021.111467.
[56] M. A. Green and Z. Zhou, "Improved silicon solar cells by tuning angular response to solar trajectory," *Nature Communications,* vol. 16, no. 1, p. 251, 2025/01/02 2025, doi: 10.1038/s41467-024-55681-1.
[57] J. Kangsabanik, M. K. Svendsen, A. Taghizadeh, A. Crovetto, and K. S. Thygesen, "Indirect Band Gap Semiconductors for Thin-Film Photovoltaics: High-Throughput Calculation of Phonon-Assisted Absorption," *Journal of the American Chemical Society,* vol. 144, no. 43, pp. 19872–19883, 2022/11/02 2022, doi: 10.1021/jacs.2c07567.

[58] J. Nelson, *The Physics of Solar Cells*. World Scientific Publishing Company, 2003.
[59] T. Trupke *et al.*, "Temperature dependence of the radiative recombination coefficient of intrinsic crystalline silicon," *Journal of Applied Physics,* vol. 94, no. 8, pp. 4930–4937, 2003, doi: 10.1063/1.1610231.
[60] P. P. Altermatt, F. Geelhaar, T. Trupke, X. Dai, A. Neisser, and E. Daub, "Injection dependence of spontaneous radiative recombination in crystalline silicon: Experimental verification and theoretical analysis," *Applied Physics Letters,* vol. 88, no. 26, 2006, doi: 10.1063/1.2218041.
[61] A. Schenk, "Finite-temperature full random-phase approximation model of band gap narrowing for silicon device simulation," *Journal of Applied Physics,* vol. 84, no. 7, pp. 3684–3695, 1998, doi: 10.1063/1.368545.
[62] J. Dziewior and W. Schmid, "Auger coefficients for highly doped and highly excited silicon," *Applied Physics Letters,* vol. 31, no. 5, pp. 346–348, 1977, doi: 10.1063/1.89694.
[63] A. Richter, S. W. Glunz, F. Werner, J. Schmidt, and A. Cuevas, "Improved quantitative description of Auger recombination in crystalline silicon," *Physical Review B,* vol. 86, no. 16, p. 165202, 10/09/ 2012, doi: 10.1103/PhysRevB.86.165202.
[64] A. G. Aberle, *Crystalline silicon solar cells: advanced surface passivation and analysis*. 1999.
[65] R. N. Hall, "Electron-Hole Recombination in Germanium," *Physical Review,* vol. 87, no. 2, pp. 387–387, 07/15/ 1952, doi: 10.1103/PhysRev.87.387.
[66] A. J. Blundell, A. E. Garside, I. Williams, and R. G. Hibberd, "Silicon power rectifiers," *Proceedings of the IEE - Part A: Power Engineering,* vol. 108, no. 40, pp. 273–293, 1961, doi: doi:10.1049/pi-a.1961.0057.
[67] S. S. Li, *Semiconductor Physical Electronics*. Springer, 2006.
[68] P. Martín, A. Cano, I. García, and I. Rey-Stolle, "Review of intrinsic vs. extrinsic recombination in germanium thermophotovoltaic converters," *Solar Energy Materials and Solar Cells,* vol. 291, p. 113741, 2025/10/01/ 2025, doi: https://doi.org/10.1016/j.solmat.2025.113741.
[69] M. J. Kerr and A. Cuevas, "General parameterization of Auger recombination in crystalline silicon," *Journal of Applied Physics,* vol. 91, no. 4, pp. 2473–2480, 2002, doi: 10.1063/1.1432476.
[70] A. G. Aberle, "Surface passivation of crystalline silicon solar cells: a review," *Progress in Photovoltaics: Research and Applications,* vol. 8, no. 5, pp. 473–487, 2000, doi: https://doi.org/10.1002/1099-159X(200009/10)8:5<473::AID-PIP337>3.0.CO;2-D.
[71] Y. Shi *et al.*, "Towards accurate atom scale characterisation of hydrogen passivation of interfaces in TOPCon architectures," *Solar Energy Materials and Solar Cells,* vol. 246, p. 111915, 2022/10/01/ 2022, doi: https://doi.org/10.1016/j.solmat.2022.111915.
[72] Z. J. Rad *et al.*, "Decreasing Interface Defect Densities via Silicon Oxide Passivation at Temperatures Below 450 °C," *ACS Applied Materials & Interfaces,* vol. 12, no. 41, pp. 46933–46941, 2020/10/14 2020, doi: 10.1021/acsami.0c12636.
[73] R. V. K. Chavali, S. De Wolf, and M. A. Alam, "Device physics underlying silicon heterojunction and passivating-contact solar cells: A topical review," *Progress in Photovoltaics: Research and Applications,* vol. 26, no. 4, pp. 241–260, 2018, doi: https://doi.org/10.1002/pip.2959.
[74] S. W. Glunz *et al.*, "Silicon-based passivating contacts: The TOPCon route," *Progress in Photovoltaics: Research and Applications,* vol. 31, no. 4, pp. 341–359, 2023, doi: https://doi.org/10.1002/pip.3522.
[75] D. T. Stevenson and R. J. Keyes, "Measurement of Carrier Lifetimes in Germanium and Silicon," *Journal of Applied Physics,* vol. 26, no. 2, pp. 190–195, 1955, doi: 10.1063/1.1721958.
[76] L. L. Keung and C. Li-Jen, "Analysis of the interaction of a laser pulse with a silicon wafer: Determination of bulk lifetime and surface recombination velocity," *Journal of Applied Physics,* vol. 61, 1987. [Online]. Available: http://link.aip.org/link/?JAP/61/2282/1.
[77] A. B. Sproul, "Dimensionless solution of the equation describing the effect of surface recombination on carrier decay in semiconductors," *Journal of Applied Physics,* vol. 76, no. 5, pp. 2851–2854, 1994, doi: 10.1063/1.357521.

[78] A. Kimmerle, J. Greulich, and A. Wolf, "Carrier-diffusion corrected J0-analysis of charge carrier lifetime measurements for increased consistency," *Solar Energy Materials and Solar Cells,* vol. 142, pp. 116–122, 2015/11/01/ 2015, doi: https://doi.org/10.1016/j.solmat.2015.06.043.
[79] A. Cuevas and R. A. Sinton, "Prediction of the open-circuit voltage of solar cells from the steady-state photoconductance," *Progress in Photovoltaics: Research and Applications,* vol. 5, no. 2, pp. 79–90, 1997, doi: https://doi.org/10.1002/(SICI)1099-159X(199703/04)5:2<79::AID-PIP155>3.0.CO;2-J.
[80] S. Enkhardt. "Trina Solar achieves 24.5% efficiency for 210 mm p-type PERC solar cell." PV Magazine. https://www.pv-magazine.com/2022/07/13/trina-solar-achieves-24-5-efficiency-for-210-mm-p-type-perc-solar-cell/ (accessed 30/03/2026.
[81] E. Bellini. "JinkoSolar achieves record-breaking 26.66% efficiency for TOPCon solar cell based on M10-size wafer." PV Magazine. https://www.pv-magazine.com/2026/02/25/jinkosolar-achieves-record-breaking-26-66-efficiency-for-topcon-solar-cell-based-on-m10-size-wafer/ (accessed 30/03/2026.
[82] E. Bellini. "Longi reveals details of world's most efficient silicon solar cell." PV Magazine. https://www.pv-magazine.com/2025/11/20/longi-reveals-details-of-worlds-most-efficient-silicon-solar-cell/ (accessed 30/03/2026.
[83] E. Bellini. "A closer look at Longi's world record-breaking, 26.81%-efficient heterojunction solar cell." PV Magazine. https://www.pv-magazine.com/2023/05/08/a-closer-look-at-longis-world-record-breaking-26-81-efficient-heterojunction-solar-cell/ (accessed 30/03/2026.
[84] Y. Zhang, M. Kim, L. Wang, P. Verlinden, and B. Hallam, "Design considerations for multi-terawatt scale manufacturing of existing and future photovoltaic technologies: challenges and opportunities related to silver, indium and bismuth consumption," *Energy & Environmental Science,* vol. 14, pp. 5587–5610, 09/27 2021, doi: 10.1039/D1EE01814K.
[85] K. K. N. S.M. Sze, *Physics of Semiconductor Devices*. John Wiley & Sons, Inc. , 2006.
[86] S. Calnan and A. N. Tiwari, "High mobility transparent conducting oxides for thin film solar cells," *Thin Solid Films,* vol. 518, no. 7, pp. 1839–1849, 2010/01/31/ 2010, doi: https://doi.org/10.1016/j.tsf.2009.09.044.
[87] S. C. Dixon, D. O. Scanlon, C. J. Carmalt, and I. P. Parkin, "n-Type doped transparent conducting binary oxides: an overview," *Journal of Materials Chemistry C,* 10.1039/C6TC01881E vol. 4, no. 29, pp. 6946–6961, 2016, doi: 10.1039/C6TC01881E.
[88] M. Morales-Masis, S. De Wolf, R. Woods-Robinson, J. W. Ager, and C. Ballif, "Transparent Electrodes for Efficient Optoelectronics," *Advanced Electronic Materials,* vol. 3, no. 5, p. 1600529, 2017, doi: https://doi.org/10.1002/aelm.201600529.
[89] E. Conwell and V. F. Weisskopf, "Theory of Impurity Scattering in Semiconductors," *Physical Review,* vol. 77, no. 3, pp. 388–390, 02/01/ 1950, doi: 10.1103/PhysRev.77.388.
[90] K. L. Chopra, S. Major, and D. K. Pandya, "Transparent conductors—A status review," *Thin Solid Films,* vol. 102, no. 1, pp. 1–46, 1983/04/08/ 1983, doi: https://doi.org/10.1016/0040-6090(83)90256-0.
[91] R. G. Gordon, "Criteria for Choosing Transparent Conductors," *MRS Bulletin,* vol. 25, no. 8, pp. 52–57, 2000/08/01 2000, doi: 10.1557/mrs2000.151.
[92] T. Kim *et al.*, "Megahertz-wave-transmitting conducting polymer electrode for device-to-device integration," (in eng), *Nat Commun,* vol. 10, no. 1, p. 653, Feb 8 2019, doi: 10.1038/s41467-019-08552-z.
[93] S. Kim *et al.*, "Free-carrier absorption and Burstein–Moss shift effect on quantum efficiency in heterojunction silicon solar cells," *Vacuum,* vol. 108, pp. 39–44, 2014/10/01/ 2014, doi: https://doi.org/10.1016/j.vacuum.2014.05.015.
[94] E. Köhnen *et al.*, "Highly efficient monolithic perovskite silicon tandem solar cells: analyzing the influence of current mismatch on device performance," *Sustainable Energy & Fuels,* 10.1039/C9SE00120D vol. 3, no. 8, pp. 1995–2005, 2019, doi: 10.1039/C9SE00120D.
[95] M. De Bastiani *et al.*, "Efficient bifacial monolithic perovskite/silicon tandem solar cells via bandgap engineering," *Nature Energy,* vol. 6, pp. 1–9, 02/01 2021, doi: 10.1038/s41560-020-00756-8.
[96] E. Aydin *et al.*, "Sputtered transparent electrodes for optoelectronic devices: Induced damage and mitigation strategies," *Matter,* vol. 4, no. 11, pp. 3549–3584, 2021, doi: 10.1016/j.matt.2021.09.021.

[97] F. Saitta *et al.*, "De-coupling of optical and electrical properties in front TCO using the bilayer concept for thin-film solar cells," *Solar Energy Materials and Solar Cells,* vol. 290, p. 113723, 2025/09/15/ 2025, doi: https://doi.org/10.1016/j.solmat.2025.113723.
[98] G. Drewelow *et al.*, "Work function investigations of Al-doped ZnO for band-alignment in electronic and optoelectronic applications," *Applied Surface Science,* vol. 484, pp. 990–998, 2019/08/01/ 2019, doi: https://doi.org/10.1016/j.apsusc.2019.04.079.
[99] C. Han, "High-Mobility TCO-Based Contacting Schemes for c-Si Solar Cells," Doctor of Philosophy, Delft University of Technology, 2022.
[100] J. Yu *et al.*, "Reliability of transparent conductive oxide in ambient acid and implications for silicon solar cells," *eScience,* vol. 4, no. 3, p. 100241, 2024/06/01/ 2024, doi: https://doi.org/10.1016/j.esci.2024.100241.
[101] M. De Bastiani *et al.*, "Mechanical Reliability of Fullerene/Tin Oxide Interfaces in Monolithic Perovskite/Silicon Tandem Cells," *ACS Energy Letters,* vol. 7, no. 2, pp. 827–833, 2022/02/11 2022, doi: 10.1021/acsenergylett.1c02148.
[102] A. A. Said *et al.*, "Perovskite/Silicon Tandem Photovoltaics: Long-Term Stability through Interface Engineering," *Energy & Fuels,* vol. 39, no. 22, pp. 10134–10149, 2025/06/05 2025, doi: 10.1021/acs.energyfuels.5c00511.
[103] Y.-M. Xie *et al.*, "Understanding the role of interconnecting layer on determining monolithic perovskite/organic tandem device carrier recombination properties," *Journal of Energy Chemistry,* vol. 71, 03/01 2022, doi: 10.1016/j.jechem.2022.03.019.
[104] M. De Bastiani, A. Subbiah, E. Aydin, F. Isikgor, T. Allen, and S. De Wolf, "Recombination junctions for efficient monolithic perovskite-based tandem solar cells: Physical principles, properties, processing and prospects," *Materials Horizons,* vol. 7, pp. 2791–2809, 11/01 2020, doi: 10.1039/d0mh00990c.
[105] A. Saeed, L. Wang, and Q. Miao, "High-Performance Perovskite-Based Tandem Solar Cells: Recent Advancement, Challenges, and Steps toward Industrialization," *Solar RRL,* vol. 8, no. 17, p. 2400172, 2024, doi: https://doi.org/10.1002/solr.202400172.
[106] Y. Ko, H. Park, C. Lee, Y. Kang, and Y. Jun, "Recent Progress in Interconnection Layer for Hybrid Photovoltaic Tandems," *Advanced Materials,* vol. 32, no. 51, p. 2002196, 2020, doi: https://doi.org/10.1002/adma.202002196.
[107] Y. Cheng and L. Ding, "Perovskite/Si tandem solar cells: Fundamentals, advances, challenges, and novel applications," *SusMat,* vol. 1, no. 3, pp. 324–344, 2021, doi: https://doi.org/10.1002/sus2.25.
[108] V. Sittinger *et al.*, "Indium-based transparent conductive oxides developed for perovskite and perovskite-silicon tandem solar cell applications," *Surface and Coatings Technology,* vol. 457, p. 129286, 2023/03/25/ 2023, doi: https://doi.org/10.1016/j.surfcoat.2023.129286.
[109] Y. Jin *et al.*, "Efficient and Stable Monolithic Perovskite/Silicon Tandem Solar Cells Enabled by Contact-Resistance-Tunable Indium Tin Oxide Interlayer," *Advanced Materials,* vol. 36, no. 35, p. 2404010, 2024, doi: https://doi.org/10.1002/adma.202404010.
[110] L. Mao *et al.*, "Fully Textured, Production-Line Compatible Monolithic Perovskite/Silicon Tandem Solar Cells Approaching 29% Efficiency," *Advanced Materials,* vol. 34, no. 40, p. 2206193, 2022, doi: https://doi.org/10.1002/adma.202206193.
[111] E. I. Bancu, V. Ion, S. Antohe, and N. D. Scarisoreanu, "Towards AZO Thin Films for Electronic and Optoelectronic Large-Scale Applications," *Crystals,* vol. 15, no. 8, p. 670, 2025. [Online]. Available: https://www.mdpi.com/2073-4352/15/8/670.
[112] J. Du *et al.*, "Highly transparent and conductive indium tin oxide thin films for solar cells grown by reactive thermal evaporation at low temperature," *Applied Physics A,* vol. 117, pp. 815–822, 11/01 2014, doi: 10.1007/s00339-014-8436-x.
[113] H. Wu *et al.*, "Silicon heterojunction back-contact solar cells by laser patterning," *Nature,* vol. 635, no. 8039, pp. 604–609, 2024/11/01 2024, doi: 10.1038/s41586-024-08110-8.
[114] H. Lin *et al.*, "Silicon heterojunction solar cells with up to 26.81% efficiency achieved by electrically optimized nanocrystalline-silicon hole contact layers," *Nature Energy,* vol. 8, no. 8, pp. 789–799, 2023/08/01 2023, doi: 10.1038/s41560-023-01255-2.
[115] A. Shah, "Chapter I-3-A - Thin-Film Silicon Solar Cells**The present chapter is partly an excerpt from the book Thin-Film Silicon Solar Cells, edited by Arvind Shah and published in 2010 by the EPFL Press, Lausanne [1], with contributions by Horst Schade and Friedhelm Finger. For further specialized study and for details, the reader is referred to this book," in

McEvoy's Handbook of Photovoltaics (Third Edition), S. A. Kalogirou Ed.: Academic Press, 2018, pp. 235–307.
[116] A. M. Alfantazi and R. R. Moskalyk, "Processing of indium: a review," *Minerals Engineering,* vol. 16, no. 8, pp. 687–694, 2003/08/01/ 2003, doi: https://doi.org/10.1016/S0892-6875(03)00168-7.
[117] F. Ullmann, W. Gerhartz, Y. S. Yamamoto, F. T. Campbell, R. Pfefferkorn, and J. F. Rounsaville, *Ullmann's Encyclopedia of Industrial Chemistry*. VCH, 1992.
[118] A. Mackie, "Indium Corporation: Igniting an Electronics Materials Renaissance in Upstate New York [Company Profile]," *IEEE Power Electronics Magazine,* vol. 7, no. 2, pp. 76–79, 2020, doi: 10.1109/MPEL.2020.2985855.
[119] L. Wang *et al.*, "Sustainability evaluations on material consumption for terawatt-scale manufacturing of silicon-based tandem solar cells," *Progress in Photovoltaics: Research and Applications,* vol. 31, no. 12, pp. 1442–1454, 2023, doi: https://doi.org/10.1002/pip.3687.
[120] C. Yu *et al.*, "Silicon solar cell with undoped tin oxide transparent electrode," *Nature Energy,* vol. 8, no. 10, pp. 1119–1125, 2023/10/01 2023, doi: 10.1038/s41560-023-01331-7.
[121] M. Chu *et al.*, "Atomic Layer Deposition-Based Ultrathin SnO x Buffer for High Passivation Quality in Silicon Heterojunction Solar Cells," *ACS Photonics,* vol. 12, 08/29 2025, doi: 10.1021/acsphotonics.5c00467.
[122] T. Koida, T. Matsui, and H. Sai, "Amorphous SnO2 as Earth-Abundant Stable Transparent Conductive Oxide and Its Application to Si Heterojunction Solar Cells," *Solar RRL,* vol. 7, no. 18, p. 2300381, 2023, doi: https://doi.org/10.1002/solr.202300381.
[123] J. Guo *et al.*, "Low-Cost Tin Oxide Transparent Conductive Films for Silicon Heterojunction Solar Cells," *Advanced Functional Materials,* vol. 34, no. 45, p. 2407273, 2024, doi: https://doi.org/10.1002/adfm.202407273.
[124] Y. Zakaria *et al.*, "Study of wide bandgap SnOx thin films grown by a reactive magnetron sputtering via a two-step method," *Scientific Reports,* vol. 12, no. 1, p. 15294, 2022/09/12 2022, doi: 10.1038/s41598-022-19270-w.
[125] A. Mdallal, A. Yasin, M. Mahmoud, M. A. Abdelkareem, A. H. Alami, and A. G. Olabi, "A comprehensive review on solar photovoltaics: Navigating generational shifts, innovations, and sustainability," *Sustainable Horizons,* vol. 13, p. 100137, 2025/03/01/ 2025, doi: https://doi.org/10.1016/j.horiz.2025.100137.
[126] S. Khan and E. Stamate, "Comparative Study of Aluminum-Doped Zinc Oxide, Gallium-Doped Zinc Oxide and Indium-Doped Tin Oxide Thin Films Deposited by Radio Frequency Magnetron Sputtering," *Nanomaterials,* vol. 12, no. 9, p. 1539, 2022. [Online]. Available: https://www.mdpi.com/2079-4991/12/9/1539.
[127] V. Sharma, "11 - Transparent conducting electrodes based on zinc oxide," in *Nanostructured Zinc Oxide*, K. Awasthi Ed.: Elsevier, 2021, pp. 291–318.
[128] J. Brugger, *Encyclopedia of Earth Sciences Series*. Springer Nature, 2016.
[129] S. Sood *et al.*, "Enhancing Optoelectronic Performance Through Rare-Earth-Doped ZnO: Insights and Applications," *Photonics,* vol. 12, no. 5, p. 454, 2025. [Online]. Available: https://www.mdpi.com/2304-6732/12/5/454.
[130] M. Samadi, M. Zirak, A. Naseri, E. Khorashadizade, and A. Z. Moshfegh, "Recent progress on doped ZnO nanostructures for visible-light photocatalysis," *Thin Solid Films,* vol. 605, pp. 2–19, 2016/04/30/ 2016, doi: https://doi.org/10.1016/j.tsf.2015.12.064.
[131] S. Mansy, H. Musleh, S. Shaat, J. Asad, and N. AlDahoudi, "Computational and experimental study of wurtzite phase ZnO nanoparticles," *Materials Today Communications,* vol. 35, p. 105688, 2023/06/01/ 2023, doi: https://doi.org/10.1016/j.mtcomm.2023.105688.
[132] R. Shannon, "Revised Effective Ionic Radii and Systematic Studies of Interatomic Distances in Halides and Chalcogenides," *Acta Cryst,* vol. 32, pp. 751–767, 01/01 1976.
[133] J. C. Phillips, "Ionicity of the Chemical Bond in Crystals," *Reviews of Modern Physics,* vol. 42, no. 3, pp. 317–356, 07/01/ 1970, doi: 10.1103/RevModPhys.42.317.
[134] H. Karzel *et al.*, "Lattice dynamics and hyperfine interactions in ZnO and ZnSe at high external pressures," *Physical Review B,* vol. 53, no. 17, pp. 11425–11438, 05/01/ 1996, doi: 10.1103/PhysRevB.53.11425.

[135] A. Janotti and C. G. Van de Walle, "New insights into the role of native point defects in ZnO," *Journal of Crystal Growth,* vol. 287, no. 1, pp. 58–65, 2006/01/18/ 2006, doi: https://doi.org/10.1016/j.jcrysgro.2005.10.043.
[136] H. Shimizu and W. Sato, "Interactions of intrinsic defects formed in ZnO and their contribution to electric conductivity," *Journal of Applied Physics,* vol. 126, no. 12, 2019, doi: 10.1063/1.5120887.
[137] V. Gurylev and T. P. Perng, "Defect engineering of ZnO: Review on oxygen and zinc vacancies," *Journal of the European Ceramic Society,* vol. 41, no. 10, pp. 4977–4996, 2021/08/01/ 2021, doi: https://doi.org/10.1016/j.jeurceramsoc.2021.03.031.
[138] M. R. Ahmad, A. A. Ansari, M. Dhayal, and R. Lv, "Bandgap engineering of ZnO nanomaterials for enhanced electrochemical and photocatalytic efficiency," *Renewable and Sustainable Energy Reviews,* vol. 219, p. 115767, 2025/09/01/ 2025, doi: https://doi.org/10.1016/j.rser.2025.115767.
[139] D. Zhang, W. Yu, L. Zhang, and X. Hao, "Progress in the Synthesis and Application of Transparent Conducting Film of AZO (ZnO:Al)," (in eng), *Materials (Basel),* vol. 16, no. 16, Aug 9 2023, doi: 10.3390/ma16165537.
[140] J. Wang, L. Meng, Y. Qi, M. Li, G. Shi, and M. Liu, "The Al-doping contents dependence of the crystal growth and energy band structure in Al:ZnO thin films," *Journal of Crystal Growth,* vol. 311, no. 8, pp. 2305–2308, 2009/04/01/ 2009, doi: https://doi.org/10.1016/j.jcrysgro.2009.02.039.
[141] J. Patel, R. K. Sharme, M. A. Quijada, and M. M. Rana, "A Review of Transparent Conducting Films (TCFs): Prospective ITO and AZO Deposition Methods and Applications," *Nanomaterials,* vol. 14, no. 24, p. 2013, 2024. [Online]. Available: https://www.mdpi.com/2079-4991/14/24/2013.
[142] A. Janotti and C. G. Van de Walle, "Fundamentals of zinc oxide as a semiconductor," *Reports on Progress in Physics,* vol. 72, no. 12, p. 126501, 2009/10/22 2009, doi: 10.1088/0034-4885/72/12/126501.
[143] A. Janotti and C. G. Van de Walle, "Native point defects in ZnO," *Physical Review B,* vol. 76, no. 16, p. 165202, 10/04/ 2007, doi: 10.1103/PhysRevB.76.165202.
[144] Ü. Özgür *et al.*, "A comprehensive review of ZnO materials and devices," *Journal of Applied Physics,* vol. 98, no. 4, 2005, doi: 10.1063/1.1992666.
[145] K. Vanheusden, W. L. Warren, C. H. Seager, D. R. Tallant, J. A. Voigt, and B. E. Gnade, "Mechanisms behind green photoluminescence in ZnO phosphor powders," *Journal of Applied Physics,* vol. 79, no. 10, pp. 7983–7990, 1996, doi: 10.1063/1.362349.
[146] C. Klingshirn, R. Hauschild, J. Fallert, and H. Kalt, "Room-temperature stimulated emission of ZnO: Alternatives to excitonic lasing," *Physical Review B,* vol. 75, 03/14 2007, doi: 10.1103/PhysRevB.75.115203.
[147] M. Mazur, M. Kiliszkiewicz, W. Posadowski, J. Domaradzki, A. Małachowska, and P. Sokołowski, "A Comprehensive Investigation of the Mechanical and Tribological Properties of AZO Transparent Conducting Oxide Thin Films Deposited by Medium Frequency Magnetron Sputtering," (in eng), *Materials (Basel),* vol. 17, no. 1, Dec 23 2023, doi: 10.3390/ma17010081.
[148] J. Reinders *et al.*, "Room Temperature Pulsed Laser Deposition of Aluminum Zinc Oxide (AZO): Enabling Scalable Indium-Free Transparent Conductive Oxides," *Advanced Functional Materials,* vol. 35, 11/20 2024, doi: 10.1002/adfm.202418069.
[149] F. U. Hamelmann, "Thin film zinc oxide deposited by CVD and PVD," *Journal of Physics: Conference Series,* vol. 764, no. 1, p. 012001, 2016/10/01 2016, doi: 10.1088/1742-6596/764/1/012001.
[150] R. W. Johnson, A. Hultqvist, and S. F. Bent, "A brief review of atomic layer deposition: from fundamentals to applications," *Materials Today,* vol. 17, no. 5, pp. 236–246, 2014/06/01/ 2014, doi: https://doi.org/10.1016/j.mattod.2014.04.026.
[151] B. Macco and W. M. M. Kessels, "Atomic layer deposition of conductive and semiconductive oxides," *Applied Physics Reviews,* vol. 9, no. 4, 2022, doi: 10.1063/5.0116732.
[152] J. Cai *et al.*, "A revisit to atomic layer deposition of zinc oxide using diethylzinc and water as precursors," *Journal of Materials Science,* vol. 54, no. 7, pp. 5236–5248, 2019/04/01 2019, doi: 10.1007/s10853-018-03260-3.

[153] Y. Wu, S. Potts, P. Hermkens, H. Knoops, F. Roozeboom, and W. M. M. Kessels, "Enhanced Doping Efficiency of Al-Doped ZnO by Atomic Layer Deposition Using Dimethylaluminum Isopropoxide as an Alternative Aluminum Precursor," *Chemistry of Materials,* vol. 25, pp. 4619–4622, 11/12 2013, doi: 10.1021/cm402974j.
[154] J. Elam and S. M. George, "Growth of ZnO/Al 2 O 3 Alloy Films Using Atomic Layer Deposition Techniques," *Chemistry of Materials - CHEM MATER,* vol. 15, pp. 1020–1028, 02/01 2003, doi: 10.1021/cm020607+.
[155] D. R. Zywotko and S. M. George, "Thermal Atomic Layer Etching of ZnO by a “Conversion-Etch” Mechanism Using Sequential Exposures of Hydrogen Fluoride and Trimethylaluminum," *Chemistry of Materials,* vol. 29, no. 3, pp. 1183–1191, 2017/02/14 2017, doi: 10.1021/acs.chemmater.6b04529.
[156] A. Fischer, A. Routzahn, S. M. George, and T. Lill, "Thermal atomic layer etching: A review," *Journal of Vacuum Science & Technology A,* vol. 39, no. 3, 2021, doi: 10.1116/6.0000894.
[157] T. Pisarkiewicz, K. Zakrzewska, and E. Leja, "Scattering of charge carriers in transparent and conducting thin oxide films with a non-parabolic conduction band," *Thin Solid Films,* vol. 174, pp. 217–223, 1989/07/01/ 1989, doi: https://doi.org/10.1016/0040-6090(89)90892-4.
[158] A. Yanguas-Gil, K. E. Peterson, and J. W. Elam, "Controlled Dopant Distribution and Higher Doping Efficiencies by Surface-Functionalized Atomic Layer Deposition," *Chemistry of Materials,* vol. 23, no. 19, pp. 4295–4297, 2011/10/11 2011, doi: 10.1021/cm2014576.
[159] S. E. Potts, G. Dingemans, C. Lachaud, and W. M. M. Kessels, "Plasma-enhanced and thermal atomic layer deposition of Al2O3 using dimethylaluminum isopropoxide, [Al(CH3)2(μ-OiPr)]2, as an alternative aluminum precursor," *Journal of Vacuum Science & Technology A,* vol. 30, no. 2, 2012, doi: 10.1116/1.3683057.
[160] D.-J. Lee, K.-J. Kim, S. Kim, J.-Y. Kwon, J. Xu, and K.-B. Kim, "Atomic layer deposition of Ti-doped ZnO films with enhanced electron mobility," *J. Mater. Chem. C,* vol. 1, 06/05 2013, doi: 10.1039/C3TC30469H.
[161] H. K. Park and J. Heo, "Improved efficiency of aluminum doping in ZnO thin films grown by atomic layer deposition," *Applied Surface Science,* vol. 309, pp. 133–137, 2014/08/01/ 2014, doi: https://doi.org/10.1016/j.apsusc.2014.04.205.
[162] V. Vandalon and W. M. M. Kessels, "Revisiting the growth mechanism of atomic layer deposition of Al2O3: A vibrational sum-frequency generation study," *Journal of Vacuum Science & Technology A,* vol. 35, no. 5, 2017, doi: 10.1116/1.4993597.
[163] S. B. Basuvalingam, B. Macco, H. C. M. Knoops, J. Melskens, W. M. M. Kessels, and A. A. Bol, "Comparison of thermal and plasma-enhanced atomic layer deposition of niobium oxide thin films," *Journal of Vacuum Science & Technology A,* vol. 36, no. 4, 2018, doi: 10.1116/1.5034097.
[164] J.-S. Na, Q. Peng, G. Scarel, and G. N. Parsons, "Role of Gas Doping Sequence in Surface Reactions and Dopant Incorporation during Atomic Layer Deposition of Al-Doped ZnO," *Chemistry of Materials,* vol. 21, no. 23, pp. 5585–5593, 2009/12/08 2009, doi: 10.1021/cm901404p.
[165] C. J. Cho, J. J. Pyeon, C. S. Hwang, J.-S. Kim, and S. K. Kim, "Atomic layer deposition of Ta-doped SnO2 films with enhanced dopant distribution for thermally stable capacitor electrode applications," *Applied Surface Science,* vol. 497, p. 143804, 2019/12/15/ 2019, doi: https://doi.org/10.1016/j.apsusc.2019.143804.
[166] D. Garcia-Alonso, S. E. Potts, C. A. A. van Helvoirt, M. A. Verheijen, and W. M. M. Kessels, "Atomic layer deposition of B-doped ZnO using triisopropyl borate as the boron precursor and comparison with Al-doped ZnO," *Journal of Materials Chemistry C,* 10.1039/C4TC02707H vol. 3, no. 13, pp. 3095–3107, 2015, doi: 10.1039/C4TC02707H.
[167] S. E. Potts, H. B. Profijt, R. Roelofs, and W. M. M. Kessels, "Room-Temperature ALD of Metal Oxide Thin Films by Energy-Enhanced ALD," *Chemical Vapor Deposition,* vol. 19, no. 4-6, pp. 125–133, 2013, doi: https://doi.org/10.1002/cvde.201207033.
[168] G. Dingemans, R. Seguin, P. Engelhart, M. C. M. v. d. Sanden, and W. M. M. Kessels, "Silicon surface passivation by ultrathin Al2O3 films synthesized by thermal and plasma atomic layer deposition," *physica status solidi (RRL) – Rapid Research Letters,* vol. 4, no. 1-2, pp. 10–12, 2010, doi: https://doi.org/10.1002/pssr.200903334.

[169] C. Guerra-Nuñez, M. Döbeli, J. Michler, and I. Utke, "Reaction and Growth Mechanisms in Al2O3 deposited via Atomic Layer Deposition: Elucidating the Hydrogen Source," *Chemistry of Materials,* vol. 29, no. 20, pp. 8690–8703, 2017/10/24 2017, doi: 10.1021/acs.chemmater.7b02759.
[170] J. Panigrahi, Vandana, R. Singh, C. M. S. Rauthan, and P. K. Singh, "Crystalline silicon surface passivation by thermal ALD deposited Al doped ZnO thin films," *AIP Advances,* vol. 7, no. 3, 2017, doi: 10.1063/1.4979326.
[171] M. K. Sharpe *et al.*, "Characterisation of solar cell nanolayer interfaces using time-of-flight elastic recoil detection analysis," *Solar Energy Materials and Solar Cells,* vol. 296, p. 114074, 2026/03/01/ 2026, doi: https://doi.org/10.1016/j.solmat.2025.114074.
[172] Y. Wang *et al.*, "Impact of precursor dosing on the surface passivation of AZO/AlOx stacks formed using atomic layer deposition††Electronic supplementary information (ESI) available. See DOI: https://doi.org/10.1039/d4ya00552j," *Energy Advances,* vol. 4, no. 4, pp. 553–564, 2024/11/20/ 2024, doi: https://doi.org/10.1039/d4ya00552j.
[173] U. Sharopov *et al.*, "New challenges for lithium fluoride: From dosimeter to solid-state batteries (review)," *Next Materials,* vol. 8, p. 100548, 03/02 2025, doi: 10.1016/j.nxmate.2025.100548.
[174] W. Kern, "The Evolution of Silicon Wafer Cleaning Technology," *Journal of The Electrochemical Society,* vol. 137, no. 6, p. 1887, 1990/06/01 1990, doi: 10.1149/1.2086825.
[175] M. Groner, F. Fabreguette, J. Elam, and S. M. George, "Low-Temperature Al$_2$O$_3$ Atomic Layer Deposition," *Chemistry of Materials,* vol. 16, pp. 639–645, 02/01 2004, doi: 10.1021/cm0304546.
[176] H. K. Park, B. S. Yang, S. Park, M. S. Kim, J. C. Shin, and J. Heo, "Purge-time-dependent growth of ZnO thin films by atomic layer deposition," *Journal of Alloys and Compounds,* vol. 605, pp. 124–130, 2014/08/25/ 2014, doi: https://doi.org/10.1016/j.jallcom.2014.03.169.
[177] S.-Y. Ham, Z. Jin, S. Shin, M. Kim, M. Seo, and Y.-S. Min, "Investigation of abnormally high growth-per-cycle in atomic layer deposition of Al2O3 using trimethylaluminum and water," *Applied Surface Science,* vol. 571, p. 151282, 2022/01/01/ 2022, doi: https://doi.org/10.1016/j.apsusc.2021.151282.
[178] T. Dhakal, D. Vanhart, R. Christian, A. Nandur, A. Sharma, and C. R. Westgate, "Growth morphology and electrical/optical properties of Al-doped ZnO thin films grown by atomic layer deposition," *Journal of Vacuum Science & Technology A,* vol. 30, no. 2, 2012, doi: 10.1116/1.3687939.
[179] K. G. Sun, Y. V. Li, D. B. Saint John, and T. N. Jackson, "pH-Controlled Selective Etching of Al2O3 over ZnO," *ACS Applied Materials & Interfaces,* vol. 6, no. 10, pp. 7028–7031, 2014/05/28 2014, doi: 10.1021/am501912q.
[180] H. Nagel, C. Berge, and A. G. Aberle, "Generalized analysis of quasi-steady-state and quasi-transient measurements of carrier lifetimes in semiconductors," *Journal of Applied Physics,* vol. 86, no. 11, pp. 6218–6221, 1999, doi: 10.1063/1.371633.
[181] ""Oxford interfaces lab: Sinton analysis" " https://github.com/OxfordInterfacesLab/SintonAnalysis (accessed.
[182] H. Mäckel and K. Varner. *On the determination of the emitter saturation current density from lifetime measurements of silicon devices*, doi: 10.1002/pip.2167.
[183] T. Trupke, R. A. Bardos, M. C. Schubert, and W. Warta, "Photoluminescence imaging of silicon wafers," *Applied Physics Letters,* vol. 89, no. 4, 2006, doi: 10.1063/1.2234747.
[184] F. Qing *et al.*, "A general and simple method for evaluating the electrical transport performance of graphene by the van der Pauw-Hall measurement," (in eng), *Sci Bull (Beijing),* vol. 63, no. 22, pp. 1521–1526, Nov 30 2018, doi: 10.1016/j.scib.2018.10.007.
[185] L. J. v. d. PAUW, "A METHOD OF MEASURING SPECIFIC RESISTIVITY AND HALL EFFECT OF DISCS OF ARBITRARY SHAPE," in *Semiconductor Devices: Pioneering Papers*, pp. 174–182.
[186] R. Chwang, B. J. Smith, and C. R. Crowell, "Contact size effects on the van der Pauw method for resistivity and Hall coefficient measurement," *Solid-State Electronics,* vol. 17, no. 12, pp. 1217–1227, 1974/12/01/ 1974, doi: https://doi.org/10.1016/0038-1101(74)90001-X.

[187] C. Peest, C. Schinke, R. Brendel, J. Schmidt, and K. Bothe, "Instrumentation-related uncertainty of reflectance and transmittance measurements with a two-channel spectrophotometer," *Review of Scientific Instruments,* vol. 88, no. 1, 2017, doi: 10.1063/1.4973633.
[188] L. A. Aarne Kasikov, "Calculating the Absorption Edge of Thin Films," *Bulgarian Journal of Physics,* vol. 51, pp. 311–338, 2024, doi: https://doi.org/10.55318/bgjp.2024.51.4.311.
[189] J. Tauc, R. Grigorovici, and A. Vancu, "Optical Properties and Electronic Structure of Amorphous Germanium," *physica status solidi (b),* vol. 15, no. 2, pp. 627–637, 1966, doi: https://doi.org/10.1002/pssb.19660150224.
[190] B. D. Viezbicke, S. Patel, B. E. Davis, and D. P. Birnie III, "Evaluation of the Tauc method for optical absorption edge determination: ZnO thin films as a model system," *physica status solidi (b),* vol. 252, no. 8, pp. 1700–1710, 2015, doi: https://doi.org/10.1002/pssb.201552007.
[191] E. A. Davis and N. F. Mott, "Conduction in non-crystalline systems V. Conductivity, optical absorption and photoconductivity in amorphous semiconductors," *Philosophical Magazine,* vol. 22, no. 179, pp. 0903–0922, 1970.
[192] H. Fujiwara, *Spectroscopic Ellipsometry: Principles and Applications*. 2007.
[193] J. Woollam, B. Johs, C. Herzinger, J. Hilfiker, R. Synowicki, and C. Bungay, "Overview of Variable Angle Spectroscopic Ellipsometry (VASE), Part I: Basic Theory and Typical Applications," *Proceedings of SPIE - The International Society for Optical Engineering,* vol. -1, pp. 3–28, 06/30 1999.
[194] D. Briggs and M. P. Seah, *Practical Surface Analysis, Auger and X-ray Photoelectron Spectroscopy*. Wiley, 1990.
[195] E. A. Kraut, R. W. Grant, J. R. Waldrop, and S. P. Kowalczyk, "Precise Determination of the Valence-Band Edge in X-Ray Photoemission Spectra: Application to Measurement of Semiconductor Interface Potentials," *Physical Review Letters,* vol. 44, no. 24, pp. 1620–1623, 06/16/ 1980, doi: 10.1103/PhysRevLett.44.1620.
[196] N. Fairley *et al.*, "Systematic and collaborative approach to problem solving using X-ray photoelectron spectroscopy," *Applied Surface Science Advances,* vol. 5, p. 100112, 09/01 2021, doi: 10.1016/j.apsadv.2021.100112.
[197] F. J. Himpsel, F. R. McFeely, A. Taleb-Ibrahimi, J. A. Yarmoff, and G. Hollinger, "Microscopic structure of the ${\mathrm{SiO}}_{2}$/Si interface," *Physical Review B,* vol. 38, no. 9, pp. 6084–6096, 09/15/ 1988, doi: 10.1103/PhysRevB.38.6084.
[198] "PV LightHouse. p. Cells calculators-Cells calculators." https://www.pvlighthouse.com.au (accessed.
[199] G. Held *et al.*, "Ambient-pressure endstation of the Versatile Soft X-ray (VerSoX) beamline at Diamond Light Source," *Journal of Synchrotron Radiation,* vol. 27, pp. 1153–1166, 08/17 2020, doi: 10.1107/S1600577520009157.
[200] J. Vickerman and I. Gilmore, *Surface Analysis - The Principal Techniques: Second Edition*. 2009, pp. 1–666.
[201] S. Fearn, *Secondary Ion Mass Spectrometry and Its Application to Materials Science (Second Edition)*: IOP Publishing, 2025. [Online]. Available: https://doi.org/10.1088/978-0-7503-3331-3.
[202] T. Grehl, R. Möllers, and E. Niehuis, "Low energy dual beam depth profiling: Influence of sputter and analysis beam parameters on profile performance using TOF-SIMS," *Applied Surface Science - APPL SURF SCI,* vol. 203, pp. 277–280, 01/15 2003, doi: 10.1016/S0169-4332(02)00653-0.
[203] U. Pietsch, V. Holy, and T. Baumbach, *High-Resolution X-Ray Scattering: From Thin Films to Lateral Nanostructures*. Springer New York, 2004.
[204] J. Stangl, C. Mocuta, V. Chamard, and D. Carbone, *Nanobeam X-Ray Scattering: Probing Matter at the Nanoscale*. 2013.
[205] C. Mocuta, P. Ohresser, and A. Barbier, *Artificial laminar oxide multiferroic magnetoelectric thin film structures: Elaboration methods and study by synchrotron radiation techniques*. 2020.
[206] M. Björck and G. Andersson, "GenX: An extensible X-ray reflectivity refinement program utilizing differential evolution," *Journal of Applied Crystallography - J APPL CRYST,* vol. 40, pp. 1174–1178, 12/01 2007, doi: 10.1107/S0021889807045086.

[207] P. Colombi *et al.*, "Reproducibility in X-ray reflectometry: Results from the first world-wide round-robin experiment," *Journal of Applied Crystallography,* vol. 41, pp. 143–152, 02/01 2008, doi: 10.1107/S0021889807051904.
[208] R. J. Matyi *et al.*, "The international VAMAS project on X-ray reflectivity measurements for evaluation of thin films and multilayers — Preliminary results from the second round-robin," *Thin Solid Films,* vol. 516, no. 22, pp. 7962–7966, 2008/09/30/ 2008, doi: https://doi.org/10.1016/j.tsf.2008.04.004.
[209] T. C. Huang, R. Gilles, and G. Will, "Thin-film thickness and density determination from x-ray reflectivity data using a conventional power diffractometer," *Thin Solid Films,* vol. 230, no. 2, pp. 99–101, 1993/08/10/ 1993, doi: https://doi.org/10.1016/0040-6090(93)90499-F.
[210] L. J. Bannenberg, D. J. Verhoeff, N. Jonckers Newton, M. Thijs, and H. Schreuders, "Structural and Optical Properties of Thin Film β-Ta upon Exposure to Hydrogen to Asses Its Applicability as Hydrogen Sensing Material," *ACS Applied Nano Materials,* vol. 7, no. 2, pp. 1757–1766, 2024, doi: 10.1021/acsanm.3c04902.
[211] P. F. Fewster, *X-ray Scattering from Semiconductors*. Imperial College Press, 2000.
[212] M. Birkholz, *Thin Film Analysis by X-Ray Scattering*. 2005.
[213] L. J. Bannenberg *et al.*, "Universality of the helimagnetic transition in cubic chiral magnets: Small angle neutron scattering and neutron spin echo spectroscopy studies of FeCoSi," *Physical Review B,* vol. 95, no. 14, p. 144433, 04/28/ 2017, doi: 10.1103/PhysRevB.95.144433.
[214] M. W. A. Skoda, "Recent developments in the application of X-ray and neutron reflectivity to soft-matter systems," *Current Opinion in Colloid & Interface Science,* vol. 42, pp. 41–54, 2019/08/01/ 2019, doi: https://doi.org/10.1016/j.cocis.2019.03.003.
[215] H. Fritzsche *et al.*, "A systematic neutron reflectometry study on hydrogen absorption in thin Mg1-xAlx alloy films Special issue on Neutron Scattering in Canada," *Canadian Journal of Physics,* vol. 88, no. 10, pp. 723–728, 2010/04/30/ 2010, doi: https://doi.org/10.1139/P09-085.
[216] M. Shibayama, "Neutron Reflectometry," in *Introduction to Soft Matter Neutron Scattering*, M. Shibayama Ed. Singapore: Springer Nature Singapore, 2026, pp. 155–180.
[217] A. A. v. Well, V. O. D. Haan, and H. Fredrikze, "ROG, the new neutron reflectometer at IRI, Delft," *Physica B-condensed Matter,* vol. 198, pp. 217–219, 1994.
[218] D. Schroder, "Semiconductor Material And Device Characterization," *Semiconductor Material and Device Characterization, 3rd Edition, by Dieter K. Schroder, pp. 840. ISBN 0-471-73906-5. Wiley-VCH , December 2005.,* vol. 2, 12/01 2005, doi: 10.1002/0471749095.ch2.
[219] A. Klein, "Transparent conducting oxides: Electronic structure–property relationship from photoelectron spectroscopy with in situ sample preparation," *Journal of the American Ceramic Society,* vol. 96, no. 2, pp. 331–345, 2013.
[220] W. A. Zisman, "A NEW METHOD OF MEASURING CONTACT POTENTIAL DIFFERENCES IN METALS," *Review of Scientific Instruments,* vol. 3, no. 7, pp. 367–370, 1932, doi: 10.1063/1.1748947.
[221] L. Kronik and Y. Shapira, "Surface photovoltage phenomena: theory, experiment, and applications," *Surface Science Reports,* vol. 37, no. 1, pp. 1–206, 1999/12/01/ 1999, doi: https://doi.org/10.1016/S0167-5729(99)00002-3.
[222] T. Dittrich and S. Fengler, *Surface Photovoltage Analysis of Photoactive Materials*. World Scientific, 2019.
[223] R. Bonilla, "Modelling of Kelvin probe surface voltage and photovoltage in dielectric-semiconductor interfaces," *Materials Research Express,* vol. 9, 08/01 2022, doi: 10.1088/2053-1591/ac84c8.
[224] T. Dittrich, S. Fengler, and M. Franke, "Transient surface photovoltage measurement over 12 orders of magnitude in time," *Review of Scientific Instruments,* vol. 88, no. 5, 2017, doi: 10.1063/1.4983079.
[225] T. Dittrich and S. Fengler, "Transitions in polycrystalline diamond probed by steady state, modulated and transient surface photovoltage spectroscopy," *Semiconductor Science and Technology,* vol. 38, no. 1, p. 015015, 2022/12/12 2023, doi: 10.1088/1361-6641/aca788.
[226] S. Fengler *et al.*, "Charge Transfer in c-Si(n++)/TiO2(ALD) at the Amorphous/Anatase Transition: A Transient Surface Photovoltage Spectroscopy Study," *ACS Applied Materials*

& Interfaces, vol. 12, no. 2, pp. 3140–3149, 2020/01/15 2020, doi: 10.1021/acsami.9b17592.
[227] S. Fengler, E. Zillner, and T. Dittrich, "Density of Surface States at CdSe Quantum Dots by Fitting of Temperature-Dependent Surface Photovoltage Transients with Random Walk Simulations," *The Journal of Physical Chemistry C,* vol. 117, no. 12, pp. 6462–6468, 2013/03/28 2013, doi: 10.1021/jp4002687.
[228] T. Dittrich, S. Fengler, and N. Nickel, "Surface Photovoltage Spectroscopy over Wide Time Domains for Semiconductors with Ultrawide Bandgap: Example of Gallium Oxide," *physica status solidi (a),* vol. 218, no. 18, p. 2100167, 2021, doi: https://doi.org/10.1002/pssa.202100167.
[229] H. Angermann, "Characterization of wet-chemically treated silicon interfaces by surface photovoltage measurements," *Analytical and Bioanalytical Chemistry,* vol. 374, no. 4, pp. 676–680, 2002/10/01 2002, doi: 10.1007/s00216-002-1450-4.
[230] T. Dittrich, V. Duzhko, F. Koch, V. Kytin, and J. Rappich, "Trap-limited photovoltage in ultrathin metal oxide layers," *Physical Review B,* vol. 65, no. 15, p. 155319, 04/04/ 2002, doi: 10.1103/PhysRevB.65.155319.
[231] L. Tutsch *et al.*, "Implementing transparent conducting oxides by DC sputtering on ultrathin SiOx / poly-Si passivating contacts," *Solar Energy Materials and Solar Cells,* vol. 200, p. 109960, 2019/09/15/ 2019, doi: https://doi.org/10.1016/j.solmat.2019.109960.
[232] G. Gregory, C. Feit, Z. Gao, P. Banerjee, T. Jurca, and K. O. Davis, "Improving the Passivation of Molybdenum Oxide Hole-Selective Contacts with 1 nm Hydrogenated Aluminum Oxide Films for Silicon Solar Cells," *physica status solidi (a),* vol. 217, no. 15, p. 2000093, 2020, doi: https://doi.org/10.1002/pssa.202000093.
[233] E.-C. Yun *et al.*, "Demonstration of Rapid Deuterium Annealing for High-Performance MOSFETs With Reduced Thermal Budget," *IEEE Transactions on Electron Devices,* vol. PP, pp. 1–5, 01/01 2025, doi: 10.1109/TED.2025.3615176.
[234] G. Dingemans and W. M. M. Kessels, "Status and prospects of Al2O3-based surface passivation schemes for silicon solar cells," *Journal of Vacuum Science & Technology A,* vol. 30, no. 4, 2012, doi: 10.1116/1.4728205.
[235] A. Liu, C. Sun, and D. Macdonald, "Hydrogen passivation of interstitial iron in boron-doped multicrystalline silicon during annealing," *Journal of Applied Physics,* vol. 116, no. 19, 2014, doi: 10.1063/1.4901831.
[236] K. A. Abdullin, G. Cicero, L. V. Gritsenko, S. E. Kumekov, and A. A. Markhabaeva, "Effect of annealing and hydrogen plasma treatment on the luminescence and persistent photoconductivity of polycrystalline ZnO films," *Journal of Applied Physics,* vol. 121, no. 24, 2017, doi: 10.1063/1.4989826.
[237] S. K. Misra and N. K. Pandey, "Study of activation energy and humidity sensing application of nanostructured Cu-doped ZnO thin films," *Journal of Materials Research,* vol. 31, no. 20, pp. 3214–3222, 2016/10/01 2016, doi: 10.1557/jmr.2016.322.
[238] S. Mishra *et al.*, "Structural Properties of Thin ZnO Films Deposited by ALD under O-Rich and Zn-Rich Growth Conditions and Their Relationship with Electrical Parameters," *Materials,* vol. 14, no. 14, p. 4048, 2021. [Online]. Available: https://www.mdpi.com/1996-1944/14/14/4048.
[239] Z.-Y. Ye *et al.*, "Structural, electrical, and optical properties of Ti-doped ZnO films fabricated by atomic layer deposition," *Nanoscale Research Letters,* vol. 8, no. 1, p. 108, 2013/02/27 2013, doi: 10.1186/1556-276X-8-108.
[240] Z. Gao and P. Banerjee, "Review Article: Atomic layer deposition of doped ZnO films," *Journal of Vacuum Science & Technology A,* vol. 37, no. 5, 2019, doi: 10.1116/1.5112777.
[241] J. Schumann *et al.*, "Promoting Strong Metal Support Interaction: Doping ZnO for Enhanced Activity of Cu/ZnO:M (M = Al, Ga, Mg) Catalysts," *ACS Catalysis,* vol. 5, no. 6, pp. 3260–3270, 2015/06/05 2015, doi: 10.1021/acscatal.5b00188.
[242] A. Wang *et al.*, "Effects of doping and annealing on properties of ZnO films grown by atomic layer deposition," *Nanoscale Research Letters,* vol. 10, no. 1, p. 75, 2015/02/18 2015, doi: 10.1186/s11671-015-0801-y.
[243] S. Horzum, E. Bulduk, D. Şener, and T. Serin, "Comparison of characteristic properties of Al, Ga, and In-doped ZnO thin films formed by sol-gel method," *Superlattices and*

Microstructures, vol. 159, p. 107034, 2021/11/01/ 2021, doi: https://doi.org/10.1016/j.spmi.2021.107034.
[244] B. Klehn and U. Kunze, "Nanolithography with an atomic force microscope by means of vector-scan controlled dynamic plowing," *Journal of Applied Physics,* vol. 85, no. 7, pp. 3897–3903, 1999, doi: 10.1063/1.369761.
[245] T. Ivanova, A. Harizanova, T. Koutzarova, B. Vertruyen, and R. Closset, "Deposition of Sol–Gel ZnO:Mg Films and Investigation of Their Structural and Optical Properties," *Materials,* vol. 15, no. 24, p. 8883, 2022. [Online]. Available: https://www.mdpi.com/1996-1944/15/24/8883.
[246] I. Jahan, J. Arellano, and Z. Shi, "Carrier Transport Mechanisms in Polycrystalline Semiconductors: From Grain Boundary Physics to Device Performance," *Journal of Materials Chemistry C,* vol. 13, 01/01 2025, doi: 10.1039/D5TC03750F.
[247] A. Wibowo *et al.*, "ZnO nanostructured materials for emerging solar cell applications," *RSC Advances,* vol. 10, pp. 42838–42859, 11/24 2020, doi: 10.1039/D0RA07689A.
[248] H. Zhang, F. Qu, and H. Li, "Front Transparent Passivation of CIGS-Based Solar Cells via AZO," *Molecules,* vol. 27, no. 19, p. 6285, 2022. [Online]. Available: https://www.mdpi.com/1420-3049/27/19/6285.
[249] R. Puurunen, "Surface Chemistry of Atomic Layer Deposition: A Case Study for the Trimethylaluminum/Water Process," *Journal of Applied Physics,* vol. 97, 06/30 2005, doi: 10.1063/1.1940727.
[250] M. B. Smith, "The monomer−dimer equilibria of liquid aliminum alkyls: III. Trimethylaluminum: the monomer−dimer equilibria of liquid and gaseous trimethylaluminum and triethylaluminum," *Journal of Organometallic Chemistry,* vol. 46, no. 1, pp. 31–49, 1972/12/01/ 1972, doi: https://doi.org/10.1016/S0022-328X(00)90473-X.
[251] W. Lin *et al.*, "Dopant-Free Bifacial Silicon Solar Cells," *Solar RRL,* vol. 5, no. 5, p. 2000771, 2021, doi: https://doi.org/10.1002/solr.202000771.
[252] L. Tutsch, "Implementing sputter-deposited transparent conductive metal oxides into passivating contacts for silicon solar cells," Doctoral, Fraunhofer-Institut für Solare Energiesysteme, 2020.
[253] S.-C. Her and C.-F. Chang, "Fabrication and Characterization of Indium Tin Oxide Films," *Journal of applied biomaterials & functional materials,* vol. 15, 04/01 2017, doi: 10.5301/jabfm.5000345.
[254] C. G. Van de Walle, "Hydrogen as a Cause of Doping in Zinc Oxide," *Physical Review Letters,* vol. 85, no. 5, pp. 1012–1015, 07/31/ 2000, doi: 10.1103/PhysRevLett.85.1012.
[255] R. L. Anderson, "Experiments on Ge-GaAs heterojunctions," *Solid-State Electronics,* vol. 5, no. 5, pp. 341–351, 1962/09/01/ 1962, doi: https://doi.org/10.1016/0038-1101(62)90115-6.
[256] K. Ellmer, "Resistivity of polycrystalline zinc oxide films: current status and physical limit," *Journal of Physics D: Applied Physics,* vol. 34, no. 21, p. 3097, 2001/10/23 2001, doi: 10.1088/0022-3727/34/21/301.
[257] D. C. Look, D. C. Reynolds, J. W. Hemsky, J. R. Sizelove, R. L. Jones, and R. J. Molnar, "Defect Donor and Acceptor in GaN," *Physical Review Letters,* vol. 79, no. 12, pp. 2273–2276, 09/22/ 1997, doi: 10.1103/PhysRevLett.79.2273.
[258] C. Zhang, G. Liu, X. Geng, K. Wu, and M. Debliquy, "Metal oxide semiconductors with highly concentrated oxygen vacancies for gas sensing materials: A review," *Sensors and Actuators A: Physical,* vol. 309, p. 112026, 2020/07/01/ 2020, doi: https://doi.org/10.1016/j.sna.2020.112026.
[259] A. Illiberi, R. Scherpenborg, Y. Wu, F. Roozeboom, and P. Poodt, "Spatial Atmospheric Atomic Layer Deposition of AlxZn1–xO," *ACS Applied Materials & Interfaces,* vol. 5, no. 24, pp. 13124–13128, 2013, doi: 10.1021/am404137e.
[260] G. Luka *et al.*, "The uniformity of Al distribution in aluminum-doped zinc oxide films grown by atomic layer deposition," *Materials Science and Engineering: B,* vol. 176, no. 3, pp. 237–241, 2011/02/25/ 2011, doi: https://doi.org/10.1016/j.mseb.2010.11.014.
[261] C.-H. Hsu *et al.*, "Air Annealing Effect on Oxygen Vacancy Defects in Al-doped ZnO Films Grown by High-Speed Atmospheric Atomic Layer Deposition," *Molecules,* vol. 25, p. 5043, 10/30 2020, doi: 10.3390/molecules25215043.

[262] X. Zhou *et al.*, "The Effects of Post Annealing Process on the Electrical Performance and Stability of Al-Zn-O Thin-Film Transistors," *IEEE Electron Device Letters,* vol. 41, pp. 569–572, 2020.
[263] J. G. Lu *et al.*, "Carrier concentration dependence of band gap shift in n-type ZnO:Al films," *Journal of Applied Physics,* vol. 101, no. 8, 2007, doi: 10.1063/1.2721374.
[264] J. Klein, L. Kampermann, B. Mockenhaupt, M. Behrens, J. Strunk, and G. Bacher, "Limitations of the Tauc Plot Method," *Advanced Functional Materials,* vol. 33, no. 47, p. 2304523, 2023, doi: https://doi.org/10.1002/adfm.202304523.
[265] E. Burstein, "Anomalous Optical Absorption Limit in InSb," *Physical Review,* vol. 93, no. 3, pp. 632–633, 02/01/ 1954, doi: 10.1103/PhysRev.93.632.
[266] T. S. Moss, "The Interpretation of the Properties of Indium Antimonide," *Proceedings of the Physical Society. Section B,* vol. 67, no. 10, p. 775, 1954/10/01 1954, doi: 10.1088/0370-1301/67/10/306.
[267] A. P. Roth, J. B. Webb, and D. F. Williams, "Band-gap narrowing in heavily defect-doped ZnO," *Physical Review B,* vol. 25, no. 12, pp. 7836–7839, 06/15/ 1982, doi: 10.1103/PhysRevB.25.7836.
[268] K. F. Berggren and B. E. Sernelius, "Band-gap narrowing in heavily doped many-valley semiconductors," *Physical Review B,* vol. 24, no. 4, pp. 1971–1986, 08/15/ 1981, doi: 10.1103/PhysRevB.24.1971.
[269] B. E. Sernelius, K. F. Berggren, Z. C. Jin, I. Hamberg, and C. G. Granqvist, "Band-gap tailoring of ZnO by means of heavy Al doping," *Physical Review B,* vol. 37, no. 17, pp. 10244–10248, 06/15/ 1988, doi: 10.1103/PhysRevB.37.10244.
[270] A. Schleife, F. Fuchs, C. Rödl, J. Furthmüller, and F. Bechstedt, "Band-structure and optical-transition parameters of wurtzite MgO, ZnO, and CdO from quasiparticle calculations," *physica status solidi (b),* vol. 246, p. 2150, 09/01 2009, doi: 10.1002/pssb.200945204.
[271] R. Steinberger, J. Duchoslav, M. Arndt, and D. Stifter, "X-ray photoelectron spectroscopy of the effects of Ar+ ion sputtering on the nature of some standard compounds of Zn, Cr, and Fe," *Corrosion Science,* vol. 82, pp. 154–164, 2014/05/01/ 2014, doi: https://doi.org/10.1016/j.corsci.2014.01.018.
[272] V. Tvarozek, I. Novotny, P. Sutta, S. Flickyngerova, K. Schtereva, and E. Vavrinsky, "Influence of sputtering parameters on crystalline structure of ZnO thin films," *Thin Solid Films,* vol. 515, no. 24, pp. 8756–8760, 2007/10/15/ 2007, doi: https://doi.org/10.1016/j.tsf.2007.03.125.
[273] T. Veal, P. King, and C. F. McConville, "Electronic Properties of Post-transition Metal Oxide Semiconductor Surfaces," vol. 149, 2012, pp. 127–145.
[274] J. Jia, A. Takasaki, N. Oka, and Y. Shigesato, "Experimental Observation on the Fermi Level Shift in Polycrystalline Al-Doped ZnO Films," *Journal of Applied Physics,* vol. 112, p. 013718, 07/13 2012, doi: 10.1063/1.4733969.
[275] B.-Y. Tsui, J.-C. Cheng, C. Yen, and C.-Y. Lee, "Strong Fermi-level pinning induced by argon inductively coupled plasma treatment and post-metal deposition annealing on 4H-SiC," *Solid-State Electronics,* vol. 133, 05/01 2017, doi: 10.1016/j.sse.2017.05.003.
[276] J. Bullock, A. Cuevas, T. Allen, and C. Battaglia, "Molybdenum oxide MoOx: A versatile hole contact for silicon solar cells," *Applied Physics Letters,* vol. 105, no. 23, 2014, doi: 10.1063/1.4903467.
[277] H. Kroemer, "Nobel Lecture: Quasielectric fields and band offsets: teaching electrons new tricks," *Reviews of Modern Physics,* vol. 73, no. 3, pp. 783–793, 10/22/ 2001, doi: 10.1103/RevModPhys.73.783.
[278] J. Robertson, "Band Offsets, Schottky Barrier Heights, and Their Effects on Electronic Devices," *Journal of Vacuum Science & Technology A: Vacuum, Surfaces, and Films,* vol. 31, pp. 050821–050821, 09/01 2013, doi: 10.1116/1.4818426.
[279] K. Fuchs, "The conductivity of thin metallic films according to the electron theory of metals," *Mathematical Proceedings of the Cambridge Philosophical Society,* vol. 34, no. 1, pp. 100–108, 1938, doi: 10.1017/S0305004100019952.
[280] E. H. Sondheimer, "The mean free path of electrons in metals," *Advances in Physics,* vol. 1, no. 1, pp. 1–42, 1952/01/01 1952, doi: 10.1080/00018735200101151.

[281] Y. Kajikawa, "Texture development of non-epitaxial polycrystalline ZnO films," *Journal of Crystal Growth,* vol. 289, no. 1, pp. 387–394, 2006/03/15/ 2006, doi: https://doi.org/10.1016/j.jcrysgro.2005.11.089.
[282] J. Steinhauser, S. Faÿ, N. Oliveira, E. Vallat-Sauvain, and C. Ballif, "Transition between grain boundary and intragrain scattering transport mechanisms in boron-doped zinc oxide thin films," *Applied Physics Letters,* vol. 90, no. 14, 2007, doi: 10.1063/1.2719158.
[283] S. Mridha and D. Basak, "Effect of thickness on the structural, electrical and optical properties of ZnO films," *Materials Research Bulletin,* vol. 42, no. 5, pp. 875–882, 2007/05/03/ 2007, doi: https://doi.org/10.1016/j.materresbull.2006.08.019.
[284] O. Graniel *et al.*, "Optical properties of ZnO deposited by atomic layer deposition (ALD) on Si nanowires," *Materials Science and Engineering B,* vol. 236-237, pp. 139–146, 11/01 2018, doi: 10.1016/j.mseb.2018.11.007.
[285] E. Guziewicz *et al.*, "Extremely low temperature growth of ZnO by atomic layer deposition," *Journal of Applied Physics,* vol. 103, pp. 033515–033515, 02/11 2008, doi: 10.1063/1.2836819.
[286] M. Born and E. Wolf, *Principles of Optics: Electromagnetic Theory of Propagation, Interference and Diffraction of Light*, 7 ed. Cambridge: Cambridge University Press, 1999.
[287] P. Gondoni *et al.*, "Structure-dependent optical and electrical transport properties of nanostructured Al-doped ZnO," (in eng), *Nanotechnology,* vol. 23, no. 36, p. 365706, Sep 14 2012, doi: 10.1088/0957-4484/23/36/365706.
[288] G. Dingemans, W. Beyer, M. C. M. van de Sanden, and W. M. M. Kessels, "Hydrogen induced passivation of Si interfaces by Al2O3 films and SiO2/Al2O3 stacks," *Applied Physics Letters,* vol. 97, no. 15, 2010, doi: 10.1063/1.3497014.
[289] N. H. Nickel, W. B. Jackson, and N. M. Johnson, "Light-induced creation of metastable paramagnetic defects in hydrogenated polycrystalline silicon," *Physical Review Letters,* vol. 71, no. 17, pp. 2733–2736, 10/25/ 1993, doi: 10.1103/PhysRevLett.71.2733.
[290] J. I. Pankove and N. M. Johnson, "Chapter 1 Introduction to Hydrogen in Semiconductors," in *Semiconductors and Semimetals*, vol. 34, J. I. Pankove and N. M. Johnson Eds.: Elsevier, 1991, pp. 1–15.
[291] L. Liu *et al.*, "Oxygen vacancies: The origin of n-type conductivity in ZnO," *Physical Review B,* vol. 93, no. 23, p. 235305, 06/15/ 2016, doi: 10.1103/PhysRevB.93.235305.
[292] B. Hammann, F. Schindler, J. Schön, W. Kwapil, M. C. Schubert, and S. W. Glunz, "Review on hydrogen in silicon solar cells: From its origin to its detrimental effects," *Solar Energy Materials and Solar Cells,* vol. 282, p. 113432, 2025/04/01/ 2025, doi: https://doi.org/10.1016/j.solmat.2025.113432.
[293] S. H. Lee, M. F. Bhopal, D. W. Lee, and S. H. Lee, "Review of advanced hydrogen passivation for high efficient crystalline silicon solar cells," *Materials Science in Semiconductor Processing,* vol. 79, pp. 66–73, 2018/06/01/ 2018, doi: https://doi.org/10.1016/j.mssp.2018.01.019.
[294] C. Van de Walle and J. Neugebauer, "Hydrogen in Semiconductors II," *Annual Review of Materials Research,* vol. 36, pp. 179–198, 06/28 2006, doi: 10.1146/annurev.matsci.36.010705.155428.
[295] J. Simon *et al.*, "Correlation study between LeTID defect density, hydrogen and firing profile in Ga-doped crystalline silicon," *Solar Energy Materials and Solar Cells,* vol. 260, p. 112456, 2023/09/15/ 2023, doi: https://doi.org/10.1016/j.solmat.2023.112456.
[296] B. Hammann *et al.*, "Understanding the impact of the cooling ramp of the fast-firing process on light- and elevated-temperature-induced degradation," *Solar Energy Materials and Solar Cells,* vol. 259, p. 112462, 07/12 2023, doi: 10.1016/j.solmat.2023.112462.
[297] R. Eberle, W. Kwapil, F. Schindler, M. C. Schubert, and S. W. Glunz, "Impact of the firing temperature profile on light induced degradation of multicrystalline silicon," *physica status solidi (RRL) – Rapid Research Letters,* vol. 10, no. 12, pp. 861–865, 2016, doi: https://doi.org/10.1002/pssr.201600272.
[298] R. Eberle, W. Kwapil, F. Schindler, S. W. Glunz, and M. C. Schubert, "Firing temperature profile impact on light induced degradation in multicrystalline silicon," *Energy Procedia,* vol. 124, pp. 712–717, 2017/09/01/ 2017, doi: https://doi.org/10.1016/j.egypro.2017.09.082.

[299] G. Kissinger, D. Kot, and W. Häckl, "Getter Effects in Low Oxygen and High Oxygen Czochralski Silicon Wafers," *ECS Transactions,* vol. 33 (11), p. 113, 10/01 2010, doi: 10.1149/1.3485686.
[300] J.-F. Lelièvre, J. Hofstetter, A. Peral, I. Hoces, F. Recart, and C. Cañizo, "Dissolution and gettering of iron during contact co-firing," *Energy Procedia,* vol. 8, pp. 257–262, 04/01 2011, doi: 10.1016/j.egypro.2011.06.133.
[301] N. Yamamoto *et al.*, "Development of Ga-doped ZnO transparent electrodes for liquid crystal display panels," *Thin Solid Films,* vol. 520, no. 12, pp. 4131–4138, 2012/04/02/ 2012, doi: https://doi.org/10.1016/j.tsf.2011.04.067.
[302] Y. Okada and Y. Tokumaru, "Precise determination of lattice parameter and thermal expansion coefficient of silicon between 300 and 1500 K," *Journal of Applied Physics,* vol. 56, no. 2, pp. 314–320, 1984, doi: 10.1063/1.333965.
[303] G. K. White and R. B. Roberts, "Thermal expansion of reference materials: Tungsten and α-Al2O3," 1983.
[304] F. Kersten *et al.*, "Degradation of multicrystalline silicon solar cells and modules after illumination at elevated temperature," *Solar Energy Materials and Solar Cells,* vol. 142, pp. 83–86, 06/22 2015, doi: 10.1016/j.solmat.2015.06.015.
[305] V. Popovich, J. M. Westra, R. A. C. M. M. Van Swaaij, M. Janssen, I. Bennett, and I. Richardson, *Raman spectroscopy characterization of residual stress in multicrystalline silicon solar wafers and solar cells: Relation to microstructure, defects and processing conditions*. 2011, pp. 001668–001673.
[306] Y. Zhao *et al.*, "Optimization of interface properties in p-type poly-SiOx passivating contacts through intrinsic buffer layer modification," *Solar Energy Materials and Solar Cells,* vol. 282, p. 113418, 2025/04/01/ 2025, doi: https://doi.org/10.1016/j.solmat.2025.113418.
[307] G. Dingemans, F. Einsele, W. Beyer, M. C. M. Sanden, and W. M. M. Kessels, "Influence of annealing and Al2O3 properties on the hydrogen-induced passivation of the Si/SiO2 interface," *Japanese Journal of Applied Physics,* vol. 111, 05/01 2012, doi: 10.1063/1.4709729.
[308] A. Stesmans, "Dissociation kinetics of hydrogen-passivated ${P}_{b}$ defects at the ${(111)\mathrm{S}\mathrm{i}/\mathrm{S}\mathrm{i}\mathrm{O}}_{2}$ interface," *Physical Review B,* vol. 61, no. 12, pp. 8393–8403, 03/15/ 2000, doi: 10.1103/PhysRevB.61.8393.
[309] P. Lenormand, A. Lecomte, D. Babonneau, and A. Dauger, "X-ray reflectivity, diffraction and grazing incidence small angle X-ray scattering as complementary methods in the microstructural study of sol–gel zirconia thin films," *Thin Solid Films,* vol. 495, no. 1, pp. 224–231, 2006/01/20/ 2006, doi: https://doi.org/10.1016/j.tsf.2005.08.335.
[310] J. Jensen, A. B. Oelkers, R. Toivola, D. Johnson, J. Elam, and S. M. George, "X-ray Reflectivity Characterization of ZnO/Al 2 O 3 Multilayers Prepared by Atomic Layer Deposition," *Chemistry of Materials - CHEM MATER,* vol. 14, pp. 2276–2282, 05/01 2002, doi: 10.1021/cm011587z.
[311] V. F. Sears, "Neutron scattering lengths and cross sections," *Neutron News,* vol. 3, no. 3, pp. 26–37, 1992/01/01 1992, doi: 10.1080/10448639208218770.
[312] P. Li *et al.*, "Modeling and simulation of bifacial perovskite/PERT-silicon tandem solar cells," *Solar Energy,* vol. 227, pp. 292–302, 2021/10/01/ 2021, doi: https://doi.org/10.1016/j.solener.2021.09.015.
[313] Y. Kuang *et al.*, "Enhanced Optical Absorption in Perovskite/Si Tandem Solar Cells with Nanoholes Array," (in eng), *Nanoscale Res Lett,* vol. 15, no. 1, p. 213, Nov 12 2020, doi: 10.1186/s11671-020-03445-3.
[314] S. Akhil *et al.*, "Review on perovskite silicon tandem solar cells: Status and prospects 2T, 3T and 4T for real world conditions," *Materials & Design,* vol. 211, p. 110138, 2021/12/01/ 2021, doi: https://doi.org/10.1016/j.matdes.2021.110138.
[315] C. Dong, S. Yan, D. Liu, Y. Zhu, C. Chen, and J. Tang, "Principle and Progress of Interconnection Layers in Monolithic Perovskite-Based Tandem Photovoltaics," *Advanced Energy Materials,* vol. 15, no. 13, p. 2404628, 2025, doi: https://doi.org/10.1002/aenm.202404628.
[316] P. R. Jubu, F. K. Yam, V. M. Igba, and K. P. Beh, "Tauc-plot scale and extrapolation effect on bandgap estimation from UV–vis–NIR data – A case study of β-Ga2O3," *Journal of Solid*

State Chemistry, vol. 290, p. 121576, 2020/10/01/ 2020, doi: https://doi.org/10.1016/j.jssc.2020.121576.
[317] P. Makuła, M. Pacia, and W. Macyk, "How To Correctly Determine the Band Gap Energy of Modified Semiconductor Photocatalysts Based on UV–Vis Spectra," *The Journal of Physical Chemistry Letters,* vol. 9, no. 23, pp. 6814–6817, 2018, doi: 10.1021/acs.jpclett.8b02892.
[318] H. Zhong *et al.*, "Idealizing Tauc Plot for Accurate Bandgap Determination of Semiconductor with Ultraviolet–Visible Spectroscopy: A Case Study for Cubic Boron Arsenide," *The Journal of Physical Chemistry Letters,* vol. 14, no. 29, pp. 6702–6708, 2023, doi: 10.1021/acs.jpclett.3c01416.
[319] A. Escobedo-Morales, M. S. Pedraza-Chan, I. I. Ruiz-López, E. C. Anota, M. Salazar-Villanueva, and D. Cortés-Arriagada, "Accurate determination of the band gap energy of non-translucent semiconductor materials through the Tauc method: Theoretical framework, limitations, technical hints, and automated algorithms," *Next Materials,* vol. 10, p. 101412, 2026/01/01/ 2026, doi: https://doi.org/10.1016/j.nxmate.2025.101412.
[320] E. Agocs *et al.*, "Approaches to calculate the dielectric function of ZnO around the band gap," *Thin Solid Films,* vol. 571, pp. 684–688, 2014/11/28/ 2014, doi: https://doi.org/10.1016/j.tsf.2014.03.028.
[321] M. B. Bouzourâa, Y. Battie, S. Dalmasso, M. A. Zaïbi, M. Oueslati, and A. En Naciri, "Temperature dependent optical properties of ZnO thin film using ellipsometry and photoluminescence," *Superlattices and Microstructures,* vol. 117, pp. 457–468, 2018/05/01/ 2018, doi: https://doi.org/10.1016/j.spmi.2018.03.078.
[322] R. Elilarassi and G. Chandrasekaran, "Effect of Annealing on Structural and Optical Properties of Zinc Oxide Films," *Materials Chemistry and Physics - MATER CHEM PHYS,* vol. 121, pp. 378–384, 05/01 2010, doi: 10.1016/j.matchemphys.2010.01.053.
[323] V. Pawar, P. K. Jha, S. K. Panda, P. A. Jha, and P. Singh, "Band-Gap Engineering in ZnO Thin Films: A Combined Experimental and Theoretical Study," *Physical Review Applied,* vol. 9, no. 5, p. 054001, 05/02/ 2018, doi: 10.1103/PhysRevApplied.9.054001.
[324] Q. You *et al.*, "Blue shift in absorption edge and widening of band gap of ZnO by Al doping and Al-N co-doping," *Journal of Alloys and Compounds,* vol. 644, 05/01 2015, doi: 10.1016/j.jallcom.2015.05.060.
[325] T. Minami, "Transparent conducting oxide semiconductors for transparent electrodes," *Semiconductor Science and Technology,* vol. 20, no. 4, p. S35, 2005/03/15 2005, doi: 10.1088/0268-1242/20/4/004.
[326] K. Ellmer and R. Mientus, "Carrier transport in polycrystalline transparent conductive oxides: A comparative study of zinc oxide and indium oxide," *Thin Solid Films,* vol. 516, no. 14, pp. 4620–4627, 2008/05/30/ 2008, doi: https://doi.org/10.1016/j.tsf.2007.05.084.
[327] C. Granqvist, "Transparent Conductors as Solar Energy Materials: A Panoramic Review," *Solar energy materials and solar cells,* vol. 91, pp. 1529–1598, 10/15 2007, doi: 10.1016/j.solmat.2007.04.031.
[328] T. Minami, "Chapter Five - Transparent Conductive Oxides for Transparent Electrode Applications," in *Semiconductors and Semimetals*, vol. 88, B. G. Svensson, S. J. Pearton, and C. Jagadish Eds.: Elsevier, 2013, pp. 159–200.
[329] S. Kinnunen, K. Arstila, and T. Sajavaara, "Al2O3 ALD films grown using TMA + rare isotope 2H216O and 1H218O precursors," *Applied Surface Science,* vol. 546, p. 148909, 2021/04/30/ 2021, doi: https://doi.org/10.1016/j.apsusc.2020.148909.
[330] S. Jakschik, U. Schroeder, T. Hecht, M. Gutsche, H. Seidl, and J. W. Bartha, "Crystallization behavior of thin ALD-Al2O3 films," *Thin Solid Films,* vol. 425, no. 1, pp. 216–220, 2003/02/03/ 2003, doi: https://doi.org/10.1016/S0040-6090(02)01262-2.
[331] P. Bergese, E. Bontempi, and L. E. Depero, "A simple solution to systematic errors in density determination by X-ray reflectivity: The XRR-density evaluation (XRR-DE) method," *Applied Surface Science,* vol. 253, no. 1, pp. 28–32, 2006/10/31/ 2006, doi: https://doi.org/10.1016/j.apsusc.2006.05.067.
[332] O. Ylivaara *et al.*, "Thermomechanical properties of aluminum oxide thin films made by atomic layer deposition," *Journal of Vacuum Science & Technology A,* vol. 40, p. 062414, 12/01 2022, doi: 10.1116/6.0002095.

[333] J. Werner, B. Niesen, and C. Ballif, "Perovskite/Silicon Tandem Solar Cells: Marriage of Convenience or True Love Story? – An Overview," *Advanced Materials Interfaces,* vol. 5, no. 1, p. 1700731, 2018, doi: https://doi.org/10.1002/admi.201700731.
[334] M. Yamaguchi, P. Schygulla, I. Kafedjiska, F. Dimroth, and R. Schlatmann, "Overview and future perspective of Si tandem solar cells," *Applied Physics Express,* 2026. [Online]. Available: http://iopscience.iop.org/article/10.35848/1882-0786/ae5b1d.
[335] D. C. Gleason-Rohrer, B. S. Brunschwig, and N. S. Lewis, "Measurement of the Band Bending and Surface Dipole at Chemically Functionalized Si(111)/Vacuum Interfaces," *The Journal of Physical Chemistry C,* vol. 117, no. 35, pp. 18031–18042, 2013/09/05 2013, doi: 10.1021/jp401585s.
[336] W. Melitz, J. Shen, A. C. Kummel, and S. Lee, "Kelvin probe force microscopy and its application," *Surface Science Reports,* vol. 66, no. 1, pp. 1–27, 2011/01/01/ 2011, doi: https://doi.org/10.1016/j.surfrep.2010.10.001.
[337] A. Sabioni, M. J. Ramos, and W. Ferraz, "Oxygen diffusion in pure and doped ZnO," *Materials Research,* vol. 6, pp. 173–178, 06/01 2003, doi: 10.1590/S1516-14392003000200011.
[338] A. C. S. Sabioni, A. M. J. Daniel, W. B. Ferraz, R. W. D. Pais, A.-M. Huntz, and F. Jomard, "Oxygen diffusion in Bi2O3-doped ZnO," *Materials Research,* vol. 11, pp. 221–225, 2008.
[339] H. L. Tuller, "ZnO grain boundaries: electrical activity and diffusion," *Journal of Electroceramics,* vol. 4, no. Suppl 1, pp. 33–40, 1999.
[340] P. Erhart and K. Albe, "First-principles study of migration mechanisms and diffusion of oxygen in zinc oxide," *Physical Review B,* vol. 73, no. 11, p. 115207, 03/22/ 2006, doi: 10.1103/PhysRevB.73.115207.
[341] A. S. Nowick, *Anelastic Relaxation In Crystalline Solids*. Academic Press, 2012.
[342] A. Nagaraj, N. Karthik, and S. Waddar, "Experimental and simulation of temperature distribution in absorber tube used for parabolic trough solar collector," *AIP Conference Proceedings,* vol. 2421, no. 1, 2022, doi: 10.1063/5.0076732.
[343] M. Çopuroğlu, H. Sezen, R. L. Opila, and S. Suzer, "Band-Bending at Buried SiO2/Si Interface as Probed by XPS," *ACS Applied Materials & Interfaces,* vol. 5, no. 12, pp. 5875–5881, 2013/06/26 2013, doi: 10.1021/am401696e.
[344] E. A. Kraut, R. W. Grant, J. R. Waldrop, and S. P. Kowalczyk, "Semiconductor core-level to valence-band maximum binding-energy differences: Precise determination by x-ray photoelectron spectroscopy," *Physical Review B,* vol. 28, no. 4, pp. 1965–1977, 08/15/ 1983, doi: 10.1103/PhysRevB.28.1965.
[345] P. D. C. King *et al.*, "Valence-band electronic structure of CdO, ZnO, and MgO from x-ray photoemission spectroscopy and quasi-particle-corrected density-functional theory calculations," *Physical Review B,* vol. 79, no. 20, p. 205205, 05/12/ 2009, doi: 10.1103/PhysRevB.79.205205.
[346] M. Gabás, P. Torelli, N. Barrett, M. Sacchi, and J. Barrado, "Electronic structure of Al- and Ga-doped ZnO films studied by hard X-ray photoelectron spectroscopy," *APL Materials,* vol. 2, p. 012112, 01/31 2014, doi: 10.1063/1.4863595.
[347] S. A. Chambers, L. Wang, and D. R. Baer, "Introductory guide to the application of XPS to epitaxial films and heterostructures," *Journal of Vacuum Science & Technology A,* vol. 38, no. 6, 2020, doi: 10.1116/6.0000465.
[348] T. Böker *et al.*, "Band structure of ${\mathrm{MoS}}_{2},$ ${\mathrm{MoSe}}_{2},$ and $\ensuremath{\alpha}\ensuremath{-}{\mathrm{MoTe}}_{2}:$ Angle-resolved photoelectron spectroscopy and ab initio calculations," *Physical Review B,* vol. 64, no. 23, p. 235305, 11/15/ 2001, doi: 10.1103/PhysRevB.64.235305.
[349] S. Hüfner, *Photoelectron Spectroscopy: Principles and Applications*. Springer Berlin Heidelberg, 2013.
[350] Tanuma, S., C. J. Powell, and D. R. Penn, "Calculations of electron inelastic mean free paths. IX. Data for 41 elemental solids over the 50 eV to 30 keV range," *Surface and Interface Analysis,* vol. 43, no. 3, pp. 689–713, 2011, doi: https://doi.org/10.1002/sia.3522.
[351] K. Ellmer, A. Klein, and B. Rech, *Transparent Conductive Zinc Oxide*. 2008.
[352] G. Kartopu, V. Barrioz, S. Monir, D. Lamb, and S. Irvine. *Thin Solid Films*.

[353] M. Kelly, "Historical perspectives on charging issues in XPS," *Journal of Electron Spectroscopy and Related Phenomena,* vol. 176, pp. 5–7, 01/31 2010, doi: 10.1016/j.elspec.2009.10.006.
[354] G. Greczynski and L. Hultman, "A step-by-step guide to perform x-ray photoelectron spectroscopy," *Journal of Applied Physics,* vol. 132, no. 1, 2022, doi: 10.1063/5.0086359.
[355] S. Suzer, "Differential Charging in X-ray Photoelectron Spectroscopy: A Nuisance or a Useful Tool?," *Analytical Chemistry,* vol. 75, no. 24, pp. 7026–7029, 2003/12/01 2003, doi: 10.1021/ac034823t.
[356] A. E. Hughes, C. D. Easton, T. R. Gengenbach, M. C. Biesinger, and M. Laleh, "Interpretation of complex x-ray photoelectron peak shapes. II. Case study of Fe 2p3/2 fitting applied to austenitic stainless steels 316 and 304," *Journal of Vacuum Science & Technology A,* vol. 42, no. 5, 2024, doi: 10.1116/6.0003842.
[357] Y. Gassenbauer *et al.*, "Surface states, surface potentials, and segregation at surfaces of tin-doped ${\mathrm{In}}_{2}{\mathrm{O}}_{3}$," *Physical Review B,* vol. 73, no. 24, p. 245312, 06/09/ 2006, doi: 10.1103/PhysRevB.73.245312.
[358] N. W. Ashcroft and N. D. Mermin, *Solid State Physics*. Holt, Rinehart and Winston, 1976.
[359] E. H. Poindexter and P. J. Caplan, "Electron spin resonance of inherent and process induced defects near the Si/SiO2 interface of oxidized silicon wafers," *Journal of Vacuum Science & Technology A,* vol. 6, no. 3, pp. 1352–1357, 1988, doi: 10.1116/1.575701.
[360] A. Stirling, A. Pasquarello, J. C. Charlier, and R. Car, "Dangling Bond Defects at $\mathrm{Si}\ensuremath{-}{\mathrm{SiO}}_{2}$ Interfaces: Atomic Structure of the ${\mathit{P}}_{\mathit{b}1}$ Center," *Physical Review Letters,* vol. 85, no. 13, pp. 2773–2776, 09/25/ 2000, doi: 10.1103/PhysRevLett.85.2773.
[361] E. H. Nicollian and J. R. Brews, *MOS (Metal Oxide Semiconductor) Physics and Technology*. Wiley, 2002.
[362] A. Hiraiwa, D. Matsumura, S. Okubo, and H. Kawarada, "Post-deposition-annealing effect on current conduction in Al2O3 films formed by atomic layer deposition with H2O oxidant," *Journal of Applied Physics,* vol. 121, no. 7, 2017, doi: 10.1063/1.4976211.
[363] D. Baer *et al.*, "XPS guide: Charge neutralization and binding energy referencing for insulating samples," *Journal of Vacuum Science & Technology A,* vol. 38, p. 031204, 05/01 2020, doi: 10.1116/6.0000057.
[364] B. F. Spencer *et al.*, "Characterization of buried interfaces using Ga Kα hard X-ray photoelectron spectroscopy (HAXPES)," *Faraday Discussions,* 10.1039/D2FD00021K vol. 236, no. 0, pp. 311–337, 2022, doi: 10.1039/D2FD00021K.
[365] C. Kalha *et al.*, "Hard x-ray photoelectron spectroscopy: a snapshot of the state-of-the-art in 2020," *Journal of Physics: Condensed Matter,* vol. 33, no. 23, p. 233001, 2021/05/13 2021, doi: 10.1088/1361-648X/abeacd.
[366] O. Romanyuk *et al.*, "Band Bending at Heterovalent Interfaces: Hard X-ray Photoelectron Spectroscopy of GaP/Si(001) Heterostructures," *Applied Surface Science,* vol. 565, p. 150514, 06/01 2021, doi: 10.1016/j.apsusc.2021.150514.
[367] B. Hoex, S. B. S. Heil, E. Langereis, M. C. M. van de Sanden, and W. M. M. Kessels, "Ultralow surface recombination of c-Si substrates passivated by plasma-assisted atomic layer deposited Al2O3," *Applied Physics Letters,* vol. 89, no. 4, 2006, doi: 10.1063/1.2240736.
[368] S. A. Studenikin, N. Golego, and M. Cocivera, "Optical and electrical properties of undoped ZnO films grown by spray pyrolysis of zinc nitrate solution," *Journal of Applied Physics,* vol. 83, no. 4, pp. 2104–2111, 1998, doi: 10.1063/1.366944.
[369] D. Look, G. Farlow, P. Reunchan, S. Limpijumnong, S. Zhang, and K. Nordlund, "Evidence for Native-Defect Donors in n -Type ZnO," *Physical review letters,* vol. 95, p. 225502, 12/01 2005, doi: 10.1103/PhysRevLett.95.225502.
[370] B. Hoex, J. Schmidt, P. Pohl, M. C. M. van de Sanden, and W. M. M. Kessels, "Silicon surface passivation by atomic layer deposited Al2O3," *Journal of Applied Physics,* vol. 104, no. 4, 2008, doi: 10.1063/1.2963707.
[371] E. Cartier, J. H. Stathis, and D. A. Buchanan, "Passivation and depassivation of silicon dangling bonds at the Si/SiO2 interface by atomic hydrogen," *Applied Physics Letters,* vol. 63, no. 11, pp. 1510–1512, 1993, doi: 10.1063/1.110758.

[372] A. Stesmans, "Passivation of Pb0 and Pb1 interface defects in thermal (100) Si/SiO2 with molecular hydrogen," *Applied Physics Letters,* vol. 68, no. 15, pp. 2076–2078, 1996, doi: 10.1063/1.116308.
[373] D. Chen *et al.*, "Hydrogen induced degradation: A possible mechanism for light- and elevated temperature- induced degradation in n-type silicon," *Solar Energy Materials and Solar Cells,* vol. 185, pp. 174–182, 2018/10/01/ 2018, doi: https://doi.org/10.1016/j.solmat.2018.05.034.
[374] D. Chen *et al.*, "Progress in the understanding of light- and elevated temperature-induced degradation in silicon solar cells: A review," *Progress in Photovoltaics: Research and Applications,* vol. 29, no. 11, pp. 1180–1201, 2021, doi: https://doi.org/10.1002/pip.3362.
[375] P. Hamer, B. Hallam, S. Wenham, and M. Abbott, "Manipulation of Hydrogen Charge States for Passivation of P-Type Wafers in Photovoltaics," *IEEE Journal of Photovoltaics,* vol. 4, no. 5, pp. 1252–1260, 2014, doi: 10.1109/JPHOTOV.2014.2339494.
[376] B. J. Hallam, P. G. Hamer, A. M. Ciesla née Wenham, C. E. Chan, B. Vicari Stefani, and S. Wenham, "Development of advanced hydrogenation processes for silicon solar cells via an improved understanding of the behaviour of hydrogen in silicon," *Progress in Photovoltaics: Research and Applications,* vol. 28, no. 12, pp. 1217–1238, 2020, doi: https://doi.org/10.1002/pip.3240.
[377] D. J. Graham and L. J. Gamble, "Back to the basics of time-of-flight secondary ion mass spectrometry of bio-related samples. I. Instrumentation and data collection," (in eng), *Biointerphases,* vol. 18, no. 2, p. 021201, Mar 29 2023, doi: 10.1116/6.0002477.
[378] Z. Zhu, V. Shutthanandan, and M. Engelhard, "An investigation of hydrogen depth profiling using ToF-SIMS," *Surface and Interface Analysis - SURF INTERFACE ANAL,* vol. 44, 02/01 2012, doi: 10.1002/sia.3826.
[379] J. Ekar, P. Panjan, S. Drev, and J. Kovač, "ToF-SIMS Depth Profiling of Metal, Metal Oxide, and Alloy Multilayers in Atmospheres of H2, C2H2, CO, and O2," *Journal of the American Society for Mass Spectrometry,* vol. 33, no. 1, pp. 31–44, 2022/01/05 2022, doi: 10.1021/jasms.1c00218.
[380] A. Priebe, T. Xie, G. Bürki, L. Pethö, and J. Michler, "Matrix effect in TOF-SIMS analysis of two-element inorganic thin films," *Journal of Analytical Atomic Spectrometry,* vol. 35, 04/08 2020, doi: 10.1039/C9JA00428A.
[381] R. G. Wilson, F. A. Stevie, and C. W. Magee, *Secondary Ion Mass Spectrometry: A Practical Handbook for Depth Profiling and Bulk Impurity Analysis*. Wiley, 1989.
[382] J. C. Vickerman and D. Briggs, *ToF-SIMS: Materials Analysis by Mass Spectrometry*. SurfaceSpectra, 2013.
[383] S. Pal *et al.*, "Quantification of hydrogen in nanostructured hydrogenated passivating contacts for silicon photovoltaics combining SIMS-APT-TEM: A multiscale correlative approach," *Applied Surface Science,* vol. 555, p. 149650, 2021/07/30/ 2021, doi: https://doi.org/10.1016/j.apsusc.2021.149650.
[384] A. Zalar, "Improved depth resolution by sample rotation during Auger electron spectroscopy depth profiling," *Thin Solid Films,* vol. 124, no. 3, pp. 223–230, 1985/02/22/ 1985, doi: https://doi.org/10.1016/0040-6090(85)90269-X.
[385] M. A. Robinson, D. J. Graham, and D. G. Castner, "ToF-SIMS depth profiling of cells: z-correction, 3D imaging, and sputter rate of individual NIH/3T3 fibroblasts," (in eng), *Anal Chem,* vol. 84, no. 11, pp. 4880–5, Jun 5 2012, doi: 10.1021/ac300480g.
[386] B. Paudel *et al.*, "ToF-SIMS in material research: A view from nanoscale hydrogen detection," *Materials Today,* vol. 75, pp. 149–165, 2024/06/01/ 2024, doi: https://doi.org/10.1016/j.mattod.2024.03.003.
[387] U. Almhöjd, J. Norén, A. Arvidsson, Å. Nilsson, and P. Lingström, "Analysis of carious dentine using FTIR and ToF-SIMS," *Oral health and dental management,* vol. 13, pp. 735–44, 09/01 2014.
[388] G. Dingemans, N. M. Terlinden, M. A. Verheijen, M. C. M. van de Sanden, and W. M. M. Kessels, "Controlling the fixed charge and passivation properties of Si(100)/Al2O3 interfaces using ultrathin SiO2 interlayers synthesized by atomic layer deposition," *Journal of Applied Physics,* vol. 110, no. 9, 2011, doi: 10.1063/1.3658246.
[389] A. Spool and L. Finney, "Best practices for performing quantitative TOF-SIMS analyses," *Journal of Vacuum Science & Technology A,* vol. 42, 07/01 2024, doi: 10.1116/6.0003660.

[390] S. Lehmann *et al.*, "Supercycle approach to plasma-enhanced atomic layer deposition of cobalt oxide films," *Journal of Vacuum Science & Technology A,* vol. 43, no. 5, 2025.
[391] A. Krishtal, K. Vanommeslaeghe, A. Olasz, T. Veszprémi, C. Van Alsenoy, and P. Geerlings, "Accurate interaction energies at density functional theory level by means of an efficient dispersion correction," (in eng), *J Chem Phys,* vol. 130, no. 17, p. 174101, May 7 2009, doi: 10.1063/1.3126248.
[392] N. Sousbie, L. Capello, J. Eymery, F. Rieutord, and C. Lagahe, "X-ray scattering study of hydrogen implantation in silicon," *Journal of Applied Physics,* vol. 99, 05/15 2006, doi: 10.1063/1.2198928.
[393] S. P. Harvey, F. Zhang, A. Palmstrom, J. M. Luther, K. Zhu, and J. J. Berry, "Mitigating Measurement Artifacts in TOF-SIMS Analysis of Perovskite Solar Cells," (in eng), *ACS Appl Mater Interfaces,* vol. 11, no. 34, pp. 30911–30918, Aug 28 2019, doi: 10.1021/acsami.9b09445.
[394] D. Gomes, V. P. Markevich, A. R. Peaker, and J. Coutinho, "Dynamics of Hydrogen in Silicon at Finite Temperatures from First Principles," *physica status solidi (b),* vol. 259, no. 6, p. 2100670, 2022, doi: https://doi.org/10.1002/pssb.202100670.
[395] W. Shockley and W. T. Read, "Statistics of the Recombinations of Holes and Electrons," *Physical Review,* vol. 87, no. 5, pp. 835–842, 09/01/ 1952, doi: 10.1103/PhysRev.87.835.
[396] T. Michel, "Nuclear Instruments and Methods in Physics Research - Section A: accelerators, spectrometers, detectors and associated equipment," *Nuclear Instruments and Methods in Physics Research Section A Accelerators Spectrometers Detectors and Associated Equipment,* vol. 591, pp. VII–VII, 06/11 2008, doi: 10.1016/j.nima.2008.03.098.

Appendix A: iV_{OC} data for all samples per precursor dosing condition in Chapter 4

This appendix shows the passivation metrics for the four precursor dosing recipes discussed in Chapter 4. Table A 12 lists the iV_{OC} values of five samples per group (Al-rich, Zn-deficient, optimised, H_2O-deficient), together with the group mean and standard deviation. Table A 13 summarises the J_0, iV_{OC}, and effective lifetime at 1×10^{15} cm^{-3} excess carrier density (ECD) of the champion sample from each group. Figure A 79 shows the effective lifetime, J_0, and iV_{OC} analysis plots for the optimised sample.

Table A 12 iV_{OC} values for 5 samples per condition in group A, B, C, D with the average and standard deviation values calculated. (A, B, C, D represent Al-rich, Zn-deficient, optimised, and H2O-deficient, respectively)

iV_{OC} (mV)	Group A	Group B	Group C	Group D
Sample 1	731	717	738	717
Sample 2	732	726	740	706
Sample 3	740	728	735	723
Sample 4	740	731	739	726
Sample 5	740	732	740	719
Average	736.6	726.8	738.4	718.2
Standard deviation. P	4.18	5.34	1.85	6.85

Table A 13 J_0, iV_{OC}, and lifetime (@ 1E15 ECD) values of all the champion samples in group A,B,C,D. (A, B, C, D represent Al-rich, Zn-deficient, optimised, and H2O-deficient, respectively)

	Group A	Group B	Group C	Group D
J_0 (fA/cm^2)	0.88	2.8	0.87	1.81
iV_{OC} (mV)	740	733	740	727
Lifetime (ms) @ 1E15	3.25	1.62	3.38	1.12

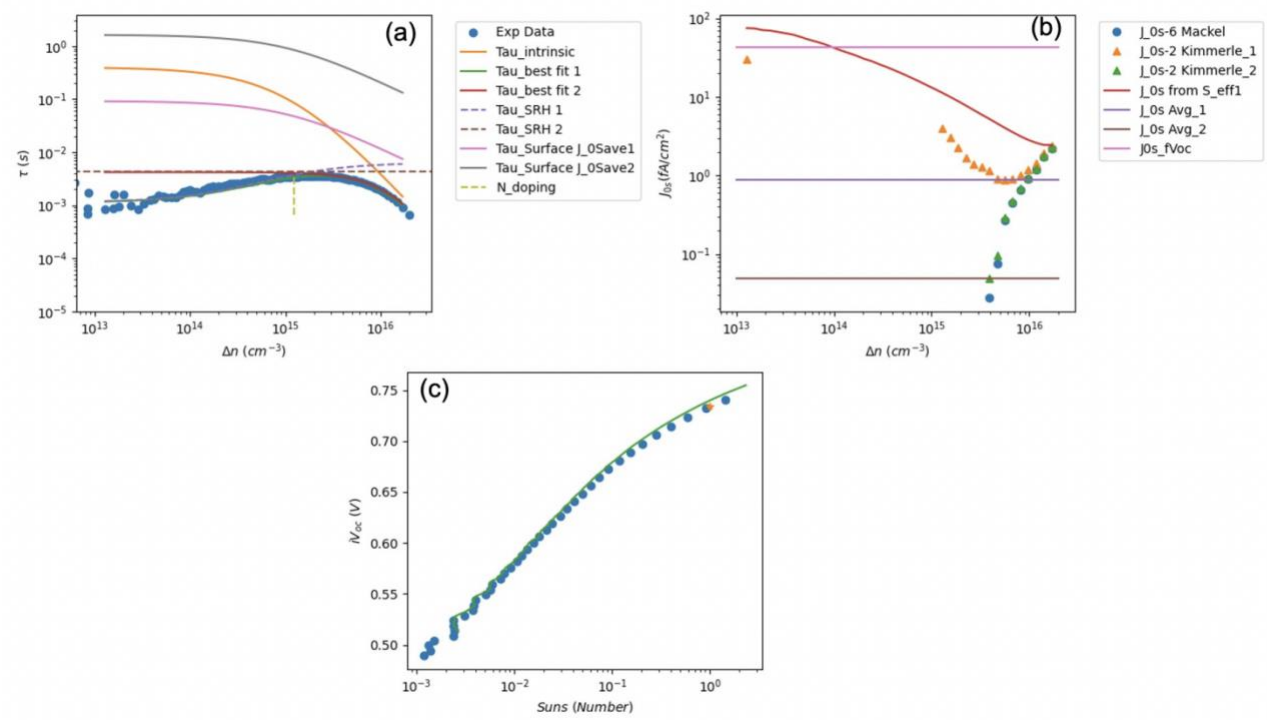


Figure A 79 (a) Effective lifetime, (b) J_0 and (c) iV_{OC} analysis plots for the highest τ_{eff} vs. Δn of samples in profile C (Optimised). Analysis is conducted following the algorithm and code reported in github.com/OxfordInterfacesLab/PySintonAnalysis.

Appendix B: Additional information on lab-and synchrotron-XPS in Chapters 4 and 6

This appendix collects the XPS fitting spectra for the quantitative analyses in Chapters 4 and 6. Figure A 80 shows the Zn $3p_{1/2}$, Zn $3p_{3/2}$, and Al 2p core-level fits for the four annealed samples from different precursor dosing ratio conditions in Chapter 4 that define the Al 2p/Zn $3p_{3/2}$ ratio in Figure 4.9 (b). Figure A 81 shows the Si 2p core-level evolution with Ar^+ sputter time through the AZO/SiO_X/Si stack, used to estimate the band bending discussed in Section 4.4.4. Figure A 82 shows the fitted band diagrams at the Si/AZO interface for as-deposited and annealed Si/2 nm AZO/2 nm AlO_X samples measured without sputtering (non-destructive synchrotron XPS), supporting the upward-band-bending observation in Section 4.4.4. Figure A 83 shows the Zn 3p and Si 2p fits for the three samples reported in Chapter 6, Table 6.2. Figure A 84 shows the Zn 3p and O 1s fits for the two annealed AZO samples reported in Chapter 6, Table 6.3.

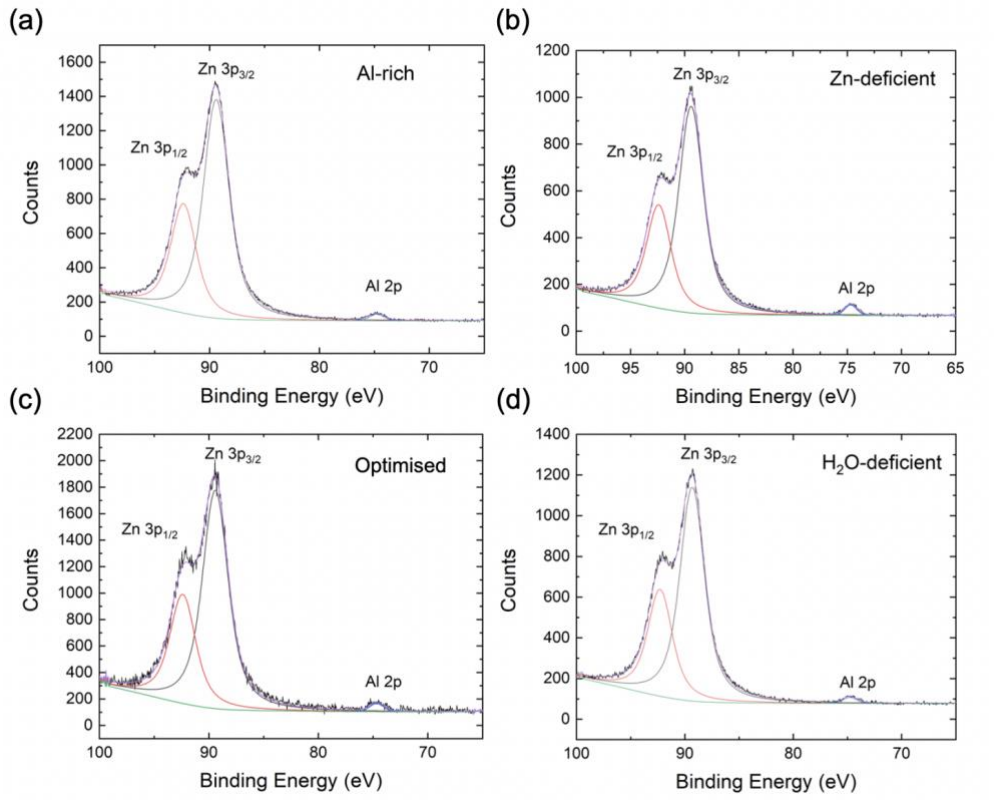


Figure A 80 XPS spectrum range covering Zn $3p_{1/2}$ & $3p_{3/2}$ and Al 2p core levels for the 4 annealed samples in Chapter 4, with fitted integrated intensity for Zn $3p_{3/2}$ and Al 2p in each case. Fitting was carried out in CasaXPS using Tougaard background and convolved Gaussian/Lorentzian lineshape.

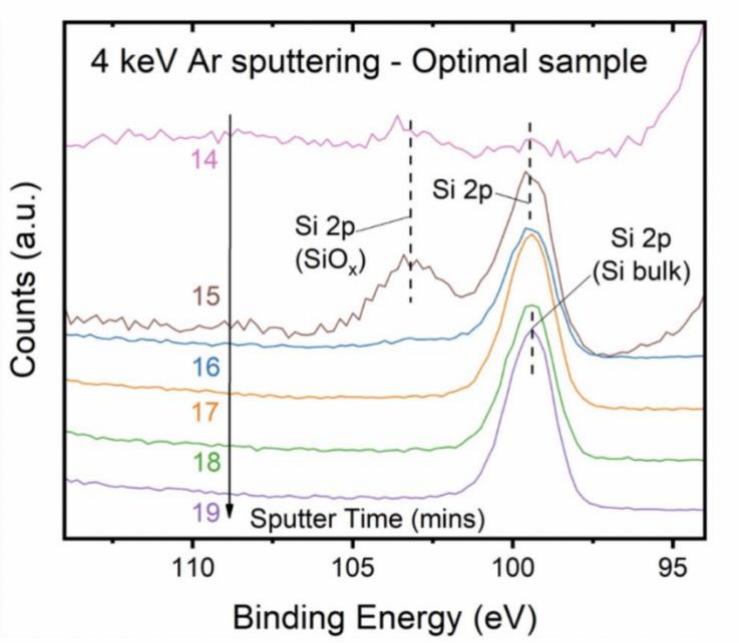


Figure A 81 XPS spectra showing Si 2p core levels at the AZO/SiO_X/Si interface under different sputter time. AZO layer is thinned by sputtering with Ar gun (4 keV) such that Si core levels can be detected and the shift in Si 2p and Zn 3p peaks relative to bulk positions allows band-bending to be estimated in Section 4.4.4

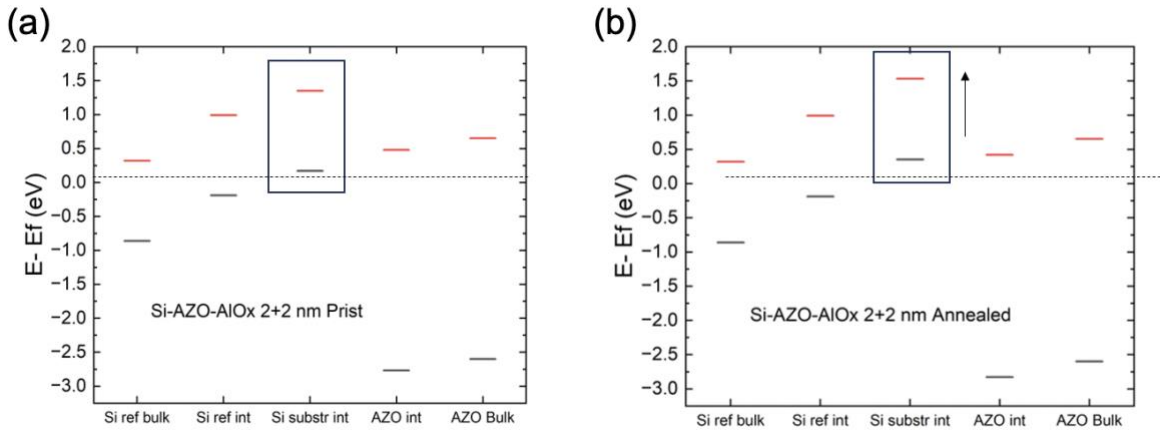


Figure A 82 The fitted band diagram of Si/AZO interface of (a) as-deposited and (b) annealed Si/2nm AZO/2nm AlO_X samples measured without sputtering via synchrotron-XPS.

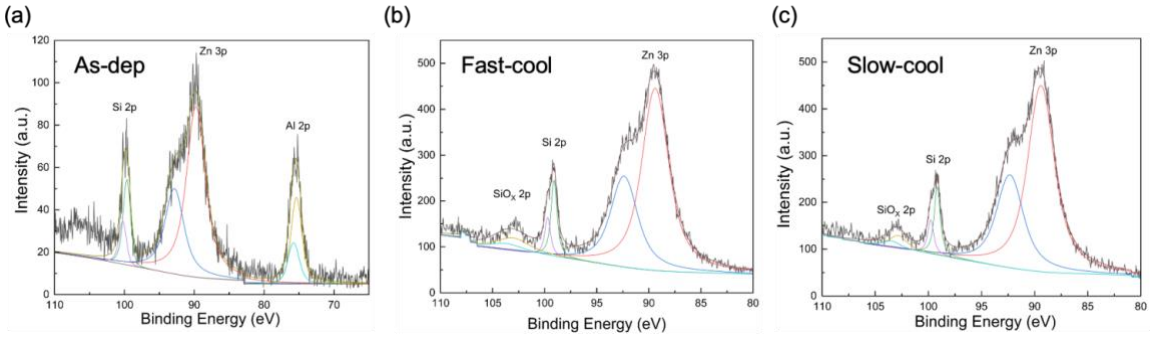


Figure A 83 The XPS spectrum for the three Si/SiO_X/2nm AZO/2nm AlO_X samples in Table 6.2, with fitted integrated intensity for Zn 3p and Si 2p in each case.

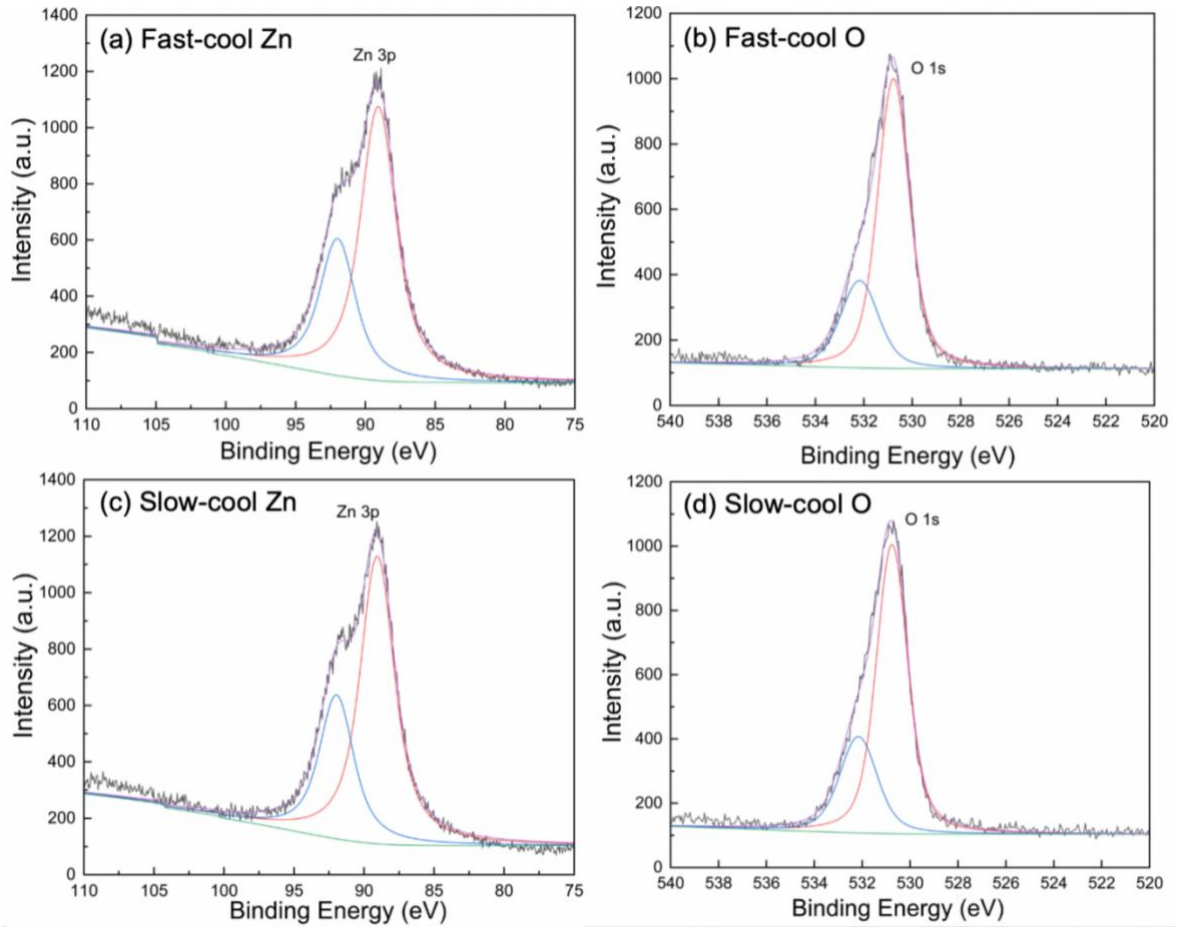


Figure A 84 The XPS spectrum for the two Si/SiO_2/annealed AZO samples in Table 6.3, with fitted integrated intensity for (a) and (c) Zn 3p, and (b) and (d) O 1s in each case.

Appendix C: Additional information on Ellipsometry data in Chapters 4

This appendix provides the full spectroscopic ellipsometry data for the four precursor-ratio AZO films summarised at 600 nm in Table 4.2. Figure A 85 shows the refractive index n as a function of wavelength (210–1690 nm) for each recipe. Figure A 86 shows the corresponding extinction coefficient k. Figure A 87 shows the measured and modelled ellipsometric curves for the optimised sample.

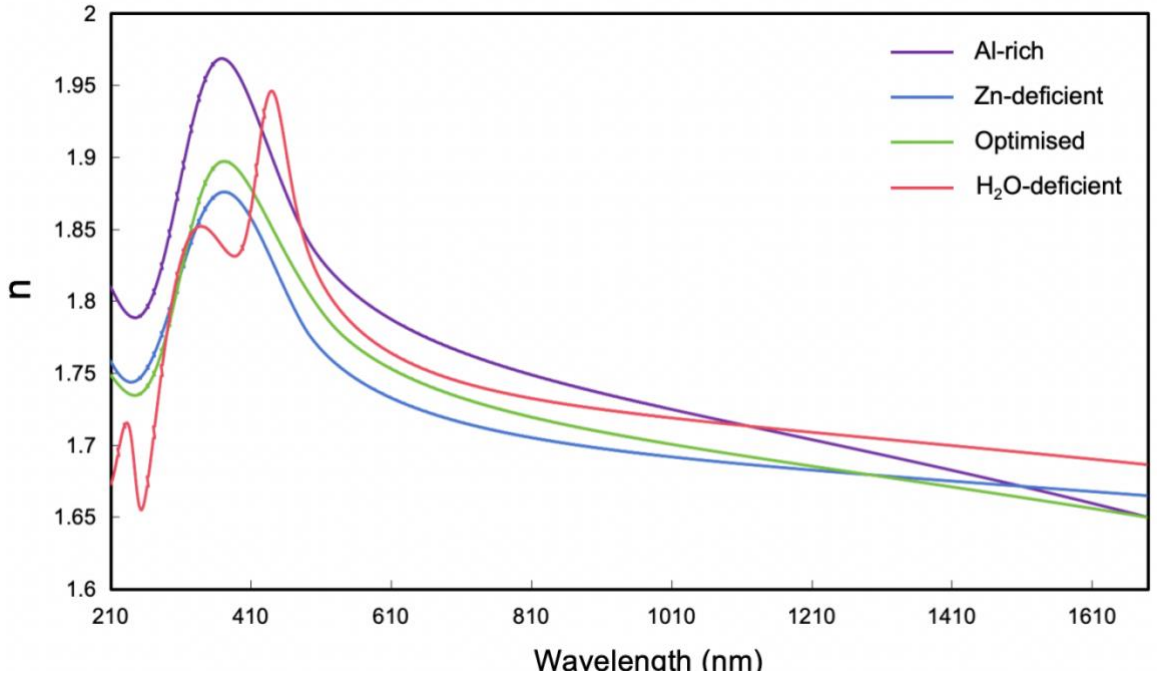


Figure A 85 Spectroscopic ellipsometry data for 40-nm-thick AZO films deposited under the four precursor pressure profiles described in Section 4.2.1. Refractive index n as a function of wavelength.

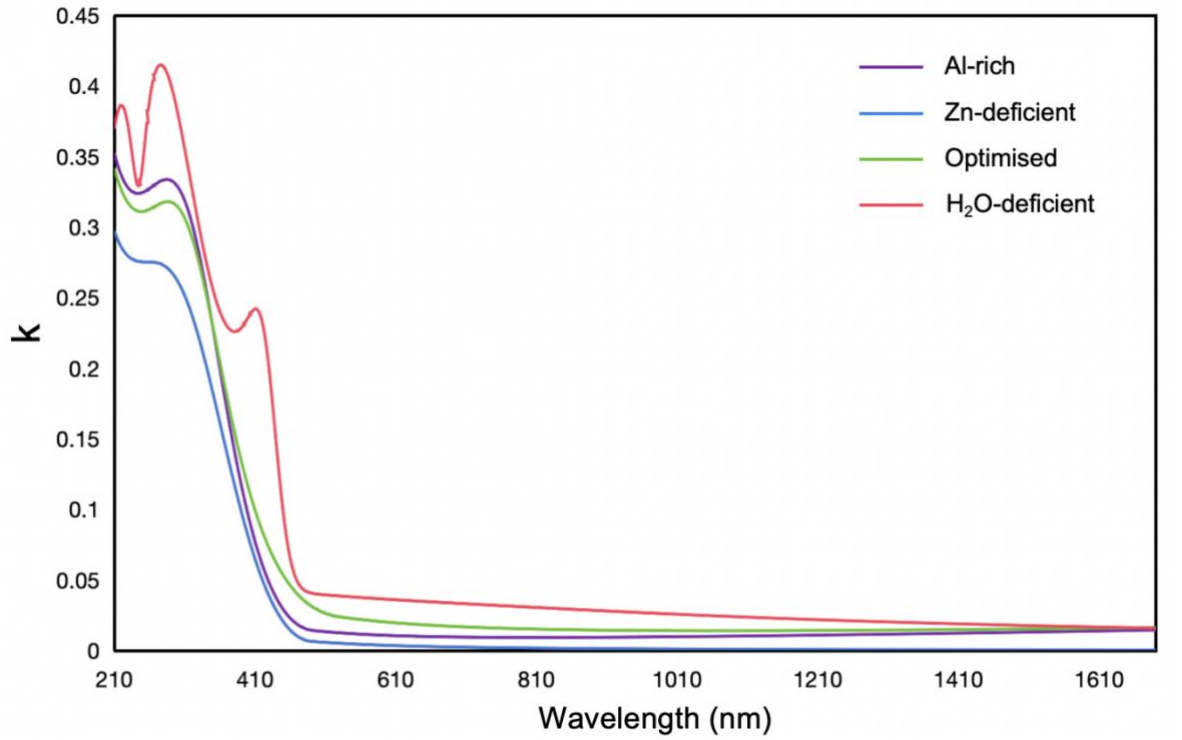


Figure A 86 Spectroscopic ellipsometry data for 40-nm-thick AZO films deposited under the four precursor pressure profiles described in Section 4.2.1. Extinction coefficient k as a function of wavelength.

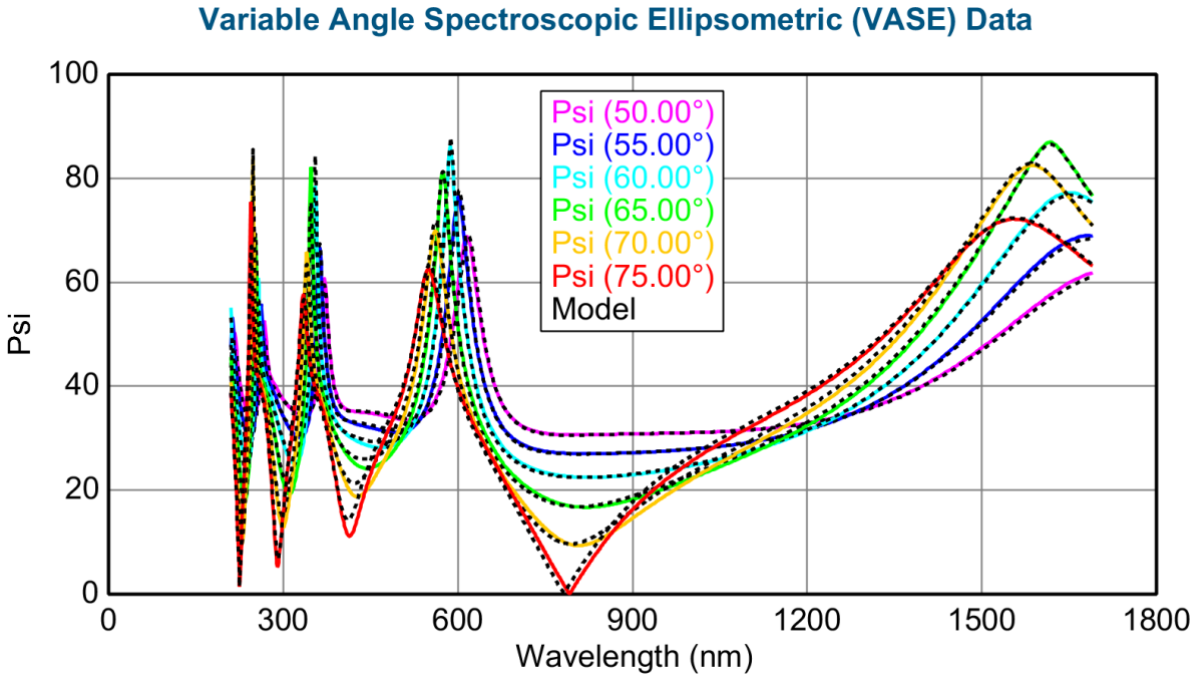


Figure A 87 The fitting curves and measured spectroscopic ellipsometric curves of the optimised sample in Chapter 4.

Appendix D: Additional data for annealing (cooling) study in Chapter 5

This appendix lists the raw effective lifetime data for the annealing and cooling studies in Chapter 5. Table A 14 reports the effective lifetime as a function of peak temperature (300–600 °C) and dwell time (5–40 min), justifying the temperature- and time-dependent choices discussed in Section 5.2.2. Table A 15 reports the four replicate lifetimes per condition behind the temperature–cooling-rate matrix plotted in Figure 5.4. Table A 16 reports the replicate lifetimes for the four cooling rates (CR1–CR4) plotted in Figure 5.5 (a), including which replicate is shown in Figure 5.5 (b). Table A 17 reports the replicate lifetimes for the five ramp-halt temperatures plotted in Figure 5.10.

Table A 14 Effective lifetime (µs @ 1E15 ECD) as a function of both peak temperature and dwell time. All samples were followed by a 10-min slow cooling after the annealing dwell. It shows the shift in passivation dynamics. Lower temperatures require extended thermal budgets to overcome the activation barrier, whereas a high temperature (600 °C) initiates rapid degradation following a brief activation window. The optimal balance is achieved at 450 °C.

Peak temperature (°C)	5 min	10 min	15 min	20 min	30 min	40 min
300	45.2	82.5	148.6	210.4	274.1	285.3
350	124.8	315.2	560.4	742.1	854.6	848.2
450	221.5	585.3	940.8	1311.8	1409.0	1154.7
600	690.8	280.5	92.3	45.6	18.2	--

Table A 15 Effective lifetime (µs @ 1E15 ECD) as a function of both peak temperature and cooling rates under the thermal profiles in Figure 5.3. Raw data for Figure 5.4.

Sample conditions	Effective Lifetime (µs @ 1E15 ECD)			
600 °C slow cool	50.8	43.5	62.9	41.34
600 °C fast cool	19.1	23.0	17.9	14.3
450 °C slow cool	1424.2	1322.1	1218.8	1407.2
450 °C fast cool	1097.6	979.6	761.4	912.3
300 °C slow cool	215.3	206.5	183.9	208.2
300 °C fast cool	194.1	212.2	203.5	207.9

Table A 16 Effective lifetime (μs @ 1E15 ECD) as a function of cooling rates (CR) under the thermal profiles in Figure 5.5 (a).

Condition (Cooling)	Sample 1	Sample 2	Sample 3	Sample 4	Mean	Std. Dev. (%)	Plotted in Figure 5.5 (b)
CR1	1682.4	1795.1	1564.8	1690.5	1683.2	5.6	Sample 1
CR2	1424.15	1322.12	1218.76	1407.19	1343.06	7.0	Sample 2
CR3	1111.6	1245.3	988.7	1121.2	1116.7	9.5	Sample 1
CR4	1097.57	979.55	761.41	912.3	937.71	15.0	Sample 4

Table A 17 Effective lifetime (μs @ 1E15 ECD) as a function of ramp halt temperature under the thermal profiles in Figure 5.10.

Ramp Halt Temp (°C)	Sample 1	Sample 2	Sample 3	Sample 4	Mean (μs)	Std. Dev. (%)
450	1409.0	1509.6	1332.3	1385.7	1409.2	5.3
400	1470.8	1516.9	1366.2	1577.4	1482.8	6.0
350	1690.6	1700.1	1833.8	1639.1	1715.9	4.8
300	1906.8	1924.0	1701.5	1777.5	1827.5	5.8
250	1372.7	1338.4	1363.8	1185.5	1315.1	6.7

Appendix E: Additional information on Time-of-Flight Elastic Recoil Detection (ToF-ERD)

This appendix presents the ToF-ERD data referenced in Section 5.6.1 to corroborate the NR-inferred hydrogen loss from the AlO_X cap. Figure A 88 (a) shows a representative Time-of-Flight versus Energy coincidence histogram for the AZO/AlO_X sample, illustrating the kinematic separation of H, C, O, Al, Si, and Zn recoils. Figure A 88 (b) reports the hydrogen concentration (at.%) at specific positions within the stack for the as-deposited and annealed samples. Figure A 88 (c) and (d) shows the full elemental depth profiles for the as-deposited and annealed states, respectively, with the atomic composition normalised to 100% at each depth. Measurements were carried out by Matthew K. Sharpe at the Surrey Ion Beam Centre using a 16 MeV $^{127}I^{8+}$ beam.

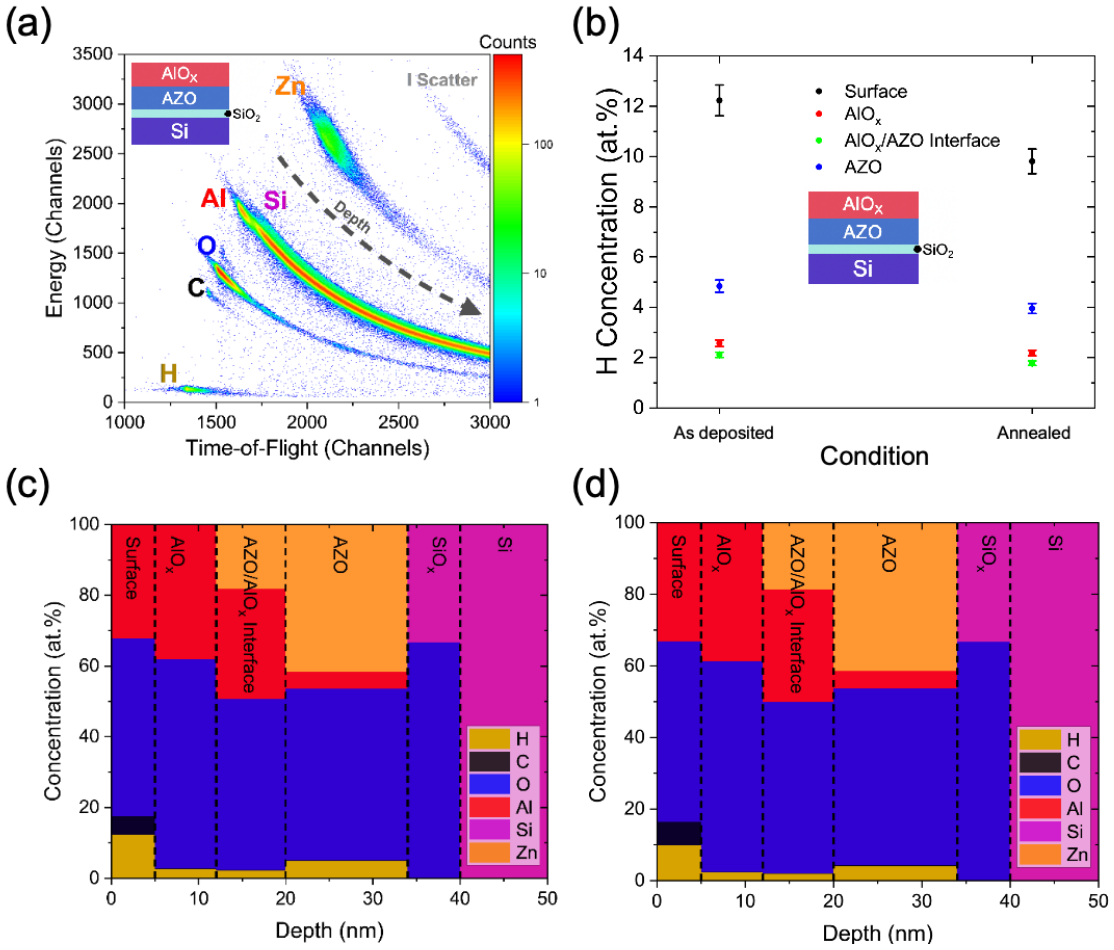


Figure A 88 ToF-ERD analysis of the passivation stacks. The ToF-ERD measurements and initial data processing presented here were performed by our collaborator Matthew K. Sharpe at the Surrey Ion Beam Centre, utilising a 16 MeV $^{127}I^{8+}$ ion beam with an incident and exit angle of 69.5° and a scattering angle of 41°. A summary of the relevant data are reproduced here from the raw datasets for comparison. (a) Representative Time-of-Flight versus Energy (ToF-E) 2D coincidence histogram for the AZO/AlO_X sample, illustrating the distinct kinematic separation of recoiled elements (H, C, O, Al, Si, and Zn). (b) Extracted hydrogen (H) concentration (at.%) at specific layer locations within the AZO/AlO_X stack, comparing the as-deposited and annealed conditions. (c, d) Elemental depth profiles obtained via modelling from the experimental data for the AZO/AlO_X samples in the (c) as-deposited and (d) annealed states. At each depth, the total atomic composition is normalised to 100% to clearly delineate the material structure.

Appendix F: Additional information on SPV and transient-SPV

This appendix provides the spatial maps and complementary transient-SPV representations referenced throughout Chapter 6. Figure A 89 shows the 2D KP-SPV maps of the pristine Si/AZO samples (never coated with AlO_x) in dark and under illumination, for both the as-deposited and slow-cooled conditions discussed in Section 6.2.1. Figure A 90 shows the 3D SPV maps of the as-deposited Si/AZO sample after AlO_X deposition and etching (Section 6.2.2). Figure A 91 shows the 2D KP-SPV maps of the annealed fast- and slow-cooled Si/AZO samples (AlO_X etched after annealing) discussed in Section 6.2.3. Figure A 92 plots the transient-SPV signal as a function of photon energy at fixed time delays from 20 ns to 2 ms for the four samples of Figure 6.1, with shaded regions A (near/sub-bandgap), B (above-bandgap early decay), and C (late-stage decay), providing a complementary view of the contour plots in Figure 6.6.

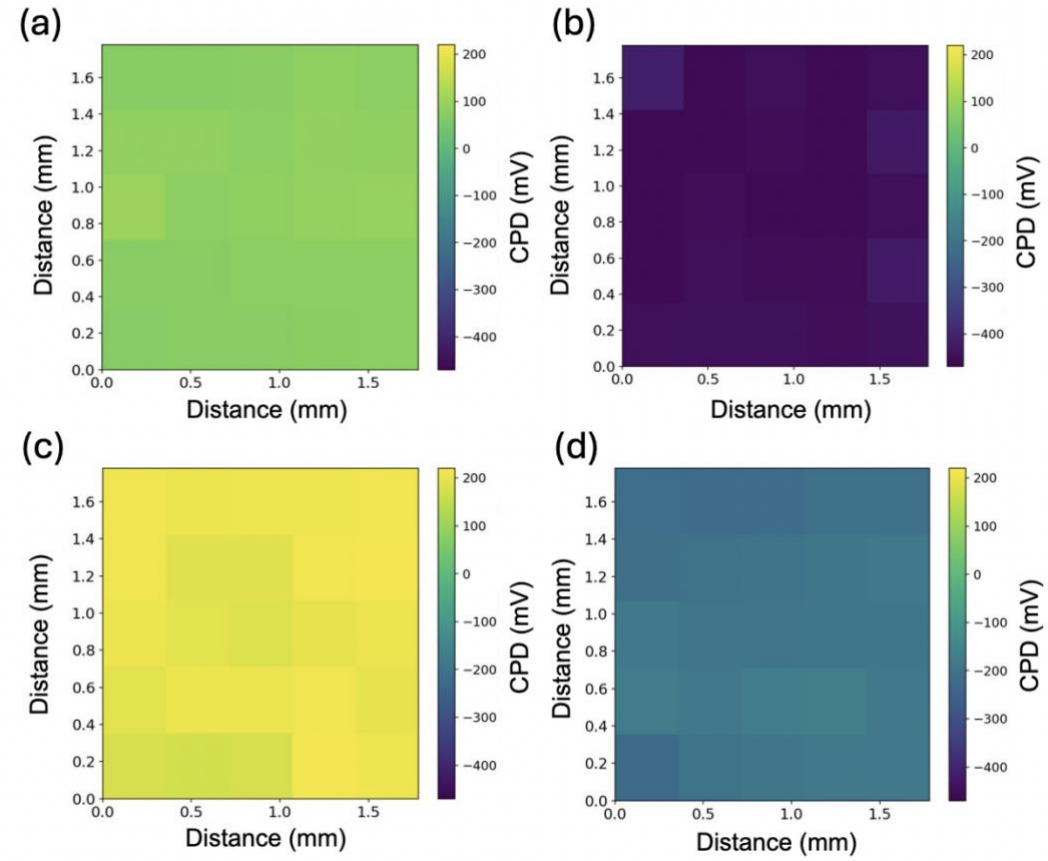


Figure A 89 2D SPV mapping of Si/AZO (AlO_X has never been deposited). (a) As-deposited sample measured in dark; (b) As-deposited sample measured under illumination; (c) Slow-cooled sample measured in dark; (d) Slow-cooled sample measured under illumination.

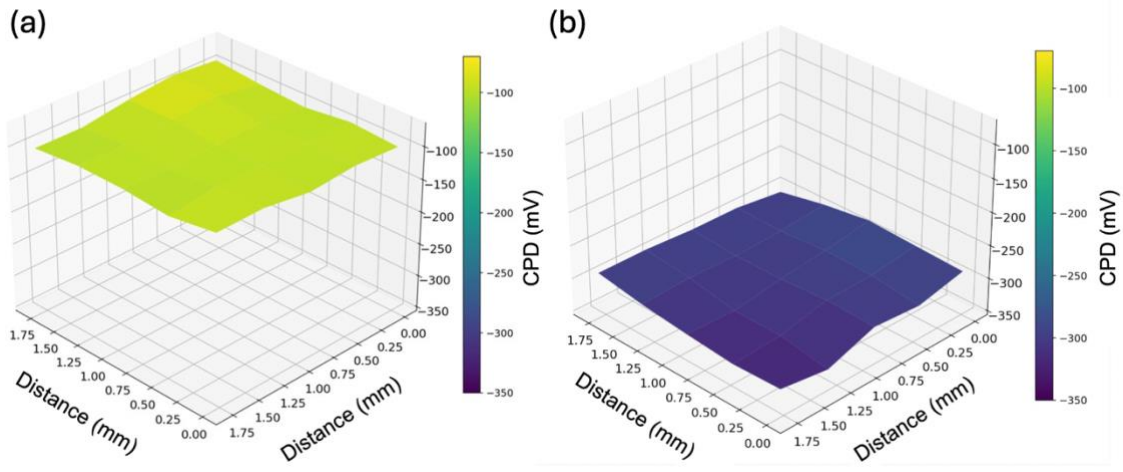


Figure A 90 3D SPV mapping of as-deposited Si/AZO (AlO_X etched before SPV measurements) (a) in dark, and (b) under illumination.

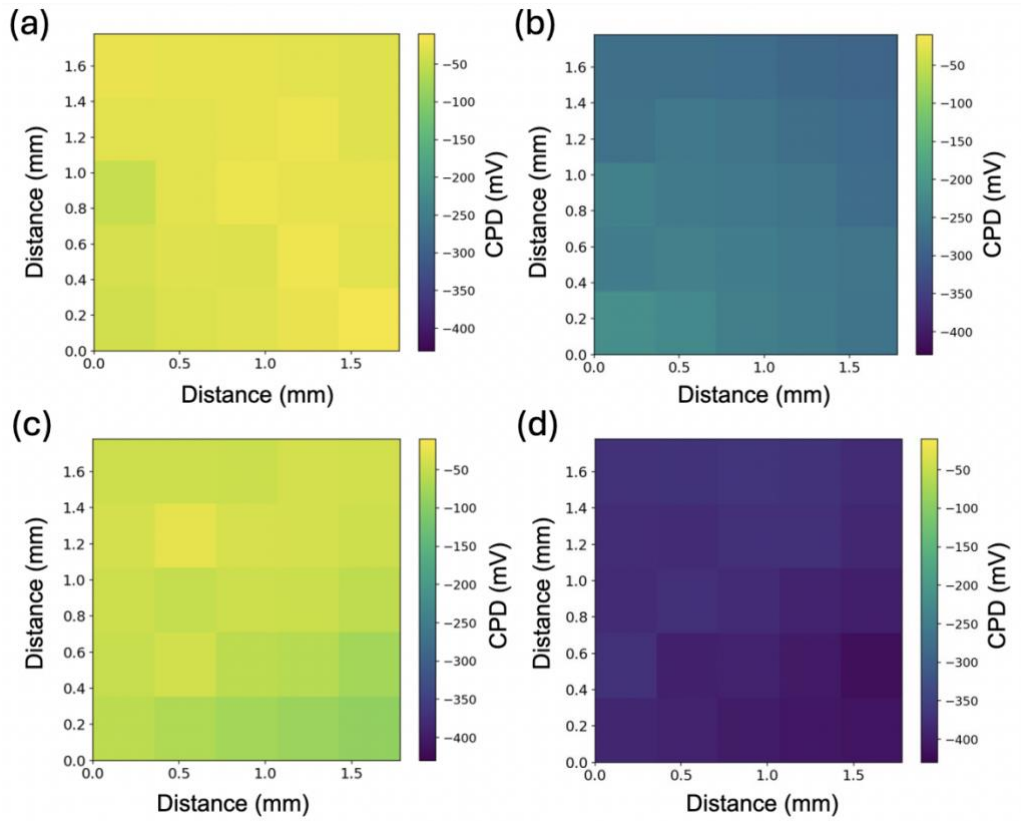


Figure A 91 2D SPV mapping of annealed AZO/AlO_X (AlO_X etched after annealing and before SPV measurements). (a) Fast-cooled sample measured in dark; (b) Fast-cooled sample measured under illumination; (c) Slow-cooled sample measured in dark; (d) Slow-cooled sample measured under illumination.

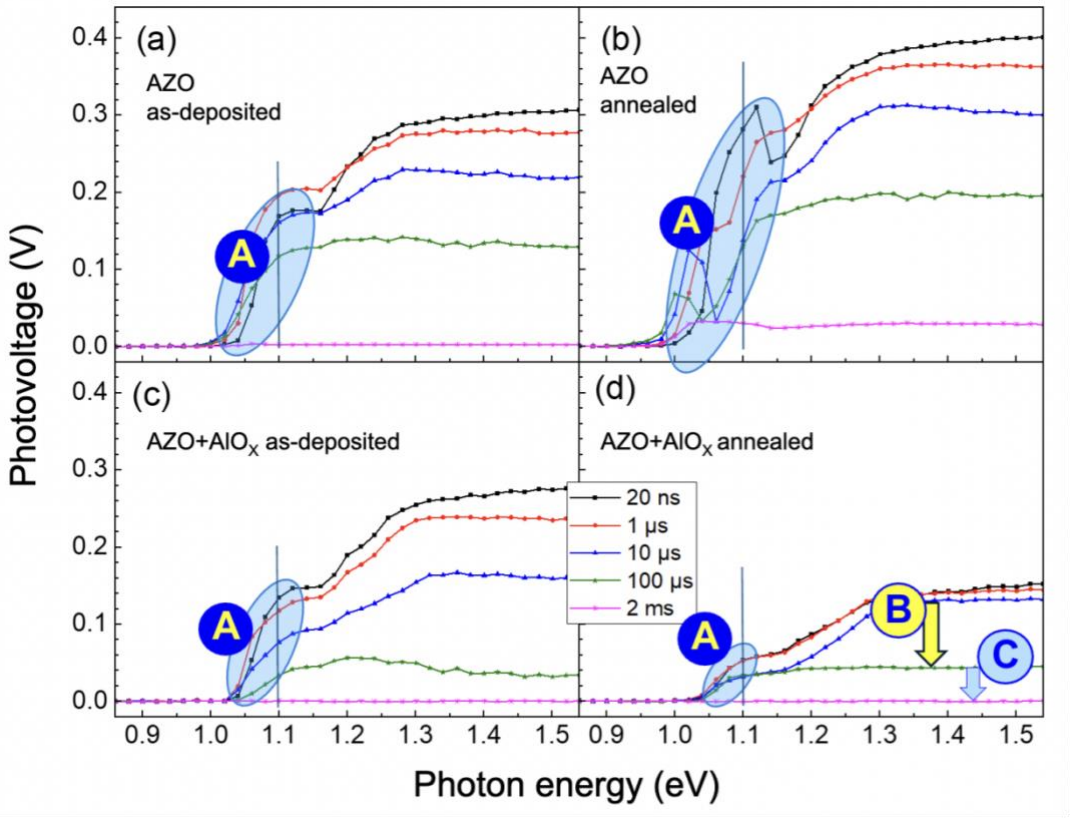


Figure A 92 The SPV signal as a function of photon energy at different time delays for the four samples, revealing details about charge separation via interface states. Shaded regions labelled A (near/sub-bandgap, photon energy $\lesssim$ 1.1 eV), B (above-bandgap early decay, 20 ns–100 µs), and C (late-stage decay, ≥100 µs).

Appendix G: Additional information on ToF-SIMS

This appendix collects the ToF-SIMS depth profiles of the bulk matrix and silicon-side fragments that support the interfacial hydrogen analysis in Section 6.5. Figure A 93 shows the Al^- and $^{68}ZnO^-$ intensities for the as-deposited and annealed AZO/AlO_X samples, indicating that the bulk matrix is relatively stable under annealing. Figure A 94 shows the $Al_2O_3^-$ intensity and the $Al_2O_3^-/AlO^-$ and ZnO_2^-/ZnO^- intensity ratios, which also remain relatively constant upon annealing. Figure A 95 shows the $^{29}SiO^-$ intensity, which cannot be adequately resolved due to the resolution limits of ToF-SIMS. Figure A 96 shows the $^{29}SiH^-/Si^-$ and $^{29}SiHO^-/Si^-$ intensity ratios; their independent behavior is discussed in Section 6.5.3 and motivates the use of the matrix-effect-mitigating $^{29}SiH^-/^{29}SiHO^-$ ratio plotted in Figure 6.11.

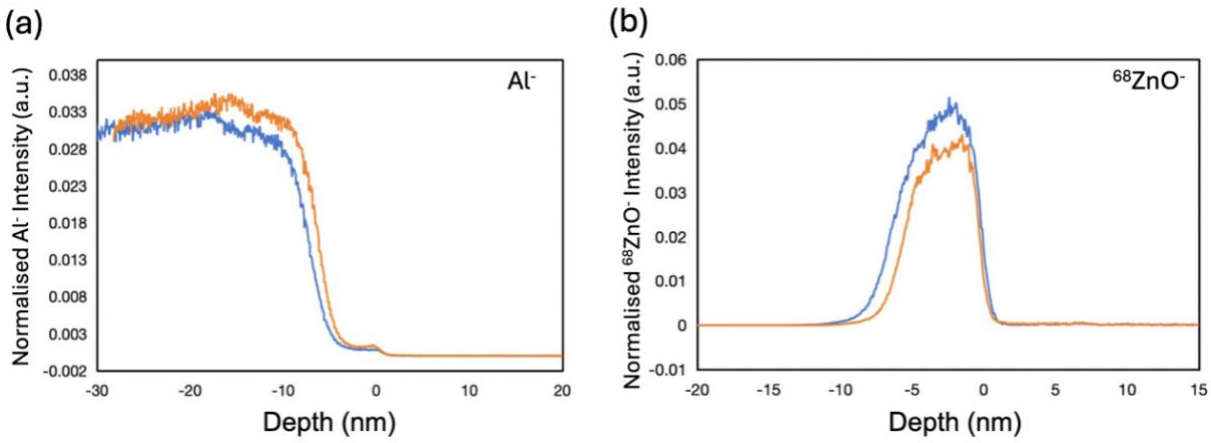


Figure A 93 ToF-SIMS results showing (a) Al^- and (b) $^{68}ZnO^-$ intensities between as-deposited (blue) and annealed (orange) standard AZO/AlO_X samples.

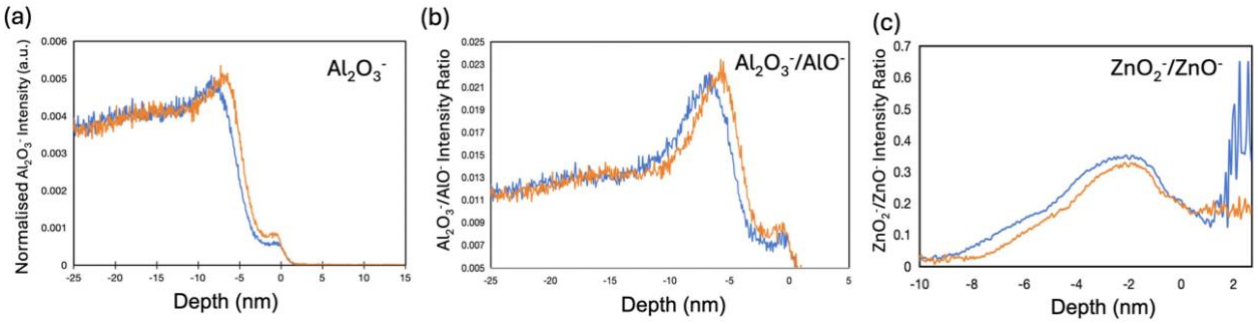


Figure A 94 ToF-SIMS results showing (a) $Al_2O_3^-$ intensity, (b) $Al_2O_3^-/AlO^-$ intensity ratios, and (c) ZnO_2^-/ZnO^- intensity ratios between as-deposited (blue) and annealed (orange) standard AZO/AlO_X samples.

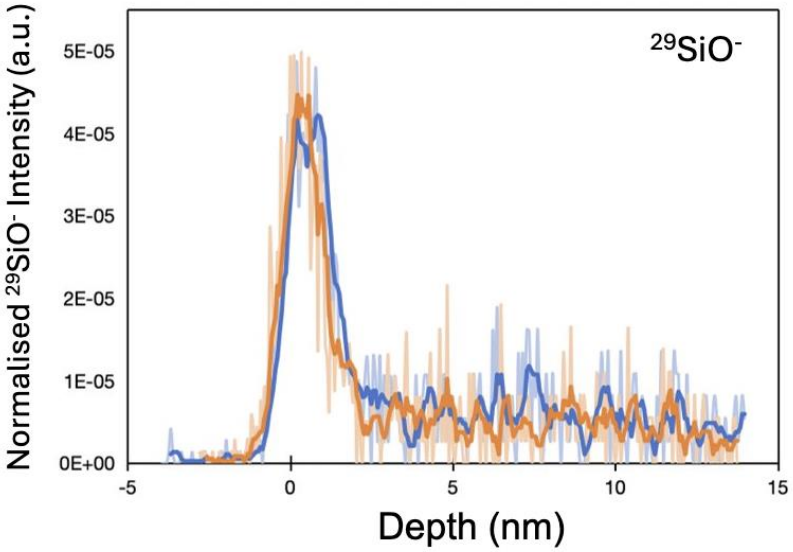


Figure A 95 ToF-SIMS results showing $^{29}SiO^-$ intensity between as-deposited (blue) and annealed (orange) standard AZO/AlO_X samples.

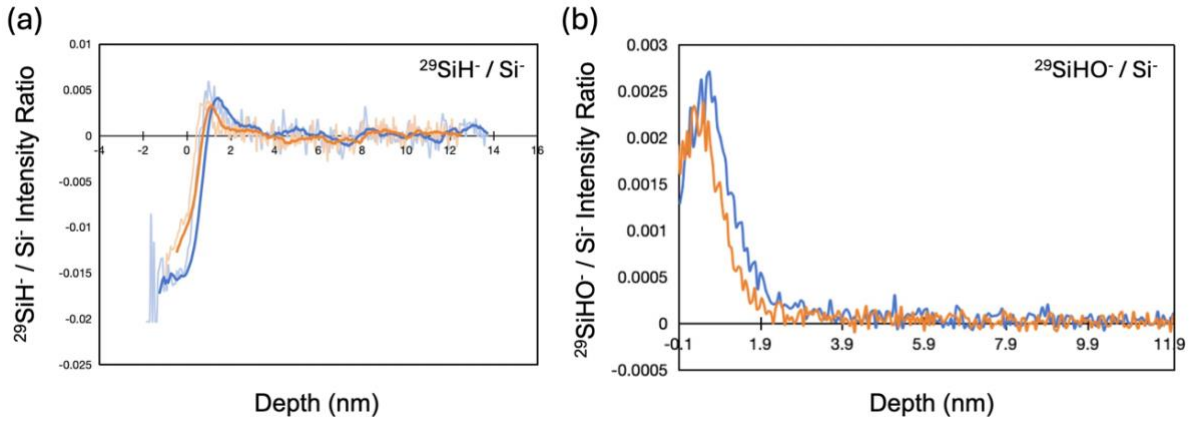


Figure A 96 ToF-SIMS results showing (a) $^{29}SiH^-/Si^-$ and (b) $^{29}SiHO^-/Si^-$ intensity ratios between as-deposited (blue) and annealed (orange) standard AZO/AlO_X samples.